PLASMA SPRAY DEPOSITION OF POLYMER COATINGS

A thesis submitted for the degree of doctor of philosophy

by

Yuqing Bao

Department of Materials Technology
Brunel University, Uxbridge

October 1995

Brunel University, Uxbridge, West London
Department of Materials Technology
Y. Bao
Plasma Spray Deposition of Polymer Coatings
1995
PhD

Abstract

This work investigates the feasibility of the use of plasma spray deposition as a method of producing high performance polymer coatings. The work concentrates on the understanding of the processing of the plasma spraying of polymers, the behaviour of polymeric materials during deposition, and the study of process-structure-properties relationships.

Processing modelling for the three stages of the evolution of a polymer deposit (droplet-splat-coating) has been carried out using heat transfer theory. A theoretical model is proposed which consists of three parts: the first part predicts the temperature profile of in-flight particles within plasma jet, the second part predicts the cooling of isolated splats impacting on a substrate and the third part, the heat transfer through the coating thickness.

The heat transfer analysis predicts that the development of large temperature gradients within the particle is a general characteristics of polymers during plasma spraying. This causes difficulties for polymer particles to be effectively molten within the plasma jet without decomposition. The theoretical calculations have predicted the effect of processing parameters on the temperature, the degree of melting and decomposition of in-flight polymer particles. With the aid of the model, the conditions for the preparation of high integrity thermoplastic deposits have been established by the control of the plasma arc power, plasma spraying distance, feedstock powder injection, torch traverse speed and feedstock particle size. The optimal deposition conditions are designed to produce effective particle melting in the plasma, extensive flow on impact, and minimal thermal degradation. The experimental work on optimizing processing parameters has confirmed the theoretical predictions.

Examination of polymer coating structures reveals that the major defects are unmelted particles, cracks and pores. Five major categories of pores have been classified. It also revealed a significant loss in crystallinity and the presence of a minor metastable phase in the plasma deposited polyamide coatings due to rapid solidification. The study has indicated that the molecular weight of a polymer plays an important role on the splat flow and coating structure. Under non-optimal deposition condition, substantial thermal degradation occurred for which a chain scission mechanism is proposed for plasma deposited polyamide coatings.

There are difficulties in achieving cross-linking during plasma spray deposition of thermosets. The theoretical calculations predict that adequate cross-linking is unlikely in a coating deposited under normal conditions, but preheating the substrate to above the cross-linking temperature improves the degree of cross-linking of the coatings substantially. In addition, the coating thickness has a major effect on the degree of cross-linking of thermosets. The calculations also predict that lowering the thermal conductivity by applying a thermal barrier undercoat and using a faster curing agent to reduce time required for the cross-linking reaction can improve the degree of cross-linking of thermoset deposits. The experimental results for the degree of cross-linking and wear resistance confirmed these predictions.

ACKNOWLEDGEMENTS

I would particularly like to thank Professor D.T. Gawne, my supervisor, for his guidance, constructive discussion and encouragement throughout the experimental programme and the preparation of the thesis.

I would like to thank my husband Dr Tao Zhang and my son Xian Peng Zhang for their support, encouragement and help.

I would also like to thank Professor M.J. Bevis, the academic and technician staff in the Department of Materials Technology for their valuable help.

The financial support of the EPSRC and MoD is gratefully acknowledged

CONTENTS

INTRODUCTION

Polymer coatings are used extensively to protect and decorate articles, components and structures. The traditional methods of applying polymers on engineering components and structures are by mainly painting in which the polymer is dissolved in a solvent, in order to provide a binder for the pigment and facilitate coverage of the substrate by application in the liquid state. Painting is a low-cost and highly developed technology but is facing increasing problems, including emission caused by the solvents in wet paints and the rising cost of waste disposal. Painting also has difficulties in the requirement for drying, which leads to substantial downtimes, as well as the control of coating thickness and the limited quality of the coatings.

The polymer powder coating process involves the formation of a polymer coating on a component by the application of a dry powder to its surface followed by stoving at an elevated-temperature. Polymer powder coating has been developed substantially over the last fifteen years: it now occupies 5-10% of the total industrial painting and is a possible alternative to painting in many cases[1]. Polymer powder coating processes have several advantages over conventional painting. One of the most significant is that they are more environmentally acceptable. There is no solvent to cause air pollution and less make-up air is required in the bake ovens than for solvent-based paints, where the volume must be high enough to keep the solvent content below explosive concentrations. In addition, powder coating involves relatively little waste as stray powder or overspray can be collected and re-used[2]. For example, in the application booth for electrostatic spraying, the overspray powder can be removed from the air, the powder recycled and the air returned to the building. In contrast, the disposal of sludge produced by overspray in conventional painting operations is becoming increasingly expensive.

Polymer powder coatings are generally applied to relatively low-cost, non-critical applications such as pipes, office equipment, refrigerators and double glazing frames. This study is aimed at investigating plasma spraying as a powder coating process for the production of high-performance polymer coatings. The work concentrates on understanding and modelling the process of plasma spraying of polymers, studying the relationships of process-structure-property, investigating the behaviour of polymers during deposition and its resulting influence on the deposit properties in order to produce sound, strongly bonded coatings of generic polymers.

CHAPTER 1. EXISTING POLYMER POWDER COATING PROCESSES

Several techniques employing powdered polymers are available for applying polymer coatings to various components. The principal ones in commercial use are electrostatic spraying and fluidized bed dipping.

1.1 Fluidized bed dipping

The fluidized bed dipping is the oldest polymer coating process and originated in W.Germany in late 1950s[3]. In this process, the coating is carried out using a fluidized bed system. The schematic diagram of a fluidized bed is shown in Figure 1.1 (after reference[4]). The fluidized bed consists of two compartments separated by a porous plate. Cold compressed air is forced through the porous plate to the compartment containing powder, causing fluidization in which the powder is suspended in a fluidized state and behaves like a liquid. The substrate to be coated is preheated above the melting point of the polymer powder in an oven and then dipped into the fluidized bed of the powder. The powder melts and forms a coating. The fluidized bed dipping process can produce polymer coatings with the thicknesses of 200 to 2000 μm, but it is difficult to apply thinner coatings of less than 200μm. In addition, this process is seldom used for large objects because of the size limit of the fluidized bed and powder reservoir required.

1.2 Electrostatic spraying

Electrostatic spraying gained commercial acceptance in early 1960s. In the electrostatic spray process, the coating powder is withdrawn from a fluidized feed hopper by clean, dry compressed air and electrostatically charged in the high voltage corona field of a spray gun[2]. The charged particles are attracted to the earthed metal substrate which is to be coated and adhere to its surface by electrostatic attraction. A typical electrostatic spray gun is shown in Figure 1.2 (after reference [5]). The coated substrate is then placed in an oven and the particles are melted and fuse together to form a continuous coating. The electrostatic spray process can be used to coat a wide variety of objects with various configurations. When powder is electrostatically applied to parts at ambient temperature, the coating thickness tends to be self-limiting (20 - 75μm)[2] since the substrate becomes insulated by the powder after the powder is deposited on the surface of the substrate. Should greater coating thicknesses be required, a preheated substrate can be used, relying on residual heat to thermally attract more powder after insulation has occurred. Variations of electrostatic spraying include hot electrostatic (flock) spraying and airstatic spraying [6].

1.3 Combustion flame spraying

The idea of spraying plastic materials adapted from metal spraying technology, has long been of interest[7]. The techniques of thermally spraying metal powder date back to the beginning of this century and in 1923 Schori took out the first patent for spraying metal powders using a combustion flame torch[8]. Had suitable plastics materials been available, this torch would have been capable of spraying them. However, no sooner had plastics been produced in a powder form suitable for flame spraying, than fluidized bed dipping(1954) and electrostatic spraying(1962) were introduced[9]. Because these methods gave a more uniform coating thickness at that time, combustion flame spraying was not favoured and indeed, these two processes remain the most popular for applying plastic coatings in polymer powder coating industry.

However, because of recent developments in polymer manufacture and spray equipment, thermal spraying of polymers, specially in the field where the conventional processes are not suitable, comes to find its own applications [10,11]. Reports have shown that thermal spraying of polymers, mainly combustion flame spray, have been applied to the areas of aerospace and aircraft industry, oil industry, newsprint and telecom, railway and constructural industry etc. in Europe, U.S.A and Japan, to produce various functional coatings, including abradable seals coatings, corrosion resistance coatings, wear protection, electrically and heat insulating coatings and decorative coatings[12,13,14,15].

Combustion flame spraying is a member of the family of thermal spraying process. There are three basic thermal spraying coating processes: combustion flame spraying, plasma spraying and electric arc spraying in which materials are melted to form liquid droplets, which are then propelled onto a substrate surface where the individual particles impact, spread and solidify into splats. These splats then incrementally build a new surface and form a coating. Combustion spray processes have several subfamilies which offer a range of quality and cost.

Flame spray uses an open or external combustion oxy-fuel jet which melts and deposits either powder or wire feedstock. The process is portable and versatile. Work can be performed on site and large objectives may be coated without the need for large tanks or furnaces. Small components may also be coated easily. This process has been used to produce polymer coatings ranging from 250μm to over 1mm in thickness[11]. However, the process depends greatly on operator skill and the surface finish of the coating may be inferior to that produced by other techniques. The polymers may suffer increased degradation from overheating compared with other polymer coating techniques mentioned above in addition to higher porosity and oxide levels[14,15,16].

D-gun, a proprietary combustion spray process, unlike the unconfined jet of flame spraying uses high pressure, higher velocity combustion shock wave to melt and accelerate particles. It has been reported to produce denser, lower oxide content deposits of high melting temperature materials than typical flame sprayed inorganic coatings[17]. No report on using D-gun to spray polymers has been found.

More recently, the high velocity oxy-fuel (HVOF) spray process has been developed[18], which is also,an internal combustion process, thus incorporating many of D-gun's improvements in coatings over conventional flame spray. HVOF has been shown to have higher combustion temperatures, longer and more efficient heating times, and higher particle velocity than conventional flame spray, leading to reported increases in deposit density and lower oxide content[18,19]. It has been applied successfully to spray aluminum-silicon/polyester abradable coatings[12].

Electric arc spraying, which uses wires as feedstock also differs significantly from the other thermal spray methods in that a highly accelerated but cool air jet atomizes a melting wire tip formed by a continuous arc between two consumable, current carrying wires. Unlike plasma and combustion spray processing, particle begins cooling immediately on leaving the molten wire tips. The cool nature of this spray process leads to substantially cooler substrate surface while assuring that the materials were molten prior to impact[20]. No report on its application in polymer coating has been found.

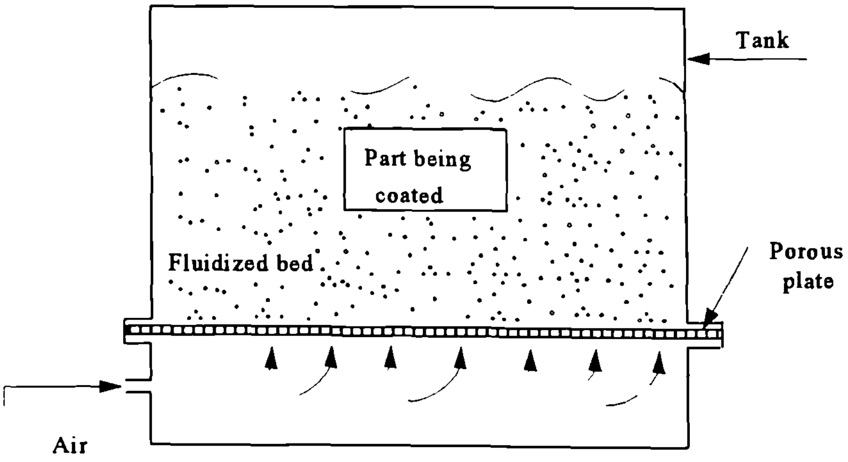

Figure 1.1 Schematic diagram of a fluidized bed.

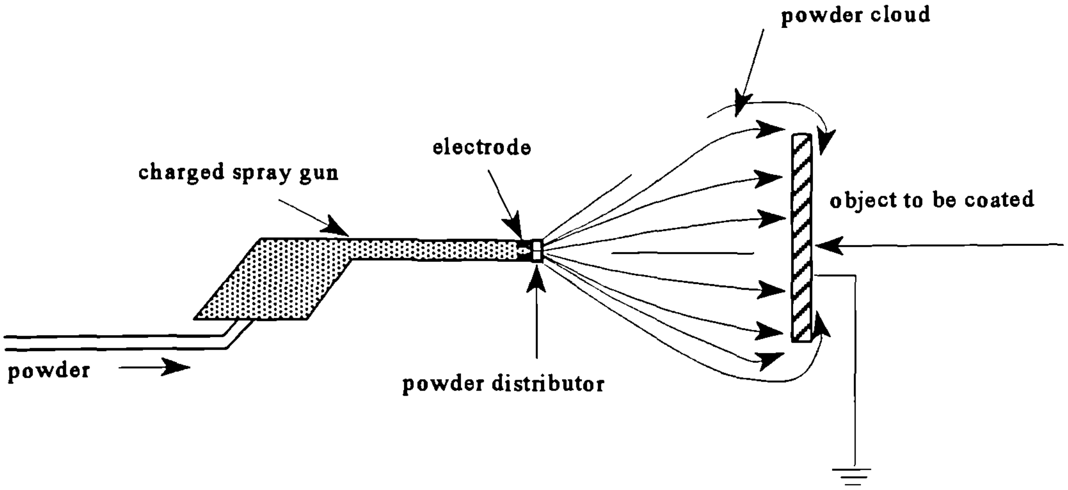

Figure 1.2 Schematic diagram of an electrostatic spray gun

CHAPTER 2. PLASMA SPRAYING PROCESS

Plasma spraying also uses high temperature gas jets to heat material feedstock but the jet is formed by heating inert gases in an electric arc not by combustion. These gases are heated to a plasma state and exit the gun with gas temperatures often exceeding 15 000 K. the powders are entrained in the hot jets by various means to provide sufficient temperature and dwell time to melt the majority of the injected particles.

The technology of plasma spraying has been developed to a high degree of sophistication for metallic and ceramic coatings but little attention has been given to polymers. Plasma spraying has major advantages over combustion flame spraying and considerable potential for upgrading the quality of existing polymer coatings: The heat source is an inert or reducing plasma gas, which suppresses the degradation/oxidation of the particles in flight. The particle velocities are up to an order of magnitude greater than those in combustion flame spraying, which may lead to substantially improved adhesion, compaction and reduced porosity. More details on plasma spray process has been summarized as following:

2.1 Plasma generation

Gases heated to temperatures higher than a few thousands degree centigrade constitute a distinctive fourth state of matter - plasma, the highly ionized state of mass - which differs from ordinary gases particularly by the following properties[21]:

1. A considerable number of inelastic collisions between molecules occur which result in the production of molecules in excited quantum states and may cause their dissociation and ionization.
2. Chemically uniform gas transfer into a gaseous mixture of various particles: molecules, atoms, positive and negative ions, electrons, photons etc.
3. It is through these charged particles that electric and magnetic field can act upon the ionized gas. Being conductive, the gas mixture can accept

energy from an electric or magnetic field. The mixture as a whole is quasi - neutral, the concentration of positive and negative particles being roughly equal at every point($n_+ \sim n_-$).

4. The neutralization of some charged particles - known as the recombination process - takes places simultaneously in plasma. Energy is released during the recombination process.

It is because of the above properties, the plasma can be used as a source of thermal and kinetic energy. The principle of the plasma spray process is to utilize the energy contained in a thermally ionized gas mixture to melt and propel fine powder particles on to a target surface such that they adhere and agglomerate to produce coatings[22]. An important mean of heat absorption in the plasma is by electron/ion/atom recombination on the surface of particle followed by conduction into the interior of the particle[23]. The heat transfer from plasma to the particle is much more effective than that in a combustion flame.

2.2 Plasma torch

The technical creation and utilization of plasma as the high temperature sources is realized in the plasma torch or the plasma gun. The functions of a plasma spray torch are to generate and sustain a captive high-temperature region so that powder particles introduced into that region can be heated and accelerated on to a workpiece. High temperature is achieved by concentrating the power of an electric arc into an extremely small volume[24] while acceleration is obtained from high jet velocity achieved by appropriate design of spraying nozzle.

The essential elements of a plasma torch are shown in figure 2.1. The anode is usually copper and cathode tungsten. A gas, normally argon, nitrogen, or a mixture of them with hydrogen or helium, is caused to flow around the cathode and through the anode which is shaped as a constricting nozzle. While the gas is flowing, a direct current arc, usually initialled with a high frequency discharge, is maintained between the electrodes, which ionizes the gas and the resulting plasma leaves the nozzle with a high velocity for a short distance. This produces a small region with an extremely high temperature into which powder particles can be introduced[25].

2.3 Processing characterization

The temperature of a plasma beam varies along its axial length and radius. A typical temperature profile of a plasma beam can be found in Figure 6.1. Local plasma temperatures in a spraying torch are normally in the range of 10000 - 15000 K and can in certain devices reach 30000 K[25]. The plasma temperature falls steadily with distance from the nozzle. From Vardelle etc.[26], the plasma jet can be divided into three regions: the core region in which the plasma temperature is relatively constant 12000 - 12500K, extending to about 10 - 12 mm from the torch nozzle. This is followed by a transition region in which the plasma temperature falls rapidly to less than 3000K at 100mm from the nozzle exit. In the last region, the gas temperature drops gradually as gas is mixed with the entrained ambient air. With such a flexible temperature profile plus its high beam velocity and inert atmosphere, the plasma spray process offer a wide range of materials which can be sprayed from low melting point materials to refractory metals and ceramics and combinations of them. Any materials with a "stable" liquid state can be deposited by the plasma spray process[27].

A high in-flight particle velocity is another advantage offered by the plasma spray process. The plasma gas flowing through the high temperature of plasma jet generates a large volume expansion, since the geometry of anode constricts such a volume expansion of plasma gas, a plasma jet with an extremely high beam velocity is formed. The velocity of a plasma jet can be up to $800ms^{-1}$, depending upon the geometry of the torch anode[28]. High beam velocity gives the powder introduced a high in-flight particle velocity, and thus high kinetic energy, which promotes the coherence of individual splats and adhesion of coating to substrate and reduces the porosity of the deposits.

In addition to its high temperature, high beam velocity and inert atmosphere, plasma spraying also provides the materials sprayed a high cooling rate (10^6 - 10^8 Ks^{-1} [29]). The plasma spray process consists essentially of two steps. Firstly, the injection of powder particles into a high temperature plasma: the powder particles are heated and accelerated to form high-velocity molten droplets. Secondly, the interaction of the droplets with the substrate (true substrate or previous deposit) involving impact,spreading and solidification of the molten droplet. Typical dwell times inside the plasma are the order of milliseconds. Spreading is accomplished within fractions of a microsecond and solidifying times are of the order of 0.1 - 10 μs[30]. In other words, an injected particle completes its melting, spreading and solidifying within 10^{-5} s to 10^{-3} s. Such a high cooling rate offers the potential for the avoidance of thermal decomposition of a polymer during spraying. The high cooling rate can also protect the substrate and previous deposit from overheating and produce coatings on to thermal sensitive materials such as polymers, glasses and papers providing certain additional substrate cooling methods are adapted. The latter can not be realized in the fluidized-bed dipping *nor the electrostatic spraying process.*

2.4 Coating formation

Plasma sprayed coatings are built up particle by particle quenched from various states of heating. Particles melting in a plasma beam acquire a spherical shapes as the result of surface tension. These particles possess high kinetic energies obtained from the high energy plasma beam. When these flying molten particles impact on the substrate, they transfer their heat to local parts of surface and cool rapidly. Their kinetic energy transforms into thermal and deformation energy at the point of impact so that the droplets experience two simultaneous phenomena: spreading and solidification[31].

There are several ways in which the impacting droplet can behave and these are classified as follows [32]:

1. When the sprayed particle is not completely molten, the thin, partially melted outer layer spreads over the deposit, whereas the unmelted particle core deforms on impact with the substrate.
2. A completely molten droplet impacts on the substrate spreads out radially into the form of a thin disc. In practice, however, the flow is often not uniform and the periphery of particle is not circular.

3. When the resultant thin disc fails to establish a sufficiently strong bond with the target surface, the outer portion of the disc either breaks off or cracks up at edges and folds in towards the centre.

After continuously impacting the surface, the molten particles of sprayed materials are deposited on one another like pancakes or lamellas until the coating is formed. The plasma coatings are therefore characterized by a layered structure, which is totally different from that of the corresponding bulk materials. The lamella (splats) are aligned in the plane of the substrate and material properties in the planar(parallel to the substrate) and transverse (perpendicular to the substrate) direction are often expected to be distinctly different. This formation mechanism leads to the inhomogeneity of the internal structure of a plasma coating. A plasma sprayed coating usually consists of splats with different sizes, semi-melted or un-melted particles, splats boundaries, particle boundaries, pores, and inside a splat: grains with different sizes and grain boundaries[23]. The density of plasma coatings is thus lower than the theoretical density of the same bulk materials. The density of plasma coatings varies within 85% to 93%[31].

2.5 Coating microstructure

There is no significant research has been undertaken on the microstructure of thermal sprayed polymer coatings. However some important phenomena observed in the plasma spraying of metallic and ceramic materials suggested that the possible interactions of high temperature plasma to the injected materials which could be the same important when the polymeric materials are to be sprayed.

As a result of the rapid quenching of splats, the structure of a plasma coating may be metastable and nonequilibrium phases may be present, e.g., alumina coatings consist of a high volume fraction of gamma in addition to the equilibrium alpha phase when the particles are only slightly superheated on impact or substrate has poor thermal conductivity (or in the outer layers of a thick coating). When the particles are highly superheated and impact on a substrate with high thermal conductivity, delta and theta may be formed in addition to gamma, with alpha suppressed[33, 34]. The proportions of the various forms of alumina present in a coating depends on the spraying conditions and the particle size of feedstock powder[35].

When spraying polymeric materials with a combustion flame, the oxidation of polymers at elevated temperature causes the modification of chemical structure and physical properties of the polymers[14,15,16]. In most reports, the interaction of plasma and particle has been considered in term of the physical effects of heating and acceleration. Chemical reaction between plasma gas and particles is generally assumed not to occur because of the inert nature of argon and helium, the gases used most frequently in plasma spraying. However, some researches indicated that if a high-velocity stream of hot, fine metallic or ceramic particle is projected through the air on to a substrate the air may be entrained into the gas stream and that oxygen in particular reacts with the surface of the powder particles while they are in flight from torch to substrate[25,32,36]. On arrival at the substrate the particles may have been oxidized and thus oxide inclusions *may be formed in the coating structure, leading to* lower as-sprayed coating density and bond and cohesion strength.

The extent of oxidation or solution of the gas in the powder in the cases where the gas is not inert is related to the transit time and temperature of the powder in the plasma, the composition of plasma gas and the amount of intermixing of plasma gas with the ambient gas between the nozzle and the substrate. The use of hydrogen to reduce the amount of oxidation during spraying may be somewhat effective; but may be due as much to a shielding effect (by reaction with oxygen from air entrained into the plasma stream) as to actual reduction of oxide formed on metallic powder[34]. Literature has also indicates that the extent of oxidation of powders in the plasma flame depends strongly on the type of torch. The differences in extent of oxidation of the coatings can be dramatic when different air-spraying torches were used[34].

In addition to above interaction, some changes in composition may occur due to selective evaporation of one component in an alloy, the decomposition to a gas, or due to reaction with atmosphere. If the loss of a component with a high vapour pressure can be predicted, it can obviously be compensated for in the powder manufacture. It must be keep in mind, however, that such a loss will be more rapid from a fine powder than a coarse powder. It becomes even more imperative to use a very narrow powder particle size distributions to ensure a homogeneous coating composition[31,34].

2.6 Main factors affecting coating quality

The quality required of a plasma sprayed coating will depend upon its fitness for the intented application, but generally a high density, coherence and adhesion to the substrate are desirable. The quality of a plasma sprayed coating is dependent upon the state of the particles when they impinge onto a substrate, while the state of particles on impact is determined by particle temperature, velocity, viscosity, density and heat and kinetic energy exchange with the substrate. Figure 2.2[37] indicates some of the parameters which will play important roles in the plasma spray process. If Ql represents the coating quality, the important factors affecting Ql may be summarised by following equation[38]:

$$\mathbf{Ql = f(Pp, Tp, Vp, Aa, As)} \qquad (2\text{-}1)$$

where: Pp - properties of the powder, Tp - temperature of particles, Vp - velocity of particles, Aa - effect of the environment, As - effect of the substrate or underlying layer.

(i). Powder properties Pp

Powder properties include their constant physical and chemical properties such as: composition, density, crystallinity, melting or softening temperature, heat and electrical conductivity and their variable properties such as: particle size, shape, components distribution, purity of grain surface and flow rate. Changing of constant powder properties involves a change in basic properties of coating and also requires corresponding variation of processing parameters. Changing of the variable properties, such as particle size, influences the heat transfer efficiency, the degree of melting of particles, average particle temperature and particle in-flight velocity in plasma jet (detail discussion in section 6.4), while the component distribution (particularly for composite powder) and purity of powder affect the structure of the coating deposited.

(ii). Particle temperature

It is generally regarded that to achieve high quality deposits, it is necessary that a large fraction of particles be molten upon arrival at the target to maximise inter-particle contact and reduce porosity[23,32,36,38]. The temperature of particles, Td, in the plasma stream should thus exceed their melting or softening temperature, Tm, that is: **Td > Tm**. To satisfy this inequality, the heat necessary to melt the particle must be less or equal to the heat that the plasma can transmit to the powder particle during its residence in the plasma stream[38]. If such a heat is not sufficient or excessive, inadequate melting or overheating of particles will occur. In each case, the low quality coating may be formed. The heat energy supplied by the plasma beam should be determined by the plasma temperature, thermal conductivity and enthalpy, beam velocity, absolute plasma viscosity and the length of plasma stream. Those conditions are governed by the processing parameters including electrode geometry, gas density, mass flow rate and arc current-voltage conditions. Arc core temperature depends on the degree to which the arc can be constricted inside the torch.

(iii). Particle velocity

In-flight particle velocity determines the resident time of a particle within plasma jet and the kinetic energy of the particle on impact with substrate. The residence time affects the average temperature and the degree of melting of particles. The kinetic energy influences the deformation and spreading of molten particle and therefore the bonding of coating to substrate, coherence and coating density. In general, as long as the dwell time of particle in the plasma stream is long enough to ensure efficient melting of particles, increasing particle velocity improves these properties. The particle velocity Vp is governed primarily by two factors: the particle size and the plasma beam velocity, The plasma beam velocity V is given by[39]:

$$V=\frac{AQ_oT}{d^2M} \qquad (2-2)$$

where Q_o is the input gas flow rate, T the gas temperature, d the nozzle diameter, M the molecular mass of plasma gas and A a constant.

(iv). Surrounding atmosphere

The action of the atmosphere may cause undesirable oxidation of materials sprayed. To control this process the spraying may be carried out by using a shield gas or in a vacuum[40,41,42,43].

(v). Substrate condition

The relevant substrate characteristics include its surface profile, temperature and physical and chemical properties. These factors influence the deformation and spreading of the particles on impact. The molten droplets impinging on a smooth glass surface, for example, burst rapidly and spread over the substrate surface, while a rapid spreading of droplet on a roughened surface is inhibited by fast cooling and surface roughness, and the solidifying droplets are captured in the surface unevenness. Contact temperature between the molten deforming particle at its impingement on substrate is one of the important parameter affecting the shape of splats and recrystallization of the material sprayed. The contact temperature is found between the temperature of particle and temperature of substrate[31]. The most important substrate physical properties are thermal conductivity and capacity. If these two properties are low the heat abstracted from the coating layer by the substrate is poor, and improves the bonding to the substrate and layer coherence and vice versa. Phase transformation may occur under rapid cooling, such as martensitic formation or the development of amorphous structures [38,44].

2.7 Main Processing parameters

The plasma spraying is a complex process involving particle acceleration, melting and rapid solidification, and Herman[23] has indicated that approximately 100 interrelated processing parameters will determine the particle temperature and velocity and thus influence the quality of the coatings obtained. Of these parameters, many are independent and must be optimized empirically in order to achieve an acceptable coating. The electric input of plasma torch (the arc power), the nozzle-substrate distance, the plasma gas composition and volume, the carrier gas and volume, powder volume fed, plasma torch traverser speed are the primary parameters which can be controlled during the spraying process. These process parameters affect the thermal and kinetic behaviour of the plasma beam, the transport and fusion of the sprayed powder material and the thermal, and kinetic characteristics of the molten particles impinging on the substrate.

(i). Plasma arc power

Plasma arc power is the product of plasma arc current and arc voltage. It can be used as parameter for an overall characteristic of the working regimes since the conditions of heating of particle and substrate greatly depend on it[45]. This factor decides to what extent are powder particles molten in the plasma jet before their deposition at the substrate[46]. High plasma arc power represents a high thermal energy output of the plasma and a correspondingly large amount of heat for the injected feedstock powder. In this spraying system(Metco 4MB), the control of the arc voltage is realized by varying the plasma gas composition and volume[47]. At a given arc current, increasing the gas volume increases the arc voltage and therefore increases the arc power. The most sensitive parameter affecting arc voltage is the gas composition, particularly the hydrogen content. The arc voltage increases greatly with increasing hydrogen content. The arc voltage decreases with increasing arc current.

(ii). Plasma gas

At present, mainly argon, nitrogen and hydrogen, sometimes helium are used as plasma gases. Argon and helium are monatomic gases and hydrogen and nitrogen are diatomic gases. The former achieves the plasma state through a single-stage process: the ionization of the gas at high temperatures, while the latter experiences a two-stage process of the dissociation of molecules into atoms and then ionization of the atoms. The diatomic gases have much higher enthalpy than monatomic gases since the plasma contains energy not only from the ionization of atoms but also from the dissociation of molecules. Thermal conductivity is an important property of plasma gases. Of all the plasma gases, hydrogen has the highest thermal conductivity (0.1754 $Wm^{-1}K^{-1}$), then helium (0.1436 $Wm^{-1}K^{-1}$), nitrogen (0.02386 $Wm^{-1}K^{-1}$) and argon (0.01633 $Wm^{-1}K^{-1}$). The temperature of the hydrogen plasma is, however, lower than any other plasma. The temperatures of argon and helium plasmas are higher than the other plasma. Both argon and helium can be readily transferred to the plasma state and provide a stable electric arc. These two gases also ensure an inert environment to the materials sprayed. The selection of plasma gases is on the basis of the desired temperature and velocity of the plasma beam and the requirement of inertness for the sprayed material and substrate. In order to get suitable enthalpy, temperature and velocity of the plasma beam, gas mixtures in different proportion are often used[31,48].

(iii). Spraying distance

Spraying distance is an important process parameter since the temperature profile of a plasma beam is the function of the distance from the nozzle. The velocity of plasma beam is also the function of the distance[26]. The particles injected are accelerated only up to a certain distance from the nozzle, where the velocity reaches its maximum value after which the particles decelerate. At too short distance the plasma beam impinges on the substrate and overheats it considerably, and also particles tend to have too short a dwell time in the beam. On the contrary, at too long distance, the particles are cooled down and decelerate substantially before impact. Both situations produce poor quality coatings.

(iv). Powder feed volume and carrying gas

To melt a powder during its flight path, a certain amount of heat is required, depending on the nature and granularity of the sprayed powder. This heat depends on the plasma arc power and the volume of the carrier gas. When powder volume is increased, the temperature and degree of melting of the particles will reduce due to the intense thermal exchange between the particles and plasma beam, and the resulting cooling of the plasma. In addition, the flow of the carrier gas must be raised to accommodate the extra powder, which also reduces the heat available for transfer to the feedstock particles. Consequently, the plasma arc power must be increased in order to increase its temperature. The powder feed rate should also be controlled to enable trajectory of powder motion to lie as closely to the axis as possible since the distribution of the plasma temperature and velocity is axially symmetric with a maximum on the axis[46].

(v). Surface preparation

To ensure that a plasma sprayed deposit adheres to its substrate, the first requirement is that the substrate is clean and ready to accept it. This means not only that all oxide scales and other foreign matter must be removed, but also that oil and machining lubricants must be eliminated. Component surface should therefore be degreased chemically[25]. Virtually all plasma sprayed coatings require a roughened substrate to increase the surface area and provide mechanical interlocking for the sprayed particles[25,38,49]

Typical surface roughening techniques include macro-roughening, chemical etching and grit-blasting[48]. The most common method of surface preparation is by abrasive blasting (grit-blasting). This removes surface scales and roughens the surface. The type of grit and blast pressure used is determined by the nature of the substrate material: for soft substrate chilled steel is used frequently. For harder substrate, an alumina or silicon carbide grit is used to achieve a sharp peaked topography and an average roughness(Ra value) of 4 - 5 μm or more[25]. Control of grit blasting parameters is essential to achieve consistently high bond strengths. The blasting time, blasting pressure and blasting angle influence the surface roughness and therefore the bond strength of the coating to the substrate. Overblasting, for example, can reduce mechanical interlocking by rounding off sharp peaks and can also embed surface scales. This leads to reduced bond strength and may cause corrosion under the coating[25,50,51].

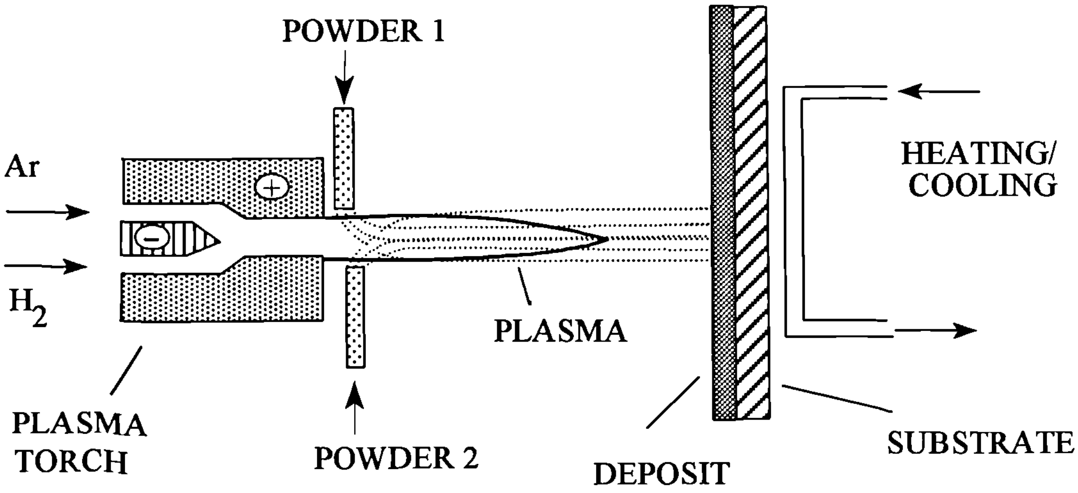

Figure 2.1 Schematic of air plasma spraying.

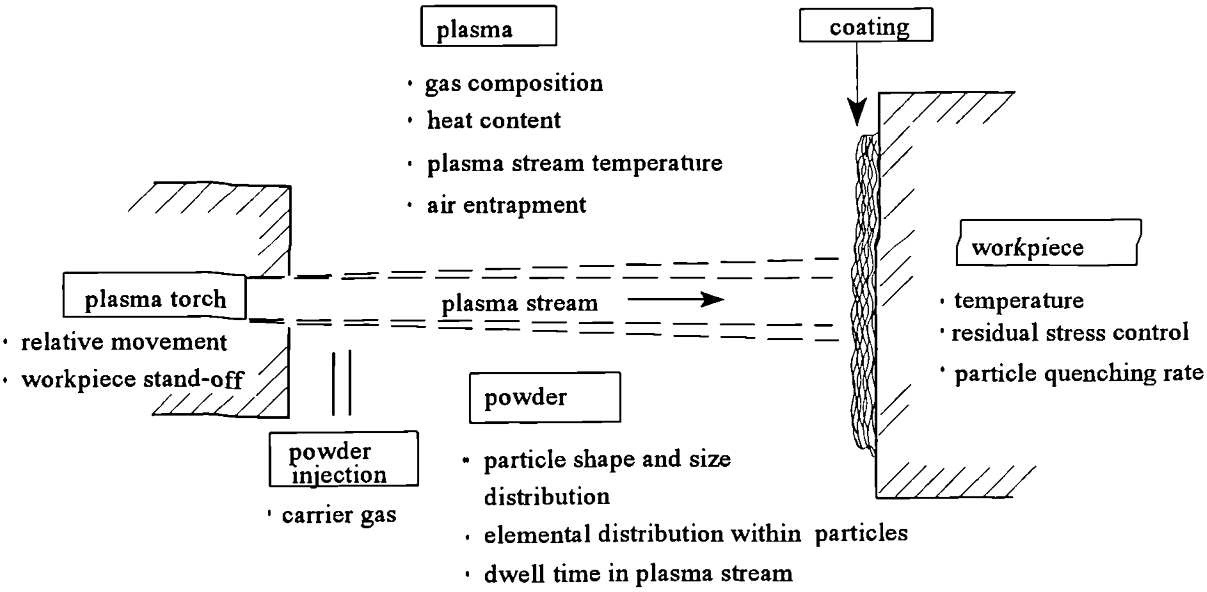

Figure 2.2 Factors affecting the quality of a plasma sprayed coating.

CHAPTER 3. APPLICATION OF HEAT TRANSFER THEORY UNDER PLASMA CONDITIONS

3.1 Background

A plasma sprayed coating is built up from particles quenched from various stages of heating. The structure and quality of a plasma sprayed coating depends critically on the condition of the particles immediately before impact with the substrate. Ideally, a particle should be molten throughout its thickness and strike substrate at a high velocity so that the material flows into the contours of the underlying surface to minimize voidage and maximize bonding. Furthermore, particle volatilisation during spraying represents an unnecessary waste of expensive materials and is to be avoided. The temperature-time conditions of the particles during deposition process is crucial to meet these requirements. For polymers, in particular, their low decomposition temperature and low thermal conductivity require more strictly control on the heating condition of particles to achieve effective melting without decomposition of particle during spraying. In the case of thermosets, there is the additional requirement of cross linking which should also be met by the temperature-time condition of particles on impact. The temperature-time condition of particles is determined by the operating conditions. A knowledge of how the temperature, velocity and heating time of particles are influenced by the operating conditions is therefore essential to achieve improved control over plasma spraying process. To do this, it is imperative to have a reliable method of determining the temperature-time conditions of particles in the plasma flame and on impact. In plasma spraying practice, accurate in situ measurement of the temperature-time conditions of the particle is both expensive and problematic[52]. The work was therefore carried out to establish a theoretical model based on heat transfer theory and some empirical boundary conditions to compute the temperature-time condition of particles under varying plasma environments. The calculated results were then checked and confirmed by the spraying practices. There are two obvious advantages for such a model assisted process development over a purely empirical approach: first, it can reduce the amount of experimental work which often means saving money and time, second, quantitatively understanding the plasma processing of polymer materials. To undertake the modelling work, this requires a through understanding of heat transfer process occurring between the plasma and entrained powder particles.

3.2 General heat transfer cases

In most industrial processes, heat is usually transferred from one part to another by a combination of modes: conduction, convection and radiation. It depends upon the level of temperature and types of substances involved as to which particular mode is important.

a. Conduction

Heat is transferred by conduction through a solid body or a fluid at rest. In the case of solid, energy is transferred by the movement of electrons within the lattice of fixed molecules, whereas for a fluid there will be direct molecular interaction as the molecules are free to move. The general equation for heat flow by conduction is expressed as[53]:

$$\frac{\partial}{\partial x}\left(k\frac{\partial T}{\partial x}\right)+\frac{\partial}{\partial y}\left(k\frac{\partial T}{\partial y}\right)+\frac{\partial}{\partial z}\left(k\frac{\partial T}{\partial z}\right)+H=\rho C_p\frac{\partial T}{\partial t} \qquad (3\text{-}1)$$

where $\partial T/\partial x$, $\partial T/\partial y$, $\partial T/\partial z$ is the temperature gradient in the x,y,z-direction respectively (Km^{-1}), and $k=k(x,y,z,T)$ is the thermal conductivity of substance involved ($Wm^{-1}K^{-1}$). C_p the specific heat of the substance ($JKg^{-1}K^{-1}$), $\partial T/\partial t$ the rate of temperature change (Ks^{-1}), and ρ the density of materials (Kgm^{-3}).

The term thermal diffusivity, α (m^2s^{-1}), has been evolved to quantify partially the rate of response of a system to a temperature change:

$$\alpha=\frac{k}{\rho C_p} \qquad (3\text{-}2)$$

A dimensionless group, called a Fourier number(F_o), has been defined to assist in the representation of transient heat flow calculations:

$$F_o=\frac{k\Delta t}{\rho C_p(\Delta x)^2} \tag{3-3}$$

where Δt is the increment of time, and Δx is the thickness of the substance being considered. The Fourier number gives an indication of speed at which a body will respond to a temperature change. Low values of F_o imply that a long period of time is required to heat or cool the body, and vice versa.

b. Convection

Convective heat transfer takes place when groups of molecules move from one place to another of different temperature. Convection is thus limited to liquids and gases and is normally concerned with heat exchange between fluids and solid boundaries. The heat transfer by convection is a function of the temperature difference between the solid T_s and the fluid T_f and the area of contact A, expressed by the equation:

$$Q=hA(T_s - T_f) \tag{3-4}$$

where Q is the heat flow (W), h is called convection heat transfer coefficient ($Wm^{-2}K^{-1}$).

The convective heat transfer coefficient h of fluid-particle may be derived from semi-empirical correlations. For a fluid medium with constant properties, the value of h is given by the following equation[54]:

$$Nu=hd/k=2.2+0.6Re^{1/2}Pr^{1/3} \tag{3-5}$$

where[53]

$$Nu = Nusselt\ number = \frac{h \times A\ characteristic\ dimension}{Thermal\ conductivity\ of\ fluid};$$

$$Re = Reynolds\ number = \frac{Velocity \times Dimension}{Kinematic\ viscosity};$$

$$Pr = Prandtl\ number = \frac{Specific\ heat \times Dynamic\ viscosity}{Thermal\ conductivity}$$

and d the particle diameter. A number of corrections are needed to make this correlation compatible with a plasma environment.

c. Radiation

Radiation, unlike conduction and convection, does not require a solid or fluid for its propagation. Radiant energy is transmitted by electromagnetic waves. The radiative heat transfer is described by equation:

$$Q=\varepsilon\sigma AT^4 \qquad (3\text{-}6)$$

where σ is Stefan-Boltzmann constant, ε the emissivity and A the area.

In the situation of heat transfer between plasma beam and entrained particles, the conduction formula is relevant in the heat flow inside particles, while the convective and radiative heat transfer occur at boundaries of particles. In order to apply the above equations to heat transfer under plasma conditions, the following modifications are required.

3.3 Heat transfer problem under plasma conditions

3.3.1 Effect of steep temperature gradients

During the heating of a particle in a plasma, the surface temperature of the particle can be in the range of 500-3000K depending upon materials sprayed while the ambient plasma temperature is around 10000K. The presence of such steep temperature gradients across the boundary layer can have an important effect on the convective heat transfer coeficient between the particle and plasma gas medium due to possible change of gas properties inside the boundary layer[52,54,55]. Many researchers use various methods to take account of the influence of the presence of the steep temperature gradients in the vicinity of the particle on the convective heat transfer rate of plasma to particle. A common feature in their methods is the introduction of correction factors to the equation deduced from cold and constant fluid medium such as equation(3-5), so that modified equation can be used for the calculation of heat transfer coefficient h under plasma conditions.

A correction factor for the drag coefficient evaluated at film temperature, which is an arithmetic mean of particle surface and plasma temperatures, was proposed by Lewis and Gauvin [55] and other authors[56,57,58] to account for the enormous temperature difference. As suggested by these authors, a kinematic viscosity ratio was used in subsequent studies to correct the heat transfer coefficient for steep temperature gradient effects. They proposed:

$$Nu_f=(2+0.515Re_f^{1/2})\left(\frac{\nu_f}{\nu_\infty}\right)^{0.15} \qquad (3\text{-}7)$$

where υ is the kinematic viscosity. The subscript f refers to properties corresponding to the film temperature, and the subscript ∞ refers to properties corresponding to the free-stream temperature.

Fiszdon[59] used following equation in his heat transfer calculation which was taken from[60] with a correction coefficient from[61].

$$Nu_f=(2+0.6Re_f^{1/2}Pr^{1/3})\left(\frac{\rho_\infty\mu_\infty}{\rho_s\mu_s}\right)^{0.6} \qquad (3\text{-}8)$$

where μ is the dynamic viscosity, ρ the density. The subscript s refers to properties corresponding to the particle surface temperature.

Lee et al [62] considered the influence of temperature on specific heat of plasma gas by introduced a ratio of specific heat and proposed the expression:

$$Nu_f = (2+0.6Re_f^{1/2}Pr_f^{1/3})\left(\frac{\rho_\infty\mu_\infty}{\rho_s\mu_s}\right)^{0.6}\left(\frac{Cp_\infty}{Cp_s}\right)^{0.38} \tag{3-9}$$

Vardelle et al [63] suggested the relation:

$$Nu_{avg} = (2+0.515Re_{avg}^{1/2}) \tag{3-10}$$

where the dimensionless numbers are defined by average properties, which are defined as:

$$\overline{\phi} \equiv \int_{T_f}^{T_\infty}\phi dT/(T_\infty - T_f) \tag{3-11}$$

$$Re_{avg} \equiv \overline{\rho}U_\infty d/\overline{\mu} \tag{3-12}$$

$$Nu_{avg} \equiv hd/\overline{k} \tag{3-13}$$

Lee et al compared above methods for calculation heat transfer coefficient and indicated that all methods except that of Ref.63 produce similar results for relatively low plasma temperatures. For plasma temperature larger than 10^4 K where ionization becomes important, the results of Ref.62 depart from the other results due to changes of the specific heat at higher temperatures. In every case, the results of Ref.63 show the highest values. It is obvious that large discrepancies exist among various approaches for calculating heat transfer coefficients.

More recently, Bourdin et al [64] have shown that the now widely accepted method

[52, 26, 64, 65] of using an integral mean value of thermal conductivity across the boundary layer k given by the expression

$$\bar{k}=\frac{1}{(T_\infty-T_S)}\int_{T_s}^{T_\infty}k(T)\,dT \qquad (3\text{-}14)$$

is more appropriate for heat transfer calculation under plasma conditions. In their calculation, the Nusselt number equals 2 and heat transfer coefficient is given by:

$$h=\frac{2}{d(T_\infty-T_S)}\int_{T_s}^{T_\infty}k(T)\,dT \qquad (3\text{-}15)$$

where k(T) is the thermal conductivity of plasma gas at temperature T. They have shown that as long as the resident time of the particles in the plasma jet is far longer than 1μs, the use of above equations to calculate the heat transfer rate to the particle is quite adequate. This method has therefore been used in the present modelling work for the calculation of heat transfer coefficient h of plasma to the particle(Section 5.1.2).

3.3.2. Noncontinuum effect

In the plasma process, the particle sizes of powder used are usually fine (in many cases less than 50μm) to facilitate complete melting. In such circumstances, the magnitude of the gas molecular mean free path may be comparable to the particle diameter[52, 66, 67]. This causes a so-called "rarefaction effect" which may exert a strong influence on heat transfer. The rarefaction effect means that there existing a boundary layer around particle in which particle heat transfer is under noncontinuum conditions and governed by individual contributions from the species in the plasma (electron, ions, neutral species) and by particle charging effects[54, 67]. In such circumstances, the continuum transport mechanisms (namely, the laws of Newton, Fourier etc.) fail to give complete description of the transport processes[66,67]. A measure of the departure from the laws of continuum transport mechanism is provided by a dimensionless parameter termed the Kundsen number Kn which is defined as[68]:

$$\mathbf{Kn}=\lambda/\mathbf{d} \tag{3-16}$$

where λ is the gas mean free path and d the particle diameter. Research in the past few years has highlighted the considerable influence of Kundsen effect on transfer phenomena in plasma-particle systems[69, 70, 71]. Chen and Pfender[69] defined a Kundsen layer around the particle. Free molecular transport is assumed within this layer, while continuum transfer prevails outside the layer. They proposed a correction factor for the ratio of the heat flux q with and without Kundsen effect:

$$\frac{q_{noncont}}{q_{cont}}=\frac{1}{1+(\frac{2-\alpha}{\alpha})(\frac{\gamma}{1+\gamma})(\frac{4}{Pr})Kn*} \tag{3-17}$$

$$Kn*=\frac{\bar{k}}{\rho\,\bar{v}\,\bar{C}_p\,r}Pr \tag{3-18}$$

where α is the thermal accommodation coefficient, γ is the specific heat ratio, $\bar{k}$ the average thermal conductivity, $\bar{C}_p$ the average specific heat, $\bar{v}$ the mean molecular velocity corresponding to the particle surface temperature, ρ the mass density and r the particle radius.

The Kundsen effect becomes substantial for small particles[69, 72]. Therefore, it is crucial for modelling work associated with thermal plasma processing when small particles (e.g. $<40\mu m$) are involved. The noncontinuum effect of heat transfer under plasma conditions has been taken into account for the present modeling work by cooperating equations (3-17) and (3-18) into calculation of heat transfer coefficient from plasma to particles.

3.3.3. Effect of radiation heat transfer

Radiative heat transfer for particles immersed into a thermal plasma includes radiation from plasma to the particles, radiative exchange among particles and radiative heat losses from particles. It has been discussed extensively by many researchers[63, 73, 74, 75] that for low particle loading, radiative exchange among particles may be neglected. Radiative heat losses from particles, depending on the situation, however, are frequenttly taken into account in modelling work[62,59 57].

Radiative heat transfer becomes important for three cases[75]: (a) large particles, (b) high surface temperatures and high emissivities of the particles and (c) low enthalpy differences between the surface of particles and the plasma. Radiation losses from particle are often negligible except for particles with surface temperature exceeding 2000K immersed in an argon or nitrogen plasma at temperatures below 4000K [63]. Seymour[76] also pointed out that radiation from the particle is only about 5% of the total heat exchange.

For high particle loading rates, the radiation exchange among particles becomes important. In this case, the radiation field produced by emitting/absorbing particles in the plasma is no longer optically thin and radiation absorbed by a particle may be substantial. Unfortunately, little is known for this particular situation.

In present study, the powder particle loading is thought to be sufficiently low to affect the temperature field, and the maxium surface temperature of polymer particles would equal to or only be slightly above the decomposition temperature of polymer (for example, polyamide < 830 K). The radiative heat transfer of particles immersed in plasma jet will thus be negelcted.

3.3.4 Internal Conduction

Internal conduction within a particle in a thermal plasma may lead to large differences between the surface and the centre temperature of a particle. Research has shown that internal heat conduction can play a significant role in the overall gas-solid heat transfer process. Particularly when the thermal conductivity of the particle material is low as in ceramics[31,65,54]. Polymeric materials have generally low thermal conductivity, and so in the present modelling work, the internal heat conduction of a particle immersed in plasma jet will be important (Section 6.2).

CHAPTER 4. PROCESS MODELLING

Heat transfer during deposition of a plasma sprayed coating can be considered to occur in three stages as depicted schematically in Figure 4.1. Stage I refers to the flight of the feedstock particle in the plasma flame, stage II the impact of a single droplet with the substrate to give a splat and stage III multiple impact of droplets to produce the coating. The present modelling work thus consists of three parts. The first part is directed at predicting the temperature profiles of the in-flight particle travelling in the plasma jet, the second part dealing with the cooling of the splat impacting on the substrate, and the third part the heat transfer through the thickness of a coating deposited on the substrate.

4.1 Part I - Calculation of temperature profile of in-flight particles

4.1.1 Assumptions

Based on the discussions in Chapter 3, the following assumptions are used in the present study for the heat transfer process of the in-flight particle:

1. The particle is assumed to be spherical.
2. The particle is exposed to a uniform atmospheric pressure thermal plasma and the relative motion between the particle and plasma will be neglected.
3. The radius of the spherical particle remains constant in the heating process up to thermal decomposition.
4. The particle loading is sufficiently low for the temperature and flow fields in the plasma to be unaffected by the injected powder.
5. Radiation from and to the particle is neglected.

4.1.2 State changes of a particle immersed in a thermal plasma

A particle injected into a thermal plasma will undergo a sequence of changes of state due to the rapidly rising temperature. The particle has a finite conductivity and as a result significant temperature differences will develop so that one or more states may exist with the particle. Four major stages may be considered: (1) solid particle: heating of the solid particle up to the melting temperature(single phase); (2) partially melted particle consisting of liquid and solid phase (two phases); (3) liquid droplet in which the temperature is between the melting and boiling temperatures (one phase); (4) vaporization of liquid droplet (two phases).

In each of above states, there are two heat transfer mechanisms involved: heat transfer between the particle and plasma gas medium by convection (neglecting radiation) and heat conduction within the particle. In state (2) and (4), the heat transfer process involves phase changes of the particle, and in state (4), involves mass transfer of the particle to the surrounding.

4.1.3 Heat-transfer analysis and equations

4.1.3.1 Single-phase particle case

The heat transfer within a spherical particle immersed in a thermal plasma can be described by the special form of general conduction equation in a spherical polar coordinate system[53]:

$$\rho C_p \frac{\partial T}{\partial t} = \frac{1}{r^2} \frac{\partial}{\partial r} (k r^2 \frac{\partial T}{\partial r}) \tag{4-1}$$

where r is the radial distance from the centre of the particle as shown in Figure 4.2. The initial condition for solving this governing equation is:
At t=0, r=R and T(r,0)=Tc (carrier gas temperature).

Equation (4-1) holds at any position within the particle: $0 < r < R$, .

By symmetry, the boundary condition at the particle centre can be written as:

$$\frac{\partial T}{\partial r}\Big|_{r=0} = 0 \tag{4-2}$$

By using L.Hopital's rule[77] yields:

$$\lim_{r\to 0}\frac{1}{r}\frac{\partial T}{\partial r}=\frac{\partial^2 T}{\partial r^2} \tag{4-3}$$

introducing equation (4-3) to equation (4-1), following equation is obtained for the heat transfer at the particle centre :

$$3k\frac{\partial^2 T}{\partial r^2}=\rho C_p\frac{\partial T}{\partial t} \tag{4-4}$$

Using a heat balance method at particle surface yields the condition for the calculation of heat transfer at outer boundary of the particle which is given by refer to Figure 4.2.

$$4\pi\left(R-\frac{\Delta r}{2}\right)^2 k\frac{(T_{s-1}-T_s)}{\Delta r} + 4\pi R^2 h(T_p-T_s) = 4\pi R^2\frac{\Delta r}{2}\rho C_p\frac{\Delta T_s}{\Delta t} \tag{4-5}$$

$$\because \quad \left(R-\frac{\Delta r}{2}\right)^2 \approx R^2-R\Delta r \tag{4-6}$$

and so equation (4-5) becomes:

$$\left(1-\frac{\Delta r}{R}\right)k(T_{s-1}-T_s) + h\Delta r(T_p-T_s) = \frac{\Delta r^2}{2}\rho C_p\frac{\Delta T_s}{\Delta t} \tag{4-7}$$

where T_p represents the plasma temperature which is a function of axis and radius distance of plasma jet, h is the convective heat transfer coefficient between plasma and particle which is affected by plasma temperature and thermal conductivity, particle surface temperature and particle dimension. The values of the parameter T_p and h will be determined in section 6.1.

Equation (4-1) to (4-7) therefore represents the necessary equations for the calculation of heat transfer of the particle immersed in a thermal plasma in a single-phase state.

4.1.3.2 Two-phase particle case

When the particle surface reaches the melting temperature, a phase change begins. The particle then consists of two layers: inner-solid and outer-liquid. and a phase boundary r_f moves inside the particle during heating process. Part of the heat delivered from the plasma is now used in the melting process. This situation can be described by a pair of heat conduction equations; one for the solid region of the spherical particle $0 < r < r_f(t)$,

$$\rho C_{pd}\frac{\partial T}{\partial t}=\frac{1}{r^2}\frac{\partial}{\partial r}\left(k_d r^2\frac{\partial T}{\partial r}\right) \tag{4-8}$$

and the other for the liquid region of $r_f(t) < r < R$

$$\rho C_{pl}\frac{\partial T}{\partial t}=\frac{1}{r^2}\frac{\partial}{\partial r}\left(k_l r^2\frac{\partial T}{\partial r}\right) \tag{4-9}$$

where the subscripts d and l refer to the solid and liquid phases respectively. At the phase change boundary (solid-liquid interface $r=r_f(t)$), by using heat balance across the phase change boundary, the following conditions hold:

$$k_l\frac{\partial T}{\partial r}\Big|_{r=r_{f-0}}=k_d\frac{\partial T}{\partial r}\Big|_{r=r_{f+0}}+\rho\Delta H_m\frac{dr_f}{dt} \tag{4-10}$$

where $T_l=T_d=T_m$, ΔH_m is the enthalpy of melting, T_m the melting temperature.

The solution for equation (4-8) to (4-10) requires the phase change boundary, $r=r_f(t)$, to be accurately traced. This requirement renders a large proportion of the available numerical schemes difficult to implement [78]. One way to overcome this problem is to reformulate the heat transfer equation in terms of enthalpy H [78,79,80,81], the sum of sensible and latent heats. In this case, the equations (4-8) to (4-10) are reduced to a single equation

$$\frac{1}{r^2}\frac{\partial}{\partial r}\left(kr^2\frac{\partial T}{\partial r}\right) = \rho\frac{\partial H}{\partial t} \qquad (4\text{-}11)$$

and the temperature is related to the enthalpy via

$$H(T) = \begin{cases} C_pT & T < T_m \\ C_pT + \Delta H_m & T > T_m \end{cases} \qquad (4\text{-}12)$$

In many cases, particularly for polymeric materials, the phase change takes place over a temperature range rather than at a single value, that is:

$$H(T) = C_{pd}T \qquad T \le T_{m-\epsilon} \qquad (4\text{-}13a)$$

$$H(T) = \overline{C_{p_m}}(T - T_{m-\epsilon}) + H(T_{m-\epsilon}) \qquad T_{m-\epsilon} < T < T_{m+\epsilon} \qquad (4\text{-}13b)$$

$$H(T) = C_{pl}(T - T_{m+\epsilon}) + H(T_{m+\epsilon}) \qquad T \ge T_{m+\epsilon} \qquad (4\text{-}13c)$$

where ε is the half temperature range of phase change, C_{ps}, C_{pl} and $\overline{C_{pm}}$ are the specific heat of particle in solid, liquid and in the melting range respectively. The corresponding heat transfer equations for the two-phase case are obtained from equation (4-13):

$$\frac{1}{r^2}\frac{\partial}{\partial r}\left(kr^2\frac{\partial T}{\partial r}\right) = \rho C_{ps}\frac{\partial T}{\partial t} \qquad T \le T_{m-\epsilon} \qquad (4\text{-}14)$$

$$\frac{1}{r^2}\frac{\partial}{\partial r}\left(kr^2\frac{\partial T}{\partial r}\right) = \rho \overline{C_{pm}}\frac{\partial T}{\partial t} \qquad T_{m-\epsilon} < T < T_{m+\epsilon} \qquad (4\text{-}15)$$

$$\frac{1}{r^2}\frac{\partial}{\partial r}\left(kr^2\frac{\partial T}{\partial r}\right) = \rho C_{pl}\frac{\partial T}{\partial t} \qquad T > T_{m+\epsilon} \qquad (4\text{-}16)$$

The remaining problem now is to determine specific heat of the particle within melting range C_{pm}.

In equation (4-13)b, if let $T=T_{m+\varepsilon}$, then

$$H(T_{m+\epsilon}) = \overline{C_{pm}}(T_{m+\epsilon} - T_{m-\epsilon}) + H(T_{m-\epsilon}) \tag{4-17}$$

In the melting temperature range, the enthalpy of polymer materials can be written as[82]:

$$H(T) = \int_{T_{m-\epsilon}}^{T} C_p(T)\,dT + \Delta H_m \frac{(T-T_{m-\epsilon})}{T_{m+\epsilon}-T_{m-\epsilon}} + H(T_{m-\epsilon}) \tag{4-18}$$

$$H(T_{m+\epsilon}) = \int_{T_{m-\epsilon}}^{T_{m+\epsilon}} C_p(T)\,dT + \Delta H_m + H(T_{m-\epsilon}) \tag{4-19}$$

where the ΔH_m is the enthalpy of the melting. If let

$$C_p(T) = \frac{1}{2}(C_{pT_{m-\epsilon}} + C_{pT_{m+\epsilon}}) \tag{4-20}$$

where $C_{pTm-\varepsilon}$ and $C_{pTm+\varepsilon}$ are specific heat at low and up extremities of melting range respectively. Equation(4-19) then changes into:

$$\begin{aligned} H(T_{m+\epsilon}) &= \int_{T_{m-\epsilon}}^{T_{m+\epsilon}} C_p dT + \Delta H_m + H(T_{m-\epsilon}) \\ &= \frac{1}{2}(C_{p_{T_{m-\epsilon}}} + C_{p_{T_{m+\epsilon}}})(T_{m+\epsilon} - T_{m-\epsilon}) + \Delta H_m + H(T_{m-\epsilon}) \\ &= [\frac{1}{2}(C_{p_{T_{m-\epsilon}}} + C_{p_{T_{m+\epsilon}}}) + \frac{\Delta H_m}{T_{m+\epsilon}-T_{m-\epsilon}}](T_{m+\epsilon} - T_{m-\epsilon}) + H(T_{m-\epsilon}) \end{aligned} \tag{4-21}$$

compare equation(4-21) with equation(4-17), yields

$$\overline{C_{pm}} = \frac{1}{2}(C_{p_{T_{m-\epsilon}}} + C_{p_{T_{m+\epsilon}}}) + \frac{\Delta H_m}{T_{m+\epsilon}-T_{m-\epsilon}} \tag{4-22}$$

This yields a new average thermal diffusivity for the powder due to phase change in the melting range and has the advantage of simplifying the computation.

Applying the $\overline{C}_{pm}$ defined by the equation (4-22) to replace C_p in the equations (4-4) and (4-7), the heat transfer at centre and surface of the particle, when their temperature reaches to melting range and phase change involved, can be calculated.

4.1.3.3 The case of thermal decomposition of the polymer

Unlike ceramics and metals, polymers can not evaporate because they consist of macromolecules and decompose before boiling[83]. The thermal degradation of polymers, however, occurs if the temperature is high enough to break the primary chemical bonds. The temperature of decomposition is generally low so that there is a serious danger of degradation of polymer particles when they are injected into a plasma jet.

When the surface temperature of a polymer particle reaches its decomposition temperature, it begins to decompose. The difference between this case and the one described above consists in the appearance of a moving outer boundary, r_e, due to the thermal decomposition of the outer layer of particle. The heat transferred from the plasma gas is now used partially for the decomposition, hence the boundary conditions at out layer($r=r_e$) are:

$$k_l\frac{\partial T}{\partial r}\Big|_{r=r_e}+\Delta H_e\frac{dr_e}{dt}=h\,(T_p-T_s)\,\Big|_{r=r_e} \qquad (4\text{-}23)$$

where the ΔHe is the heat of decomposition of the polymer, and the surface temperature will be equal to the decomposition temperature:

$$T(r_e,t)=T_e \qquad (4\text{-}24)$$

For many polymers, thermal degradation is characterized by the breaking of the weakest bond and is consequently determined by a bond dissociation energy[84,85].In present study, the value of the decomposition energy of polymers is estimated from their dissociative energy ($E_{dec} \sim E_{diss}$). For example, the weakest linkage in the polyamide chain is the C-N bond and the degradation of polyamide in inert atmosphere thus takes place by chain scission at the - NH $\vdots$ CH$_2$ - group[85]. The dissociation energy for C-N bond is 277 kJmol^{-1}[86], This value is taken as its value of the heat of decomposition in the heat transfer calculation ($\Delta He = E_{dec} = E_{diss}$).

Using the same enthalpy method as that in melting case to simplify computation, an average specific heat in decomposition temperature range is defined to incorporate the heat of decomposition in the calculation of heat transfer for the case of the surface decomposition of a particle:

$$\overline{C_{pe}} = \frac{1}{2}(C_{pTe1} + C_{pTe2}) + \frac{\Delta H_e}{T_{e2} - T_{e1}} \tag{4-25}$$

where T_{e1} and T_{e2} are the lower and up extremities of decomposition temperature range respectively, C_{pTe1} and C_{pTe2} are corresponding specific heat.

Applying the $\overline{C_{pe}}$ defined by the equation(4-25),to replace C_p in the equation(4-7), the heat transfer at the particle surface in the case of thermal decomposition can be determined.

4.1.4 Numerical solution of heat-transfer equations

The finite difference method in the explicit form[87] was used for the solution of the heat transfer equations in present study. By reference to the element in Figure 4.3, the heat transfer equations in Section 4.1.3 can be written into their finite difference equation(FDE) form as:

FDE for equation (4-1) within the particle, node i:

$$k\left[\frac{T_{i+1} - T_{i-1}}{r_i \Delta r} + \frac{T_{i+1} + T_{i-1} - 2T_i}{(\Delta r)^2}\right] = \rho C_p \frac{T_i' - T_i}{\Delta t} \tag{4-26}$$

Where T_i' is the temperature of node i at time t + Δt

FDE for equation (4-4) at the centre of the particle, node 0:

$$6k[\frac{T_1-T_0}{(\Delta r)^2}=\rho C_p(\frac{T'_0-T_0}{\Delta t}) \tag{4-27}$$

Where T_0' is the temperature of node 0 (centre node) at time t + Δt

FDE for equation (4-7) at the surface, node s:

$$k(1-\frac{\Delta r}{R})(T_{s-1} - T_s)+h\Delta r(T_p - T_s)=\frac{\Delta r^2}{2}\rho C_p\frac{T'_s - T_s}{\Delta t} \tag{4-28}$$

where T_s' is the temperature of node s(surface node) at time t + Δt
if let

$$\frac{k\Delta t}{\rho C_p(\Delta r)^2}=F_0 \qquad (\textit{Fourier number}) \tag{4-29}$$

$$\frac{h\Delta r}{k}=B_i \qquad (\textit{Biot number}) \tag{4-30}$$

the equations (4-26), (4-27) and (4-28) can be rewritten as:

$$T'_i = F_0(1 + \frac{\Delta r}{r_i})T_{i+1} + F_0(1 - \frac{\Delta r}{r_i})T_{i-1} + (1 - 2F_0)T_i \tag{4-31}$$

$$T'_0 = 6F_0\, T_1 + (1 - 6F_0)T_0 \tag{4-32}$$

$$T'_s = 2F_0(1-\frac{\Delta r}{R})T_{s-1}+[1-2F_0(1-\frac{\Delta r}{R})-2F_0B_i]T_s+2F_0B_iT_p \tag{4-33}$$

Those are the equations used for the calculation of temperature distribution of an in-flight particle travelling through the plasma jet without phases change involved.

The finite difference equations for the case of two-phase can be easily obtained by introducing average specific heat of particle within melting range, Cpm, defined by equation (4-22), into equation (4-29), and as a result a new Fourier number F_{0m} in two-phase case is defined:

$$F_{0m} = \frac{k}{\rho \overline{C_{pm}}} \frac{\Delta t}{(\Delta r)^2} \tag{4-34}$$

Replace F_0 in equations (4-31), (4-32) and (4-33) by F_{0m}, following equations can be obtained which were used for the calculation of temperature distribution of an in-flight particle in two-phase case:

$$T_i' = F_{0m}(1 + \frac{\Delta r}{r_i})T_{i+1} + F_{0m}(1 - \frac{\Delta r}{r_i})T_{i-1} + (1 - 2F_{0m})T_i \tag{4-35}$$

$$T_1' = 6F_{0m}\ T_2 + (1 - 6F_{0m})T_1 \tag{4-36}$$

$$T_s' = 2F_{0m}(1-\frac{\Delta r}{R})T_{s-1}+[1-2F_{0m}(1-\frac{\Delta r}{R})-2F_{0m}B_i]T_s+2F_0)B_iT_p \tag{4-37}$$

Similarly, a new Fourier number for the case of decomposition is defined by:

$$F_{0e} = \frac{k}{\rho \overline{C_{pe}}} \frac{\Delta t}{(\Delta r)^2} \tag{4-38}$$

and the finite difference equation for the case of decomposition can thus be obtained:

$$T_s' = 2F_{0e}(1-\frac{\Delta r}{R})T_{s-1}+[1-2F_{0e}(1-\frac{\Delta r}{R})-2F_{0e}B_i]T_s+2F_{0e}B_iT_p \tag{4-39}$$

4.1.5 Stability conditions of heat transfer equations

The stability conditions for the temperature calculation using explicit FDEs in 4.1.4

means the conditions under which the FDEs are stable and able to yield satisfactory computed solution. the stability criteria for those explicit FDEs is that the coefficients of T_o, T_i and T_s are non-negative[87]. The time Δt and space Δr cannot thus be selected arbitrarily and should be chosen to satisfy the stability criteria. This results in following conditions:

from equation(4-31): $\mathbf{1 - 2F_0 > 0}$ (4-40)
from equation(4-32): $\mathbf{1 - 6F_0 > 0}$ (4-41)
from equation(4-33): $\mathbf{1 - 2F_0 (1 - \Delta r/R) - 2F_0B_i > 0}$ (4-42)

Of these, the most restrictive one is from equation(4-41) and it yields the restriction for the selection of Δt:

$$\Delta t < \frac{1}{6}\frac{(\Delta r)^2}{\alpha} \tag{4-43}$$

$$\alpha = \frac{k}{\rho C_p} \tag{4-44}$$

for values of $\alpha = 1.8 \times 10^{-7}$ m^2s^{-1} (polyamide); $h = 2 \times 10^5$ $Wm^{-2}k^{-1}$; $R = 20\mu m$ and $\Delta r = 2\mu m$, the time step Δt should be smaller than 4×10^{-6} second. In most of present calculations, the Δt was taken as 10^{-7} second.

4.2 Part II - Cooling of particles on impact

The principal difficulty in the analysis of the heat transfer of a molten particle impacting on a substrate is the fact that the process consists of two interacting mechanisms: flattening of the particle into a splat and simultaneous solidification due to cooling. However, evidence exist that the deformation starts before the solidification[49, 88, 89], and these two processes can be treated separately.

4.2.1 Degree of flattening

On impact with the substrate, a liquid droplet from the plasma jet is thus assumed to flatten into a splat or thin discs before it solidifies[88, 90]. To simplify computation[88], a cylinder of diameter D and thickness h was used to represent the actual splat of the same volume as shown schematically in Figure 4.4.

The thickness of a splat is a significant parameter in its heat exchange to substrate which is determined by the degree of flattening of droplet on impact. However the degree of flattening of a droplet is a complicated problem influenced by many parameters, including the thermal properties of the material, temperature and velocity of the droplet on impact, the nature of the substrate and the contact area between the splat and substrate. Different equations have been used for the calculation of the degree of flattening.

An analysis of flattening and cooling of a droplet sprayed on a cold surface has been reported by Madejski[88] who considered the effects of solidification kinetics on the spreading of droplets. His work showed that the flattening degree can be expressed as the function of Reynolds, Weber and Peclet numbers related to the particle, and the freezing characteristics of the material. For plasma spraying conditions characterized by Weber and Reynolds numbers greater than 100, Macpherson[91] indicated that if spreading is complete before solidification, the degree of flattening can be calculated from Madejski's analysis using the simplified equation:

$$\mathbf{D/d = 1.2941\ Re^{0.2}} \qquad (4\text{-}45)$$

where Re is Reynolds number, $Re=\rho vd/\mu$, v is the impact velocity, ρ the density of the powder; μ the dynamic viscosity.

Yoshida[92] investigated the effects of viscosity, size and velocity variations on the deformation process at impact by using a numerical algorithm to model the impact of alumina droplets, assuming a constant temperature of droplets during deformation. He suggested following formula:

$$D/d = 0.83\ Re^{0.2} \qquad (\ 4\text{-}46\ )$$

Similar findings were made by Solonenko[93] and also by Trapaga and Szekely[94]. From a numerical representation of time-dependent spreading process, Trapaga has shown that the final splat diameter may be given by:

$$D = d\ Re^{0.2} \qquad (\ 4\text{-}47\ )$$

whereas the spreading time t_s may be approximated by the following expression:

$$t_s = 2dRe^{0.2}/3v \qquad (\ 4\text{-}48\ )$$

More recently, Fantassi et al[95] investigated the effects of particle parameters (size, velocity, temperature) on the particle flattening and splat cooling by using an experimental device comprising two high speed pyrometers. They related the experimental data of zirconia particle sprayed on a smooth steel substrate kept at a temperature below 473 K to its Reynolds number and found that the evolution of flattening degree as a function of Reynolds number is consistent with the theoretical prediction of Yoshida[92].

No reports on deformation of the polymer splats have been found. In present modelling work, the wipe test(described in section 7.1) was used to evaluated the degree of flattening which is expressed as the ratio of the diameter of the splat to that of the particle before spraying. For polyamide, for example, measured D/d is in the range of 3-5.

If d represent the diameter of a droplet, D the diameter of splat and h the thickness of the splat refer to Figure 4.4, assuming no volume change before and after flattening, it then gives

$$\frac{\pi d^3}{6} = \frac{\pi D^2 h}{4} \tag{4-50}$$

which gives

$$\frac{h}{D} = \frac{2}{3}\frac{1}{(D/d)^3} \tag{4-51}$$

If one take values of D/d as 3 - 5, the values of h/D would be of 0.025-0.005. The diameter D of the splat is thus much larger than its thickness so that, to a first approximation, the heat flow in the radial direction was neglected and the cooling of splat on substrate was simplified into a one-dimensional heat flow through the splat thickness to substrate as shown schematically in Figure 4.5

4.2.2 Heat transfer equations

Based on above assumption, the governing equation for the heat flow through the splat thickness is the one-dimensional conductive heat transfer equation:

$$\frac{k}{\rho C_p}\frac{\partial^2 T}{\partial x^2} = \frac{\partial T}{\partial t} \tag{4-52}$$

T is the temperature within the splat at a distance x from splat-substrate interface.

The finite difference method with implicit form was used for the solution of the heat transfer equation. As shown in Figure 4.5, there are five situations which show different boundary conditions. The FDE equations for each of those situation are given as following:

(a) At node 0 (substrate-air interface):

$$k_b\frac{T'_1-T'_0}{\Delta y}+h_a(T_a-T_0) = \rho_b C_{pb}\frac{\Delta y}{2}\frac{T'_0-T_0}{\Delta t} \tag{4-53}$$

(b) At node j (within substrate):

$$k_b\frac{T'_{j+1}+T'_{j-1}-2T'_j}{\Delta y} = \rho_b C_{pb}\Delta y\frac{T'_j-T_j}{\Delta t} \tag{4-54}$$

(c) At node l (splat-substrate interface):

$$k_c\frac{T'_{l+1}-T'_l}{\Delta x}+k_b\frac{T'_{l-1}-T'_l}{\Delta y} = (\rho_c C_{pc}\frac{\Delta x}{2}+\rho_b C_{pb}\frac{\Delta y}{2})\frac{T'_l-T_l}{\Delta t} \tag{4-55}$$

(d) At node i (within splat)

$$k_c\frac{T'_{i+1}+T'_{i-1}-2T'_i}{\Delta x} = \rho_c C_{pc}\Delta x\frac{T'_i-T_i}{\Delta t} \tag{4-56}$$

(e) At node n (splat-air/plasma interface):

$$k_c\frac{T'_{n-1}-T'_n}{\Delta x}+h_{en}(T_{en}-T_n)) = \rho_c C_{pc}\frac{\Delta x}{2}\frac{T'_n-T_n}{\Delta t} \tag{4-57}$$

where T_i' is the temperature of node i at time $(t+\Delta t)$, subscript c, b and a and en represent splat, substrate, air and environment respectively.

A similar analysis method was used to deal with the phase change during cooling of a splat: depending upon the temperature of the splat which determines the state of splat (liquid, solidifying range(two-phase) and solid), the C_{pc} in above FED equations may vary with the temperature as following:

$$C_p = \{ \begin{array}{ll} C_{pl} & T \geq T_{m+\epsilon} \\ \overline{C_{pm}} & T_{m-\epsilon} < T < T_{m+\epsilon} \\ C_{ps} & T \leq T_{m-\epsilon} \end{array} \tag{4-58}$$

where ϵ is the half temperature range of phase change. C_{pl}, C_{pm} and C_{ps} are the specific heat of splat at liquid, in solidifying range and solid state respectively. Since solidification of the material is an reverse process of the melting. the $\overline{C}_{pm}$ can be obtained by equation (4-22).

4.3 Part III - Temperature distribution within a coating

The temperature distribution within a plasma deposited coating during or after processing is influenced by factors including the temperature of the splats on impact and substrate conditions. The prediction of the temperature field within a coating enables an estimation of the resulting residual stress and particularly degree of cross-linking for thermoset materials.

4.3.1 Microstructure of coatings

Plasma sprayed polymer coatings do not possess a homogeneous microstructure and consist of features including pores, cracks, impurities, unmolten particles and splats (section 7.1). The existing of these features, particularly the pores and cracks, influences the heat transfer within the coatings.

The pores and cracks can be treated as second phases randomly distributed in the coating material matrix, the existing of which may modify the thermal conductivity of matrix material. The influence of the porosity on the thermal conductivity of the matrix materials has been analyzed in many papers [96, 97, 98, 99]. Progelhof et al [97] cite 25 models which help to predict the effective thermal conductivity (the conductivity of the porous material) knowing the volume fraction of a second phase such as porosity, the thermal conductivity of the matrix and the thermal conductivity of the second phase. Some useful models were summarised in reference [96], which has also given comments on the models. In present model, however, considering the porosity of a plasma sprayed coating not to be a constant but a variable varying with the processing parameters and feedstock particle size (Section 7.2 and 7.4), the coating in the calculation is at first assumed to be a uniform structure and the presence of pores and other defects is neglected.

4.3.2 Heat transfer equations

It was first considered that the dimension of the coating in the plane parallel to the coating-substrate interface is much larger than its thickness so that, to a first approximation, the heat flow in the latter plane may be neglected. The heat transfer problem can thus be simplified to a one-dimensional flow between the environment, the coating and the substrate as shown schematically in Figure 4.6. Therefore the governing equation for the heat conduction within the coating is:

$$\frac{k}{\rho C_p}\frac{\partial^2 T}{\partial x^2} = \frac{\partial T}{\partial t} \qquad (4\text{-}59)$$

where T is the temperature within the coating at a distance, x, from the substrate-coating interface at time t; k, ρ and Cp are the thermal conductivity, density and specific heat of the coating respectively.

A finite difference method in the implicit form was used to solve the heat transfer equation and because of neglecting the influence the existing of the defects and splat boundary, the coating may be treated as an enlarged splat, so the same boundary conditions described in Equations (4-53), (4-54), (4-55), (4-56) and (4-57) were used.

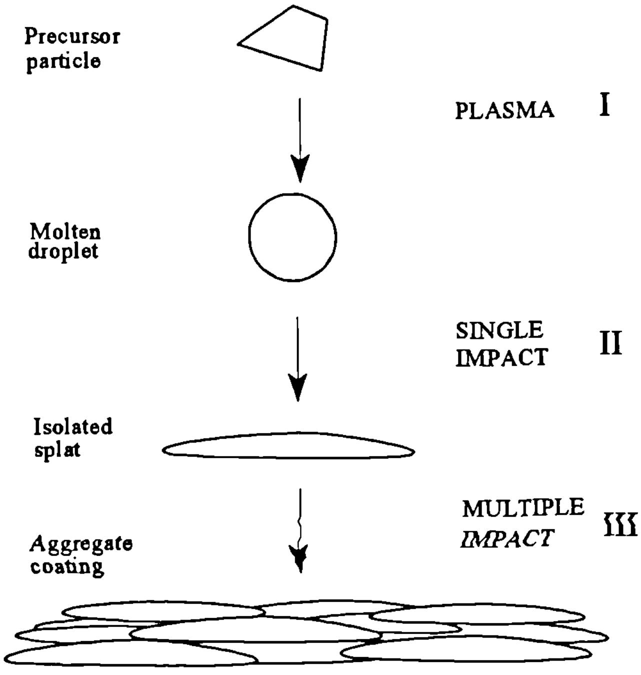

Figure 4.1 Schematic showing the stages of the evolution of the coating

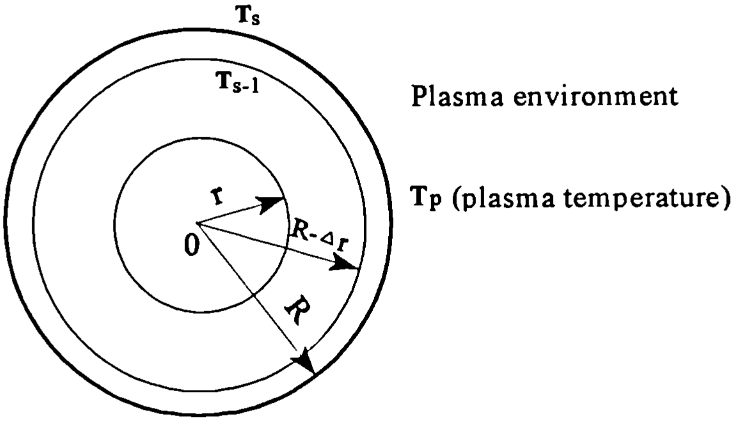

Figure 4.2 Schematic showing a single-phase particle of radius R and surface temperature Ts in a plasma environment.

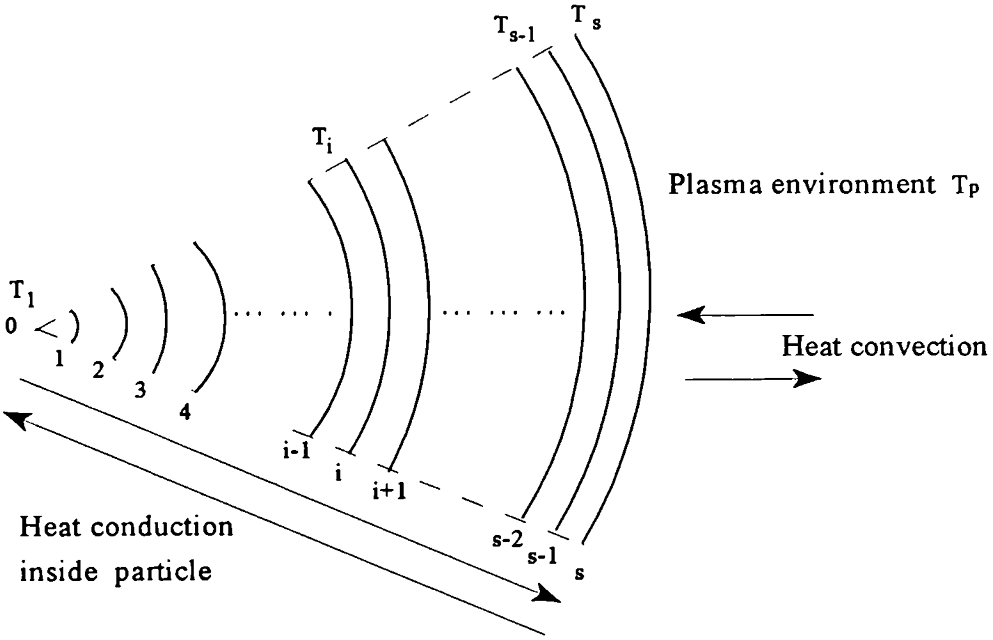

Figure 4.3 Schematic showing differential elements within the particle for the heat transfer analysis

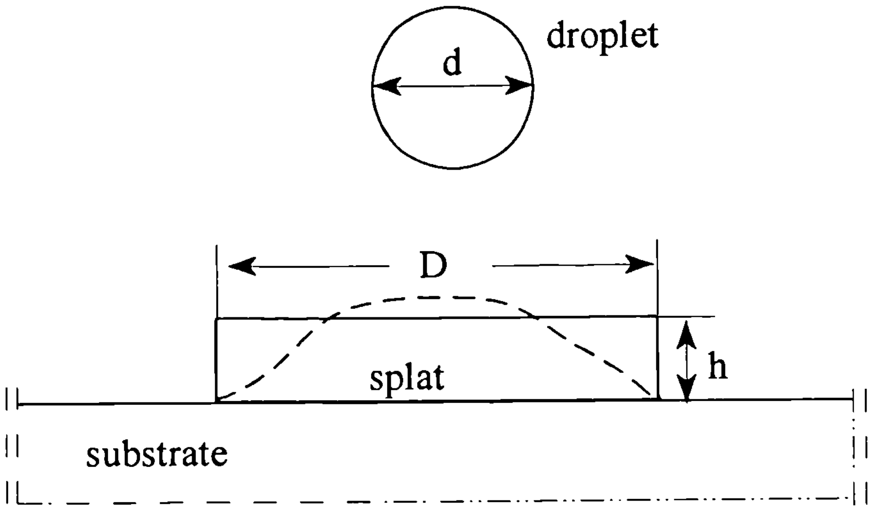

Figure 4.4 Schematic showing the deformation of a molten particle

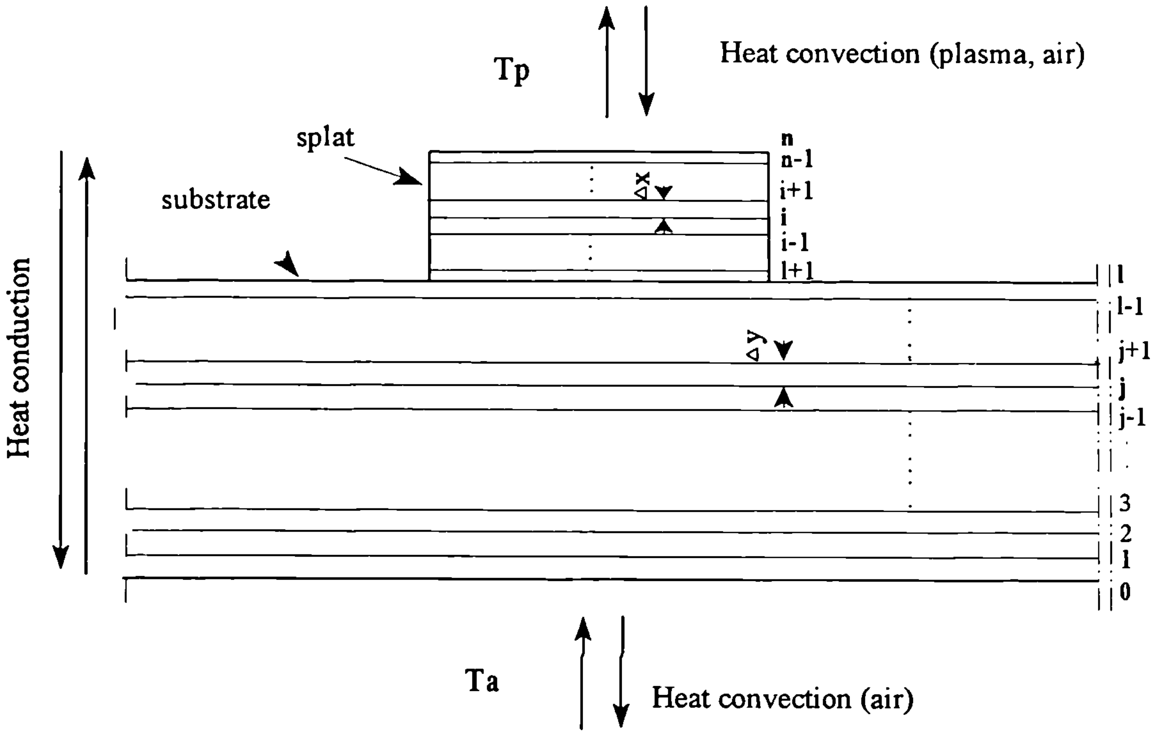

Figure 4.5 Schematic showing differential elements for the heat transfer analysis

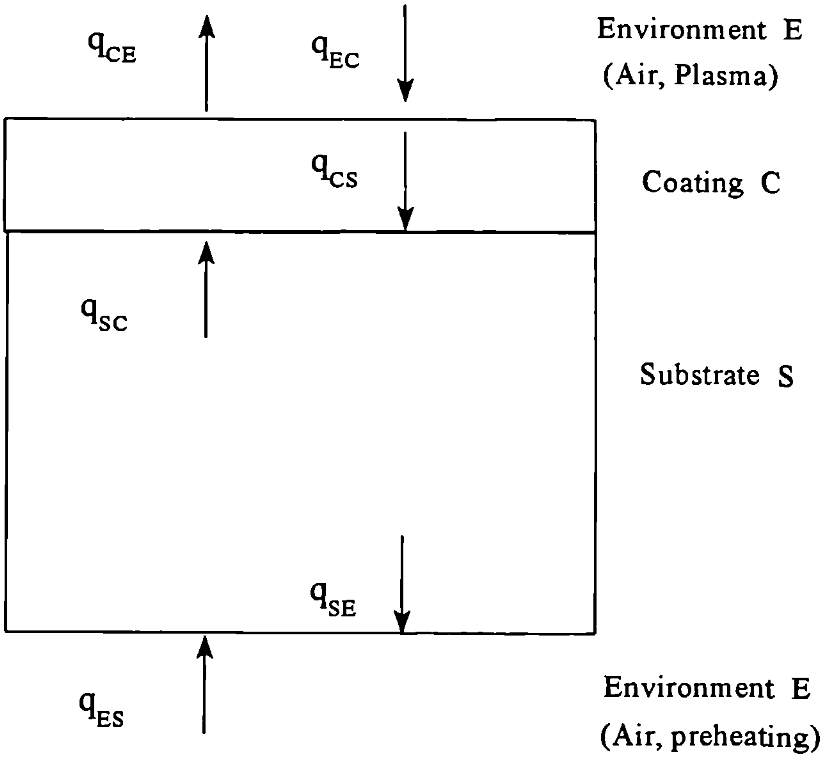

Figure 4.6 Schematic of heat flow during the cooling of a plasma sprayed coating. q is the heat flow with respect to the environment (E), the coating (C), or the substrate (S).

CHAPTER 5. EXPERIMENTAL DETAILS AND TECHNIQUES

5.1 Materials

Two thermoplastics, polyamide 11 supplied by Atochem Ltd. and polymethylmethacrylate supplied by ICI plc., and a series of thermoset epoxies supplied by Shell plc. were investigated as coating materials.

5.1.1 Polyamide

Polyamide 11 is a semi-crystalline thermoplastic material. It is one of the members of polyamide family, also called nylon, and is a well established engineering material. The other members include polyamide 6, 6.6, 6.10, 6.11, 6.12, and 12. All polyamides have the amide (-CO-NH-) group, the link that joins the repeating hydrocarbon units of various lengths. The polyamides are usually identified numerically using the number of carbon atoms in the basic unit of the polymer chains[85].

Polyamide has a proven record of toughness in respect of impact strength, flexibility and wear resistance. It has a coefficient of friction almost as low as PTFE, but better abrasion resistance, and is much cheaper. As a good wear resistance material, polyamide finds wide industrial application. For example, polyamides possess high wear resistance under three-body abrasion, and so they are used widely in many industries such as mining and cement manufacturing, where dust-laden atmospheres exist alongside moving machinery. Another application relies on the erosion and cavitation resistance of polyamides which is important for components subjected to high-speed movement in fluids. Polyamides have been successful in replacing metallic materials, such as bronze, in applications: such as propeller blades in small coastal and naval vessels, where they show much less damage from cavitation and erosion. The resistance of polyamide to sea-water corrosion is in this application an additional factor in its favour. Unlike metals, polymer and particularly polyamides are capable of working effectively in dry conditions or after only an initial smear of lubricant. On this basis polyamides are often chosen in sliding mechanisms or bearing applications where it is impractical or inconvenient to lubricate the surface from external source. Polyamide has also good electrical insulation and good chemical resistance to alkalis, inorganic salts, most solvents, and organic acids[15, 85].

Polyamide powder was one of the first powder available for coating in the early days of powder coating(1950s). It has continued to be used in various forms during the four decades that have elapsed since then, and its popularity is still high, since powder manufacturer has tailored the powder to suit different purposes. Of the polyamide family, polyamide 11 and 12 give the best performance in term of low water absorption, high dimensional stability, and good melt flow characteristics when used for coating. Consequently, these are the only two polyamides used for coating industry. Latterly, polyamide 11 has become the world's most widely used polyamide for coating purposes[15]. The raw feed stock for polyamide 11 is castor oil which, after processing, yields an 11 carbon atom polyamide with the chemical formula $H(HN\text{-}(CH_2)_{10}\text{-}CO)_nOH$[85].

Figure 5.1 gives a SEM micrograph of as-received polyamide 11 powder and Figure 5.2 its particle size distribution evaluated from SEM observation. These Figures revealed that as-received polyamide 11 powder has an equiaxed angular particle morphology and a mean size of 85 μm with 90% of particles between 50μm and 150μm. As-received polyamide 11 powder was sieved into four different particle size range in order to investigate the influence of the particle size of the feedstock powder on the coating properties and process. They were: 150-90μm, 90-75μm, 75-53μm and 53-38μm. The technique details of as-received polyamide 11 powder are given in Table 5.1.

5.1.2 Polymethylmethacrylate (PMMA)

Polymethylmethacrylate is an atactic polymer and since the methyl and ester groups are incapable of being interchanged in a crystal lattice, this polymer is therefore amorphous and transparent. Since the substituents on the alpha-carbon atom restrict chain flexibility, and the side groups are polar and relatively small, there is fairly substantial inter-chain attraction[100]. The polymer is therefore hard and rigid with a glass transition temperature of 105 °C. The surface hardness of PMMA, in particular Diakon grades, and its resistance to scratching are exceptionally high for a plastic material, being approximately the same as aluminum and therefore in a number of applications PMMA is used as a coating to improve the scratch resistance of softer surfaces and substrates[100,101]. Three grades of PMMA with different molecular weight were used in present study. They were Diakon DP300 having a weight average molecular weight of 1,800,000; Diakon DA100 having a weight average molecular weight of 600,000 and Diakon MG101 with a weight average molecular weight of 80,000. The details of those three PMMA are given in Table 5.1.

The SEM micrographs of as-received PMMA powders can be found in Figures 5.3a, 5.4a and 5.5a, which show that two Diakon grades of PMMA have a perfect spheroidal shape suggesting good flow ability, and MG101 grade consists of crushed spherical particles which still possesses good flow ability. The particle size distribution for the three grades of PMMA evaluated from SEM observation are shown in Figure 5.3b, 5.4b and 5.5b. Those Figure reveal that: as-received MG101 powder has a mean size of 180μm with 90% of particles between 80μm and 300μm, as-received Diakon DA100 powder has a mean size of 60μm with 90% of particles between 30μm and 90μm, and as-received Diakon DP300 powder has a mean size of 50μm with 90% of particles between 10μm and 90μm. The emphasis on the plasma spraying of PMMAs were placed on the study of influence of molecular weight of polymers on the plasma process.

5.1.3. Epoxy resins

The epoxy resins are thermosetting materials. The epoxy-resin molecule is characterized by the reactive epoxy or ethoxyline groups, which is a three-membered oxide ring[102]:

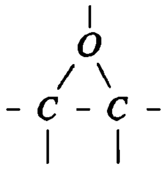

Before they can be used for most their applications, epoxy resins need to be converted by means of cross-linking reaction, through epoxy groups or through hydroxyls or other groups present in their molecules, into a three-dimensional infusible network held together by valence bonds. In epoxy resin technology, this conversion is called curing, hardening or cross-linking, and is achieved by the addition of a curing agent (hardener)[102,103].

The cured epoxy resins possess a number of unusual valuable properties: such as high toughness, high adhesive properties and very inert chemically. Since numerous curing agents for the epoxies are available, and the epoxies are compatible with a wide variety of modifiers, The properties of the cured epoxy-resin system can be engineered to widely diverse specifications depending upon the applications[104,105,106].

Of end-use applications of epoxy resins, nearly half are surface coatings[107], including conventional paints and powder coatings. An commercial epoxy powder usually contains, in addition to the resin, a curing agent, flow-control agent, pigments and fillers. The choice of each item depends upon the method of manufacture of the powder and also the manner of application. Epoxy powder coatings can be formulated so as to have excellent chemical resistance, impact resistance, and electrical properties, these being chiefly determined by the nature of the curing agent. Three epoxy powders have been used in present study. The technical details and characterization of the epoxy powders can be found in Chapter 8.

5.1.4 Substrate

The substrate material used in present study was mainly a plain carbon steel (EN8 grade) plate of thickness 6mm or 3mm, which was degreased and surface roughened by grit blasting before applying coating. Detail procedure is given in Section 5.3.

5.2 Plasma spray system

Plasma spraying was carried out using a Metco MN plasma spray system. This system is comprised of a type MRN power supply unit, a type 4ME heat exchanger, a type 4MB plasma spray gun, a type MCN control unit and a type 4MP powder feed with a fluidized bed hopper[47]. The schematic of the system is shown in Figure 5.6. The power supply unit provides electrical power, the ignition circuitry, and water distribution components for gun operation and gun cooling. In addition, it provides electrical signals to the control unit for monitoring voltage and current and also serves as a connection for input power to the control unit. The heat exchanger is used to recirculate conditioned water to cool the spray gun and the water-cooled electric power gun cables. The heat exchanger utilizes plant water, at plant pressure, to cool the conditioned gun cooling water. Plant water flow is controlled by a solenoid in the heat exchanger. The flow of gun cooling water is controlled by the heat exchanger water pump. The control unit is the central control unit for the MN plasma spray system. It is manually operated to control and monitor all the functions necessary to initiate and maintain a plasma spray process. All controls required for supplying and monitoring electricity, plasma gas, compressed air and cooling water used by the gun are grouped into one console. During operation, electricity, cooling water, compressed air and plasma gases are supplied to the gun from the control unit and power supply. The positively-charged nozzle and negatively-charged electrode generate a high-energy arc in the gap between the nozzle and electrode. Plasma gases enter the gun through the gun insulator assembly and pass through a gas ring. The reaction between the arc and the plasma gases cause the gases to ionize. The result is a high-temperature plasma flame, which emerges from the exit bore of nozzle at a high velocity. Spray powder is fed to the gun at a preset flow rate from the powder feed unit, through a powder feed hose to the powder port located above the gun nozzle. The powder is carried to the gun by carrier gas supplied to the powder feeder which is the same gas as the primary plasma gas and injected to the plasma flame through the powder port. The powder is melted by the plasma flame and the molten particles propelled from the gun to the surface being coated.

Nitrogen or argon was used as the primary plasma gas, hydrogen as the secondary plasma gas in present study. The plasma arc power levels were controlled by preselecting the gun current and the flow of gases which specified in standard cubic feet per hour at a standard temperature and pressure. Voltage could be read from a console display which varied with the combination and flow of plasma gases. The gun was manipulated manually or using traverse units (Metco, type HHT-Br horizontal traverse unit and type HVT-Br vertical traverse unit).

5.3 Preparation of substrate

Preparation of the substrate prior to spraying involved the following steps:

- Each sample was de-burred and radiused to reduce stress concentration on the edges.
- Each sample was wipe cleaned and then degreased in an acetone solution at room temperature.
- Samples were grit blasted using a Guyson model 3000R grit blast unit and an alumina grit (Metcolite C grade) under a blast pressure of 4 bar, blast angle of 90° and a blast distance of 100-150mm to give a surface roughness of 6-8μm Ra measured using a Surftronic 3^+ profilometer (Rank Taylor Hobson Ltd., Leicester, UK).
- Oil-free compressed air was used to remove the loose grits from each sample and then acetone final washing.
- Plasma spraying was performed within two hours after grit blasting

Specially pre-treatments of substrate for the purpose of investigation of substrate pre-treatment on the adhesion of the coatings to steel substrate are described in section 7.5.1.

5.4 Experimental Techniques for the characterisation of materials

5.4.1 Optical and scanning electron microscopy

Optical and scanning electron microscopy, as most powerful methods for examining and understanding the microstructure of materials, were used to examine the morphologies, particle sizes and size distribution of feedstock powders used and that of individual splats produced by wipe testing. They were also used for the observation of the surface feature of as-deposited coatings; the interface structure between the coating and substrate; the microstructure of through-thickness cross section of the coatings; the fracture surface characters under tensile loading; the wear traces of the coatings from sliding wear tests and wear debris produced during wear tests .

A Cambridge S250 Microscopy was used in the secondary electron mode, accelerating voltages in the range 10 to 25kV were applied. The no-conductive polymer samples were sputter coated with gold or platinum prior to examination to reduce charging.

The examination for the through-thickness cross section of coatings include fracture surface examination and polished surface examination. The specimen for fracture surface examination were prepared by separating the coating from the substrate, immersing in liquid nitrogen and fracturing through the thickness by bending. The polished specimens were prepared by first cutting carefully the sections of coated substrate, mounting the samples in a cold set liquid resin(Araldite MY .753 resin and HY951 hardener), then wet grinding on a wheel covered by silicon carbide discs at 550 RPM, using a grit size series of 180-320-1200-2000-4000, and finally polishing them with 1 and 0.25μm diamond paste(Struers standard diamond paste) on a rotating metal wheel covered with DP-MICRO polishing cloths(Struers).

5.4.2 Differential scanning calorimetry (DSC)

The DSC technique was used to characterise the thermal characters of polymers before and after plasma spraying, including glass transition temperatures, melting temperatures (range), the enthalpy of fusion (plastics) and specific heat. All these are necessary parameters for the heat transfer calculations and important information for the analysis of the behaviour of polymers during plasma spraying, such as the degradation and phase transition. It was also used to monitor the cross-linking rate of thermoset and detect the degree of cross-linking of thermoset coatings[107].

A Pekin Elmer DSC-7 Differential Scanning Calorimeter was used. In this instrument, both sample and inert reference were heated (or cooled) at the same liner rate over a preset temperature range and maintained in a thermal null state at all times. When any physical or chemical changes of the sample occur, involving the absorption or evolution of energy, an equivalent amount of energy (electrical power) would be applied or removed to the sample to compensate for energy change occurring in sample and keep thermal equilibrium of the system. The amount of power required to maintain the system at thermal equilibrium is directly proportional to the energy changes occurring in the sample, and was directly measured, in the other word, the heat flow to or from the sample was directly measured and in differential power units(milliwatts)[108].

The sample for measurement was prepared by peeling the coating off the substrate and cutting into very fine pieces. The measurement was carried out at a liner heating rate of 10°C/min in dry nitrogen atmosphere.

5.4.3 Infrared spectroscopy

The energy of the vibrations of most polymer functional groups corresponds to that of the infrared region of the electromagnetic spectrum. The vibration frequencies of functional groups, characteristic of that functional group, may be detected and measured in an infrared spectrum[109]. In present study, the infrared spectroscopy technique was used to detect whether or not modifications of microstructure and composition of the polymers occurred during spraying as an aid to understanding their behaviour.

A Perkin Elmer 680 series Infrared spectrophotometer was used. In this device, the radiation emitted by the infrared light source is split into two beams of equal intensity, and one beam is arranged to pass through the sample which absorbs radiation of wavenumber corresponding to its characteristic vibrational frequencies, whilst the other serves as reference. The relative energy of two beams in terms of electronic signals is then measured[110]. The measurement was carried out under a medium slit and 6 minute scan time.

Depending on nature of the polymers, several methods were used to prepare testing samples including mixing fine polymer powder with KBr powder and pressing into disc; hot pressing powder and coating sample into thin film (10-20μm) and microtoming sectioning coating sample with MSE sledge microtome into thin film(10-20μm) and then placing in the between of two KBr discs.

5.4.4 X-ray diffraction

X-rays are electromagnetic radiation within wavelength ~ 0.1nm. When x-rays interact with a crystalline material they are subject to diffraction which produces a series of strongly diffracted beams leaving the crystal in defined and predicted directions. Different crystalline structure has its characteristic diffraction pattern. Therefore the x-ray diffraction technique can be used to provide information concerning the nature and arrangement of atoms in a crystal lattice. The relationship between the crystal lattice, the incident radiation and the resultant diffraction pattern is given by Braggs Law[111]:

$$\mathbf{n\lambda = 2d \sin \theta} \tag{5-1}$$

where λ is the wavelength of the incident radiation, d is the spacing between specific crystal planes which make an angle θ with the incident radiation and n is an integer.

X-ray diffraction technique was , in present study, used to detect whether or not plasma deposition cause any changes in structure of materials sprayed that might be revealed by this technique. A Phillips PW1050 Diffractometer was used. the sample was scanned by nickel filtered CuKα radiation which has a wavelength of 0.15418 nm at a scan rate of 2 degree per minute. The sample of as-deposited coating was cut into dimension of approximately 10mm x10mm and stuck to the sample holder by plasticine. The feedstock powder sample was mixed with a glue, poured into the sample holder (10mm x 10mm x 3mm) and pressed to ensure it would stay on during scanning.

5.4.5 Thermogravimetric analysis (TGA)

This technique can provide quantitative information about the thermal decomposition of polymeric materials from which the thermal stability of the polymer can be evaluated. The information of polymer decomposition at elevated temperature is important for both thermal calculation and processing parameters selection.

A Perkin-Elmer Model TGS-2 Thermogravimetric Analyzer with a Perkin-Elmer AR-2 recording balance was used. It involves continuous weighing of the sample as it is subject to a precisely controlled temperature environment. The relationship of weight loss of sample to be examined to the temperature at different heating rates can therefore be found out. The experiment was carried out in atmosphere condition.

5.5 Experimental techniques for the evaluation of coating properties

5.5.1 Density measurement

The density of plasma sprayed coatings is frequently quoted as an important index to evaluate the quality of the coatings. In fact the principal reason of the measurement of the density is to determine porosity which has a profound effect on many end-use properties of the coatings. The bulk density of the coatings was measured by the mercury displacement method using a Doulten Densometer[112]. Refering to Figure 5.7, the procedure of the measurement is as following:

- weigh the coating sample peeled from substrate in a top-pan balance and note gave a weight W_1;
- pour approximately 1 kg of clean mercury into a 100 ml beaker and place centrally on the balance under the saddle, lower the saddle into the mercury until the pointer attached to the saddle just touches the surface of the mercury and then set the balance to zero;
- raised the saddle and place the sample on to the surface of the mercury, lower the saddle to immerse the sample into the mercury until the pointer just touches the surface of the mercury. Note the balance weight of W_2.

The bulk density of the coating, dc, may be calculated from the expression:

$$d_c = \frac{W_1 \, d_{mercury}}{W_2} \qquad (5\text{-}2)$$

where $d_{mercury}$ represent the density of mercury which is 1353 kgm^{-3} under the test conditions used.

5.5.2 Wear performance

The sliding wear behaviour of the coatings was assessed using a reciprocating pin-on-flat machine (as shown in Figure 5.8) with two types of pin contact surface: a stainless steel ball and Rockwell diamond. The stainless steel ball was of diameter 12.7mm and the Rockwell diamond consisted of a regular cone with a 120 degree included angle. Both counterface materials were wipe cleaned and acetone degreased prior to each test. Loads of 20N, 40N, or 60N, depending coating materials, were applied to the steel ball, and 4N to the diamond counterface respectively during tests. The steel ball or diamond tip slide at 50 cycles per minute over a track length of 30mm on the flat coating specimen, which gives a relative velocity of the counterface with respect to the coating specimen of 0.05 ms^{-1}. Tests were carried out under dry and ambient conditions. Wear depth of the coatings was evaluated by using a linear variable differential transducer attached to the counterface arm. Friction of the coatings was measured using the same apparatus simultaneously. Friction was assessed by attaching a linear variable differential transducer to a beam positioned in front of the counterface arm.

5.5.3 Tensile properties

The stress-strain character of the coatings under tensile loading and tensile strength at breaking can be obtained from tensile test. The tensile properties of the coatings was measured by following the procedure of ASTM D638 standard testing method[113]. The test specimens were prepared by die cutting free-standing coatings into the dimension required. The dimensions of the die was that of Type 4 die in BS 903(BS 903: part A2:1989[114] with a overall length of 50mm, end width of 8.5±0.5mm, length of narrow section of 16±1.0mm and width of narrow section of 4±0.1mm .The tensile testing was undertaken using an Instron Model TT-C tensile testing machine with a cross-head speed of 5mm $\min^{-1}$. The specimens were ground to a surface roughness of 0.5-0.6μm Ra before testing. The reported tensile test result is the mean value of five test results.

5.5.4 Adhesion test

The adhesion of the polymer coatings to the steel substrate was determined using the direct pull-off technique conforming to ISO 4624 and BS 3900-E10 standard[115]. The measurement was performed by using an Elcometer Adhesion Tester. An aluminium test dolly was first adhesively bonded to the coating, and then the tensile force required to detach the coating from the substrate was measured with the tester. The adhesives used to bond coating to test dolly was Araldite 2005(CIBA-GEIGY, high peel and shear strength) and REDUX 419 NA. The polymer coating surface was roughened with carbide paper and the test dolly was grit-blasted before applying the adhesive in order to maximize the strength of the adhesive joint. There were three type of failure pattern recorded during testing. An adhesion failure was characterized by fracture at the coating-substrate interface, a adhesive failure by fracture at the adhesive-coating interface or internal adhesive, and a cohesive failure by fracture within the coating itself.

5.5.5 Viscosity measurement

The viscosity of a dilute polymer solution depends on the nature of polymer and solvent, the concentration of the polymer solution, the average molecular weight and molecular weight distribution of the polymer. Therefore the monitoring of the change of solution viscosity of polymer materials before and after plasma spraying may offer useful information to evaluate the microstructure change and possible degradation of the polymer during plasma spraying. The solution viscosity of the polymer powder and coatings was measured at 25°C by following the procedure in ASTM D 445 and D446 using a Ubbelohde Viscometer[116,117]. The solution was prepared by peeling coatings from substrate, cutting them into small pieces, and then dissolving them in metal-cresol at room temperature. The viscosity of polymer was determined over a range of polymer concentration.

Table 5.1 Technical data of as-received polyamide 11 and PMMA powders

Data	Polyamide 11	PMMA	PMMA	PMMA
Grade	Rilsan BHURX	Diakon DP300	Diakon DA100	MG101
Supplier	Atochem	ICI	ICI	ICI
Crystallinity	semi	amorphous	amorphous	amorphous
Mean size / μm	85	50	60	180
Density / Mgm^3	1.040	1.118	1.118	1.118
Glass tran. temp. / °C	46	105	105	105
Melting/softening temp. / °C	186	160	160	160

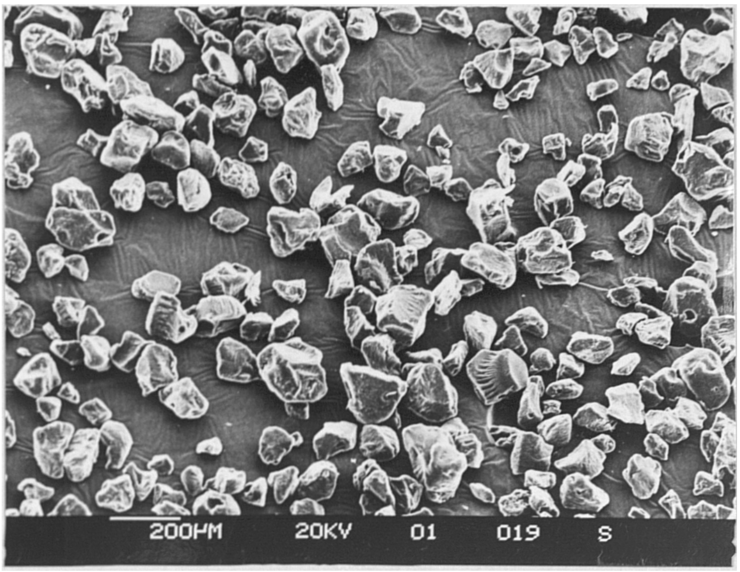

Figure 5.1 SEM micrograph of as-received polyamide 11 powder

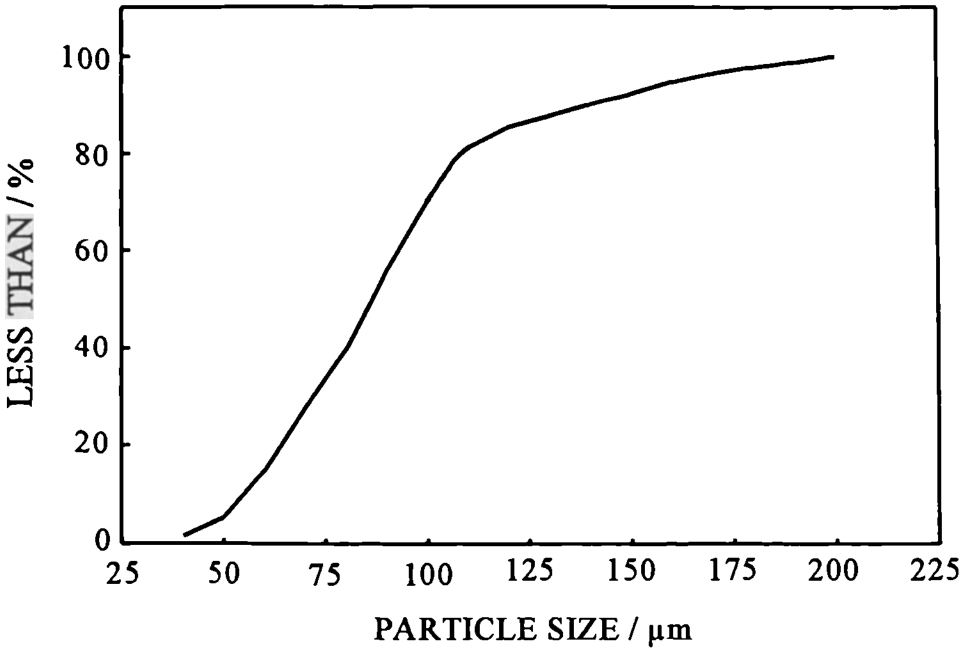

Figure 5.2 Particle size distribution of as-received polyamide powder

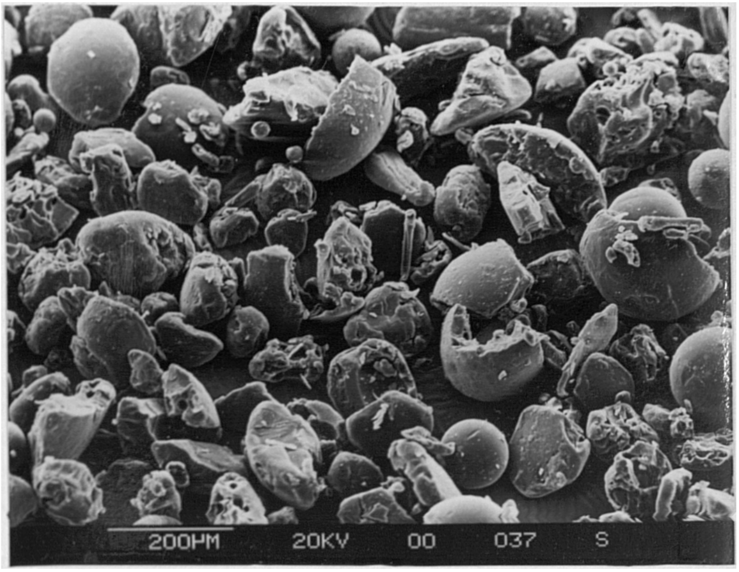

Figure 5.3a SEM micrograph of as-received PMMA(MG101 grade) powder

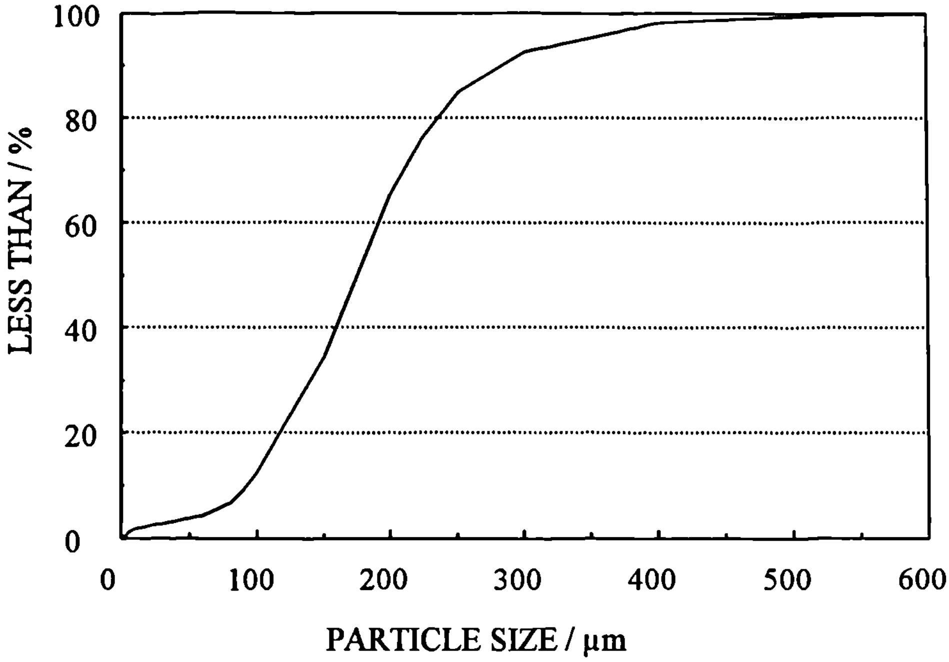

Figure 5.3b Particle size distribution of as-received PMMA(MG101 grade) powder

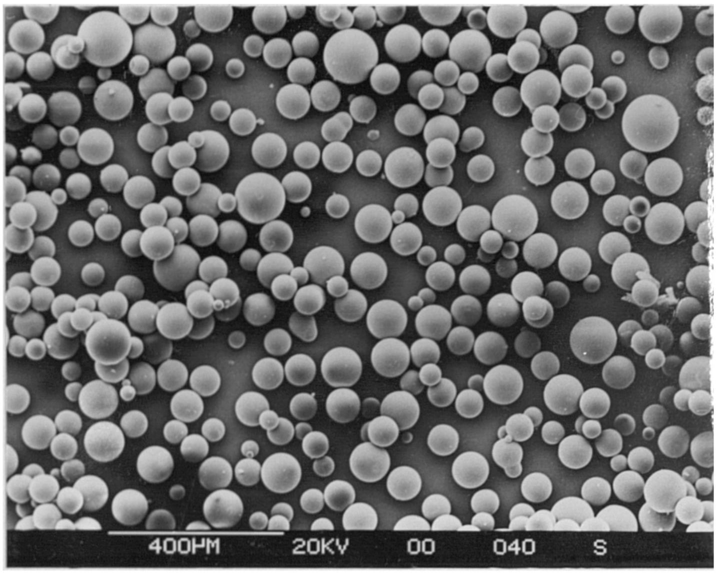

Figure 5.4a SEM micrograph of as-received PMMA(DA100 grade) powder

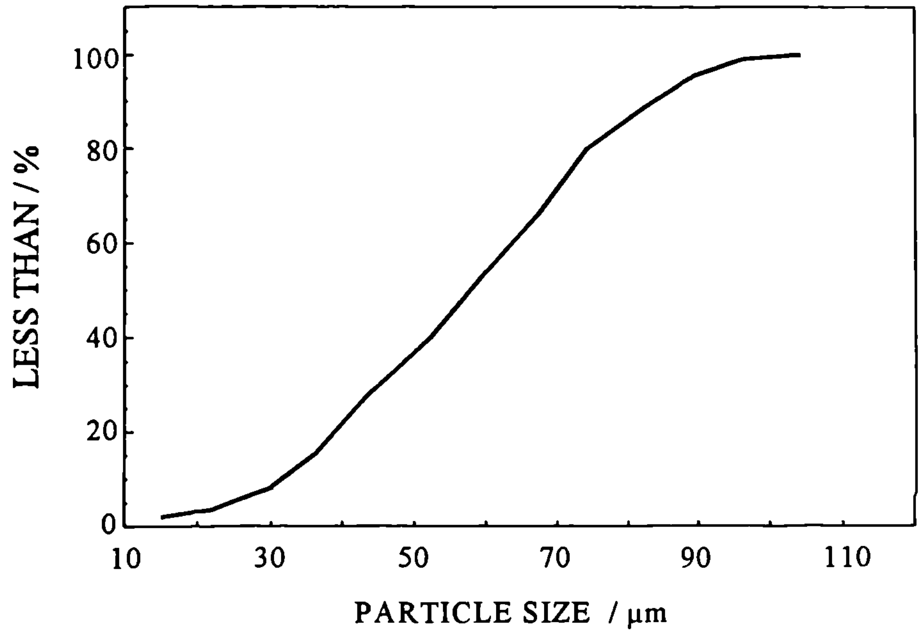

Figure 5.4b Particle size distribution of as-received PMMA(DA100 grade) powder

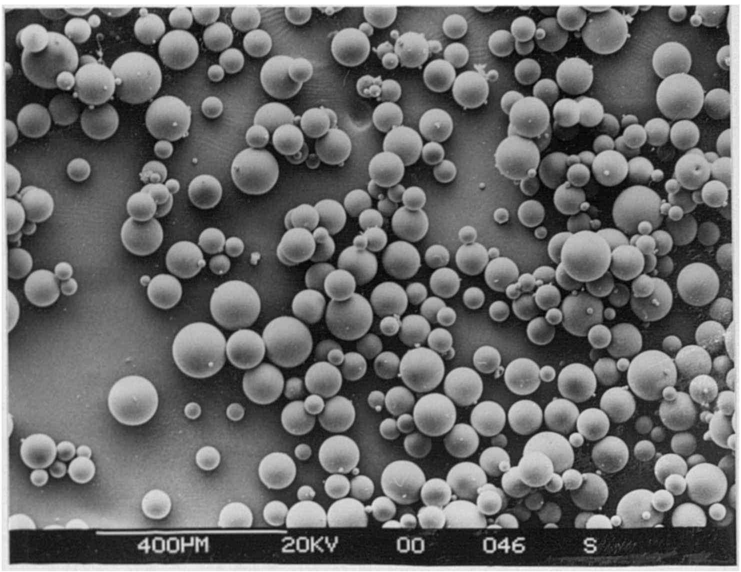

Figure 5.5a SEM micrograph of as-received PMMA(DP300 grade) powder

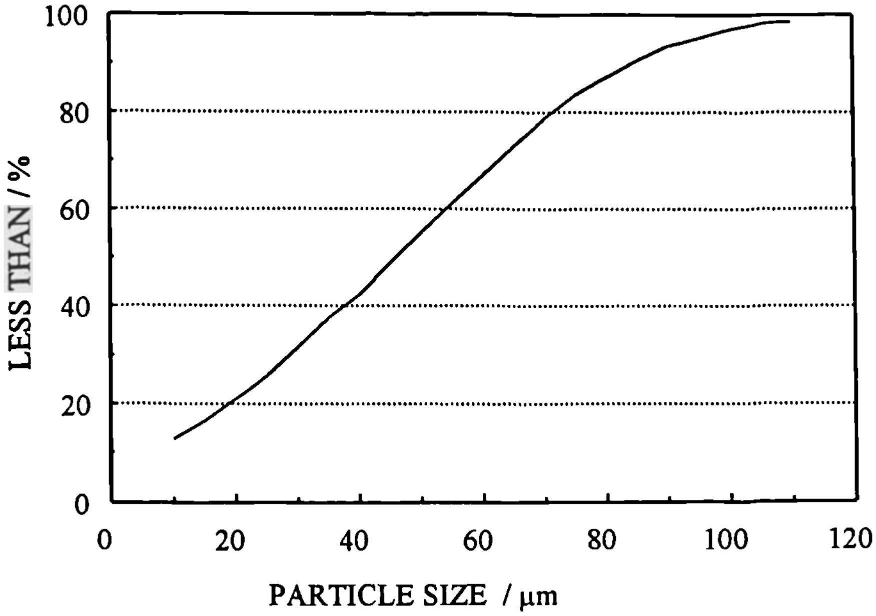

Figure 5.5b Particle size distribution of as-received PMMA(DP300 grade) powder

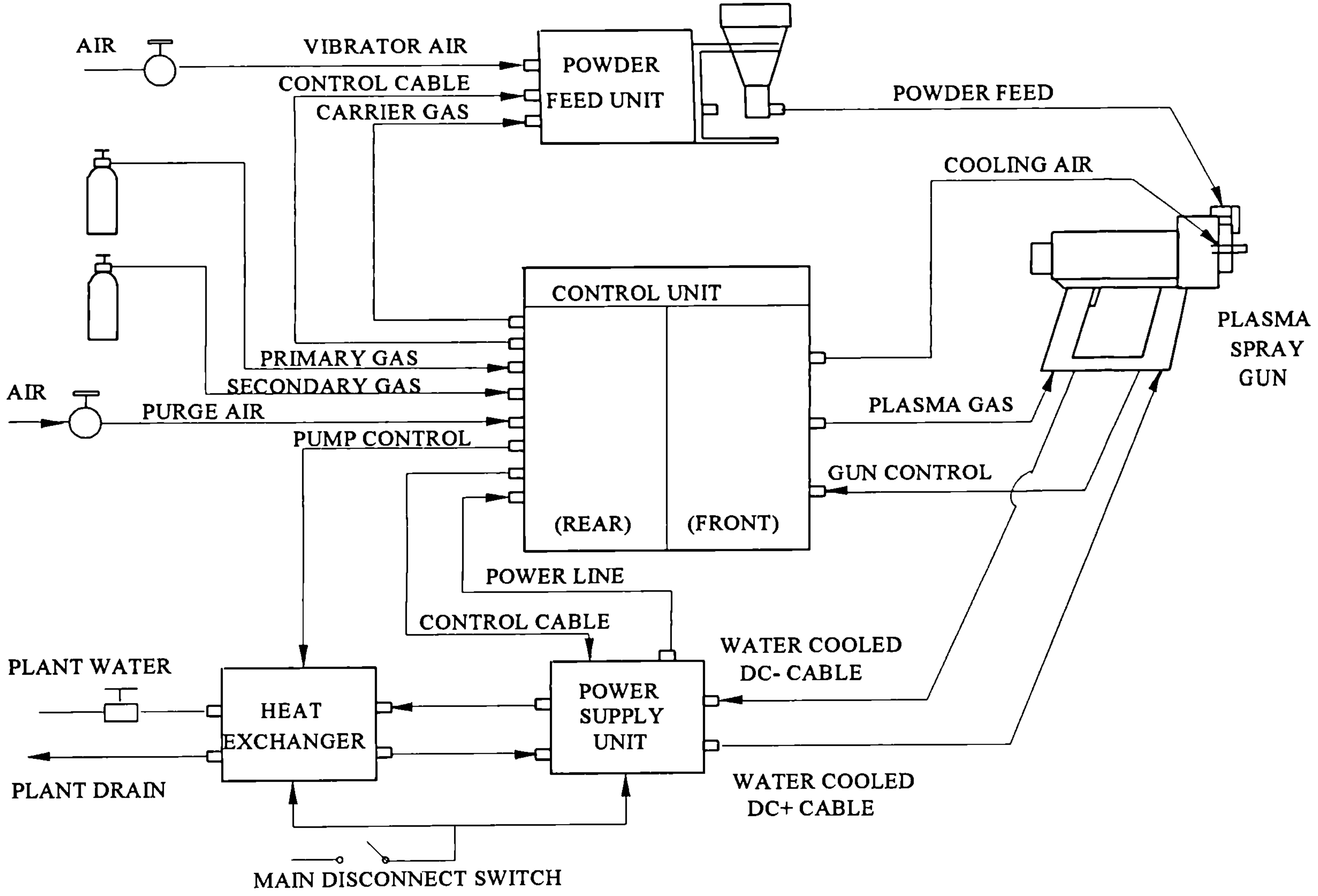

Figure 5.6 Schematic of MN plasma spray system

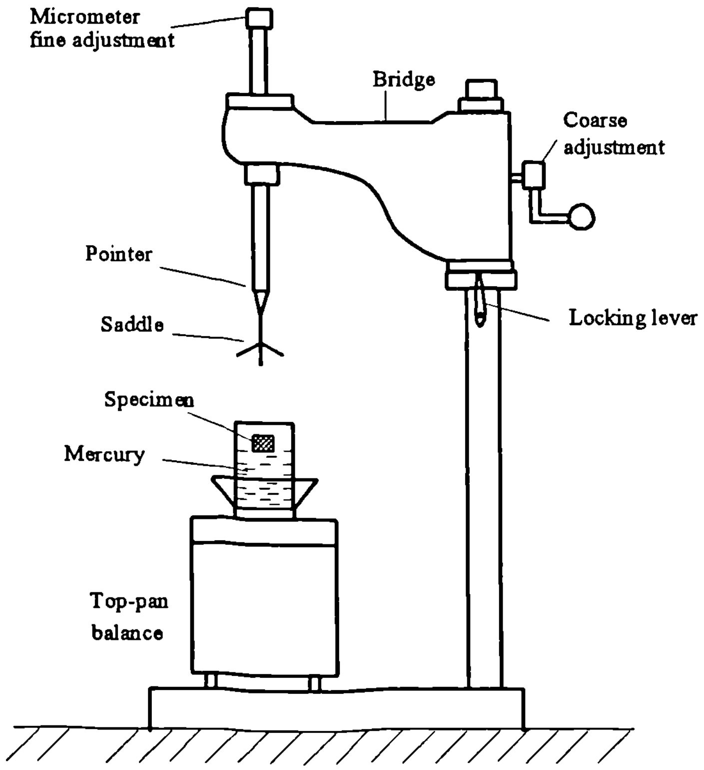

Figure 5.7 Schematic of the bulk density measurement apparatus

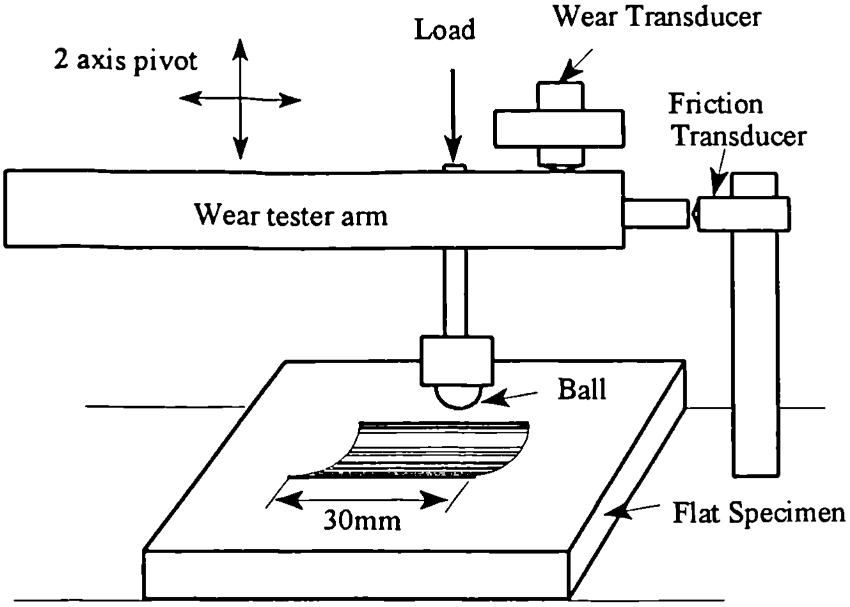

Figure 5.8 Schematic showing reciprocating ball-on-flat wear test.

CHAPTER 6. PREDICTION OF TEMPERATURE PROFILES OF IN-FLIGHT PARTICLES IN A PLASMA JET

This chapter focuses on the results and discussion of the thermal calculations, particularly on the temperature profiles of in-flight particles in plasma jet and their relation to the plasma processing parameters.

6.1 Determination of variables required in thermal calculations

The accuracy of the theoretical calculation depends markedly on the accuracy of the determination of variables in the heat transfer equations such as the plasma temperature, convective heat transfer coefficient and Kundsen number. In addition, it also depends on the accuracy of the physical and thermal property data of materials considered. This section discussed how those variables were determined.

6.1.1 Plasma temperature field

In thermal calculation, plasma temperature Tp is a very important variable. To simplify the calculations, the plasma temperature may be treated as a variable independent of axis and radius distance from nozzle exit[63, 65]. The advantage of such treatment is that it avoids the difficult problem of obtaining the temperature profile data of plasma jet at varying conditions. However there are a few plasma temperature field data reported which were produced from experimental measurements under limited plasma conditions[26, 31]. The current thermal calculations have used these experimental measurements. In particular, the plasma temperature profiles measured by M. Vardelle and A. Vardelle [26] were used in present study. The raw data are given in Figure 6.1, and this enables plasma temperature to be treated as the function of distance.

If a flight path of an in-flight particle is known, the latter experimental data [26] can be fitted into the equations of plasma temperature against spray distance by the least square method. The in-flight particles may be assumed to travel towards the substrate along the plasma central axis. This is, however, only an ideal case. Usually, the powder particles, introduced perpendicularly into the plasma jet, follow a flight path of conical shape as shown in Figure 6.2[31]. In present study, the particles were thus assumed to move towards the target along the AB line (Figure 6.1) which was thought to be more close to practical case. The temperature profiles of Vardelle et al [26] on this line can therefore be fitted into the following equations:

for the Ar/H_2 plasma:

$$T_p=1.15\times10^4-2.23\times10^2z+1.78z^2-5.75\times10^{-3}z^3+5.32\times10^{-6}z^4 \qquad (6\text{-}1)$$

for the N_2/H_2 plasma:

$$T_p=1.05\times10^4-1.72\times10^2z+1.09z^2-2.34\times10^{-3}z^3 \qquad (6\text{-}2)$$

where z is the axil distance from nozzle exit. Correlation coefficient for equation (6-1) is 0.9975 and correlation coefficient for equation (6-2) is 0.9948.

The plasma temperature fields determined by equation (6-1) and (6-2) were introduced into the heat transfer equations in Chapter 4 for the calculation of heat transfer of in-flight particle and splats on impact in plasma environments.

6.1.2 Convective heat transfer coefficient h

Convective heat transfer was considered as dominate heat exchange between the plasma jet and the in-flight particle boundary. The influence of radiative heat transfer on overall heat exchange was considered to be minor and was ignored (Section 3.3.3). Based on the review in section 3.3, Bourdin et al.'s method of integral average thermal conductivity[63] was selected for the determination of the convective heat transfer coefficient h. For the convenience of discussion, the definition of integral thermal conductivity, k, across the boundary layer (equation (3-14)) is rewritten as the following:

$$\bar{k}=\frac{1}{(T_p-T_s)}\int_{T_s}^{T_p}k(T)dT \tag{6-3}$$

The application of equation(6-3) can be considerably simplified by splitting the integral with respect to some reference temperature T_0=300K, as follows:

$$\bar{k}=\frac{1}{(T_p-T_s)}[\int_{300}^{T_p}k(T)dT-\int_{300}^{T_s}k(T)dT] \tag{6-4}$$

or

$$\bar{k}=\frac{1}{(T_p-T_s)}[I(T_p)-I(T_s)] \tag{6-5}$$

where, I(T), which is known as the "heat conduction potential", is defined as:

$$I(T)=\int_{300}^{T}k(T)dT \tag{6-6}$$

therefore the convective heat transfer coefficient h can be expressed as:

$$h=\frac{2}{d(T_p-T_s)}[I(T_p)-I(T_s)] \tag{6-7}$$

Based on the available literature data, the integrated thermal conductivity, I(T), was calculated using equation (6-6) by Bourdin et al., for different gases at atmospheric pressure and the results given in Figure 6.3 together with the corresponding values of thermal conductivity as function of temperature. Their calculated results(Figure 6.3) were, in the present study, fitted by the least-square method into following equation for the argon plasma:

$$I(T)_{Ar} = 48.5 - 6.94\times10^{-2}T_p + 4.98\times10^{-5}T_p^2 - 6.25\times 10^{-9}T_p^3 + 3.92\times10^{-13}T_p^4 \tag{6-8}$$

for the nitrogen plasma:

$$\mathbf{I(T)_{N2} = -104.6 + 0.96T_p - 7.34\times10^{-4}T_p^{2} + 1.59\times10^{-7}T_p^{3} - 7.63\times10^{-12}T_p^{4}} \qquad (6\text{-}9)$$

for the hydrogen plasma:

$$\mathbf{I(T)_{H2} = 17792.5 - 27.6T_p + 0.116T_p^{2} - 1.33\times10^{-6}T_p^{3} + 4.27\times10^{-11}T_p^{4}} \qquad (6\text{-}10)$$

and for the mixed plasma:

$$\mathbf{I(T)_{mix} = aI(T)_{Ar}) + bI(T)_{N2} + cI(T)_{H2}} \qquad (6\text{-}11)$$

where T_p is the plasma temperature, a, b, c are volume fraction of argon, nitrogen and hydrogen plasma in the mixed plasma. Correlation coefficient for equation (6-8) is 0.9993; for equation (6-9) is 0.9957 and for equation(6-10) is 0.9972.

Equations (6-7) to (6-11) were then introduced into the heat transfer equations in Chapter 4, for the calculation of convective heat transfer coefficient subject to various temperatures and plasma gas combination in present processing modelling.

6.1.3 Physical and thermal properties of materials

The heat transfer rate and behaviour of materials in thermal plasma depend greatly on the properties of materials. An important and difficult task in the theoretical analysis was to collect the appropriate data for the material properties, which is the basis of theoretical calculations. The physical and thermal properties of the powder materials used in theoretical analysis were, in the present study, obtained by either experimental measurements or from the literature. For example, the specific heat, enthalpy of fusion, melting or soften temperature range, glass transition temperature, and cross-linking temperature range of the polymer materials were measured using DSC technique; the decomposition temperatures of the polymers were measured by a TGA technique, while thermal decomposition energy of the polymers was evaluated from the bond dissociation energy of the weakest bond. The details of the physical and thermal properties of materials used in this chapter and corresponding data source are given in Table 6.1.

6.1.4 In-flight particle velocity

Above discussion indicates that the heating extent of a particle in a plasma jet depends on the plasma temperature, plasma thermal character and the thermal properties of the particle. Another variable which is equally important is its residence time within the plasma jet, which is determined by the particle velocity. When a particle is injected into a plasma jet, it at first accelerates to maximum and then decelerates. The particle velocity is thus a function of radius and axis distance from nozzle exit of the plasma jet [26]. Directly measuring the particle velocity is very difficult and no experimental data on in-flight polymer particle velocity have been reported.

In present thermal calculations, the particle velocity of the polymer powder is assumed to be independent of its position in plasma jet for the purpose of simplyfying calculations. The particle is assumed to travel through the plasma jet at a constant velocity which is the average velocity of the in-flight particle within the jet. The average particle velocity is estimated by referring to Vardelle's experimental measurements on in-flight alumina particles[26], which was then modified by the density of the polymers: for example, the velocity is related to particle mass, a 18 μm alumina particle has a approximately equivalent mass of 60-70 μm polyamide particle, the particle velocity of the former in Vardelle's temperature field is ~ 240 ms^{-1}, the velocity of the latter was thus taken as 240 ms^{-1}. However, such estimate is rough and particle velocity is governed by the particle size and the plasma parameters (section 2.2). A range of polymer particle velocities were used in thermal calculations, and the effect of the velocities on the heating of polymer particles was studied.

6.2 Heating of in-flight polymer particles in thermal plasmas

From the viewpoint of their thermal properties, polymeric materials posses low thermal conductivities, low melting temperatures and decomposition temperatures compared with metals and ceramics. The thermal character of polymers is likely to affect their behaviour on heating in the plasma. To understand the behaviour of polymers in thermal plasmas, it is necessary to compare the heating process of in-flight polymer particles in the plasma jet with that of other materials.

The temperature profiles of in-flight particles of three materials which were tungsten(metal), alumina(ceramic) and polyamide(polymer) were calculated using the established processing model(Part I). In the calculation, the particles were assumed to be spheroidal with diameter of 60μm, and immersed in an argon+5%hydrogen plasma. The initial temperature of particles were taken as 300K. The calculated results are shown in Figure 6.4, in which the temperature profiles of in-flight particles are expressed as a function of resident time of particles in the plasma.

It can be seen from Figure 6.4 that the temperature at the particle centre rises more slowly than that at the surface for all materials. The effect is particularly marked for polyamide, where the temperature at surface has reached its higher thermal decomposition temperature(830K) while the temperature at the centre is still 300K. A notable characteristic is that the surface temperature of the polyamide particle rises significantly more rapidly than that of the tungsten and alumina particles, while its centre temperature rise significantly more slowly. This results in a large temperature gradient developing within the polyamide particle. In contrast, the temperature difference between surface and centre of the alumina particle is relatively small, while that of tungsten is almost negligible compared with the polyamide particle.

The development of a large temperature gradient within a particle is related to the internal heat conduction developed within the particle. The conductive heat flux is proportional to thermal conductivity and temperature difference in terms of Fourier's law[53]. Polyamide has a low thermal conductivity of 0.29 $Wm^{-1}k^{-1}$ compared with 110 $Wm^{-1}k^{-1}$ for tungsten, and 6.3 $Wm^{-1}k^{-1}$ for alumina. In addition, it has a low thermal decomposition temperature (upper limit 830K above which its surface temperature cannot rise). Thus, the thermal properties of polyamide lead to its high resistance to internal heat conduction which causes the temperature rises rapidly at the surface and slowly at the centre of the particle.

The role of the internal conduction in the overall heat transfer can be judged by the Biot number, which serves as a criterion for determing the relative importance of the internal heat conduction within a particle[31]. The Biot number is defined as the ratio of convective to conductive heat transfer and expressed as a dimensionless group as following:

$$B_i = \frac{h\Delta x}{k} \qquad (6\text{-}12)$$

Under plasma conditions, the Biot number can be calculated by following equation[63]:

$$B_i = \frac{\bar{k}}{k} \qquad (6\text{-}13)$$

where k is the average thermal conductivity of the plasma across the boundary defined in equation (6-3) and k the thermal conductivity of the material constituting the particle. Equation (6-13) indicates that for particles immersed into thermal plasma, this criterion depends heavily on the thermal conductivity of the plasma beam and the nature of the material constituting the particle. If $Bi < 1$, it means that the average thermal conductivity of the plasma across the particle boundary is less than the internal heat conductivity of the particle and thus the overall heat supply is limited by the process taking place in the plasma beam. Some researchers have reported[54, 56] that the internal conduction resistance of the particle is negligible if $Bi \ll 0.1$. If $Bi > 1$, the overall heat transfer is apparently controlled by the internal heat conduction developed within the particle. The Biot numbers calculated using equation (6-13) are 1.3 for polyamide, 0.06 for alumina and 0.004 for tungsten particle respectively, when the particles with an initial temperature of 300 K were immersed into a 10000 K argon plus 5% hydrogen plasma. The calculated Biot number values suggest that the polyamide particles posses a much higher resistance to internal heat conduction than that tungsten or alumina particles when they are immersed in the same plasma surrounding, which is the basis of the behaviour in Figure 6.4.

From equation (6-13), under the same plasma conditions, the Biot numbers of the materials sprayed are mainly determined by their thermal conductivities (polyamide: $0.29Wm^{-1}K^{-1}$, alumina: $6.3Wm^{-1}K^{-1}$, tungsten: $110Wm^{-1}K^{-1}$). The thermal conductivity of most engineering polymers is less than $0.5Wm^{-1}K^{-1}$[118]. As a result, high internal heat conduction resistance leading to the development of large temperature gradients within particles should be expected to be a general characteristic of heating polymer particles in a thermal plasma. In summary, the heating of polymer particles in a thermal plasma is limited by internal heat conduction, whereas the heating of high conductivity materials, such as metals, tends to be controlled much more by the heat supplied by the plasma.

Figure 6.5 shows the calculated temperatures at the particle surface(Ts), at the half-radius($T_{1/2}$) and at the centre of a 80μm diameter polyamide particle travelling at $250ms^{-1}$ through an argon-hydrogen plasma, as a function of distance between the gun nozzle and substrate. It is noted that at a spraying distance of 160mm only 75 vol% of the particle exceeds the melting temperature. This indicates that a direct effect of the large temperature difference developed within a particle is to lower the degree of melting of an in-flight particle. This has major implications for the formation of the plasma deposited coatings.

Figure 6.6 gives a detailed calculated temperature profile within a 60μm-diameter polyamide particle travelling at 240 ms^{-1} through the plasma jet, as a function of resident time and particle radius. It shows that the particle surface reaches its thermal decomposition temperature only after 50μs of entering the plasma jet, which is long before it arrives at the substrate surface(~500-1000μs). As a result, the surface layers of a polymer particle are being continuously removed while in the plasma, and the particle size is correspondingly being reduced. This predicts that a difficulty in the plasma spraying of polymers will be the mass loss of the feedstock particles caused by thermal decomposition of particle surface in the plasma jet. The results also show that after approximately 300μs, the temperature at particle surface stops increasing and starts to fall gradually although the plasma temperature at this position is still above 5000 K(Figure 6.1). However, the internal temperature of particle continues to increase due to internal heat conduction. The particle can then be observed leaving the high temperature zone of plasma with the result that its surface temperature falls below the thermal decomposition temperature but remains above its melting temperature in the molten state until impact with the substrate. The model predicts that it is practicable to plasma spray polymers.

It should be mentioned that the removal of surface layers of the in-flight particle is due to the thermal decomposition of the particle at temperatures above its decomposition temperature. In the current calculation, this was treated using the following methodology: a spheroidal particle was divided into n layers with the same thickness (Figure 4.3), when the temperature of a thin surface layer s reaches the lower limit of its decomposition range, it begins to decompose and the heat energy transferred from plasma gas is partially consumed by the bond dissociation energy (section 4.1.3.3). Theoretically, the mass loss should occur concurrently with its decomposition. However, the surface layer s was assumed not to be removed until it reached the upper limit of its thermal decomposition temperature range. This assumption is required for the application of the FDE method.

6.3. Effect of processing parameters on temperature profiles of in-flight polymer particles

The above analysis and the heat transfer analysis in section 4.1.3 indicate that the temperature profile of an in-flight particle depends greatly upon the thermal conductivity of the particle and the properties of plasma temperature field (temperature and convective heat transfer coefficient). The latter is influenced by the plasma processing parameters. The following section is aimed at predicting the influence of the plasma processing parameters on the temperature profiles of polymer in-flight particles using the theoretical model(Part I).

6.3.1 Plasma gases

To examine the influence of the plasma gas, the temperatures at the surface and centre of a 60μm polyamide particle travelling at 240ms^{-1} through different plasmas were calculated as a function of the residence time of the particle in the plasma jet. The results are shown in Figure 6.7. The plasma temperature is assumed to be constant at 10,000K in this computation owing to the lack of plasma temperature field data for pure gases as a function of plasma conditions.

Figure 6.7 shows that when the particle is immersed in argon plasma, the temperature at surface rises more slowly than it does in a nitrogen or hydrogen plasma. The particle immersed in hydrogen plasma shows the highest rate of surface temperature rise. As a result, the surface of the particle starts to volatilize after 3μs immersed in a hydrogen plasma, and 8μs in a nitrogen plasma compared with 90μs in argon plasma. The particle volatilizes completely after 10μs immersed in hydrogen plasma, 70μs in nitrogen plasma and 800μs in argon plasma.

Such a significant variation is due to the effect of different convective heat transfer coefficient of plasma gases. As shown in Figure 6.3, the hydrogen plasma has the highest thermal conductivity and highest heat conduction potential which gives the highest average heat conductivity across a boundary and therefore the highest convective heat transfer coefficient. This allows the highest heat flux to the particle surface compared with other gases under the same plasma temperature conditions (equations(6.5) and (6.7)). However, owing to the limitation of internal heat conduction resistance of polymer, this heat flux can not be conducted fast enough to the interior of the particle. As a result, the temperature at the particle surface rises much more rapidly than that in other gases and causes the particle to decompose rapidly. The thermal conductivity and heat conduction potential of nitrogen plasma are in the between hydrogen and argon, and therefore the rising rate of temperature at the particle surface in nitrogen plasma is in the between hydrogen and argon.

It should be mentioned that above calculation was carried out at a constant plasma temperature of 10,000 K and the influence of plasma gases on the particle velocity was not able to be incorporated in the calculation because of the lack of relevant data. However for the purposes of comparison, it can still help in the understanding how the thermal conductivity of the gases affects the thermal history of polymers in a thermal plasma. In particular, it predicts that argon is the best choice of primary plasma gas in order to minimize thermal decomposition of the polymers. In practice, however, many other factors such as gas enthalpy and gas velocity are important, which are related to plasma gas composition and should also be considered when selecting the optimal plasma gas composition.

6.3.2 Plasma arc power

Plasma arc power, which is the product of arc current and arc voltage, reflects the thermal energy output of plasma to the injected particles (Section 2.7). Figure 6.8a and Figure 6.8b show the influence of plasma arc powers on the calculated temperatures at the centre (Tc) and the half-radius ($T_{1/2}$) of a 60μm diameter polyamide particle travelling at 240ms^{1} in the argon-hydrogen plasma respectively. The horizontal line, Tm, shown in Figure 6.8 and in subsequent Figures) represents the lower limit of the melting range of polyamide 11 material and line Td the lower limit of the decomposition range of polyamide 11 material. The value of Tm was 437 K as determined by DSC, while the value of Td at 630 K was determined by TGA. Thermal decomposition during TGA was taken to begin when the polyamide reached Td and significant weight losses were recorded. The values of arc power listed in Figures 6.8a and 6.8b were determined experimentally: at a given 400A arc current, a series of arc voltage readings were taken by adjusting the ratio of the argon to hydrogen, and the values of arc power were thus obtained. The ratios of argon to hydrogen were taken into account when calculating the convective heat transfer coefficient of the plasma to the particles.

The data in Figure 6.8 show that the arc power has an important effect on the particle temperatures: at low arc power levels, such as 15kW, for example, at the stand-off distance of 130 mm (practical spraying distance), a 60μm polyamide particle is not melted at the centre nor at the half radius. With an increase of the arc power, the average temperature of the particle increases significantly. For example, when the arc power exceeds 22kW, the temperatures at the half radius of the particle rises to above the lower limit of its melting temperature range. Increasing the arc power to 33kW, the temperature at half-radius reaches to its decomposition range at a stand-off distance of only 45mm which is too short for practical operation.

Figure 6.9 shows the influence of plasma arc power on the melting rate of a 60 μm polyamide particle travelling at 240 ms^{-1}. ΔRm in Figure 6.9 represents the thickness of the melting layer, which is the function of the residence time of the particle within the plasma flame and ΔRm increases with residence time. Figure 6.9 indicates that the particle melts much faster under high arc power. However, it is also noted that at a stand-off distance of 130 mm, even under 30kW arc power, a solid core of 6 μm diameter still remains within the particle due to the high internal heat transfer resistance of polyamide. The degree of melting of the particle, as quantified by the volume fraction of melted layer over the initial particle volume, was calculated at varying arc power levels and the results are given in Figure 6.10. The results show that at a stand-off distance of 130 mm and an arc power of 15kW, 70% volume fraction of the particle melts. At 22kW, 82% melts and at 30 kW, 98% melts. The theoretical model is thus able to show the extent to which the precursor particle melts increases with the increase of the plasma arc power level.

Figure 6.11 shows the effect of plasma arc power on the radius changes of a 60μm polyamide particle travelling at 240 ms^{-1}, due to the mass loss caused by surface decomposition. It indicates that the calculated particle radius decreases substantially at high arc power levels. For example, the particle radius reduces from 30μm to 14μm by the time a 130mm spraying distance has been reached under 33kW arc power, but only to 28μm under 22kW. Corresponding effects on the extent of volume loss of particles is shown in Figure 6.12 which indicates that at a stand-off distance of 130mm the volume loss of the particle is 90% under 33kW and 16% under 22kW arc power. The degree of volume loss of particle due to thermal decomposition increases with the increase of plasma arc power levels.

The above calculations indicate that at low plasma arc power levels, the particle cannot melt effectively. Increasing power levels improves the melting of in-flight particle but at the expenses of thermal decomposition. A balance is required for practical operation which gives the particle maximum melting and minium decomposition. This is the optimal arc power level. The determination of the optimal arc power level is difficult since it depends upon many factors. One such factor is the particle velocity in the plasma jet which is considered in the following section.

6.3.3 Particle velocity

The influence of arc power levels on the melting and decomposition of particles shown in Figures 6.8 to 6.12, which were calculated on the basis of a fixed in-flight particle velocity of 240ms^{-1}. The situation changes with the in-flight particle velocity as shown by Figure 6.13 to 6.18. These figures give the calculated temperatures at the half-radius of a 60μm diameter polyamide particle travelling at different in-flight particle velocities through an argon-hydrogen plasma under different arc power levels. It can been seen that at a stand-off distance of 130mm: at 15kW arc power level, the $T_{1/2}$ of the particle reaches the melting range only when the particle velocity is equal or less than 200ms^{-1} (Figure 6.13); at 22kW, the in-flight velocity of 120 ms^{-1} is too slow and therefore causes the temperature of the particle ($T_{1/2}$) rising to its decomposition temperature (Figure 6.14); at 26kW, the optimal in-flight velocity ought to be in the range of 160-240ms^{1} for a stand-off distance of 130mm (Figure 6.15); at 28kW, the velocities of less than 160ms^{-1} should be avoided and the optimal velocity is in the range of 200-300 ms^{-1} (Figure 6.16); at 30kW, 200ms^{-1} should not be selected and 240-300ms^{-1} is the optimal velocity range (Figure 6.17) and at 33kW, even 300ms^{-1} is too slow(Figure 6.18).

The above calculations indicate that the plasma arc power and the in-flight particle velocity are inter-related: higher arc power level requires correspondingly higher particle velocity to avoid overheating and lower arc power level needs lower particle velocity to ensure melting properly. This inter-relation of the plasma arc power to particle velocity and its influence on the average temperatures($T_{1/2}$) of a 60μm polyamide (at 140 mm spraying distance) is summarised in Figure 6.19. The suitable combinations of plasma arc power and particle velocity are those that lie in the region between Tm and Td.

The velocity of an in-flight particle travelling through plasma jet determines its residence time in the plasma flame and hence affects the thermal history of the particle in the plasma jet. Figure 6.19 also indicates clearly that the average temperature of in-flight particle increases with decreasing velocity under any arc power level. This implies that the degree of melting and decomposition of polyamide particles are sensitive to the particle velocity. A high particle velocity avoids overheating of the particle but reduces the degree of melting of owing to its reduced residence time in the plasma.

Although Figure 6.19 shows that the combinations of low arc power and low particle velocity are good theoretical choices for heating a 60μm polyamide 11 particle. In practice, however, not just a single polymer particle but a stream of particles are to be heated up in plasma jet, which requires the plasma to supply adequate heat output which is proportional to the plasma arc power. This suggests that a higher plasma arc power may be necessary to supply the stream of particles with sufficient heat energy and this in turn may result in a higher particle velocity required.

It is important that the selection of plasma arc power and correspondingly particle velocity should be matched with a suitable particle size to ensure adequate melting in order that the advantages of high velocity on coating properties, such as adhesion and density, can be realized.

6.4 Effect of particle size on the temperature profile of in-flight polymer particles

Large temperature gradients have been predicted to develop in in-flight polymer particles due to their high internal heat conductance resistance (section 6.2) and as a result the degree of melting of the particle is reduced (Figure 6.5). However, if the material of the particle possesses a high decomposition temperature, then its conductive heat transfer rate can be improved by raising its surface temperature (Fourier's Law[53]). Metals and ceramics have high decomposition (or vaporization) temperatures and this enables their melting to be promoted by increasing the input energy of the plasma by, for example, raising the plasma arc power. The low decomposition temperature of polymers, however, presents difficulties. The control of particle size of polymer precursor powder is likely to play an important role in overcoming this difficulty.

Figure 6.20 shows the calculated temperature at the half-radius (Figure 20a) and centre (Figure 20b) of polyamide particles with various diameters as a function of spraying distance. The particles were immersed in an argon-hydrogen plasma of 22 kW arc power with in-flight velocities of 240ms^{-1}. The calculated results show that the particle size has an important effect on the particle temperature: large particles, for example, 80μm and 100μm particle were not melted at their half-radius even at a distance of 200mm from the nozzle exit, while the 20μm particle reaches its upper decomposition temperature(Td) at only 30mm, which is, in fact, impracticable short for spraying. The smaller particles have shorter path for heat conduction from the surface to the centre, and therefore require a shorter time and less energy to heat up. As a result, the temperature rises much faster than in large particles.

Figure 6.21 gives the influence of the particle size on the progress of melting in the polyamide particles. As shown in the top right hand of this figure, the Rm in vertical axis represents the position of the liquid-solid interface within the particles, which moves towards the centre of the particle with increasing residence time of the particle in the flame. Figure 6.21 indicates that the melting rate of the particle increases rapidly with decreasing particle size. Figure 6.22 shows the influence of particle size on the degree of melting of polyamide powder under the same plasma conditions and indicates that the calculated degree of melting decreases substantially with increasing particle size: for example, a 20μm particle is fully melted at a distance of 20mm, while a 40μm particle is not completely melted until a distance of 90mm is reached . A 100μm particle is only 55% melted at 130mm.

Figure 6.23 shows the effect of particle size on the particle radius variation of polyamide powders travelling at 240 ms^{-1} through an argon-hydrogen plasma of 22 kW. It indicates that the calculated particle radius reduces substantially with decreasing feedstock particle size under the same plasma conditions. For example, a 40 μm particle reduces to 32 μm by the time a 130 mm spraying distance has been reached but a 100 μm particle is only reduced to 99 μm in the same time. Figure 6.24 gives the effect of feedstock particle size on the extent of volume loss of particles due to surface decomposition and indicates that the calculated extent of particle loss increases significantly with the decrease of the particle size. For example, 20μm particle completely volatilized at the distance of 63mm, while at the distance of 160mm the extent of volatilization is 44% for a 40μm particle, 19% for a 60μm particle and 3% for 100μm particle.

The above theoretical calculations indicate conflicting effects of particle size: reducing the size improves melting but also leads to high volume loss rate. A 20μm particle totally disappears in the flame whereas a 100μm particle cannot be sufficiently melted under the plasma conditions considered. There is, therefore, an optimal particle size which under the current conditions is 40 to 60μm for polyamide. The optimum will, of course, be a function of the plasma spraying parameters such as the arc power level.

6.5 Summary

The theoretical analysis and calculations in this chapter have indicated that the heat transfer feature of polymer particles in a thermal plasma differs markedly from that of metals and ceramics primarily because of the high internal heat conduction resistance and low thermal decomposition temperature of polymers. The high internal thermal resistance creates large temperature gradients within the particle, results in its surface temperature rising significantly more rapidly than that of a metal or ceramic, and consequently, lowers the degree of particle melting. A low decomposition temperature promotes the thermal degradation of polymers. The key to the thermal spray deposition of polymers is thus to achieve a balance between maximizing melting and minimizing degradation. This balance can be reached by control of the feedstock particle size and the process parameters.

The plasma gases affect the thermal history of polymer particle greatly, owing to the influence of the thermal conductivity of the plasma gases on the convective heat transfer rate of the plasma to the particle. The argon is the best choice of primary plasma gas for the spraying of polymers in order to minimize thermal decomposition of polymers.

Plasma arc power is an important parameter affecting the temperature, degree of melting and the extent of decomposition of in-flight polymer particles. At low plasma arc power levels, the particle cannot be melted effectively. Increasing power levels rise the temperature and improves the melting of in-flight particle but at the expenses of thermal decomposition. The optimal arc power level is to give the particle maximum melting and minium decomposition.

The plasma arc power and the in-flight particle velocity are inter-related: higher arc power level requires correspondingly higher particle velocity to avoid overheating and the lower arc power level needs lower particle velocity to ensure melting properly. The particle temperature increases with decreasing velocity under any arc power level. For a given arc power level, the high particle velocity avoids overheating of the particle but reduces the degree of melting owing to the reduced residence time in the plasma. The best combination of plasma arc power and particle velocity is to ensure the particle temperature lies in the region between Tm and Td.

The theoretical calculations also indicate conflicting effects of feedstock particle size: reducing the size improves melting but also leads to high volume loss rate. There is, therefore, an optimal particle size for certain spaying conditions. For example, under the operating condition of 22 kW arc power and argon plus 5% hydrogen plasma, the optimal particle size is 40 to 60 μm for polyamide.

Table 6.1 Physical and thermodynamic data for the materials under study

Material	Density /Mgm^{-3}	Melting temperature /K	Decomposition temperature /K	Specific heat /Jkg^{-1}K^{-1}	Thermal conductivity /Wm^{-1}K	Enthalpy of Fusion /MJ kg^{-1}	Enthalpy of decomposition /MJ kg^{-1}
polyamide	$1.04^{\text{manufacturer}}$	$437\text{-}470^{\text{DSC}}$	$630\text{-}830^{\text{TGA}}$	2328^{DSC}	0.29[85]	0.076^{DSC}	0.277[84]
PMMA	$1.118^{\text{manufacturer}}$	$>400^{\text{DSC}}$	$480\text{-}650^{\text{TGA}}$	1380^{DSC}	0.19[84]		
alumina	3.90	2300-2500	4000	1242	6.3[119]	1.0	24.7
tungsten	19.35	3600-3700	6200	170	110[120]	0.19	4.62

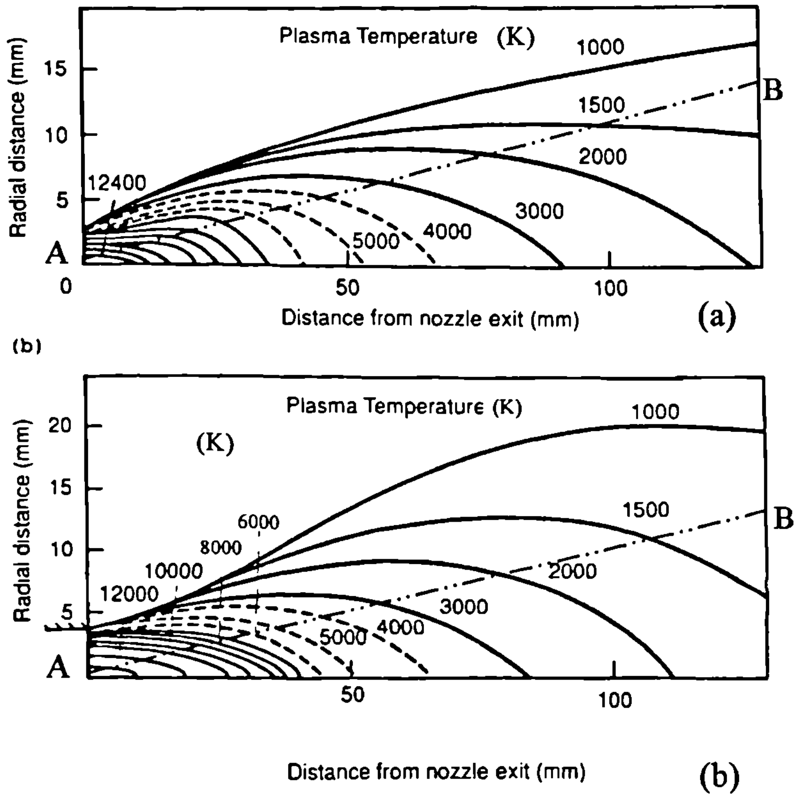

Figure 6.1 Temperature distribution of (a) a nitrogen-hydrogen plasma, (b) an argon-hydrogen plasma.

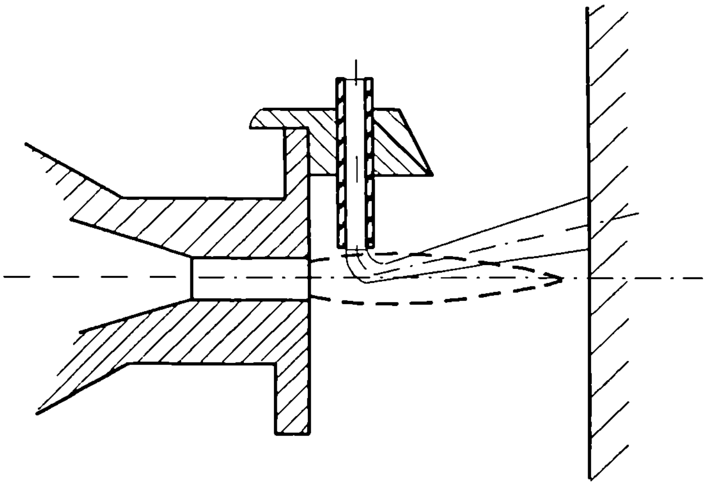

Figure 6.2 Inclination of beam of molten particle in plasma beam.

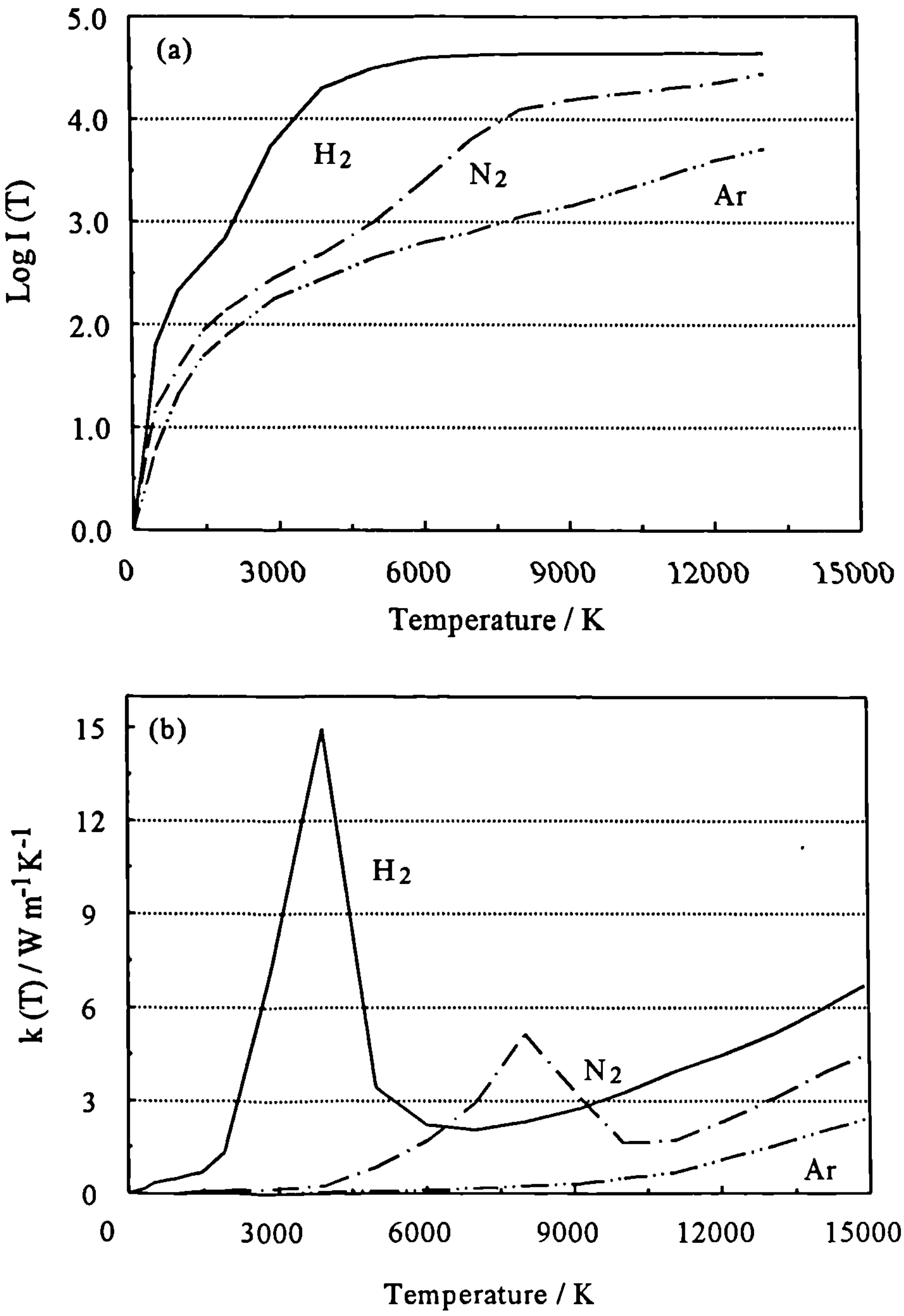

Figure 6.3 The integrated thermal conductivity (a) and thermal conductivity (b) for different gases as a function of temperature.

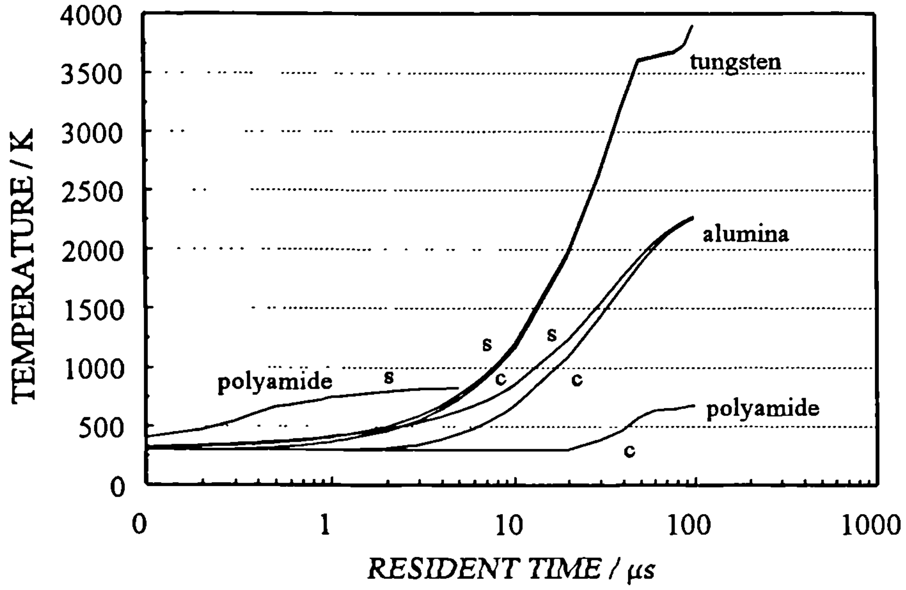

Figure 6.4 Calculated temperature rise of tungsten, alumina and polyamide particles in a thermal plasma. S and c refer to the surface and centre of each particle.

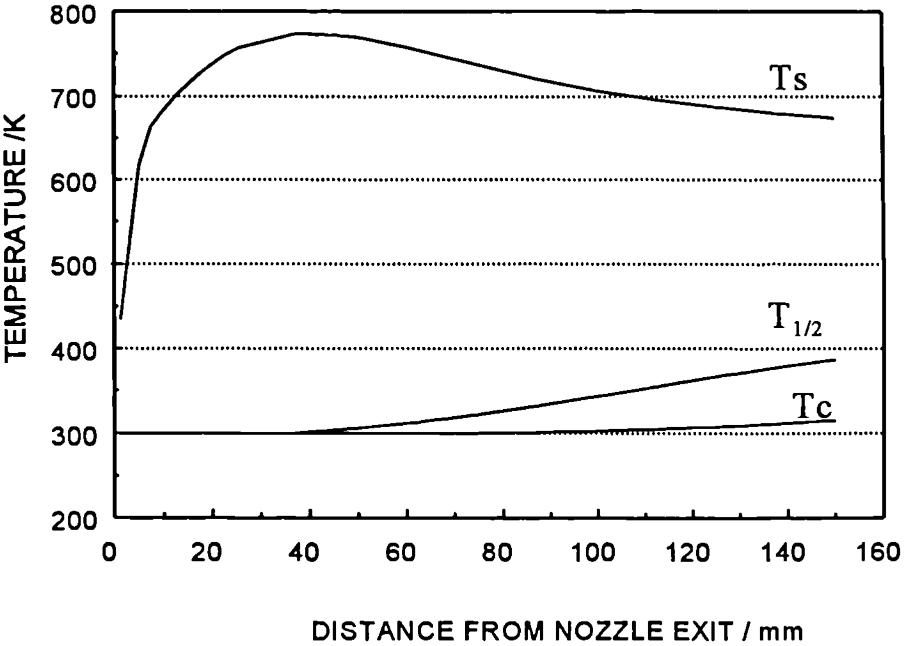

Figure 6.5 Calculated temperatures at the particle surface(Ts), half-radius ($T_{1/2}$) and centre (Tc) for a 80 μm polyamide 11 particle.

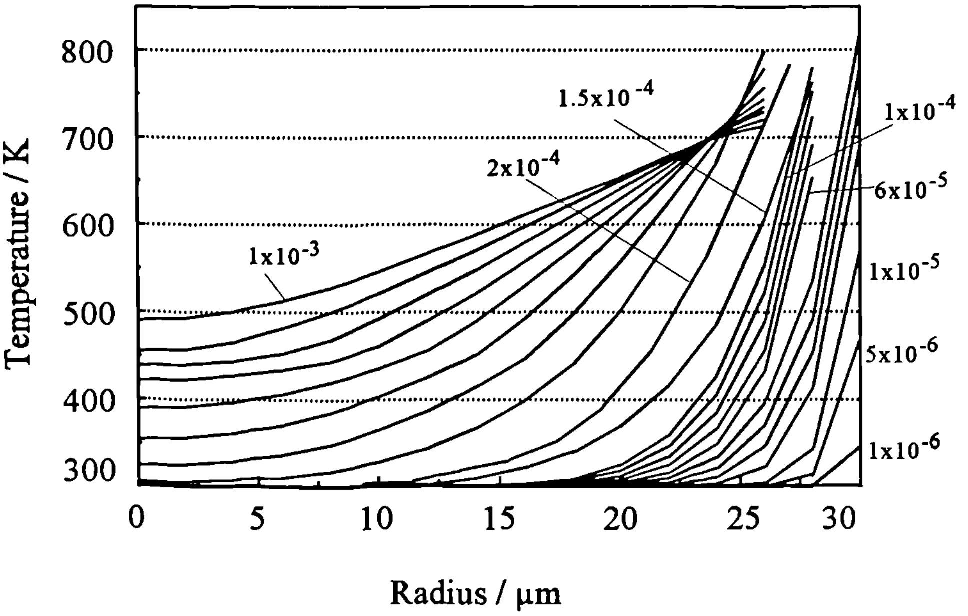

Figure 6.6 Temperature distribution within a polyamide particle flying at 240 m/s in an argon-hydrogen plasma.

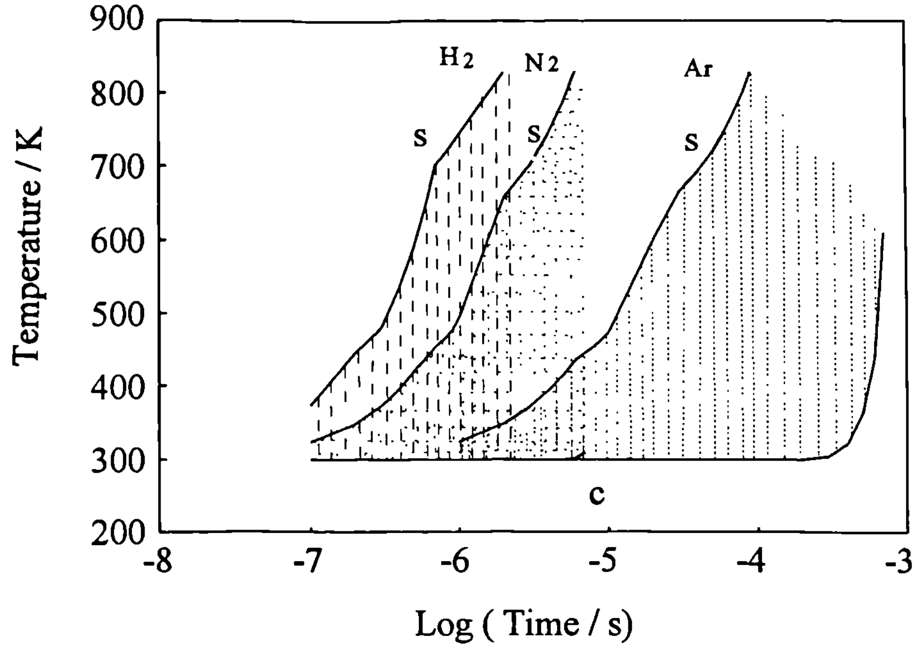

Figure 6.7 Temperature histories at surface (s) and centre (c) of a 60 μm diameter polyamide particle immersed in different plasma gases.

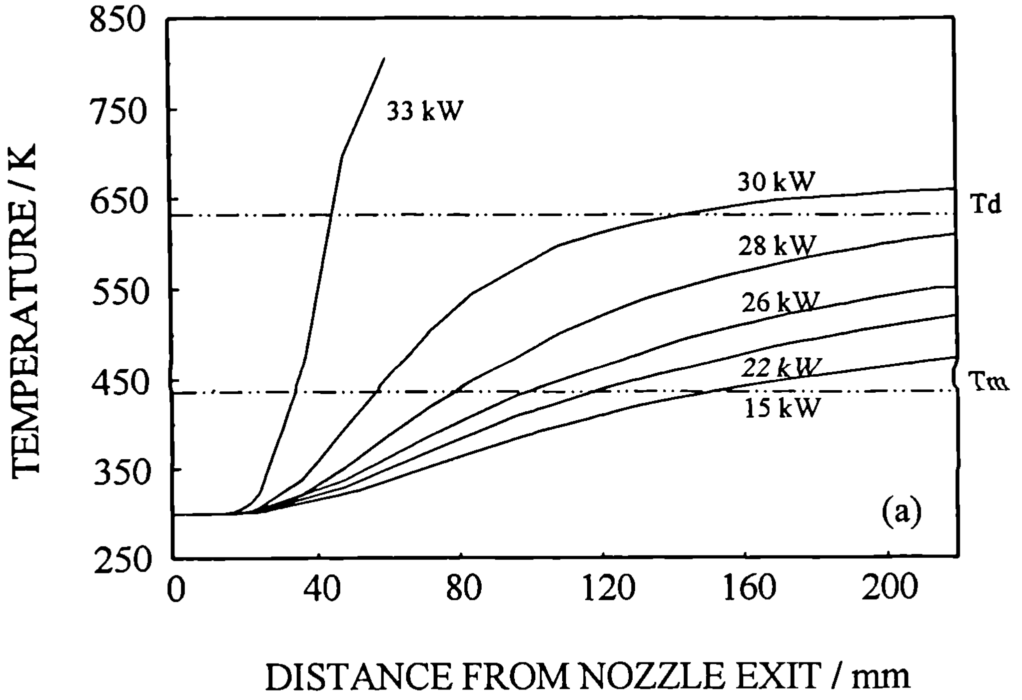

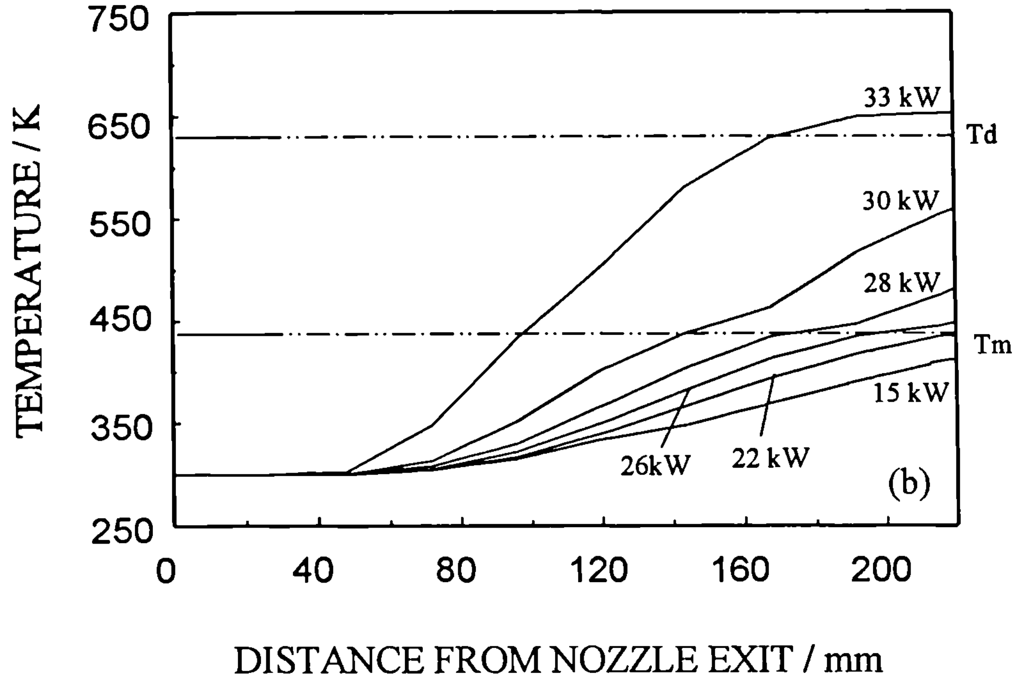

Figure 6.8 The effect of plasma arc power on calculated particle temperature as a function of spray distance (a) at half-radius, (b) at centre.

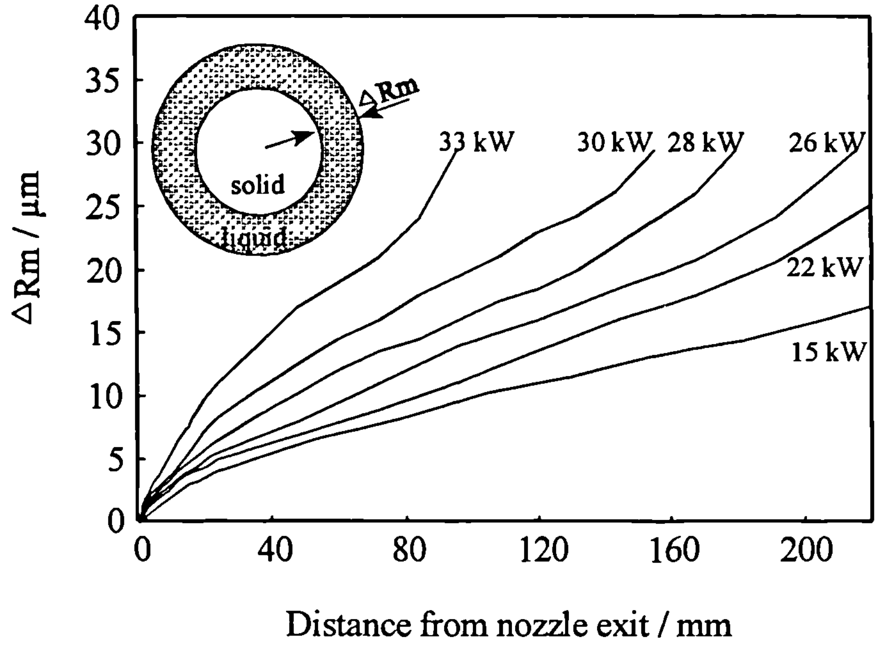

Figure 6.9 The effect of arc power on the calculated position of the liquid-solid interface in a 60μm polyamide particle.

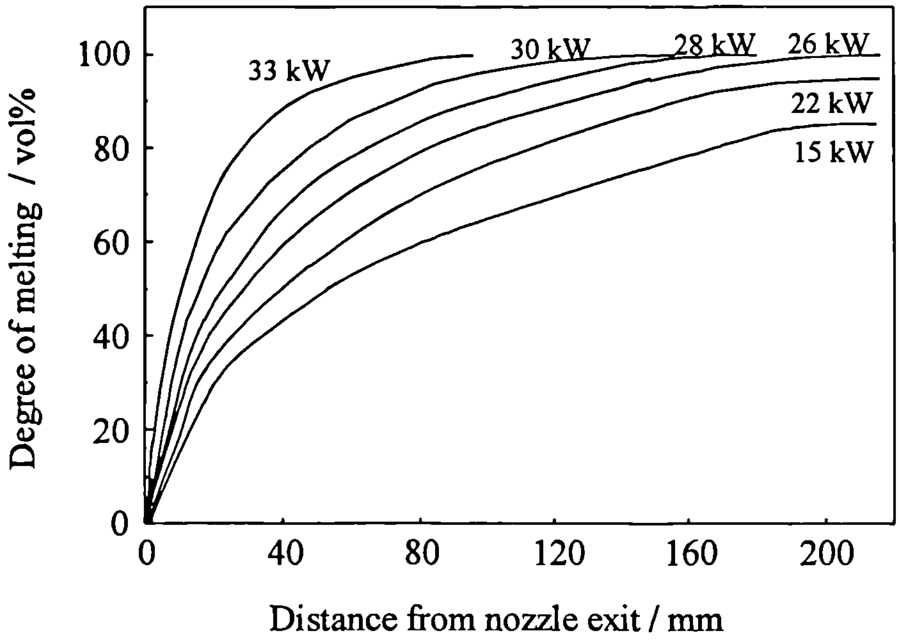

Figure 6. 10 The effect of arc power on the degree of melting of the in-flight polyamide particle

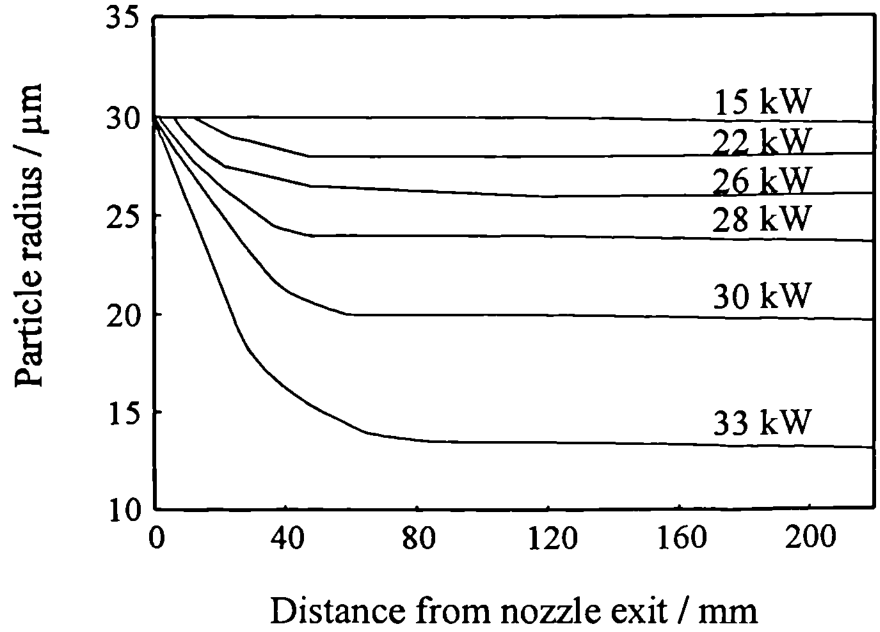

Figure 6.11 The effect of plasma arc power on the particle radius during flight in the plasma jet.

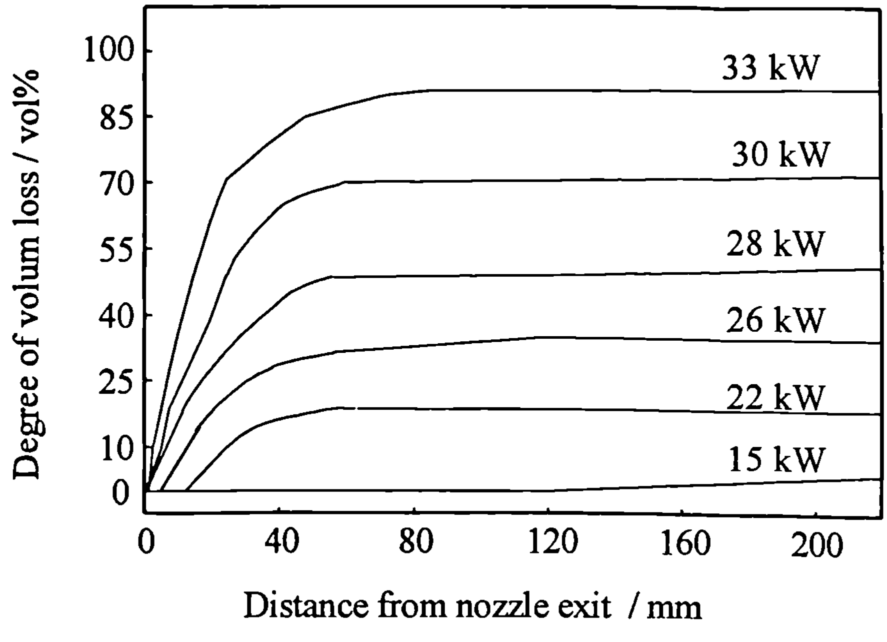

Figure 6.12 The effect of arc power on the volume loss of a polyamide in-flight particle

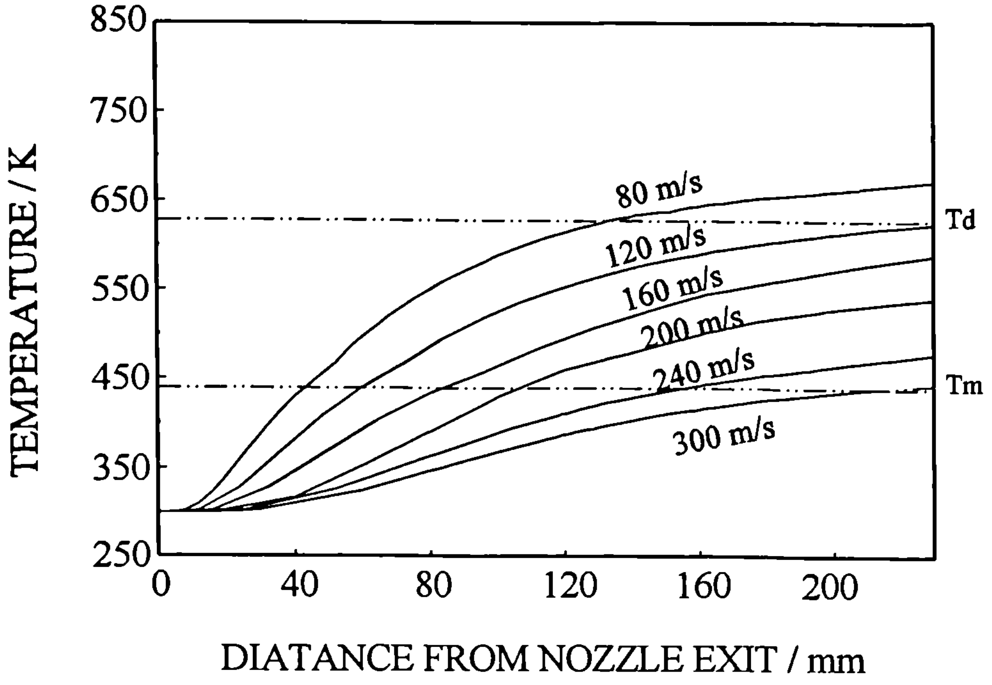

Figure 6.13 The effect of particle velocity on the temperature at half-radius of polyamide particle . Plasma arc power is 15kW

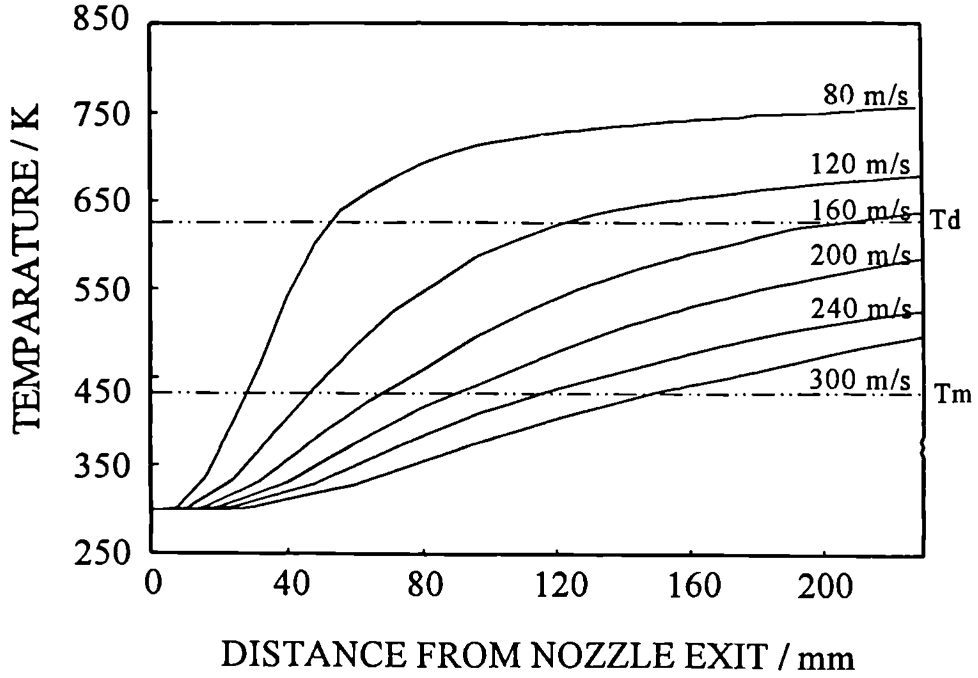

Figure 6.14 The effect of particle velocity on the temperature at half-radius of polyamide particle . Plasma arc power is 21 kW

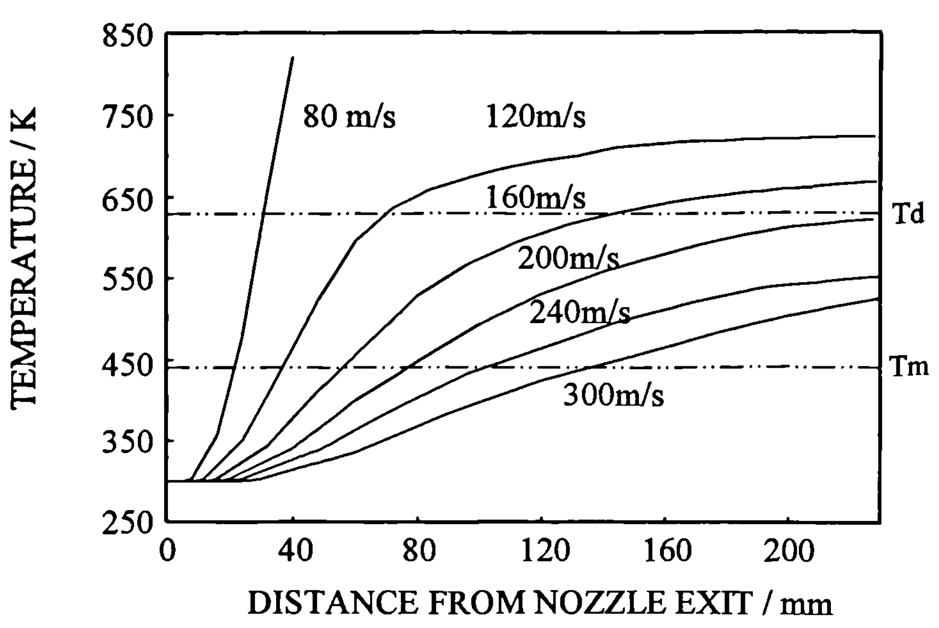

Figure 6.15 The effect of particle velocity on the temeprature at half-radius of a polyamide particle. Plasma arc power is 26 kW.

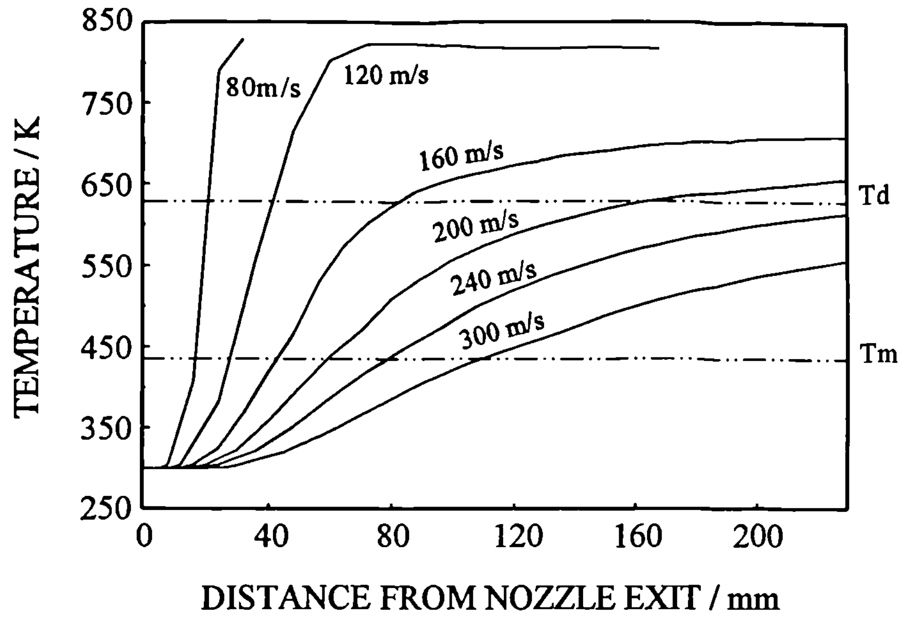

Figure 6.16 The effect of particle velocity on the temperature at half-radius of a polyamide particle. Plasma arc power is 28 kW.

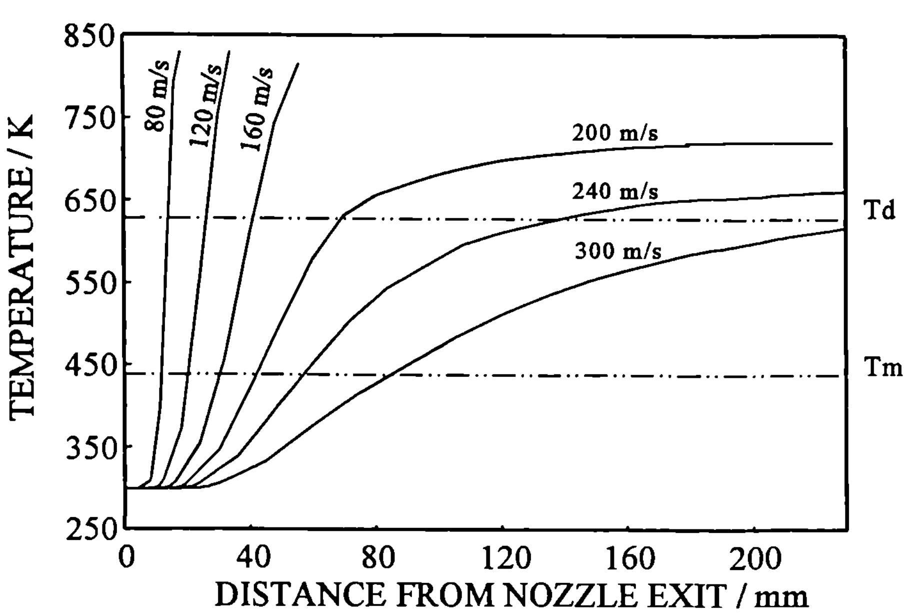

Figure 6.17 The effect of particle velocity on the temperature at half-radius of a polyamide particle. Plasma arc power is 30 kW.

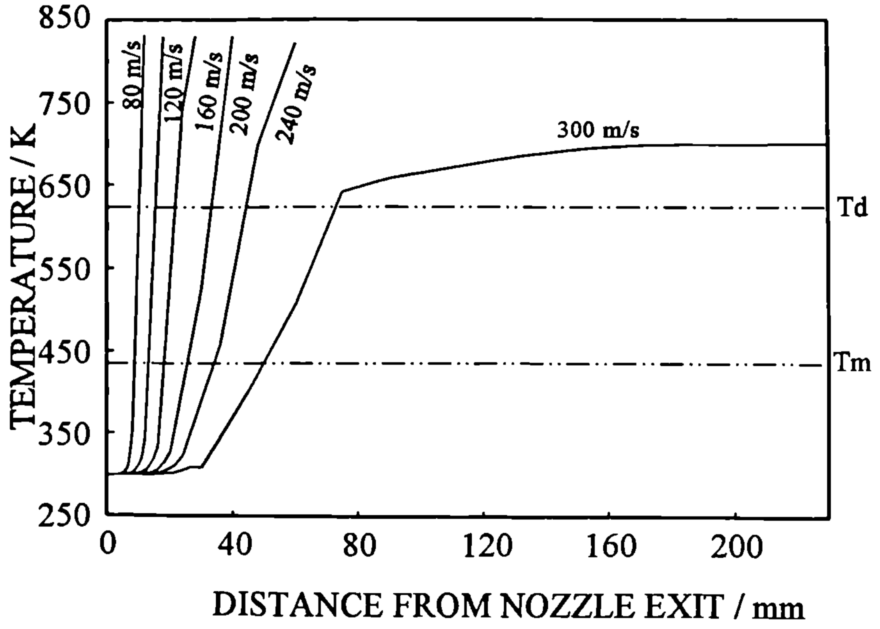

Figure 6.18 The effect of particle velocity on the temperature at half-radius of a polyamide particle. Plasma arc power is 33 kW.

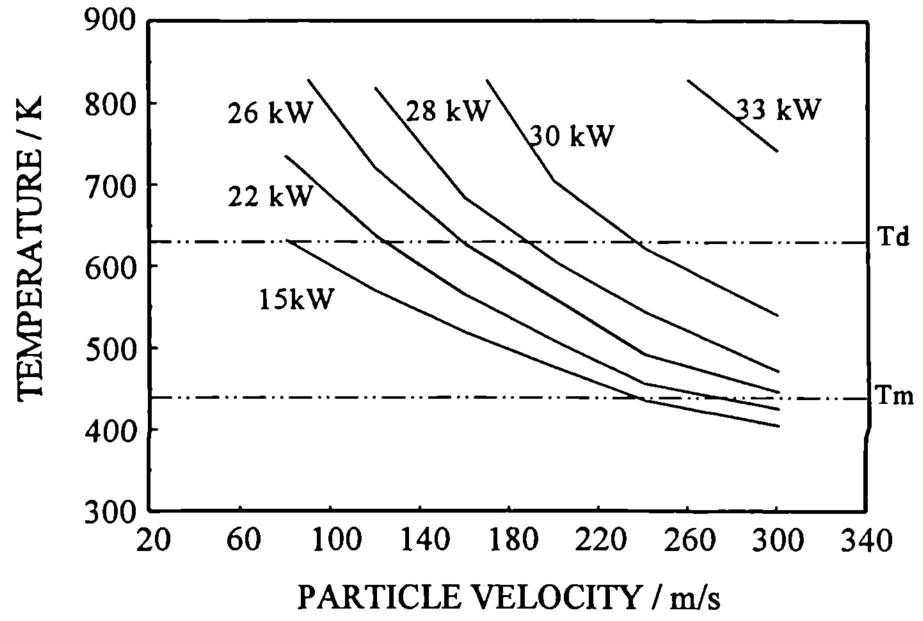

Figure 6.19 The relationship of plasma arc power to the particle velocity

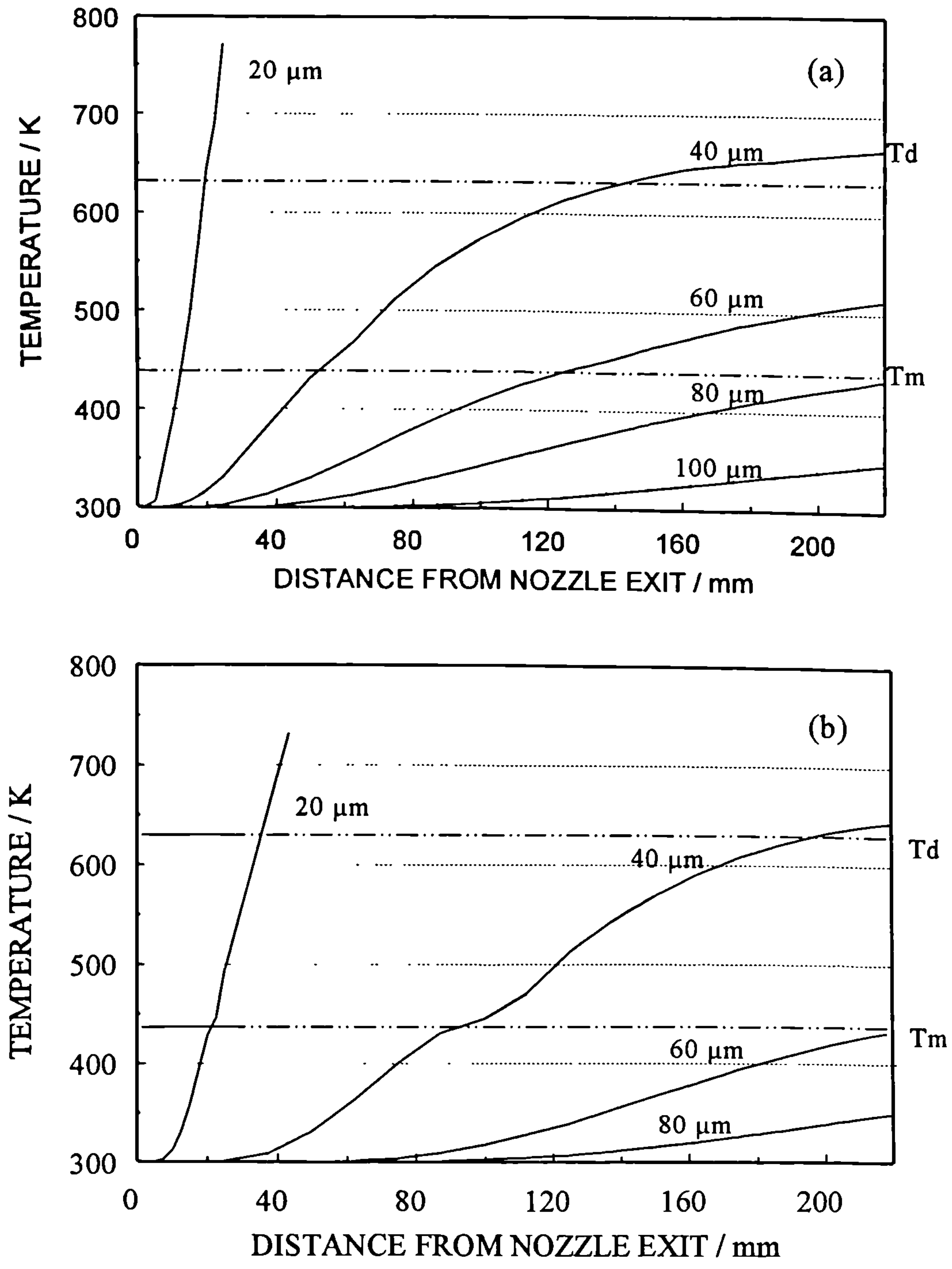

Figure 6.20 The effect of particle size on calculated particle temperature: (a) at half-radius; (b) at center as a function of spraying distance.

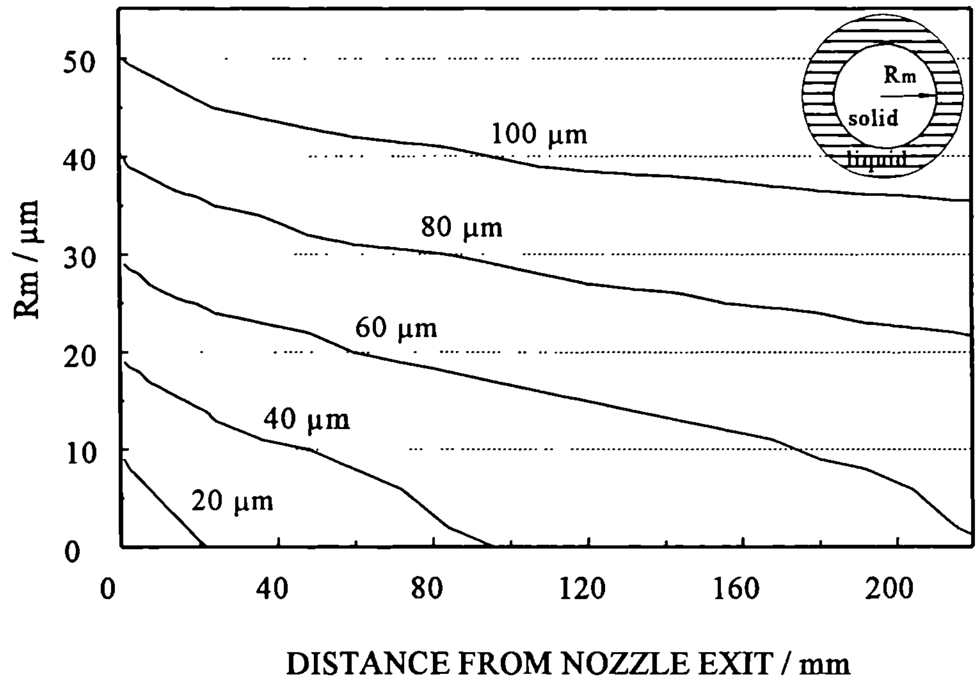

Figure 6.21 The effect of particle size on the calculated position of the liquid-solid interface in the polyamide particles

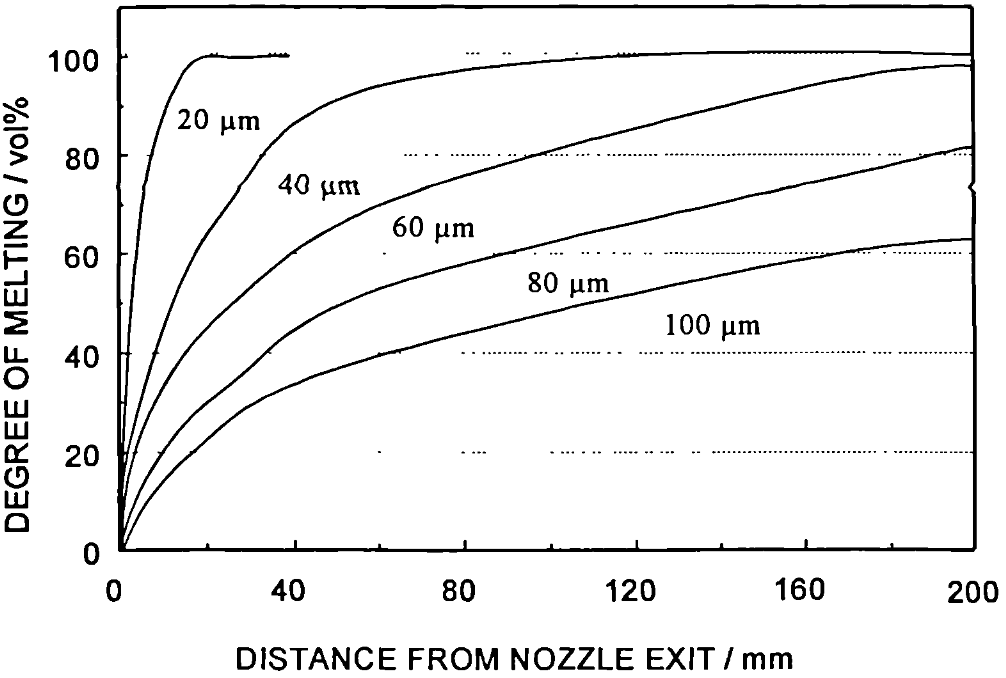

Figure 6.22 The effect of particle size on the calculated degree of melting of polyamide powders

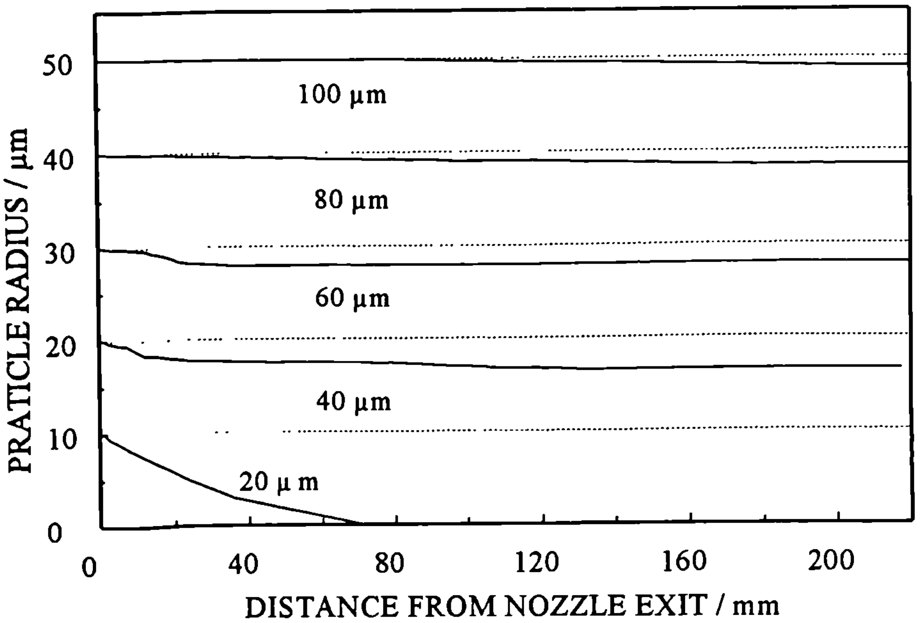

Figure 6.23 The effect of particle size on the calculated particle radius of polyamide powders.

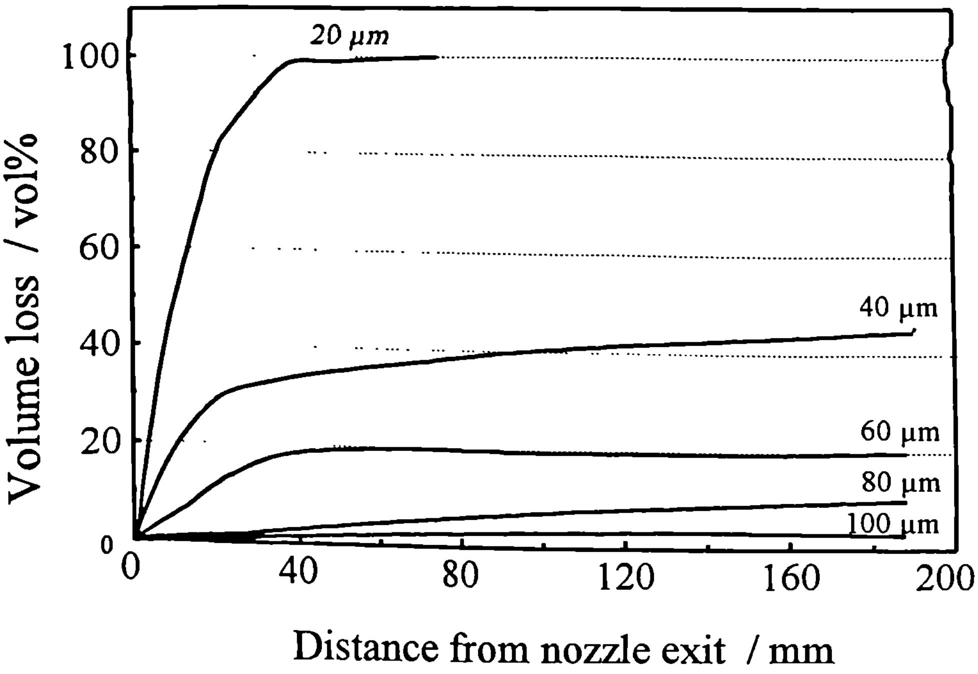

Figure 6.24 Effect of particle size on the calculated volume loss of polyamide 11 powders

CHAPTER7. EXPERIMENTAL RESULTS AND DISCUSSION - THERMOPLASTICS

This chapter gives the experimental results of the plasma spraying of thermoplastics and discusses the formation and structure of the thermoplastic coatings, optimal operation conditions, the behaviour of polymer during plasma deposition, the properties of polymer coatings and the main factors affecting the coating quality and properties.

7.1 **Formation and structure of polymer coatings**

7.1.1 Wipe test

An insight into the formation of the plasma deposits may be gained from the wipe test, which consists of traversing the plasma torch across the polished steel surface sufficiently rapidly so that the individual particles or splats do not overlap one another on impact with the substrate surface and isolated splats can be observed. Figure 7.1 gives the morphologies of polyamide particles produced in wipe test at 21 kW plasma arc power. It shows that the isolated splats of polyamide produced by this technique are generally circular and thicker at the centre; the splats produced by the finer precursor powder (53-75 μm, Figure 7.1a) appear to have melted extensively on impact, whereas those from the coarser powder (90-150 μm, Figure 7.1b) are only partially molten. Figure 7.2 gives a group of splats produced by PMMA particles in wipe test which shows the influence of particle size on the extent of the flow of the splats (DA100 grade): particle diameters of 120μm (Figure 7.2a) exhibit negligible flow whereas those of 20μm (Figure 7.2d) show extensive flow. In addition, the splats from the large particles contain bubbles which is attributed to the poor conductivity of PMMA.

The extent of the flow of the polymer particles depends on factors including the melt viscosity of the particle, particle velocity, wettability between the splat and substrate and substrate conditions (temperature and surface roughness). However the variation shown in Figure 7.1 and 7.2 may only be due to the difference in melt viscosity and particle velocity since other factors were the same. For a given polymer material, the melt viscosity of the particle depends heavily on the temperature and the degree of melting of the particle. As predicted in Figure 6.20 to 6.23, the average temperatures and the degree of melting of the polymer particles increase with reducing feedstock particle size. As a result, the melt viscosity of the particle decreases and therefore the extent of the flow increases with the decrease of the particle size. The experimental observation thus verified the theoretical predictions given in Figure 6.20-6.23.

Figure 7.3 shows the effect of plasma arc power on the flow of incident particles of as-received polyamide 11 powder in wipe test. It can be observed that under 18kW arc power level(Figure 7.3a), The large particles have almost the same shape as that of the feedstock powder (Figure 5.2) but the sharp edge of the original particles has shown to be rounded off implying that only partial melting of the large particles occurred. Some smaller particles can be seen to have flattened which implies effective melting. Some of the large particles were observed to have bounced off from substrate during spraying due to the poor melting. The extent of flow of particles significantly improved under 23kW arc power levels shown in Figure 7.3b. Figure 7.4 gives the effect of arc power levels on the morphology of PMMA particle produced in the wipe test. It can be seen that under 14 kW arc power (Figure 7.4a), majority of particle have the same size as that of the feedstock powder suggesting only superficial melting of the particle occurred. The degree of flow of particles increase with the increase of plasma arc power levels as shown in Figure 7.4b, which gives morphology of the PMMA particle produced in wipe test using 27 kW plasma arc power.

The variation of the extent of the flow of the polymer particles with plasma arc powers may be explained by the influence of the plasma arc powers on the particle temperature and the degree of melting: low arc power supplies particle insufficient thermal energy so that particle possesses low temperatures and the degree of melting (Figure 6.8 to 6.10). As a result, the particle has high melting viscosity and thus exhibits the low degree of flow. The increase of arc power levels increased the temperature and the degree of melting of particle and thus the extent of flow. This experimental observation is consistent with the theoretical prediction given in Figure 6.8 to 6.10.

7.1.2 Deposition mechanism

Examination of polished through-thickness sections of the plasma-sprayed coatings revealed that the polyamide deposits were composed of elongated regions with the major axis parallel to the coating-substrate interface, as shown in Figure 7.5. Whereas examining the top surface parallel to the interface indicated that those regions possessed an equiaxed or disc-like shapes(Figure 7.6). The polyamide deposit is therefore composed of overlapping flatten particles or disc-like splats.

The above observations suggest the following mechanism of polymer coating formation. Precursor powder injected into the plasma jet is accelerated and heated to form a liquid droplet during flight. On impact with the substrate, the droplet spreads out over the surface and rapidly solidifies to form a disc shaped splat. Under the optimal spraying conditions, many such impacts occur on a given area and the deposit is built up from a series of overlapping splats.

A significant variation in aspect ratio of splats was observed in Figure 7.5 and although this is partly due to the geometrical effect of sectioning discs through their thickness, it is also considered to be a consequence of the feedstock particle size distribution and the differing degrees of flow of the molten particles impinging the substrate. The extent of particle flow on impact is an important factor in the coating formation, since suitable flow allows the splat to run into the contours of the underlying surface to minimise voids and knit into neighbouring splats to enhance intersplat bonding. However, excessive flow can lead to breakup of the splat at its periphery resulting in creation of new surfaces and voidage. Since the wettability between the splat and the underlying material which will generally be good because it is the same material and substrate conditions were the same, the variation in droplet flow is likely to be due to differing temperatures and velocity attained by the particles in the plasma jet. This can arise from a number of reasons including a non-ideal particle trajectories in the plasma jet, which may result in different temperatures and degree of melting of the particles, or the wide particle size distribution of feedstock powder of which large particles cannot obtain sufficient time for heat conduction to their centre. In extreme cases, this can lead to incomplete melting of particles or even unmelted particles included in the coating which constitute defects within the coating.

7.1.3 Defects within polymer coatings

Figure 7.7 shows a polished through-thickness section of the plasma-sprayed coating: the feature towards the left-hand side of the Figure 7.7 is an inadequately melted particle exhibiting poor flow and consequent voids around its periphery. The void in the centre of Figure 7.7 is attributed to an unmelted particle, which was subsequently pulled out during polishing for microstructural examination.

Incomplete melting resulting in insufficiently low viscosity and particle flow on impact with the substrate has two deleterious effects on coating structure: void formation due to lack of conformity with neighbouring splats and weak inter-splat bonding as evidenced by particle pull-out on light polishing.

Figure 7.8 shows long elongated voids between neighbouring splats suggesting gas entrapment between the coating particle during spraying. The high aspect ratio and sharp curvature of these voids, together with their alignment along the splat boundaries would indicate a particularly adverse effect on mechanical properties under tensile stress systems.

Figure 7.9 shows a coating deposited with a arc power of 18 kW exhibiting a number of features. The particles labelled P on Figure 7.9 only partially melted during deposition(as evidenced by their roughly equiaxed shape and similar size to the feed particles) while that labelled M denotes a fully melted particle which flowed on impact with the substrate to form a disc-like splat; the boundary of a splat is indicated with an arrow. The feature labelled I is an elongated void formed by entrapping gas in the interstices between the splats, which may be promoted by inadequate flow as the molten particles strick the substrate. The feature marked D is a spherical void. The formation of the spherical D type voids are likely to have occurred in an environment of lower viscosity and higher particle temperatures associated with the higher arc power levels. The formation mechanism of this type of void will be discussed in later chapters.

The fine pores which were observed pre-existing in the feedstock powder particles (Figure 7.10) are also likely to develop into spherical voids during plasma deposition: the gas entrapped in the pores will heat up and expand. The increment of the gas volume is proportional to the increment of the temperature, for example , if the temperature of the gas within the pores rises from 300 K to 800 K the gas volume would increase by 2.7 time according to the ideal gas equation [121]. Other possibilities including additives, moisture and impurity can bring the pores within the coatings during their evaporation caused by high temperature plasma.

7.2 **Operating conditions**

The heat transfer analysis has shown that the optimum operating conditions for plasma spraying of polymer coatings may differ from those for metals and ceramics, primarily because of the much lower decomposition temperatures, thermal conductivities and densities of polymers. The current work shows that although the optimum operating range is large enough for the practical deposition of polymers, conformity to certain processing parameters is essential.

7.2.1 Plasma torch traverse speed

The plasma torch traverse speed refers to the speed of plasma torch scanning over the target. It has been found that the plasma traverse speed has a major effect on the plasma spraying of polymers. For example, the quality of polyamide 11 coatings, as measured by its wear rate, was found to deteriorate rapidly for traverse speeds below 100ms^{-1} as shown in Figure 7.11a. A similar find for PMMA coatings is shown in

Figure 7.11b, which gives the influence of torch traverse speed on the wear of PMMA coatings(DP300 grade).

The slow traverse speeds produced deposits with a relatively dark appearance, which suggest that significant degradation of the polymer had taken place. The degradation is most likely to be caused by overheating of the substrate or previously deposited coatings since the slow traverse impart much more thermal energy on a given area per pass of the torch. A further verifying experiments was carried out: a PMMA coating was prepared, traverse with one pass by the plasma jet without the injection of the powder and the weight loss of the coating caused by reheating was measured; the procedure was repeated for a range of plasma torch speeds. The results in Figure 7.12 show that the resulting weight loss of the coatings decreases markedly with increasing torch speed suggesting that substantial thermal decomposition take place at low traverse speeds.

It was found that both polyamide 11 and PMMA cannot be deposited at the traverse speed below 30ms^{-1}. The critical traverse speed above which no substantial degradation of the deposit takes place is a crucial parameter for plasma spraying of polymers. The critical speed was 100mms^{-1} for polyamide 11 and PMMA under the current conditions but the value in general will depend upon the spray parameter used. Such as the torch-to-substrate distance and substrate cooling conditions. All subsequent spraying in this work was performed with a torch traverse speed of 150mms^{1}.

7.2.2 Plasma arc power

Figure 7.13 gives the effect of the plasma arc power on the wear rate of polyamide 11 coatings: Figure 7.13a shows the wear rate on ball-on-flat test and Figure 7.13b the reciprocating diamond scratch test. Both figures show that an optimum arc power level for wear resistance of polyamide 11 exist: the coatings exhibits high wear rates at both low and high power levels with a minimum at 21kW.

Examination of the microstructure revealed major differences in microstructure of the coatings produced with different plasma arc powers. Figure 7.14 shows a deposit produced under low(10kW) arc power: the constituent particles are the same size and shape of the feedstock powder(Figure 5.2) indicating that only superficial melting of the particles has taken place. However, sufficient melting of the particle surfaces has occurred to enable them to bond together to form an aggregate, albeit with a high porosity due to the interstices between the particles.

A coating produced under the optimal arc power(21kW) is shown in Figure 7.15. The coating indicates a dense, coherent structure with little evidence of voids or unmelted particles. Finally, Figure 7.16 is taken from a coating deposited under a high arc power(28kW). In this case, a high volume fraction of spherical (D type) voids are visible in a well-melted structure. The volume fraction of those voids increased rapidly in coatings deposited above the optimal arc power, implying that those voids might be related to the thermal degradation of polymer. It is likely that gaseous products generated by thermal degradation could not diffuse to surface rapidly because of rapid solidification of the coating layer and remained in the coating to form pores. It is also possible that the degradation of the particles initiated in the plasma flame and progressed within the coating and generating gaseous products since overlapping splats possess low thermal conductivity and could not dissipate heat rapidly.

Quantitative microscopy on coating cross-sections indicated that there was also a minimum in porosity at the 21 kW arc power (Figure 7.17). The particles within the coatings produced at below the arc power level exhibited less flow due to lower temperatures and lower degree of melting of the particles, which resulted in high proportional interstices pores (Figure 7.14). Those interstices pores decreased with the increase of the arc power levels since the degree of melting of the particles increased with the arc power (Figure 7.15). However excessive heat energy of high arc power promoted the thermal degradation of polymer and caused the proportion of D type pore to be increased (Figure 7.6). Therefore the overall porosity increases again at above optimal arc power level. Figure 7.14 to 7.17 have suggested that the variation of wear resistance of the coatings with the plasma arc powers is due to the change of the coating structure with the arc powers, particularly the porosity of the coatings.

An optimal arc power range of 23-27kW giving a minimum wear rate was also obtained for PMMA coatings produced with all the PMMA grades(MG101, DA100 and DP300) as shown in Figure 7.18, suggesting a similar mechanism for all grades. Figure 7.19 shows that the same optimal arc power range for maximum bulk density of the PMMA coatings exist: the coatings exhibited lower bulk density at both lower and higher than optimal power range. Figures 7.20 gives the SEM micrographs of through-thickness cross section of the PMMA coatings (DA100 grade) produced with different arc powers. It shows significant differences in microstructure with the arc power levels: the deposit produced under low arc power(11kW) consists of poorly melted particles resulting in high porosity, weak interparticle bonding and thus high wear rate. Increasing the arc power to 22kW improves the degree of melting (Figure 7.20b) and so the wear resistance. Raising the arc power to 35kW increases the degree of particle melting further but at the expense of increased porosity (Figure 7.20c) and therefore reduced wear resistance.

It was noted that compared with polyamide coatings, the PMMA particles exhibited less flow and produced coatings with higher porosity. This is likely due to their higher melt viscosity relative to polyamide at elevated temperatures, which is related to the nature of the polymer structure[82].

7.2.3 Nozzle size

Heat transfer analysis has indicated that the particle temperature, the degree of melting and the extent of degradation of polymer particles are influenced greatly by the particle velocity. As indicated in section 2.7. the particle velocity is governed primarily by the particle size and the plasma beam velocity, while the beam velocity is controlled by the plasma gas flow rate, plasma temperature and the nozzle diameter (Equation 2.2). Increasing the gas temperature by inputting high energy appears an unsuitable method to increase beam velocity for polymers owing to the problems with degradation as shown in above experimental results and theoretical calculations in chapter 6. The selection of gas flow rate and particularly nozzle diameter offer alternative means of control of beam velocity. It was found experimentally that high velocity nozzle is essential for plasma spraying of polymers: for example, only the nozzle with 5mm exit diameter can produce satisfactory polymer coatings; the nozzle with 8mm exit diameter produced coatings with dark brown appearance and also very low deposition efficiency suggesting high degree of thermal degradation of polymers. It should be mentioned that the nozzle size selected was for the Metco MN plasma system, when other spraying equipment is used, the appropriate nozzle size may change.

7.2.4 Powder injection

The position and angle of the powder injection are important practical variables. If the injection point is too close to the plasma jet, the incoming powder stream is melted prematurely before injection resulting in blockage of the powder port. This is not a difficulty normally encountered with ceramic or metallic powders owing to their much higher melting points, and adjustment will often be necessary when changing to polymeric powders. There are large temperature gradients within the plasma jet: the temperature is highest at the nozzle exit in the centre of the jet and decreases with increasing distance from the nozzle down the central axis(downstream) and at right angles to it. Particle injected at right angles to plasma jet axis will therefore experience much higher temperatures than those injected downstream at 45 ° degrees to the axis. The work has shown that satisfactory coatings can only be produced with coarse precursor powders providing they were injected at 90 degrees in order to ensure complete melting, whereas fine powders required injection at 45° degrees downstream to avoid excessive overheating leading to thermal degradation and vaporization. The physical penetration of the plasma jet by polymer particle is difficult due to their low density and optimal adjustment of the carrier gas, transporting the precursor powder from the hopper to the injection point, is required.

7.3 Polymer behaviour during plasma spraying

When polymer particles are immersed into a plasma jet, heat exchange occurs between the plasma and the particles. In addition, the high temperature environment of the plasma may cause other interactions between plasma and polymer resulting in modification to the polymer microstructure including variations in molecular chain length and crystallinity. Since the physical properties and processing characteristics of high polymers depends on critically on their structure, particularly on the molecular chain length, it is important to know the possible variation of polymer during plasma process and the influence of polymer structure on the plasma process.

7.3.1 Polymer degradation

Degradation of a polymer is a process involving rupture of chemical bonds in the main chain of the macromolecule. *When a polymer is heated, the energy of thermal* motion at some points of the macromolecule, owing to thermal energy fluctuation, becomes commensurable with the energy of the chemical bonds and rupture of the bond may occur. Heat transfer analysis and above experimental results have indicated the occurrence of thermal degradation of polymer during plasma spraying. This is practically very important because the properties of polymeric materials depend to a great extent on the length of their chains. The degradation mechanism and its effect on the coating quality were thus investigated.

The majority of work reported in the literature on the degradation of polyamide has been carried out on polyamide 6 and polyamide 6.6 and no systematic investigation of polyamide 11 is available[122,123,124,125]. Straus and Wall[123] have pointed out that the weakest linkage in the polyamide chain is the C-N bond since this has a significantly lower bond strength than the C-C bond (277 $kJmol^{-1}$ and 335 $kJmol^{-1}$ respectively). Degradation of polyamide 6 and polyamide 6.6 in inert atmosphere has thus been concluded to take place by scission at the -NH.CH_2- group [123,124]. It seems likely that a similar mechanism occurs in polyamide 11:

$$\text{-CO}\cdot\text{NH}\cdot\text{CH}_2(\text{CH}_2)_9\cdot\text{CO}\cdot\text{NH} \;\vdots\; \text{CH}_2(\text{CH}_2)_9\text{CO}\cdot\text{NH-} \qquad (7\text{-}1)$$

with scission producing one fragment with a carbonamide end and another with an unsaturated hydrocarbon:

$$\text{-CO}\cdot\text{NH}\cdot\text{CH}_2(\text{CH}_2)_9\cdot\text{CO}\cdot\text{NH}_2 + \text{CH}_2\text{:CH}(\text{CH}_2)_8\cdot\text{CO}\cdot\text{NH-} \qquad (7\text{-}2)$$

The carbonamide group then splits off water to form a carbonitrile:

$$\text{-CO}\cdot\text{NH}\cdot\text{CH}_2(\text{CH}_2)_9\cdot\text{CO}\cdot\text{NH}_2 \rightarrow \text{CO}\cdot\ \text{NH}\cdot\text{CH}_2(\text{CH}_2)_9\cdot\text{C}\vdots\text{N} + \text{H}_2\text{O} \qquad (7\text{-}3)$$

The water produced by the above process can hydrolyse the amide groups along the chain to give free amino and carboxyl end-groups:

$$\text{R}\cdot\text{NH}\cdot\text{CO}\cdot\text{R}' + \text{H}_2\text{O} \rightarrow \text{R}\cdot\text{NH}_2 + \text{R}'\cdot\text{COOH} \qquad (7\text{-}4)$$

These end groups can interact in a number of ways to produce gaseous products [120,122] including:

$$\begin{aligned}&\text{-CO}\cdot\text{NH}\cdot(\text{CH}_2)_9\cdot\text{COOH}+\text{COOH}(\text{CH}_2)_9\cdot\text{NH}\cdot\text{CO-}\\ &\rightarrow\ \text{-CO}\cdot\text{NH}\cdot(\text{CH}_2)_9\cdot\text{CO}(\text{CH}_2)_9\cdot\text{NH}\cdot\text{CO-}+\text{CO}_2+\text{H}_2\text{O}\end{aligned} \qquad (7\text{-}5)$$

The infrared spectra from the polyamide 11 coatings sprayed in the current investigation were not significantly different from that of the precursor powder (Figure 7.21). This is in agreement with the data of Achhammer et al [119] who found no significant change in infrared data on the degradation of bulk polyamide 6 under an inert atmosphere. These results suggests that no substantial oxidation of the polymer takes place even though plasma spraying is carried out in air. The entrainment of air into the plasma jet does not therefore cause noticeable oxidation; it may produce gas entrapment in the coating but good operating practices can reduce this to a low level.

The sequence of reactions proposed above relies upon chain scission, which should reduce the molecular mass of the coating relative to the precursor powder. Solution viscosities were thus investigated in order to provide further information on molecular mass, since according to the Mark-Houwink equation [126]:

$$[\eta] = KM^{\alpha} \qquad (7\text{-}6)$$

$$[\eta] = \lim_{c \to 0} \eta_{red} \qquad (7\text{-}7)$$

where $[\eta]$ is the intrinsic viscosity, η_{red} is called reduced viscosity or viscosity number which can be obtained experimentally, M is the molecular weight and K and α are empirical constants depending upon the nature of the solvent. Using the subscripts c and p to denote the coating and powder respectively:

$$\frac{[\eta]_c}{[\eta]_p} = \left(\frac{M_c}{M_p}\right)^{\alpha} \qquad (7\text{-}8)$$

The fractional reduction in the molecular mass of the coating relative to the precursor powder is given by M_r, where

$$M_r = \frac{M_p - M_c}{M_p}$$

$$M_r = 1 - \left(\frac{M_c}{M_p}\right) \qquad (7\text{-}9)$$

and combining this with equation (7-8) gives:

$$M_r = 1 - \left(\frac{[\eta]_c}{[\eta]_p}\right)^{\frac{1}{\alpha}} \qquad (7\text{-}10)$$

The experimental data for η_{red} using m-cresol as a solvent are presented in Figure 7.22 for the powder and high arc power coating and yield $[\eta]_c = 0.088$ and $[\eta]_p =$

0.102. Although the parameter α has not been determined for polyamide 11, its value for the similar polyamide 6.6 is 0.61 and substituting this along with the above viscosities into equation (7-10) gives $M_r = 0.21$. The results show that the molecular weight of this particular polyamide 11 sample has decreased by approximately 20%. It is emphasised that this applies to the high arc power coating which suffered substantial degradation and the molecular mass reduction would be much less for an optimal polyamide 11 coating. A molecular mass reduction of 20% in itself produces a relatively small deterioration in mechanical properties of polyamide [86] but the presence of the voids is likely to produce a major detrimental effect.

The experimental findings are thus consistent with a scission-based mechanism of thermal degradation leading to the evolution of gaseous products and the reduction of molecular weight. This mechanism can cause serious porosity at high arc power levels (Figure 7.16 and 7.17) due to the generation of high temperatures within the particles in the plasma, while optimization of the operating conditions can reduce degradation to minor proportions as demonstrated in Figures 7.15.

7.3.2 Polymer molecular weight

The solution viscosity measurement of polyamide 11 coatings has implies the reduction of molecular weight relative to feedstock powder during plasma process. A quantitative systematic investigation was carried out based on PMMA powders.

Three grades of PMMA were investigated: MG101, DA100 and DP300 with weight average molecular weights of 0.08×10^6 , 0.6×10^6 and 1.8×10^6 respectively. Those three powders were plasma sprayed under different plasma conditions. The molecular weights and molecular weight distributions of the PMMA powders and the coatings were determined by ICI using a gel permeation chromatography technique. Figure 7.23 shows the effect of plasma arc power on the molecular weight of PMMA grades: Figure 7.23a shows the effect on the number average molecular weight and Figure 7.23b the effect on the weight average molecular weight. Zero arc power in both figures refers to the feedstock powder. Figure 23 indicates that the molecular weight of three grades PMMA coatings has, to some degree, decreased relative to that of corresponding feedstock powders. It has also revealed that the extent of molecular weight reduction increased with increasing plasma arc powers. Figure 7.24 gives an ratio of the molecular weight of a coating to that of the feedstock powder which gives a quantitative value of the extent of the reduction of the molecular weight as a function of plasma arc power. Figure 7.24a is that of MG101 grade, Figure 7.24b DA100 grade and Figure 7.24c DP300 grade. It can be observed that the extent of molecular weight reduction of three PMMA grades increased with the plasma arc power significantly: for example, a DA100 coating produced with 11 kW arc power shows approximately 35% reduction in number average molecular weight and 36% in weight average molecular weight relative to those of the powder. The same coating produced under 29kW has about 62% reduction in number average molecular weight and 58% in weight average molecular weight. DP300 grade shows a similar behaviour as that of DA100 grade but the extent of molecular weight reduction of MG101 grade appears smaller than the others. As shown in Figure 5.3 the average particle size of MG101 grade is larger than the others, many of which are too big to be effectively melted (Figure 7.2). The unmelted core of particle remains the same molecular weight as that of the feedstock powder and therefore the overall extent of molecular weight reduction appears smaller.

The reduction of molecular weights of PMMA during plasma spraying is the consequence of thermal degradation under the influence of high thermal energy supplied by plasma beam. When the temperature of the polymer in the plasma beam is so high that primary chemical bonds could be separated, the chain rupture occurs and results in the degradation of the materials. The degree of degradation of the PMMA may be thought to be influenced by the output of thermal energy of plasma and the rate of heat diffuse within the polymer particle which is determined by the thermal conductivity and particle size. The high plasma thermal energy output associated with high plasma arc power supplies the surface of the particle excessive heat which can not be dissipated effectively because of the poor thermal conductivity of PMMA. As a result, the temperature at the surface of a PMMA particle rises rapidly and results in chain breakage. However, since plasma spraying is an rapid solidification process, its high cooling rate causes the degradation reaction to terminate rapidly and the products of degradation with shorter chains remain the coatings so that the average molecular weight of the coatings reduces relative to that of the feedstock powders.

The processing behaviour and many end-use properties of polymers are not only influenced by the average molecular weight but also by the width and the shape of molecular weight distributions(MWD). The comparison of the profile of molecular weight distribution of PMMA(DA100 grade) coatings with that of the powder is shown in Figure 7.25. It is noted that the MWD changes on plasma spraying with an increase in the volume fraction of lower molecular weight molecules at the expense of a decrease in the volume fraction of high molecular weight molecules which results in the average molecular weight reduction. The effect becomes more pronounced at high arc power levels. The "most probable" peaks of two coatings can be observed to have moved towards lower molecular weights. The peak values are 4.4×10^5 for powder, 2.4×10^5 for the coating produced under 23kW arc power and 1.6×10^5 for the coating produced under 35 kW. However all those peak values are in the range of 10^5 to 10^6. This observation is practical useful since a noticeable change in properties of a polymer is detected only if its molecular mass is decreased approximately tenfold[86]. The result further indicates that the high plasma arc power levels cause significantly degradation during the plasma spraying of PMMA materials.

It was reported[127,128,129] that the degradation mechanism of PMMA at elevated temperatures in an inert atmosphere was depolymerization with random chain scission as the initiation step. If this is the case in the plasma process, the monomer molecules generated by degradation would superheated and nucleate to form bubbles (PMMA starts to degrade above 473 K and the boiling temperature of its monomer is 373 K). The rapid solidification of the droplets prevents the bubbles from diffusing to the coating surface and they therefore remain within the coatings forming pores. Since the degree of degradation of PMMA increased with increasing plasma arc power, the porosity resulting from this mechanism shows an increase with arc power as observed in Figure 7.20c.

The infrared spectra of the powders and the coatings of three grades of PMMA were measured and results are given in Figure 7.26. No significant differences between the infrared spectra of the powder and coatings were observed for the PMMA grades from Figure 7.26. Also there are no new peaks observed in the coatings. This means that no new substance results from the reaction of the powder to the plasma or its surroundings, such as oxidation with entrapped air in the plasma. The results confirmed that a major degradation mechanism is depolymerization leading ultimately to gaseous monomer and increased porosity.

It should be mentioned that although no oxidized products were observed in the PMMA coatings, the presence of oxygen from entrapped air in plasma beam may accelerate the depolymerization reaction[128]. If this is a case the porosity of PMMA coatings would be reduced if spraying is carried out in a controlled atmosphere.

7.3.3 Influence of Molecular weight on splat flow

The flow and spreading of a molten droplet is greatly dependent of its melt viscosity, while the most important structural variable determining this viscosity is the molecular weight or alternatively, the chain length as represented by the simple expression[126]:

$$\log \eta = 3.4 \log Mw + A$$

where η, Mw and A are viscosity, molecular weight and an empirical constant respectively.

The melt viscosities of three grades of PMMA were calculated using above equation and results are plotted in Figure 7.27 as a function of temperature. The viscosity differences of three grades of PMMA are significant.

The wipe test was used to study the flow of individual PMMA particles on impact with the substrate. Figure 7.28 shows the SEM micrographs of the isolated splats produced in wipe test under the same operation conditions with three grades of

PMMA powders. It is noted that the splats produced with middle molecular weight PMMA (DA100 grade, $Mw = 1.8 \times 10^6$, Figure 7.28a) exhibited significantly better flow than that of highest molecular weight PMMA (DP300 grade, $Mw=0.6\times10^6$, Figure 7.28b). Figure 7.28c gives the splats produced with lowest molecular weight grade (MG101, $Mw=0.08\times10^6$): considering the splats produced with particle sizes of similar size to that of DA100 and DP300 grades, they show the better flow. Some large particles appear to have a low degree of melting and some have even bounced off from the substrate leaving traces seen clearly in this SEM photograph, which supports the explanation for the less molecular weight reduction occurred in plasma deposited MG101 coatings (Figure 7.24). It can therefore be considered that the extent of PMMA particle flow on impact with the substrate increases with decreasing molecular weight. Further examination of coating structures revealed that the high porosity level of the high molecular weight PMMA coating was associated with the poor flow of particles on impact. This is shown in Figure 7.19 which gives the comparison of the bulk densities of three grades of PMMA as a function of plasma arc power. In the optimal arc power range, the DA100 grade shows the highest density. The direct comparison of the lowest molecular weight grade MG101 with the other grade is difficult owing to its larger feedstock particle size. This lower the degree of melting of the particles so as to affect the flow and spread of particle on impact. However, MG 101 still appears denser than DP300 grade produced in the optimal arc power range.

7.3.4 Physical transformations of polymers

Plasma spraying is an rapid solidification process during which the particles injected "quench" down to surrounding temperature from various high temperature states. This non-equilibrium cooling process is known to result in modifications to the crystal structure of some ceramics and metals[31,35]. This section investigates whether or not the non-equilibrium conditions would affect the microstructure of polymers .

The X-ray diffractometer traces from the polyamide 11 feedstock powder and plasma sprayed coating are shown in Figure 7.29. Polyamide 11 crystallizes in a triclinic structure[130] and both the powder and coating show evidence of crystalline and amorphous phases(Figure 7.29). However, the peaks are not as well defined for the coating as in the powder, which suggests that there is a larger volume fraction of the amorphous phase in the deposit.

A group of DSC traces for the polyamide 11 coatings and powder are given in Figure 7.30. It is observed that the area of the endothermic peaks of the coatings, caused by the melting of the polyamide, reduced relative to that of feedstock powder. The integral value of endothermic peak represents the enthalpy difference of fusion (crystallization) of the materials which reflects the crystallinity of the polymer. Therefore the results suggests that the fraction of disordered phases in polymer coatings increased relative to that in the feedstock powder. The amorphous fraction in the coatings therefore increased relative to that of the feedstock powder. It is also observed that the main peak shifted to a higher temperature and a additional small peak appeared in the DSC traces of polyamide 11 coatings, which was eliminated on remelting. This suggests the formation of metastable phases of polyamide 11 under the rapid cooling rates in plasma spray deposition. Rapid solidification is also a possible contributory factor in the formation of the increased amorphous fraction in the coatings. A further factor affecting the enthalpy difference, however, is likely to be degradation, particularly since the coating produced with a low traverse speed coating (which was significantly degraded) showed the smallest peak area (Figure 7.30). The reduced chain length due to thermal degradation is likely to decrease the enthalpy difference of fusion of polyamide [132].

7.4 Particle size of polymer feedstock powder

The theoretical analysis and the studies on isolated PMMA and polyamide splats have revealed that the melting, flow, spreading and decomposition of the particles depend strongly upon the particle size of feedstock powder. These factors are important in determining the coating structure. A systematic experimental study was therefore carried out to investigate the influence of particle size of feedstock powder on the structure and properties of the coatings sprayed. The polyamide 11 powder was used for this investigation.

The as-received polyamide 11 powder was classified into five different particle size ranges by sieving: 38-53μm, 53-75μm, 75-90μm, 90-125μm and 125-150μm. The powders were plasma sprayed and the structure and properties of the coatings produced were evaluated.

Figure 7.31 shows the effect of feedstock particle size on the bulk density of the coatings sprayed with the optimum arc power of 20-23kW and argon-hydrogen plasma. The results shows that the density of the coatings increases (from 0.83Mgm^{-3} to o.93Mgm^{3}) with the decrease of the particle size. The densest coating was achieved with the 38-53μm feedstock particle size. The second best was produced by the 53-75μm powder. This effect of particle size on density relates to the viscous flow of the particles on impact with the substrate and previously deposited coating. A high temperature and degree of melting gives a sufficiently low viscosity for the polymer to flow readily *into the irregularities of the underlying surface topography.* This generates tightly knitted splats in coating aggregate and minimizes the voidage of the coatings. The lower average temperature and the degree of melting of coarse particles results in a higher melting viscosity and inadequate splat flow with a consequent decrease in coating densities. Figure 7.32a to 7.32d give the through-thickness sections of polyamide coatings produced with 38-53μm, 53-75μm, 90-125μm and 125-150μm feedstock powder respectively. It can be observed that the porosity of the coating decreased with the decrease of the particle size of the feedstock powder. For example, high proportion of interstitial voids exists within the coating produced by 125-150μm powder, while the coating produced by 38-53μm feedstock powders exhibits a dense structure.

The influence of the particle size on the wear resistance of the coatings is shown in Figure 7.33: the wear depth after 5000 cycles of the coatings made with the 38-53μm was 9μm compared with 31μm for coarsest feedstock powder (125-150μm). The study on wear mechanism of polyamide 11 coatings (detailed discussion in section 7.6.3) has shown that the main mechanism of materials removal is polyamide adhering to the sliding counterface and fracture occurring along the underlying splat boundary. The presence of pores and unmelted particles which gives poor bonding of splats in the coatings therefore promotes inter-splat fracture and local damage and adversely affects wear resistance of the coatings. A further benefit arising from refining the feedstock particle size is a much improved surface finish in terms of reduced roughness and surface flaws (Figure 7.34), which also was found to reduce the coefficient of friction of the coatings(Figure 7.35). Both cases would improve the wear resistance of the coatings.

Size classification also resulted in a significant improvement in tensile strength (27 MPa to 42 MPa) and total tensile elongation(27% to 37%) as shown in Figure 7.36, which are associated with the reduction of porosity and unmelted particles as shown in Figure 7.32a to 7.32d.

Above results indicate that particle size control of polyamide 11 feedstock powder substantially improved the density, tensile properties and wear resistance of the plasma sprayed coatings. Maximum quality was obtained with a feedstock particle size of 38-53μm, which is consistent with the theoretical predication in Chapter 6.

7.5 Coating properties and the factors affecting the properties

7.5.1 Adhesion of the coatings

The term adhesion denotes the sum of surface forces by which particles of different mass attract one another. From the view point of plasma spray technology the term "adhesion" is used also to designate the force necessary to tear off a unit area of coating from the substrate[133, 134]. The adhesion of coatings is critical to their industrial exploitation. There is no work in the available literature on the adhesion of plasma sprayed polymer coatings to their substrate. An experimental work programme has thus been carried out to investigate the important process parameters on the adhesion of polyamide 11 and PMMA coatings to steel substrate.

(a) Plasma spraying conditions

The plasma spraying conditions create the thermal and kinetic characteristic of plasma beam, the transport and fusion of the sprayed powder material and the thermal and kinetic characteristics of the impinging molten powder. As these characteristics affect the process of bonding between coating and the substrate, it is necessary to determine experimentally the optimal parameters for the polymer materials.

It has been observed that there is an optimal spray distance for the adhesion of polyamide 11 coatings to the steel (preheated to 323 K) at around 100mm, under the optimum arc power range of 20-23kW (Figure 7.37). SEM examination on the interface after adhesion failure of the coating sprayed at 50mm is shown in Figure 7.38. It reveals that the contact area between the coating and substrate (as shown by the fracture surface in Figure 7.38) is relatively small . A similarly low contact area was observed for the coatings deposited at the spray distances above the optimal distance.

Figure 7.39 gives a SEM micrograph showing the interface of the polyamide coating after adhesion failure at an adhesion strength of 6 MPa. The contact area between the coating and substrate can be observed to have increased significantly, suggesting the adhesion of the coating to the substrate is proportional to the contact area between the coating sprayed and the substrate.

The true contact area of the coating with substrate depends on the true contact of the molten splats with substrate, and the latter is determined by the extent of the deformation (flattening) and flow of the droplets on impact with substrate. For a given material and particle size, the extent of the deformation and flow are dominated by the degree of melting, contact temperature and velocity(affecting kinetic energy) on impact. The theoretical analysis in Chapter 6 shows that the temperature in the interior of a polyamide particle is unlikely to be above the melting temperature of polyamide at a spray distance of 50mm under the operating condition used due to too short a residence time of the particle in the flame (Figure 6.20). Low melting degree of the particle leads to poor flow on impact with the substrate and thus a relatively low contact area between the splats and substrate. At long spray distances, the temperature and velocity of the plasma jet are substantially reduced due to its distance from the arc and air entrainment, which causes the cooling and deceleration of in-flight particle. Consequently, the particle flow on impact is reduced, which leads to a low true contact area between the splats and the substrate and results in poor adhesion.

Figure 7.40 shows the influence of plasma arc power on the adhesion of PMMA coatings to the steel substrate preheated to 353 K. It indicates that low arc power levels results in poor adhesion of PMMA coatings. Figure 7.41 gives a SEM micrograph showing adhesion failure of a PMMA coating deposited at 16 kW arc power indicating a corresponding low contact area between the coating and the substrate. Referring to Figure 6.8-6.10 in theoretical calculations, the low arc power levels are not able to melt the particles completely, resulting in poor particle flow on impact, and therefore low contact area and poor adhesion. The adhesion of PMMA coating increase with increasing arc power owing to increasing degree of melting and kinetic energy. However, too high an arc power led to an unacceptable coating structure in terms of high porosity as shown in Figure 7.20c. Similar situation has been observed for polyamide 11 coatings.

Plasma gas flow rate has been found to play an important role on the adhesion of polymer coatings to the steel substrate. Figure 7.42 shows the influence of plasma gas flow rate on the adhesion of polyamide 11 coatings to the steel substrate. The coatings were sprayed under the conditions of 21kW arc power, 100mm spray distance and a 5mm diameter nozzle (Metco's smallest nozzle). It is noted that the adhesive strength of polyamide coatings drops with increasing gas flow rate.

A high input gas flow rate will produce a high plasma beam velocity from Equation (2-2), which results in high particle velocities. From the viewpoint of increasing kinetic energy on impact, high particle velocity would favourably affect adhesion of the coating to substrate. However, Figure 6.13 to 6.18 from theoretical analysis suggest that high particle velocities can result in incomplete melting which, together with the cooling effect of the larger gas volume, is likely to be the cause of the poor adhesion at high plasma gas flow rates. It was also found that when a gas flow rate of below $2m^3h^{-1}$ was used the deposition efficiency of polyamide was too low to produce reasonable coatings because of the high rate of decomposition. It should note that the data plotted in Figure 7.42 was obtained by using high velocity nozzle, and that the relationship may change for a different nozzle size.

The effect of feedstock powder feed rate on coating adhesion was determined using a series of polyamide coatings sprayed using 21-23kW arc power, 100mm spray distance and 5mm diameter nozzle. The results are plotted in Figure 7.43. It shows that increasing the feed rate drastically reduced the coating adhesion, which is attributed to incomplete melting of the excessive mass of powder due to the limited enthalpy of the plasma jet. However, the deposition rate was observed to have decreased with decreasing powder feed rate, particularly, at feed rates of less than 10g min^{1}, which is too low for practical operation.

(b) Substrate preheating

The polyamide 11 was plasma sprayed using the conditions of 21-23kW arc power, 100mm spray distance and 5mm nozzle on to the substrates preheated to a series of temperatures and the adhesion of them were measured. The substrate was preheated using the plasma torch and its temperature monitored by a contacting thermocouple. The influence of substrate temperatures on the coating adhesion is given in the following table(Table 7.1):

Table 7.1. The effect of substrate preheating on the coating adhesion

Sample	Coating material	Subs.temp. /C	Adhesive strength/MPa	Failure mode
ST1	polyamide	50	6	adhesion
ST2	polyamide	150	>13	adhesive
ST3	polyamide	180	>13	adhesive
ST4	polyamide	220	>10	adhesive
ST5	polyamide	300	>9	adhesive

Two main types of failure were found during adhesion testing: true adhesion failure by fracture along the coating-substrate interface (designated "adhesion" in table 7.1) or fracture within the adhesive itself (designated "adhesive" in Table 7.1). The latter adhesive was that used to bond the specimen coating to the aluminum dolly as described in Chapter 5. The results in the Table 7.1 show that preheating the substrate provides a substantial improvement in the adhesion of polyamide 11 coatings to steel.

Figure 7.44 gives a SEM micrograph of a polyamide 11 coating with a high adhesive strength of >13MPa, pulled off at the interface using a sharp knife applied at the edge. It reveals that the coating has an intimate contact with the substrate. The extensive plastic deformation of the splats observed in the Figure 7.44 suggests the strong bonding between the coating and substrate. Figure 7.45 gives a SEM micrograph of polished cross-section of coating-substrate interface of polyamide 11 on steel, showing intimate contact between the coating and steel.

From the viewpoint of increasing the contact area between the coating and substrate, preheating substrate up to the melting temperature of the polymer or above can reduce substantially the cooling rate of the splats (Figure 8.4), promote their flow and thus increase the adhesion of the coating to the substrate. Since the flow of the particle increases with temperature, the adhesion of the coating to the substrate will also increase with the temperature of the substrate. However, heating the substrate to temperatures in excess of 220 °C gave an increased density of pores at adhesive interface as shown in Figure 7.46 and some discoloration of the coating, which indicates the occurrence of significant degradation. Therefore, the control of the substrate temperature is very important and the suitable preheating temperature must be selected close to the lower limit of the melting range of the polymer.

Many specialists believe that the bond of substrate and coating is complex and is conditioned by mechanical bonding (wedge bonding and anchor interlocking), the formation of chemical bonds between the coating and substrate, as well as the formation of forces of physical interaction[32,45,49]. Preheating substrate to above 100 °C can remove the moisture from substrate surface and promote the true contact of splats to the substrate, which benefits all these adhesion mechanisms. Preheating the substrate may also affect the formation of chemical bonding. During the plasma process, the molten in-flight particles produce extremely high local pressures where they strike the substrate surface, which further cleans the contact surface, brings the particle and substrate into intimate contact and may also lead to plastic strain on particles and the surface layer of the substrate. The atoms of the particle surface may be excited due to high temperature and strain and chemical reactions at the interface can possibly occur if the kinetic conditions of the reaction (time and temperature) can be met. The kinetics of the formation of the chemical bonds during the plasma process is likely to obey the laws characteristic for chemical reactions of the first order[45]. The temperature of the zone of contact between the sprayed particles and the substrate is thus the decisive variable in the process of chemical bond formation, since the reaction time necessary for the course of the reaction depends greatly on the reaction temperature. Preheating the substrate retards the reduction of the contact temperature and creates the time necessary for the formation of chemical bonds and thus improves the adhesion of the coatings. In addition, heating the substrate may reduce the residual stress by reducing cooling rate of the coating to the benefit of the adhesion of the coatings.

(b) Substrate pretreatment

Substrate surface preparation is an essential supplementary technology of the spraying process. The aim of preparation is to ensure favourable geometrical and energy properties of surface layers of the substrate for strong bond formation between the coating and the substrate, both from the viewpoint of mechanical anchoring and microweld formation.

The steel substrate was pretreated in three ways:

(i) Chemical cleaning (Pyrocleaner)

(ii) Etching (citric acid)

(iii) Mechanical roughening (grit blasting)

Pyrocleaner is an alkaline cleaner which gives steel a clean and degreased surface without addition surface roughening. Citric acid can remove oxide and rust from the steel surface and give a clean, etching, and reactive surface. The grit blasting was controlled to gives a roughness of 7 μm Ra as measured with Surtronic 3+ profilmeter (Rank Taylor Hobson Ltd.), and as a result it produces a larger specific surface area and reactive surface. The steel was then plasma sprayed with polyamide 11 or PMMA. The adhesion of the coatings to the substrates was evaluated and the results are given in Table 7.2 :

Table 7.2 Effect of pretreatment on coating adhesion

No.	Coating	Pretreatment	Substrate Temp. (°C)	Adhesive strength (MPa)	Failure mode
A1	polyamide	Grit blasting	50	4	adhesion
A2	polyamide	Pyrocleaner	50	< 0.5	adhesion
A3	polyamide	citric acid	50	2	adhesion
A4	polyamide	grit blasting	150	>13	adhesive
A5	polyamide	Pyrocleaner	150	3	adhesion
A6	polyamide	citric acid	150	>10	adhesive
A7	PMMA	grit blasting	80	5	adhesion
A8	PMMA	Pyrocleaner	80	0.5	adhesion

Low adhesive strengths were found for all pretreatment at a substrate temperature of 50 °C. Heating the substrate to 150 °C during spraying substantially improved the adhesion particularly for the grit blasted substrate and etched substrate. The results indicate that the rough surfaces produced by grit blasting or etching give superior adhesion to the clean, smooth surface produced by chemical cleaning.

7. 5.2 Tensile properties

(a) Stress-strain characteristics

To study the stress-strain characteristics of plasma deposited polyamide coatings, the same grade of polyamide 11 powder was thermally compressed into a specimen of 500μm thick and then tensile tested under the same condition as that of plasma coatings (section 5.5.3). The tensile stress-strain curves of both thermally compressed specimen and plasma sprayed coating deposited at optimal conditions are plotted in Figure 7.47: the plasma sprayed coating exhibits a brittle character as indicated by its fracturing while deforming elastically, whereas the thermally compressed sample behaves in a typical ductile manner: the initial deformation is elastic, which is followed by yielding, a region of plastic deformation and finally ductile tearing. The plasma sprayed coating has also lower tensile strength and much lower strain ability (elongation). Tensile strengths of 37 MPa and 48 MPa, and total elongations of 27% and 170% were obtained for the coating and the thermally compressed specimens respectively.

Examination of the plasma coating indicates that its structure consist mainly of overlapping splats with differing extent of flow giving a layered structure (section 7.1). Comparing with the bulk material, the boundaries of the splats and layers are relatively weak regions since the molecules at the boundaries generally possess higher energy than interior and the microcracks are most likely to generate and propagate along the boundaries resulting in brittle fracture characteristic of the coating.

It was found that the tensile behaviour of the polymer coatings were influenced by operating conditions. For example, the coating deposited under a sub-optimal arc power of 18kW gave a tensile strength of 20 MPa and a total elongation to fracture of 9%, whereas the coating sprayed at the optimal power of 21kW gave a tensile strength of 37 MPa and total elongation of 27%. The examination of fracture surface from the tensile specimen of the 18 kW coating has revealed that the fracture surface is brittle in nature (Figure 7.48). It can be observed that the large interstice pores oriented perpendicularly to the applied stress, which result from the incomplete melting of the particles, form the most severe flaws within the coating and behaves as stress raisers. These flaws are therefore detrimental to the fracture strength. They become unstable and propagate spontaneously once the stress at the tips of the flaws has exceeded the critical stress under the applied load, leading to brittle fracture and the observed low fracture strength. However, the fracture surface of the 21kW arc power coating displays a appreciable plastic deformation in the vicinity of the pores

- microscopic ductility (Figure 7.49) in marked contrast to the low arc power coating. These results indicate that the flaws that are present in the coating, such as pores and unmelted particles also promote fracture of the plasma sprayed coating at low fracture strengths, and sufficient particle melting and strong bonding between splats as found in the optimal coating may allow stress transfer across the splat boundaries and plastic deformation of the polyamide to take place, which improves the tensile properties of the coatings. Figure 7.50 shows that there is a negative association between tensile strength and porosity as expected for the coatings.

7.5.3 Wear behaviour

As stated in Section 5.1, because of its low friction coefficient, polyamide is frequently used as wear resistant material. The wear behaviour of plasma deposited polyamide coatings was thus investigated. The wear resistance of the polyamide coatings was also used as an indicator of the quality of the coatings sprayed .

Figure 7.51 shows the progress of sliding wear of polyamide 11 coatings against a stainless steel ball. An initial period of rapid wear or running-in was observed over the first 500 cycles followed by a more gradual equilibrium wear period. A similar pattern of behaviour was observed under reciprocating sliding wear with the Rockwell diamond stylus as shown in Figure 7.52. The initial high wear rate period is attributed to the removal of protrusions and high spots on the original surface, and misalignments between the sliding surfaces. The high spots and misalignments existing in contacting surfaces bear very high local load and high contact stress which leads to the observed initial severe wear. As sliding progress, the high spots and misalignments are removed, the contact stresses reduce with the increase in the true contact area and the wear transforms into the much milder equilibrium stage.

Figure 7.53 is a scanning electron micrograph from the sliding surface of polyamide coating after wear against the stainless steel ball. The worn surface contains shallow pits which appear to have been caused by material being pulled out of the surface. Examination of the steel and diamond counterfaces revealed evidence of polyamide transfer films, indicating that adhesive wear is a major material-removal mechanism. The debris particles collected during the wear test, as shown in Figure 7.54, consisted of flat platelets of polyamide 11 similar dimensions to the splats making up the deposit. It appears likely therefore that the polyamide adheres to sliding counterface and fractures along the underlying splat boundary to generate a debris particle. There are also grooves visible parallel to the sliding direction(bottom left of Figure 7.55) indicative of abrasive wear caused by asperities from the harder counterface ploughing out the softer polyamide surface.

Both of the above wear mechanisms involve plastic deformation followed by fracture to produce a debris particle and generate a unit of wear. The resistance to fracture and ductility of the coatings will therefore play a crucial role, which depends greatly on the structure of the coatings. The presence of voids and microcracks within the coating act as stress concentrators and enhance local damage as shown in Figure 7.56, which is detrimental to the wear resistance. The observed relationship between the porosity and wear rate of the polyamide 11 coatings given in Figure 7.57 may be understand on this basis. The bonding between splats also play an important role owing to its effect on the fracture strength and ductility of the coatings. The observed relationships between wear rate and process parameters(Section 7.2) can thus be understood in terms of the effect of structure on tensile ductility: the coatings produced with optimal operating conditions and particle size exhibited maximum coating density and tensile ductility and, therefore, the best wear performance.

7.6 Summary

Wipe test was used to examine the flow of the individual polymer particles on impact with steel substrate. The results reveal that the extent of particle flow increases with decreasing feedstock particle size and increasing plasma arc power owing to the influence of the particle size and arc power on the temperature and degree of melting of in-flight particles. The test results verifies the theoretical prediction in Chapter 6.

Polyamide 11 and PMMA coatings can be deposited by plasma spraying.

Microstructural examination showed that the plasma sprayed polymer deposits are composed of overlapping disc-shaped splats. There are significant variation in the extent of the flow of the particles on impact with the substrate due to the varying temperature and degree of melting of particles on impact.

Incompletely melted particles and pores are significant defects within the coatings. The major types of pore observed in the deposits include: (a) those associated with unmelted particles, (b) those resulting from inadequate splat flow, (c) those caused by gas entrapment, (d) those resulting from thermal degradation of the polymer during deposition, and (e) those pre-existing within feedstock particles.

Plasma torch traverse speed has a major effect on the plasma spraying of polymers. The critical traverse speed above which no substantial degradation of the deposit takes place is a crucial parameter for plasma spraying of polymers. The critical speed was 100mms^{1} for polyamide 11 and PMMA under the condition used.

An optimal arc power for wear resistance of polyamide 11 coatings was found to exist: the coating exhibited high wear rate at both low and high power with a minimum at 21kW. Examination of the microstructure revealed major differences in microstructure of the coatings produced with different plasma arc power levels: low power levels give incomplete melting and thus high proportional interstices pores, and high level cause thermal degradation and thus high proportional spherical pores.

A high speed nozzle (5mm) is important for the plasma spraying of polymers to obtain required high particle velocity to reduce the thermal degradation. The position and angle of the powder injection are important practical variables: if too close to the plasma jet, the incoming powder stream is melted prematurely before injection resulting in blockage of the powder port. The coarse feedstock powders require to be injected into the plasma stream at 90 degree to ensure complete melting, and fine feedstock powders need injection at 45 degree to avoid excessive overheating.

The study on the thermal degradation of polyamide suggests a chain scission mechanism: the weakest linkage in the polyamide chain is the C-N bond and therefore the degradation of polyamide in inert atmosphere takes place by scission at the -NH·CH_2- group. This thermal degradation mechanism would result in the evolution of gaseous products and the reduction of the molecular weight of the deposits. Infrared spectra from the polyamide 11 coatings sprayed in the current study were not significantly different from that of the feedstock powder. No substantial oxidation was found to take place. The solution viscosity of the polyamide 11 coatings reduced relative to that of the feedstock powder suggesting the reduction of molecular weight of the coatings relative to that of the feedstock powder. The experimental findings are thus consistent with a scission-based mechanism.

The molecular weight of the PMMA coatings decreases with increasing arc power. The profile of the molecular weight distribution changes significantly on plasma spraying with an increase in the volume fraction of small molecules at the expense of a decrease in the volume fraction of large molecules; the effect becoming more pronounced at high arc power levels. The degradation mechanism of PMMA at elevated temperatures and an inert atmosphere was depolymerization with random chain scission as the initiation step, leading ultimately to the gaseous monomer and increase porosity. No significant differences between the infrared spectra of the powder and coatings were observed for the PMMA grades implying that no detectable oxidation occurred.

The extent of particle flow of PMMA on impact with the substrate increases with decreasing molecular weight due to the influence of molecular weight on the melt viscosity of the splats. Examination of coating structures revealed that the high porosity level of the high molecular weight PMMA coating was associated with the poor flow of particles on impact.

The fraction of disordered phases in polyamide 11 coatings increased relative to that in the feedstock powder, which was found through x-ray diffraction and DSC measurement: the diffraction peaks are not as well defined for the coating as in the powder, and the enthalpy of fusion (crystallization) of the coatings reduced relative to that of the powder. Evidence also suggest the formation of metastable phases of polyamide 11 under the rapid cooling rate in plasma deposition.

As-received polyamide 11 powder was classified into five different particle size range: 38-53μm, 53-75μm, 75-90μm, 90-125μm and 125-150μm. The Particle size classification substantially improved the density, wear resistance, tensile properties and surface finish of plasma sprayed polyamide 11 coatings. This is mainly due to the influence of particle size of feedstock powder on the temperature and degree of melting of the particles. Maximum quality was obtained with a feedstock particle size of 38-53μm, which is consistent with the theoretical prediction in Chapter 6.

The adhesion of the plasma sprayed polymer coatings to steel was investigated. It was found that the adhesive strength of the polymer coatings to steel was influenced significantly by the plasma processing conditions. There is an optimum spray distance for the adhesion of polyamide 11 coatings at around 100mm under 20-23kW plasma arc power.

SEM examination on the interface reveals that the contact area between the coating and steel substrate for the coatings produced at shorter and longer than optimal distance is relatively small. Plasma arc power shows influence on the adhesion of the polymer coatings *to steel substrate: low arc power, which gives a small coating-*substrate contact area, results in poor adhesion of the polymer coatings. Plasma gas flow rate also influences the adhesion of the polymer coatings to the steel substrate. The adhesive strength of polyamide coatings drops with increasing gas flow rate. Those influences of processing conditions on the coating adhesion are related to their influences on the extent of the deformation and flow of the particles on impact with substrate as predicted by the theoretical calculation in Chapter 6. In addition, increasing the feedstock powder feed rate drastically reduced the coating adhesion owing to the limited enthalpy of the plasma jet resulting in incomplete particle melting.

Preheating steel substrate up to the melting (softening) temperature of the polymer or above substantially improved the coating adhesion. SEM examination reveals an intimate contact between the coating and substrate. Preheating substrate may also promote the formation of chemical bonds between the coating and substrate.

The steel substrate was pretreated in three ways: Pyrocleaner(chemical cleaning without surface roughening), citric acid(chemical etching) and grit blasting. The results indicate that the rough surfaces produced by grit blasting or etching give superior adhesion to the clean, smooth surface produced by chemical cleaning.

Compared with bulk material, the plasma sprayed polyamide coatings exhibits a lower tensile strength and a brittle stress-strain characteristics. This is caused by the layered structure of the plasma sprayed coating since the microcracks are most likely to generate and propagate along the boundaries of the splats or layers. The defects, such as incomplete melting particles and pores, form the most severe flaws within the coating and are detrimental to the tensile strength of the coating. The coating sprayed at optimal condition displays a appreciable microscopic ductility and gives much higher tensile strength than non-optimal coatings. The tensile strength of polyamide 11 coatings increased with decreasing porosity.

A two stage wear progress(running-in and equilibrium wear) was observed for the sliding wear of plasma sprayed polyamide 11 coatings against a stainless steel ball and the Rockwell diamond stylus. The adhesive wear is a major wear mechanism in polyamide 11 coatings with fracture occurring along the splat boundaries. The presence of pores and microcracks within the coating act as stress concentrators and enhance local damage reducing wear resistance of the coatings. The wear rate increase with increasing porosity of the coatings.

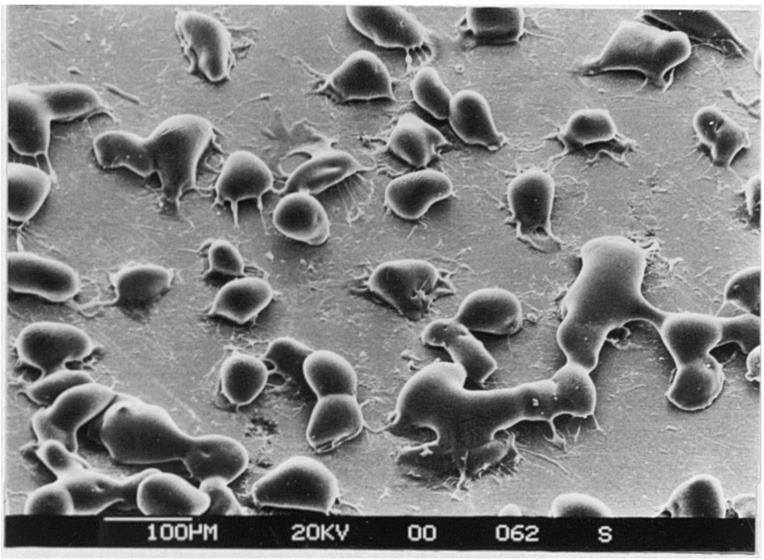

(a)

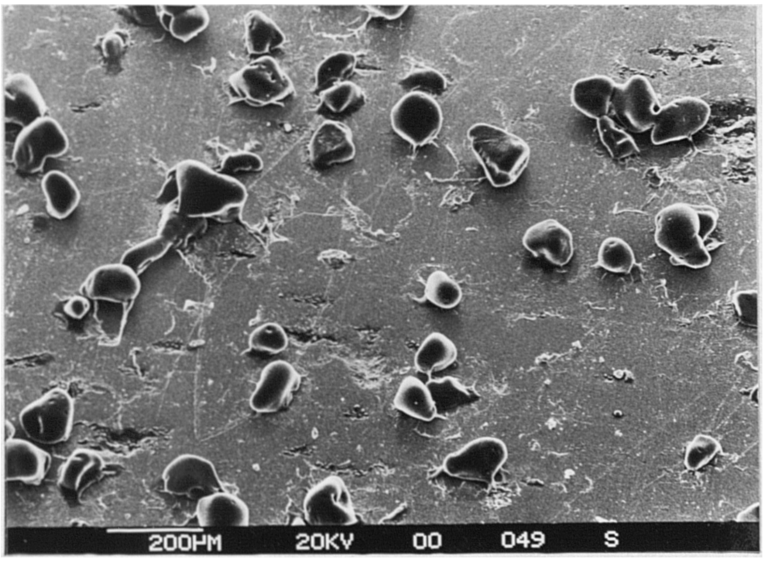

(b)

Figure 7.1 Morphologies of polyamide particles produced in the wipe test: (a) 53-75 μm powder, (b) 90-150 μm powder

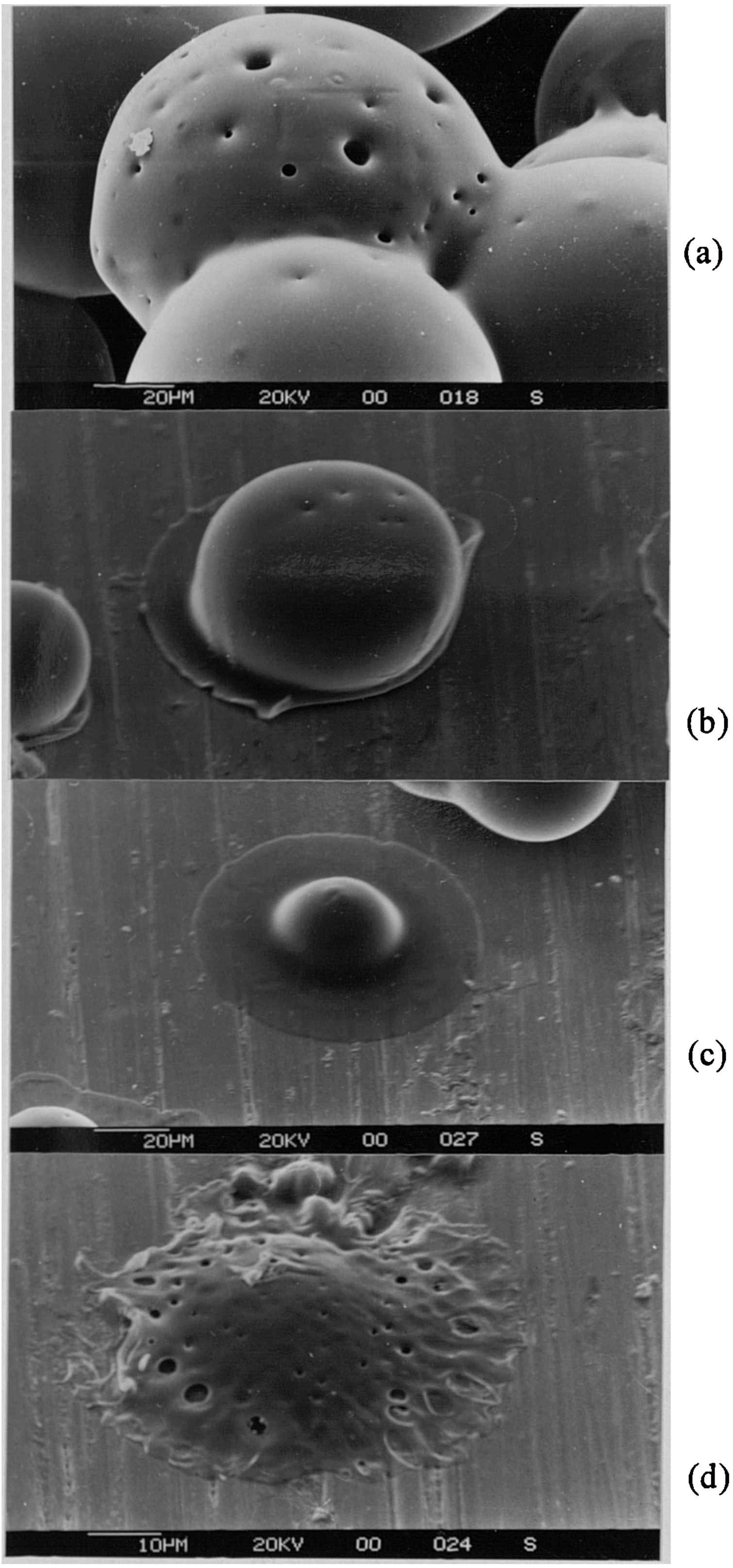

Figure 7.2 Effect of PMMA particle size on particle melting and impact flow in the wipe test.

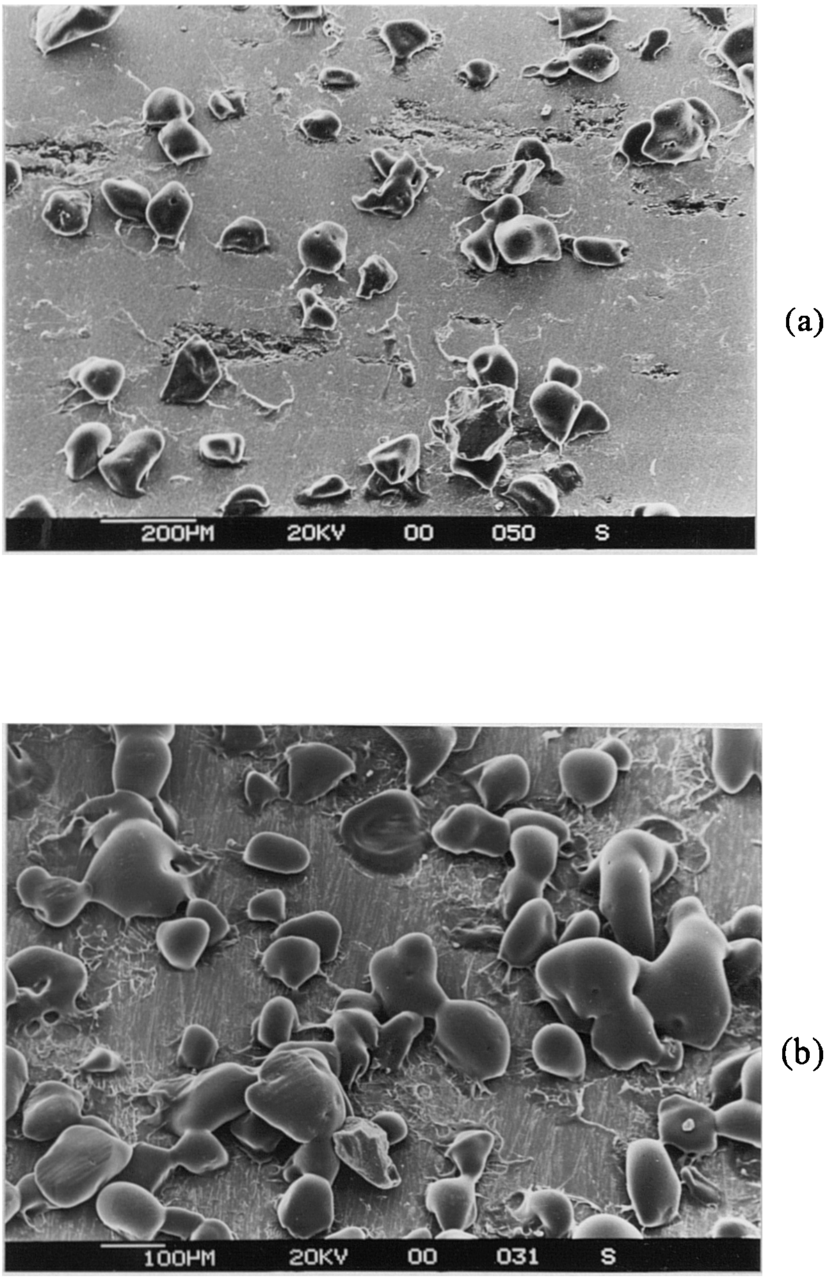

Figure 7.3 Effect of plasma arc power on the melting and impact flow of polyamide particle in the wipe test: (a) 18 kW, (b) 23 kW.

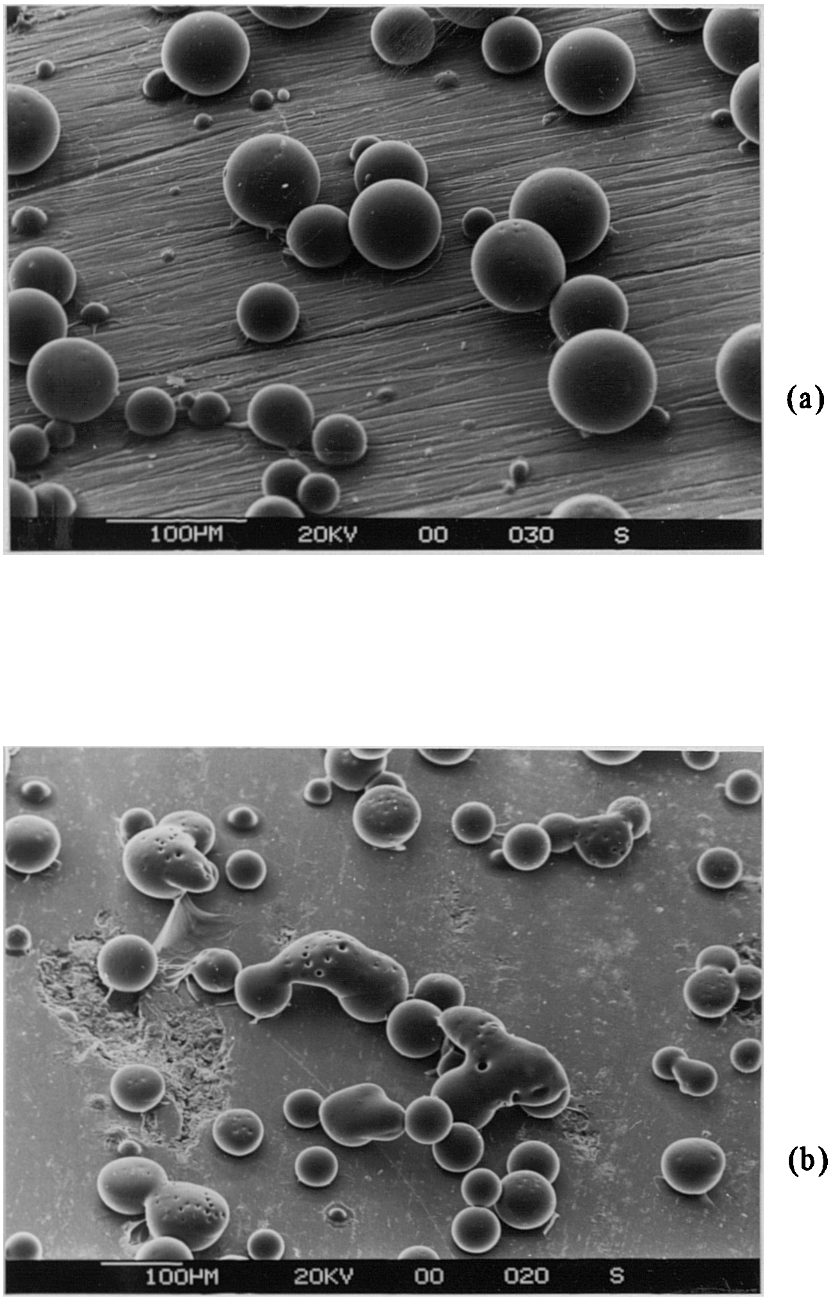

Figure 7.4 Effect of plasma arc power on the morphology of PMMA particles produced in the wipe test: (a) 14 kW, (b) 27 kW.

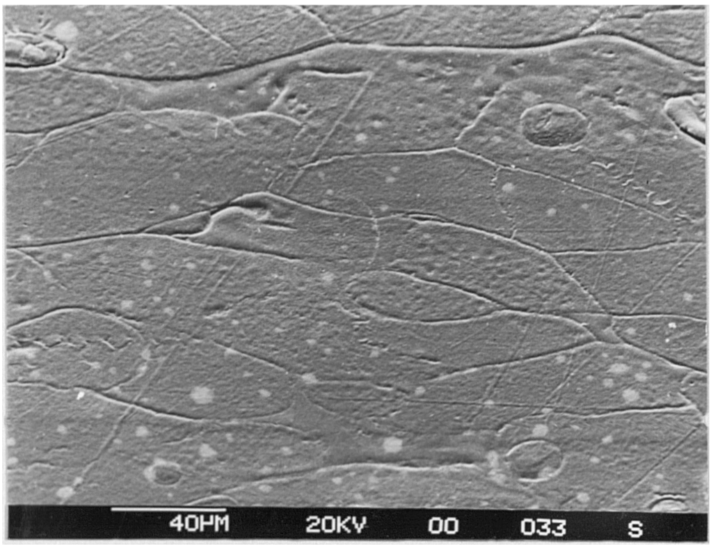

Figure 7.5 SEM micrograph of a polished through-thickness section of polyamide 11 coating.

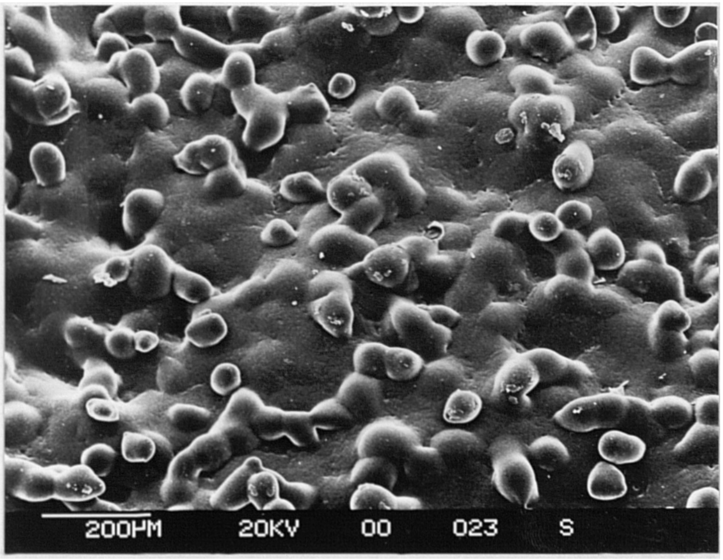

Figure 7.6 SEM micrograph of the top surface parallel to interface of polyamide 11 coating.

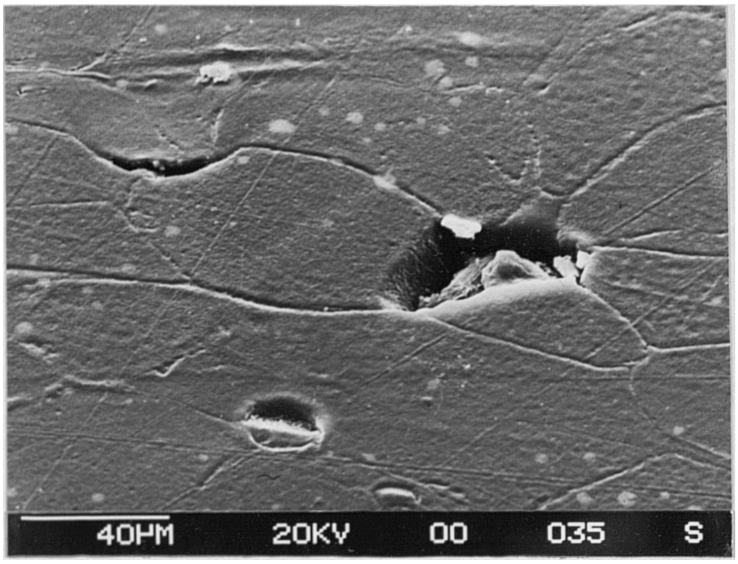

Figure 7.7 SEM micrograph of a polished through-thickness section of polyamide 11 coating, showing a partially melted particle and voids

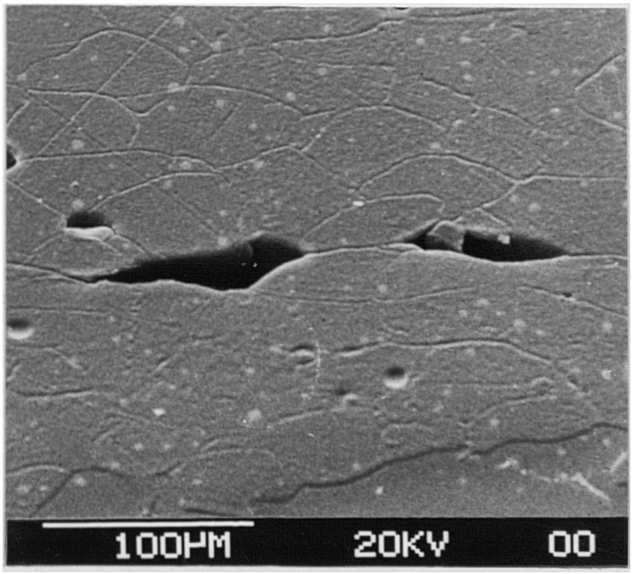

Figure 7.8 SEM micrograph of a polished through-thickness section of polyamide 11 coating, showing gas entrapments between splats.

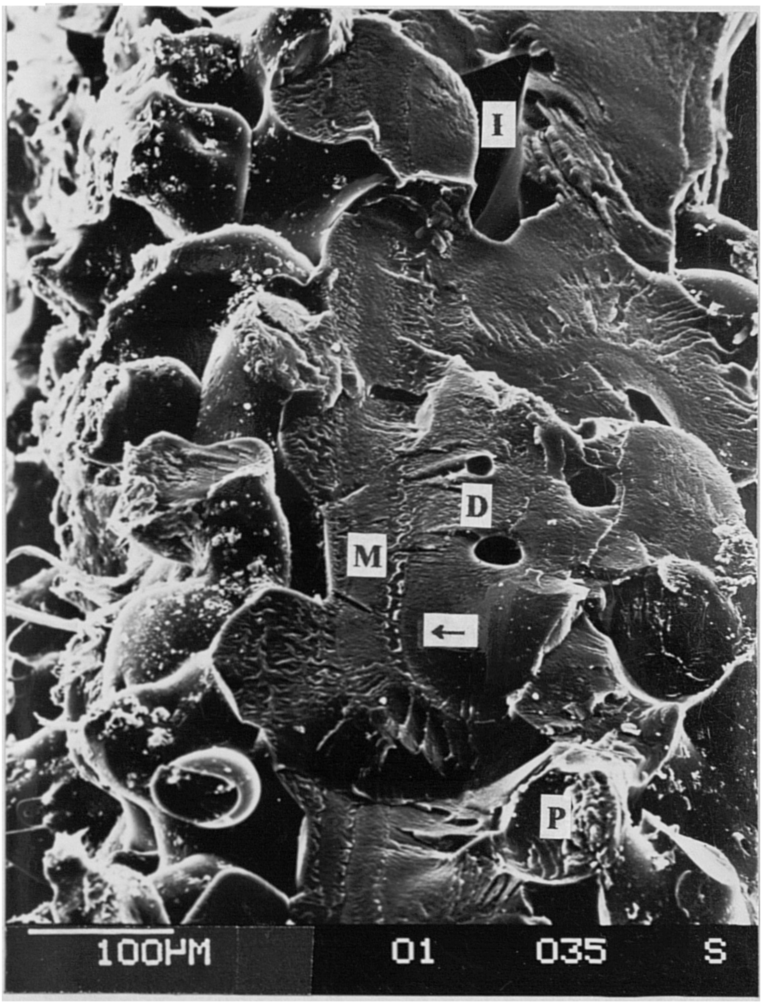

Figure 7.9 SEM micrograph of through-thickness section of polyamide 11 coating produced under sub-optimal arc power (18 kW). P denotes a partially melted particle, M a fully melted particle, I a void from entrapped gas in interstices between particles, D a spherical void in the interior of a melted particle and arrow a boundary of splats.

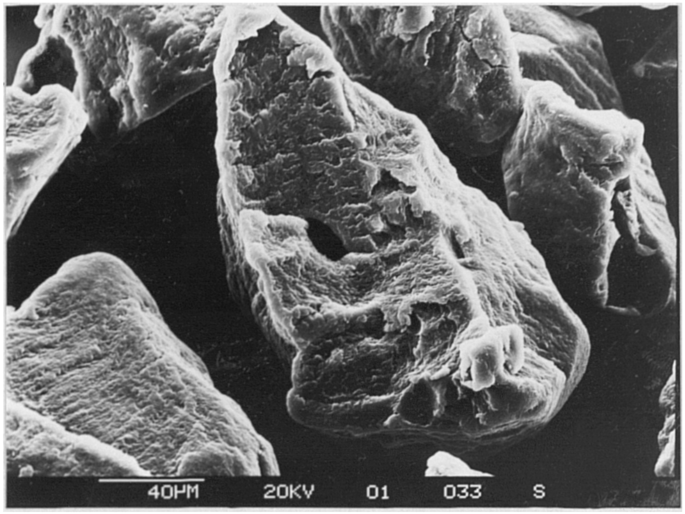

Figure 7.10 SEM micrograph of feedstock particle of polyamide 11 showing pre-existing pores.

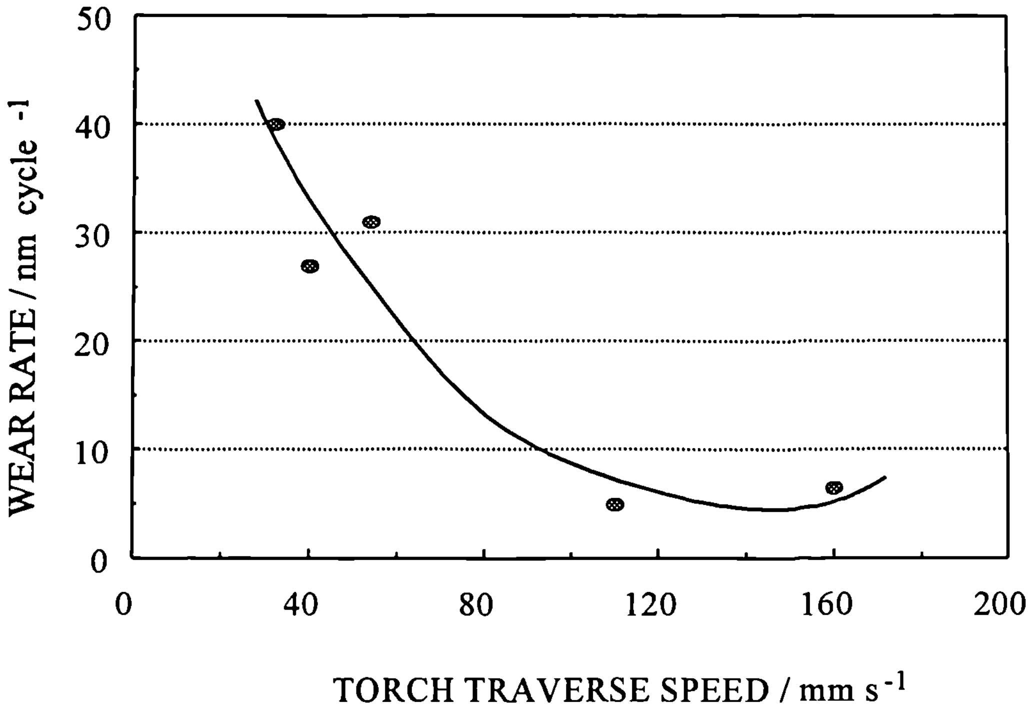

Figure 7.11a Effect of torch traverse speed on wear of polyamide 11 coatings in ball on flat test.

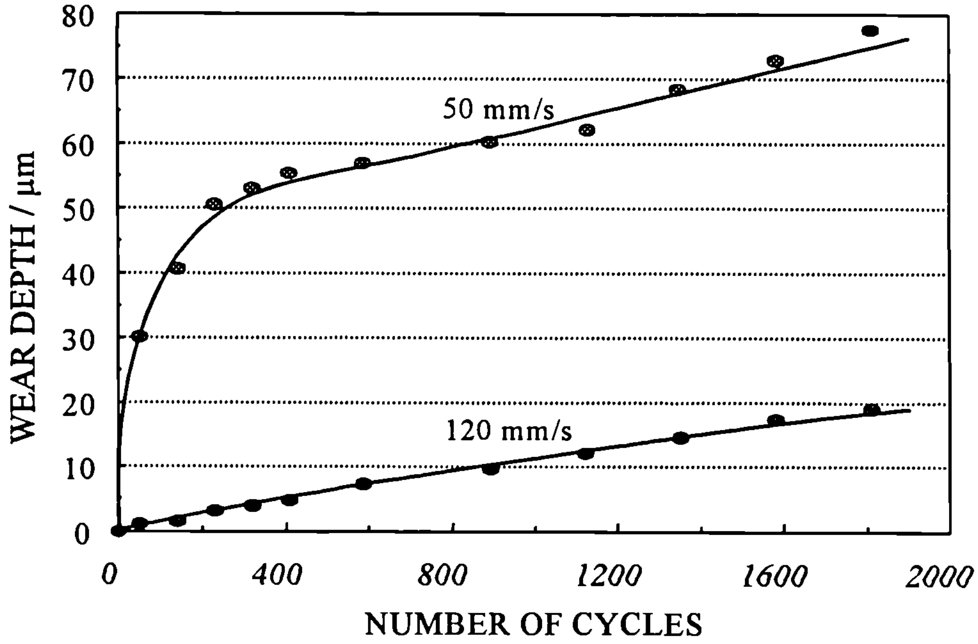

Figure 7.11b Effect of torch traverse speed on the wear of plasma sprayed PMMA coatings (DP300 grade).

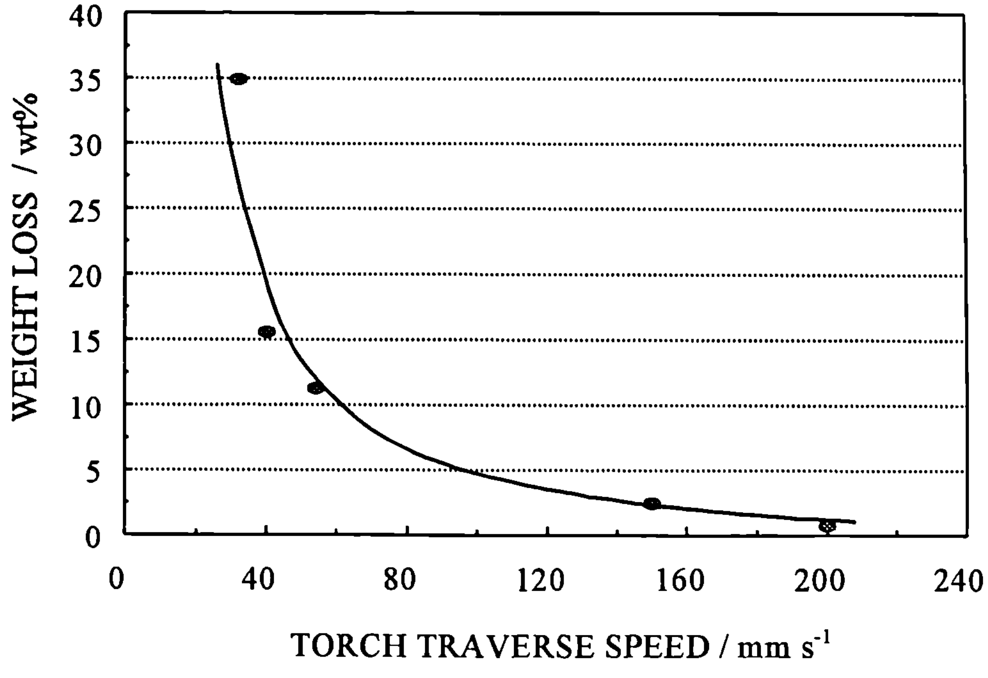

Figure 7.12 Effect of torch traverse speed on weight loss of PMMA (DA100) plasma sprayed coatings.

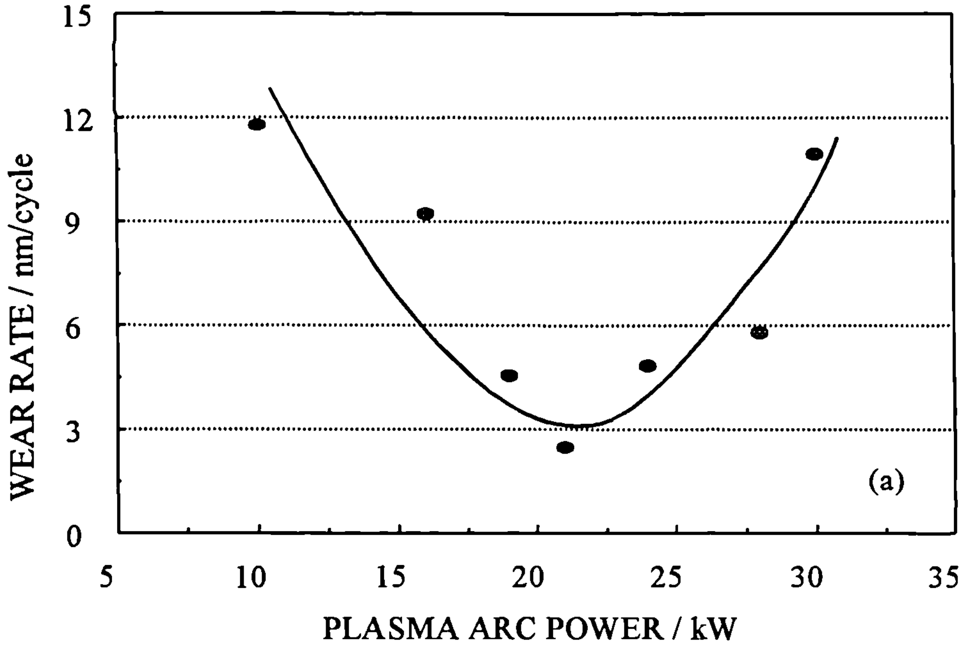

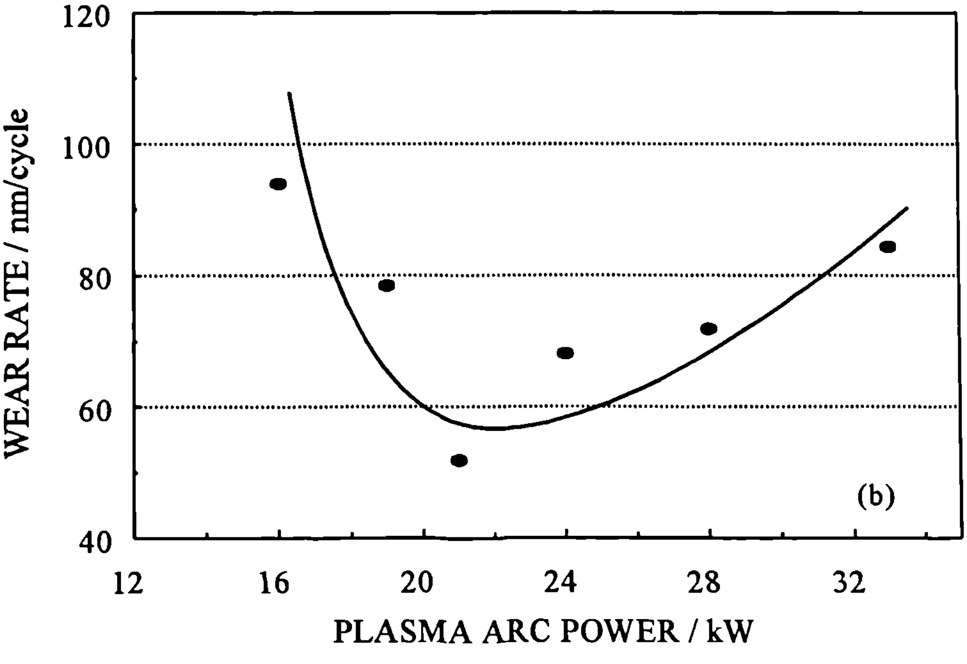

Figure 7.13 Effect of plasma arc power on wear rate of plasma sprayed polyamide 11 coatings: (a) against stainless steel ball; (b) against Rockwell diamond.

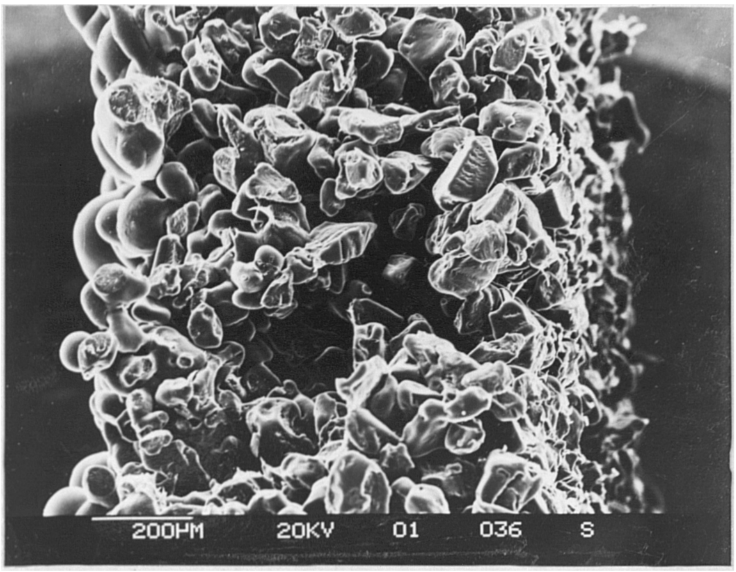

Figure 7.14 SEM micrograph of through-thickness section of polyamide 11 coating produced under low arc power (10 kW).

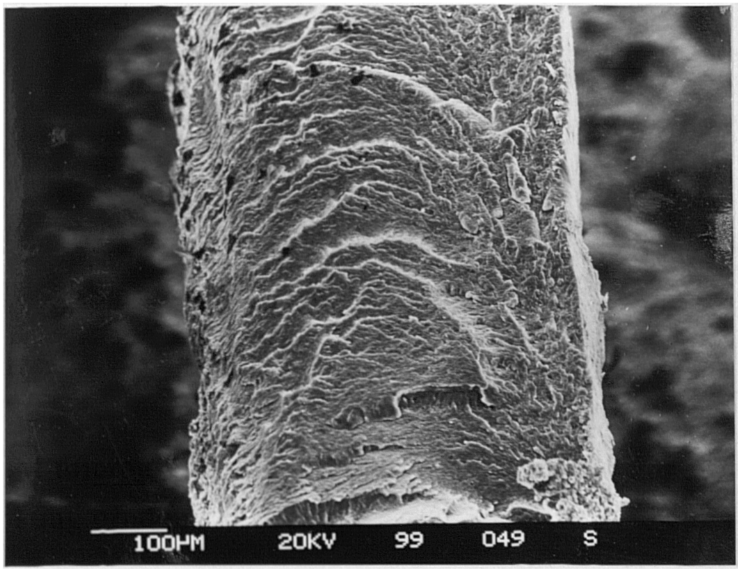

Figure 7.15 SEM micrograph of through-thickness section of polyamide 11 coating produced under optimal arc power (21 kW).

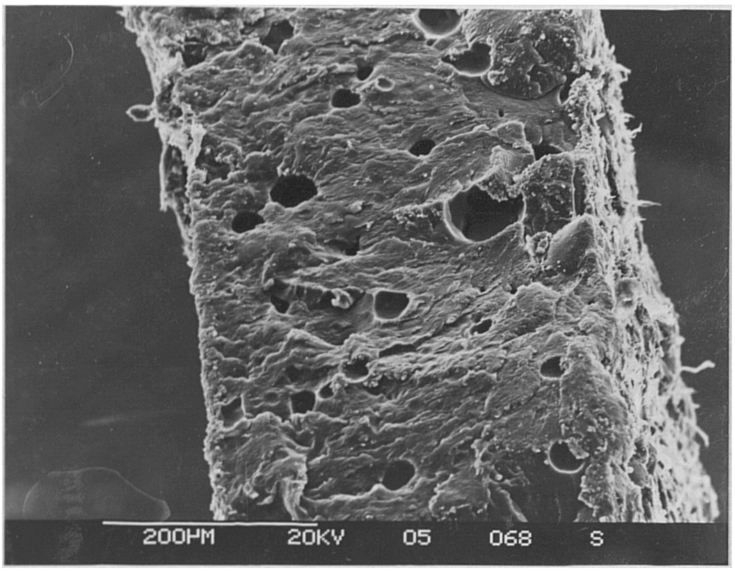

Figure 7.16 SEM microgaph of through-thickness section of polyamide 11 coating produced under high arc power (29 kW).

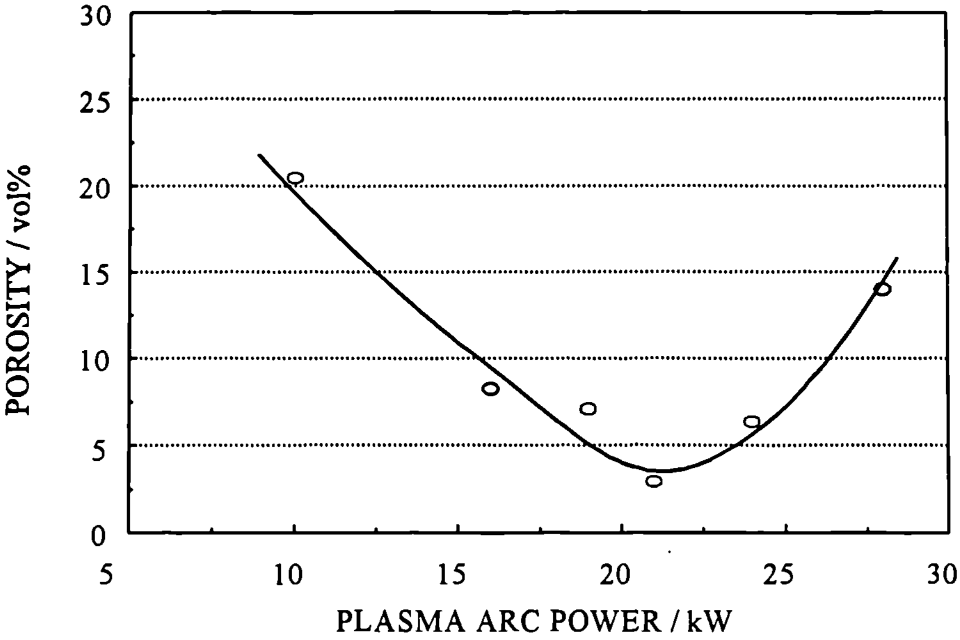

Figure 7.17 Effect of arc power on the porosity of plasma sprayed polyamide 11 coatings.

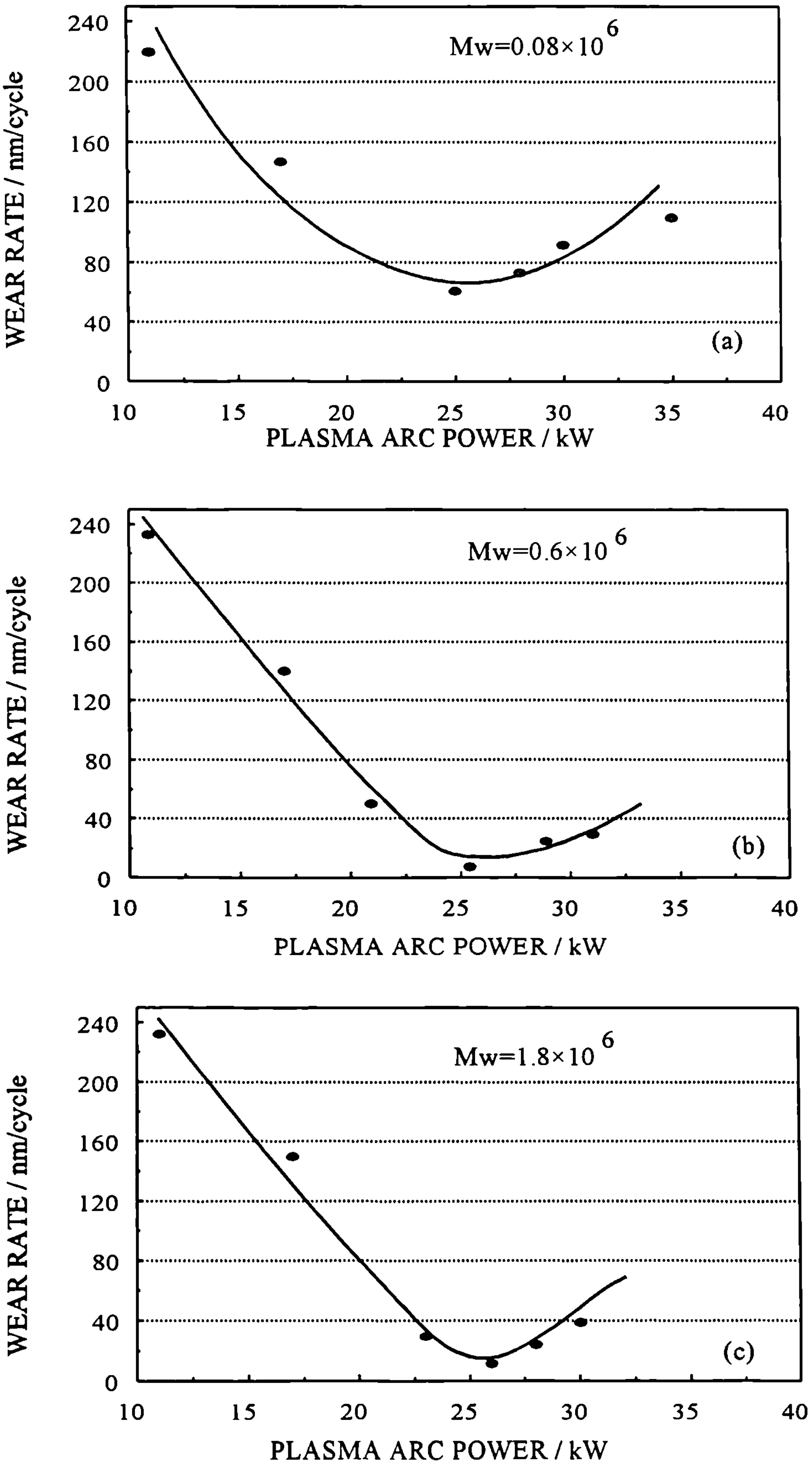

Figure 7.18 Effect of arc power on the wear rate of plasma sprayed PMMA coatings: (a) MG101 grade; (b) DA100 grade; (c) DP300 garde.

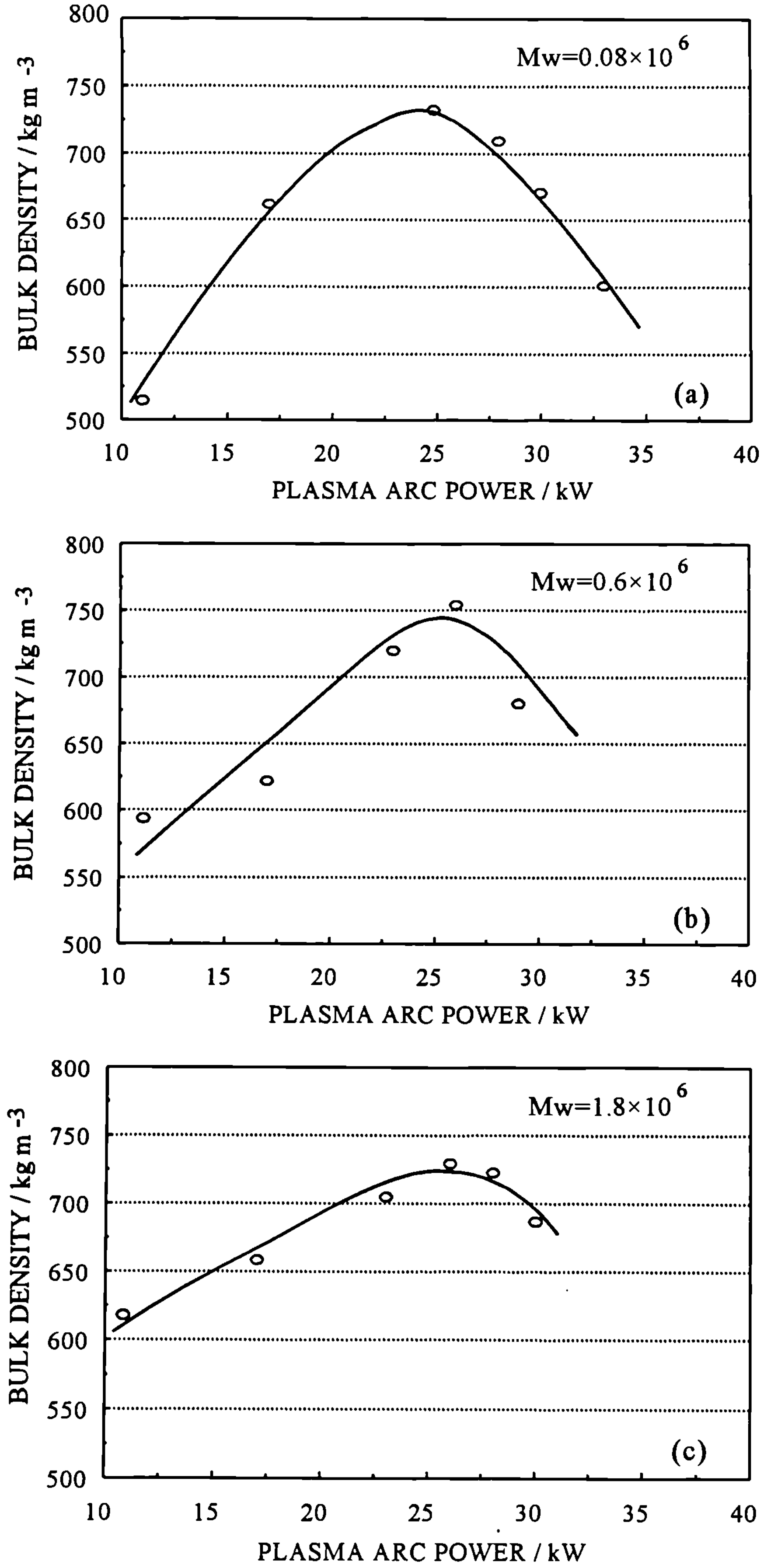

Figure 7.19 Effect of arc power on the density of plasma sprayed PMMA coatings: (a) MG101 grade; (b) DA100 grade; (c) DP300 grade.

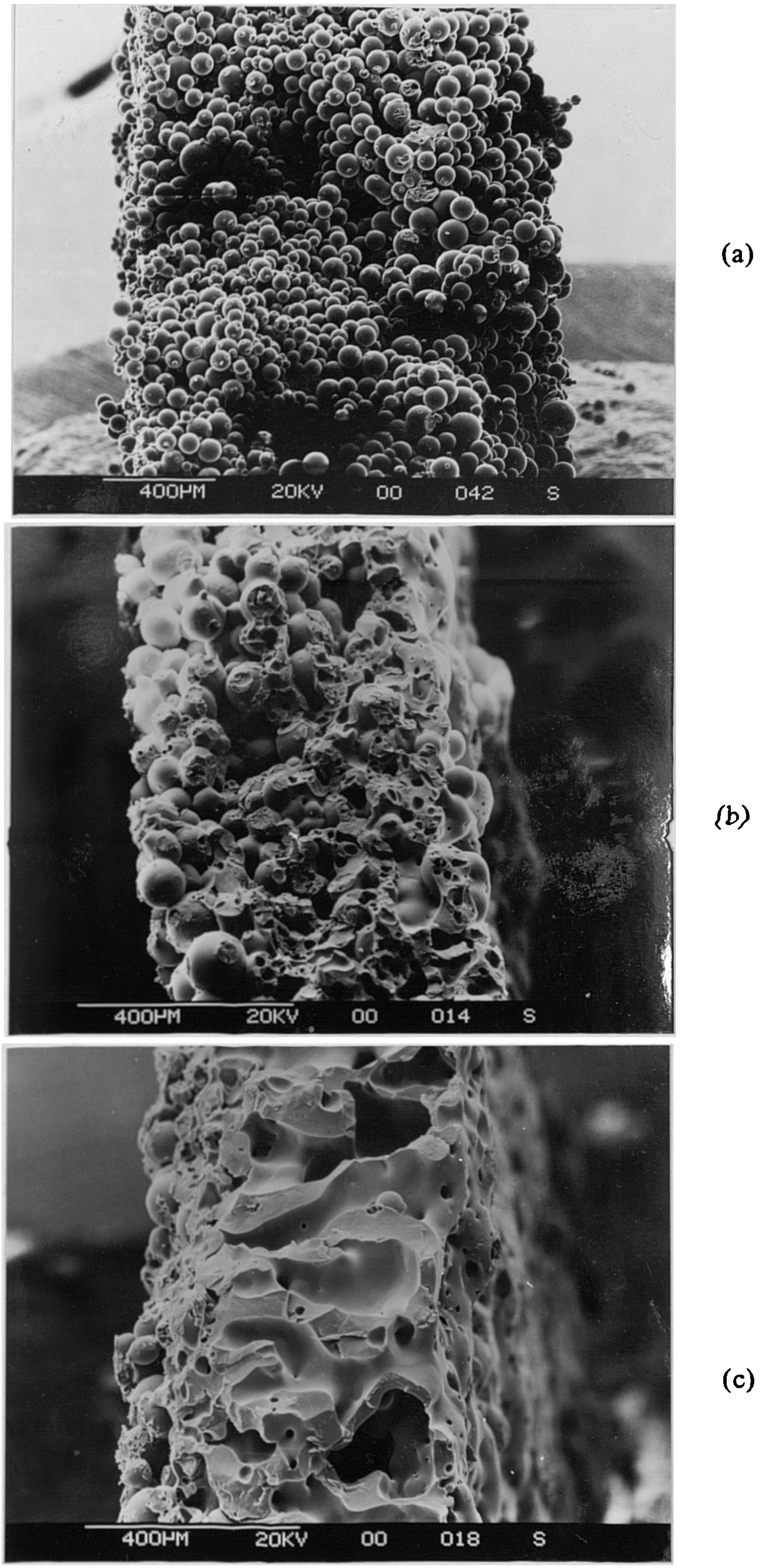

Figure 7.20 SEM micrographs of through-thickness section of plasma sprayed PMMA coatings(DA100) produced at: (a) 11kW; (b) 21kW; (c) 35kW.

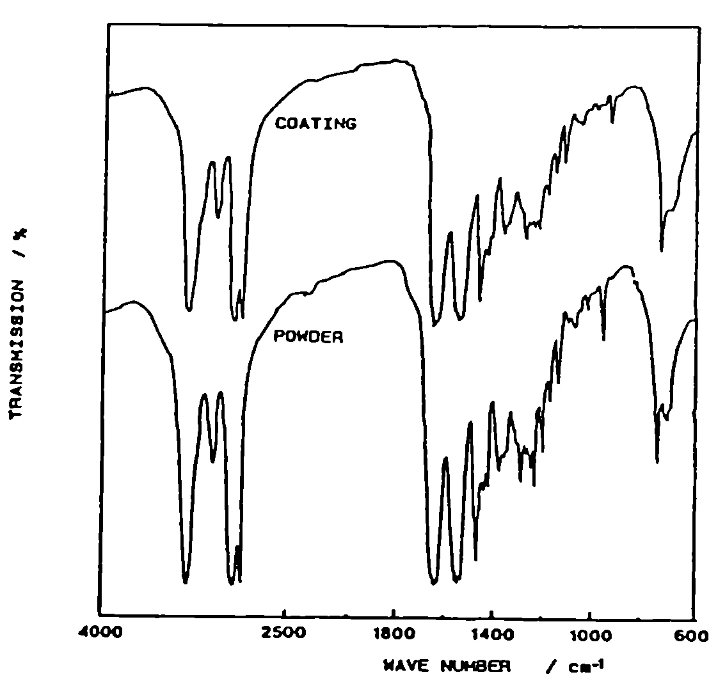

Figure 7. 21 Infrared spectra of polyamide 11 powder and coating

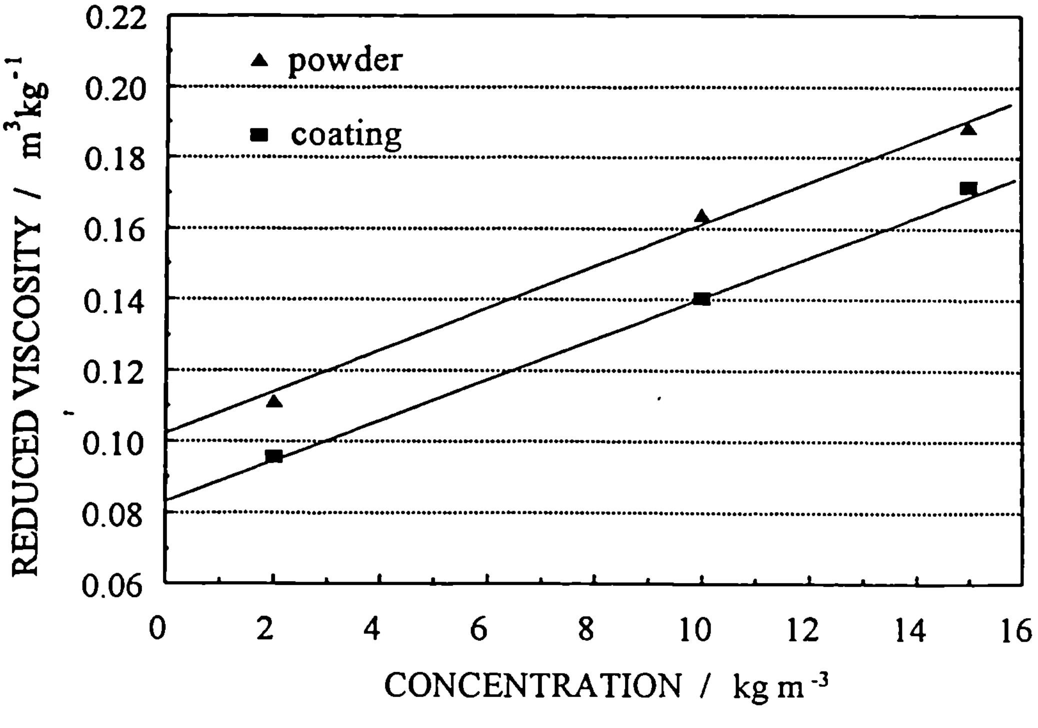

Figure 7.22 Reduced viscosity of polyamide 11 powder and coating.

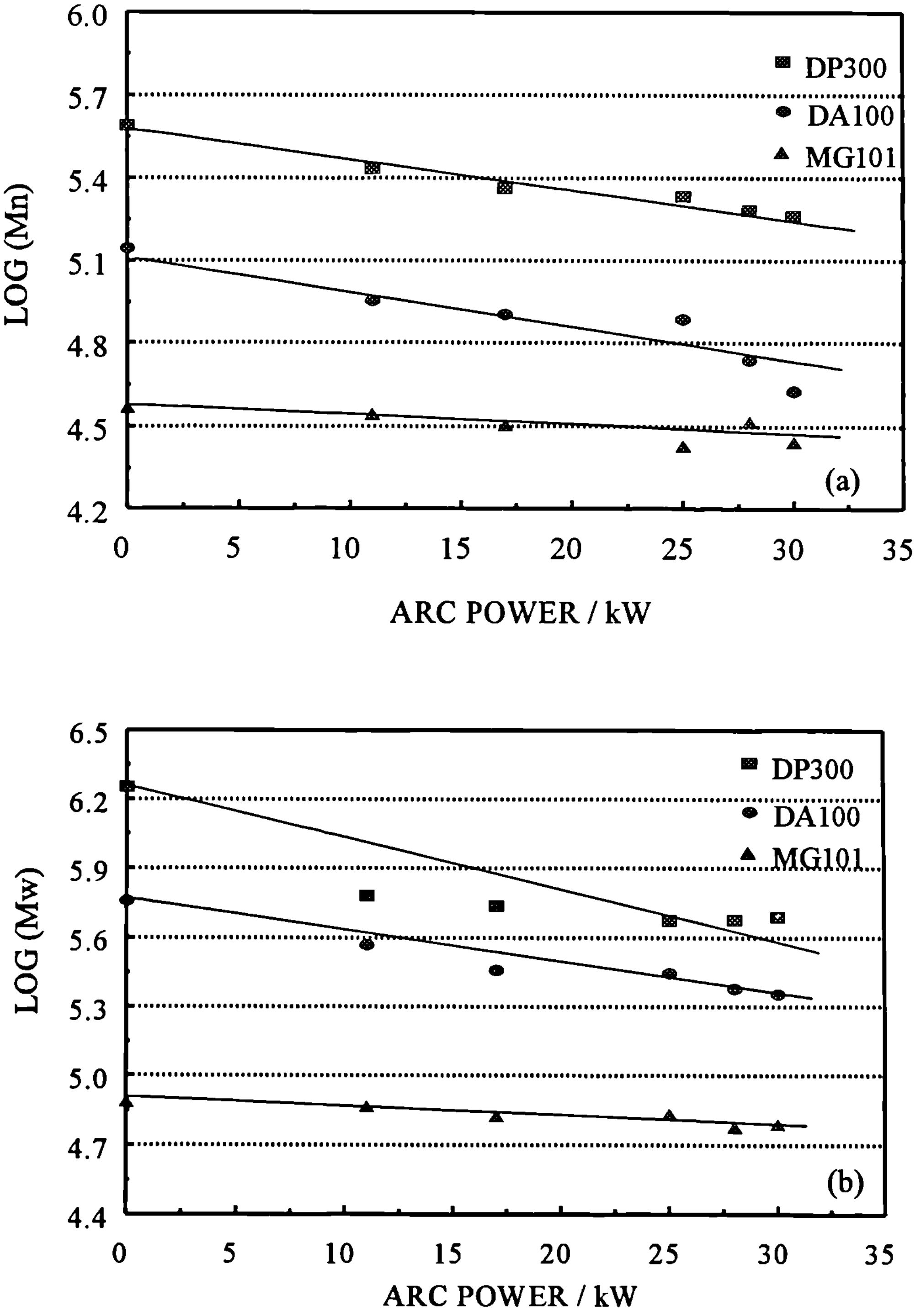

Figure 7.23 Effect of arc power on the molecular weight of PMMA grades: (a) number average molecular weight, (b) weight average molecular weight

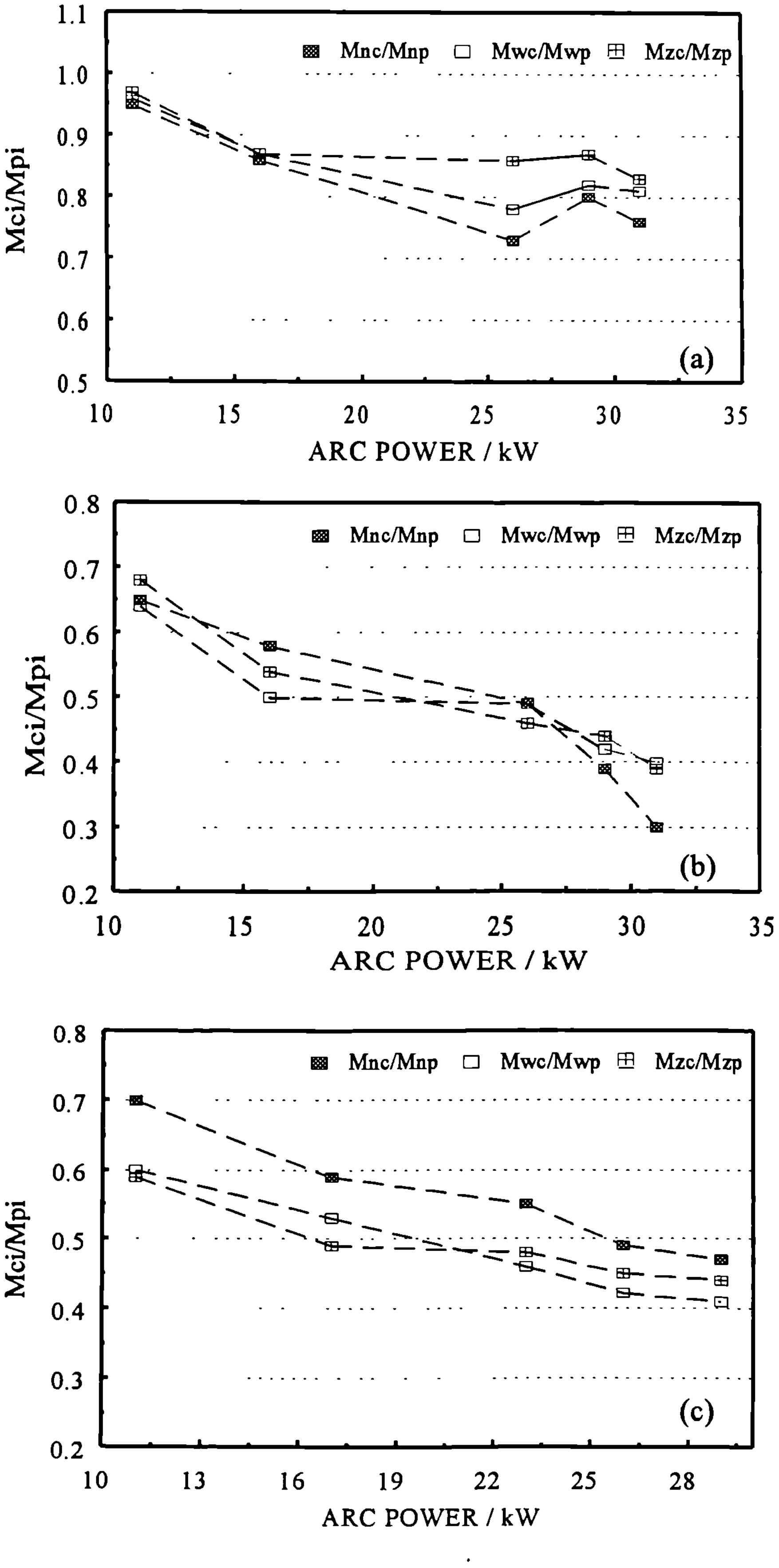

Figure 7.24 Effect of plasma arc power on the ratio of molecular weight of the coating to that of the feedstock powder for PMMA grades: (a) MG101, (b) DA100, (c) DP300.

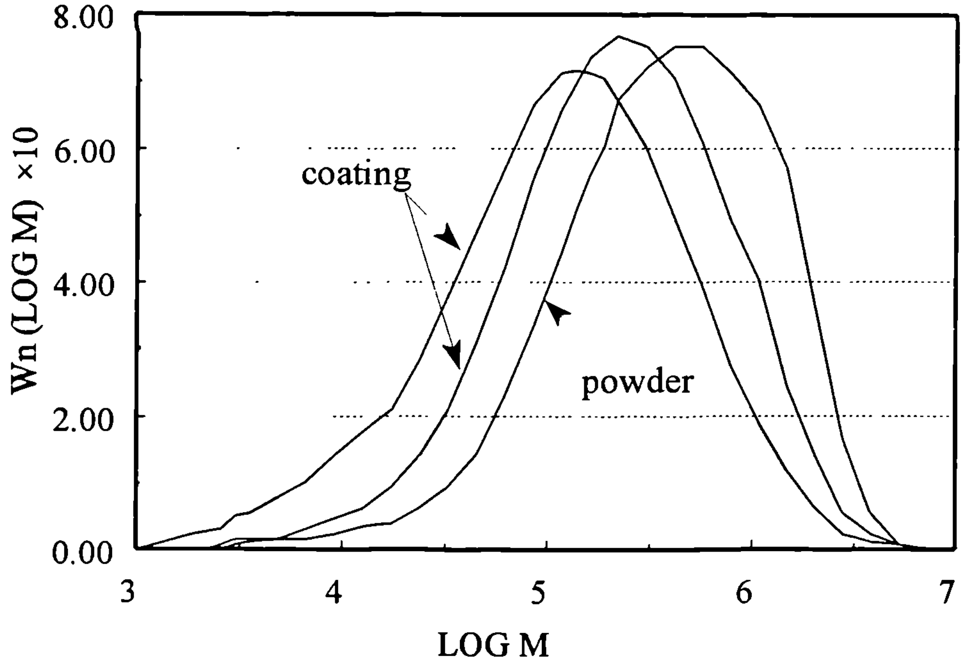

Figure 7.25 Effect of plasma spraying on the molecular weight distribution of PMMA (DA100 grade). Curves given for the feed powder and coating sprayed at 21 kW and 35 kW arc power

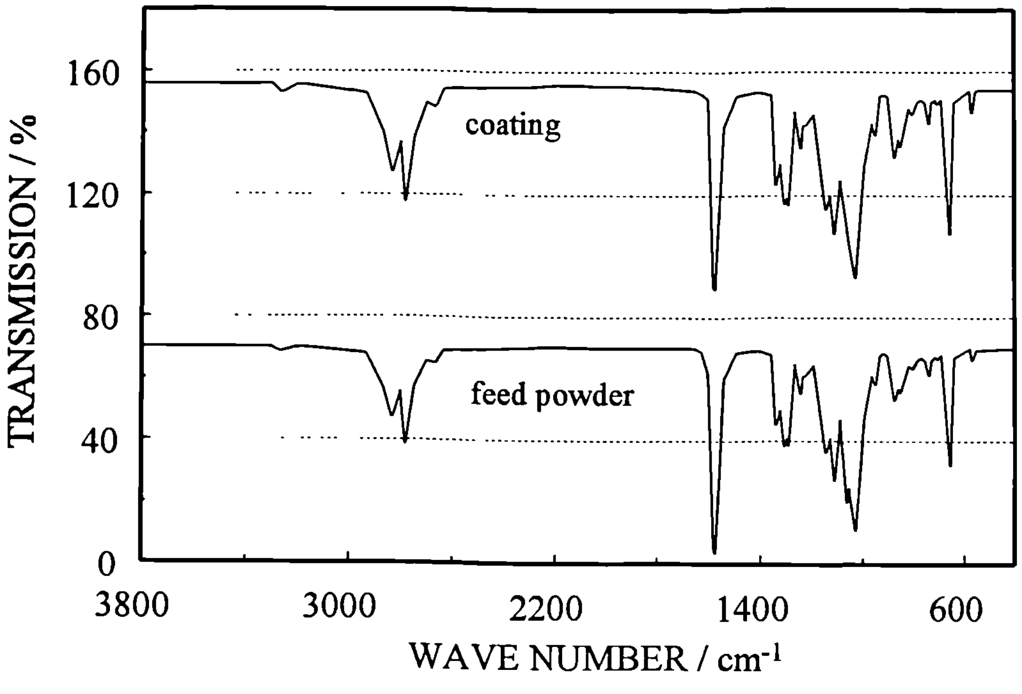

Figure 7.26a Infrared spectra of PMMA (MG101 grade) feed powder and coating

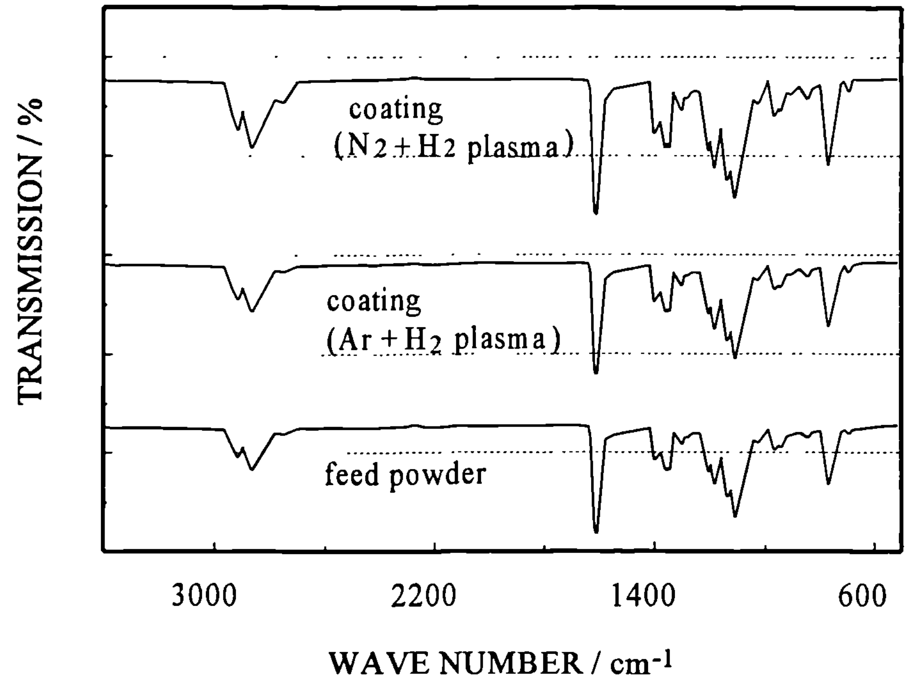

Figure 7.26b Infrared spectra of PMMA (DA100 grade) feed powder and coatings

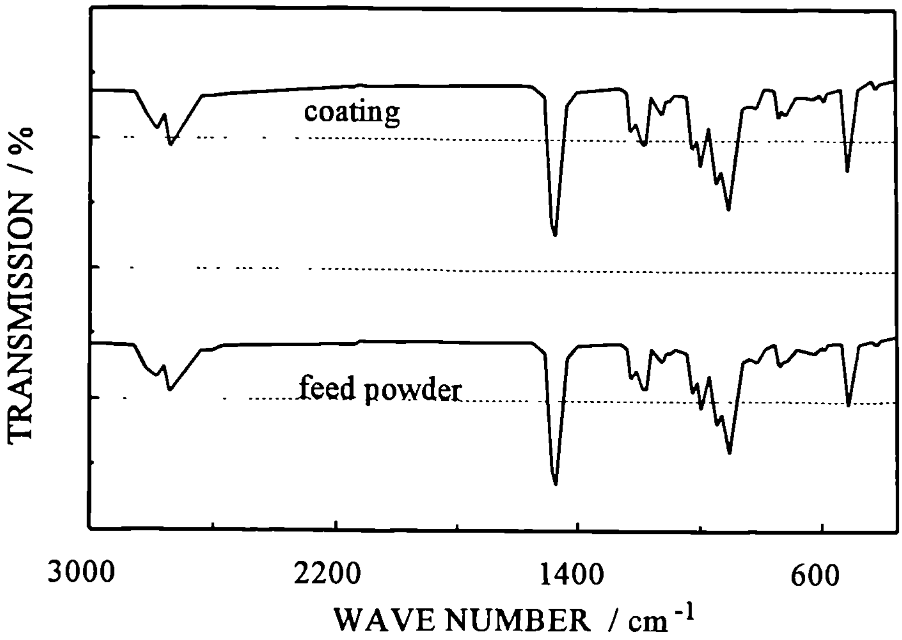

Figure 7.26c Infrared spectra of PMMA (DP300 grade) feed powder and coatings

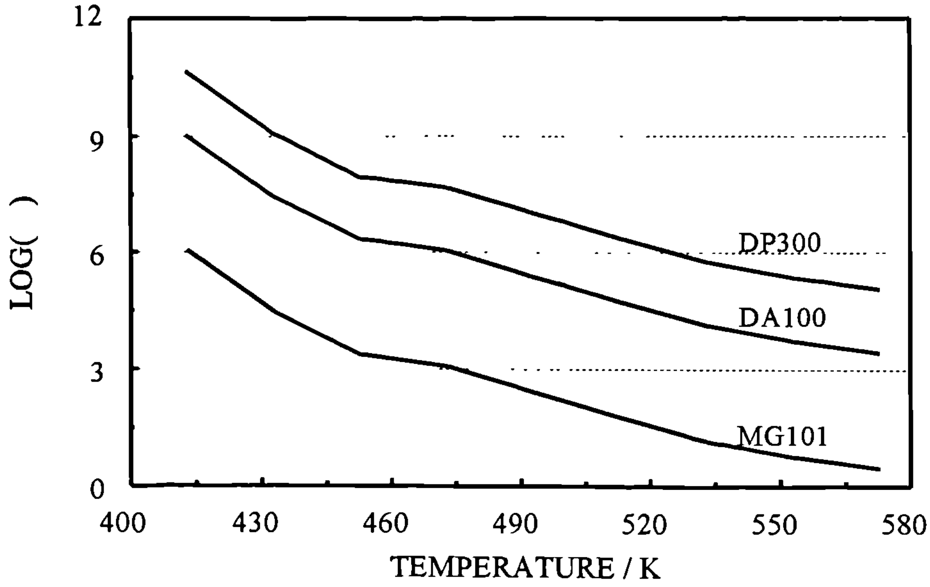

Figure 7.27 Calculated melt viscosity of PMMA feedstock powders

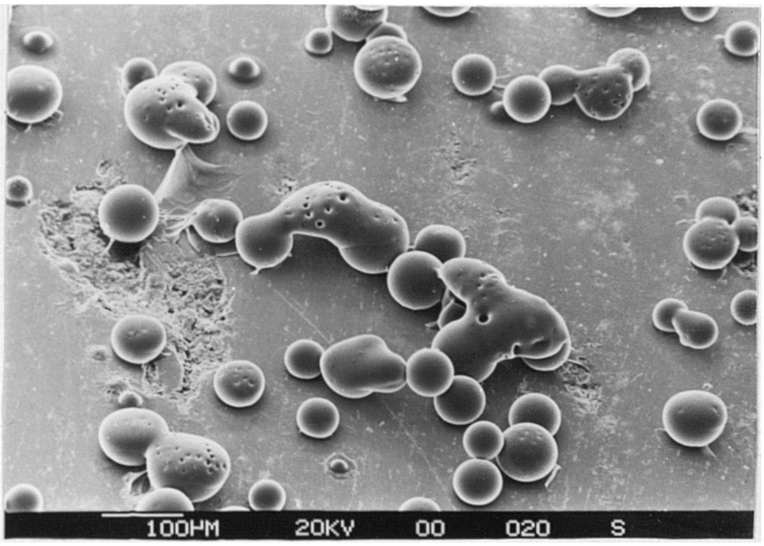

Figure 7.28a Morphologies of PMMA (DA100 grade) particles produced in the wipe test.

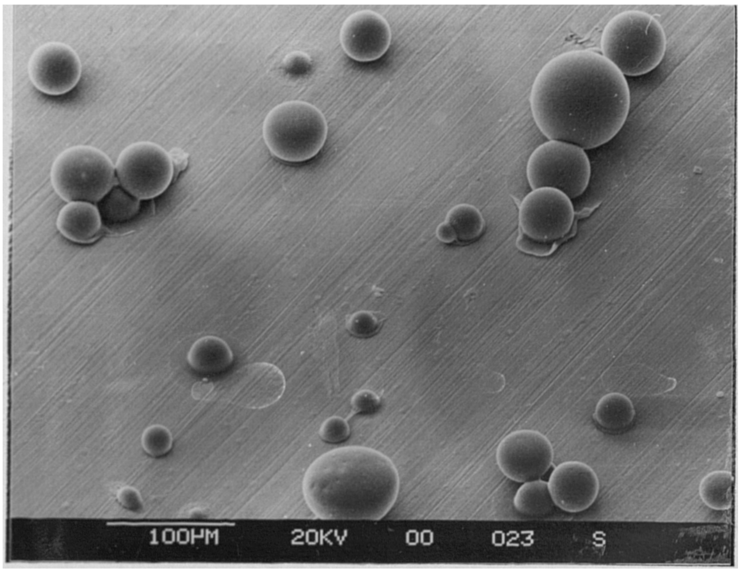

Figure 7.28b Morphologies of PMMA (DP300 grade) particles produced in the wipe test.

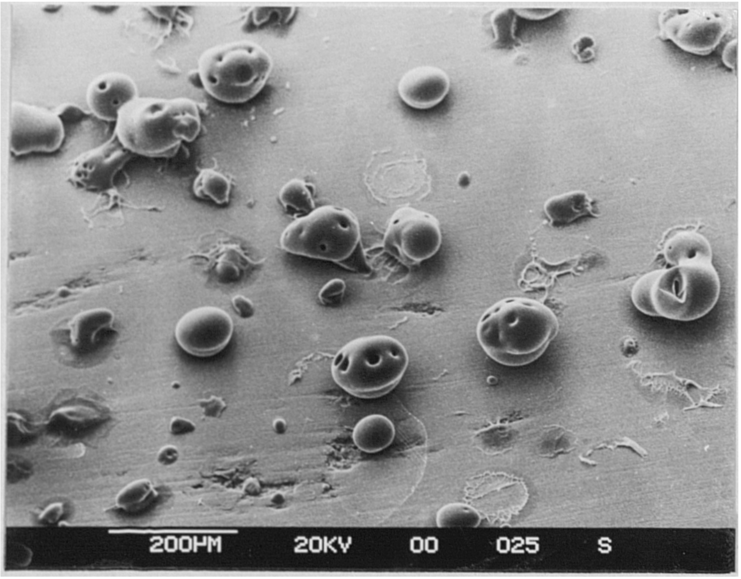

Figure 7.28c Morphologies of PMMA (MG101 grade) particles produced in the wipe test.

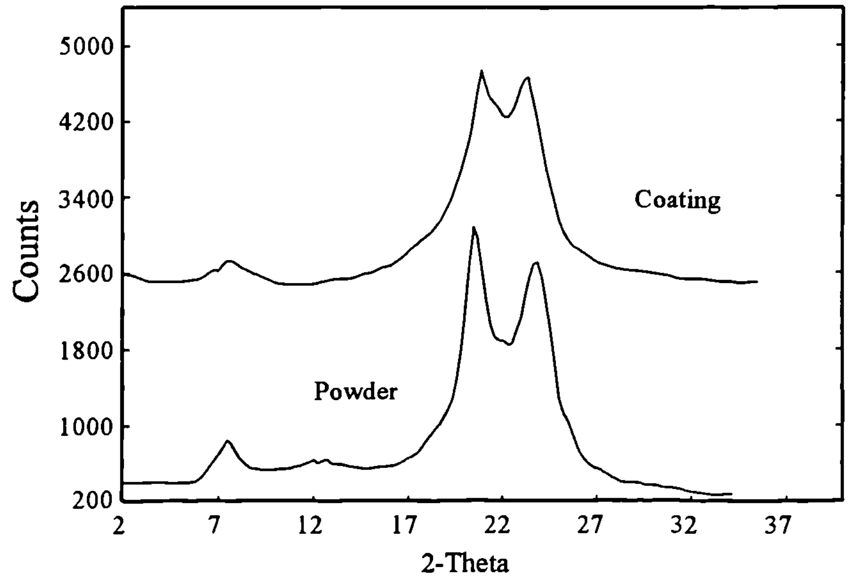

Figure 7.29 X-ray diffractometer traces for polyamide 11 feedstock powder and coating.

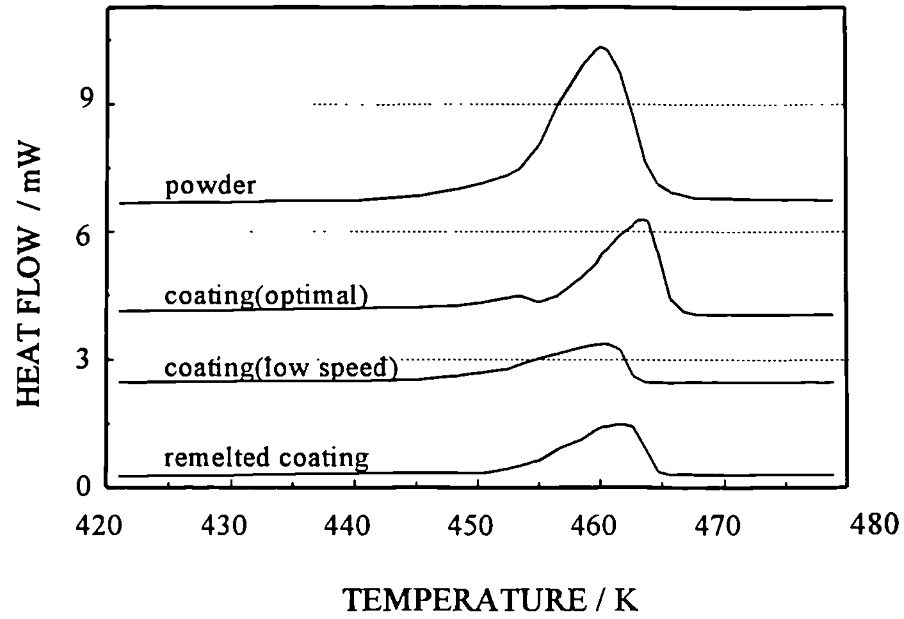

Figure 7.30 Differential scanning calorimetry traces for polyamide 11 coatings and feedstock powder.

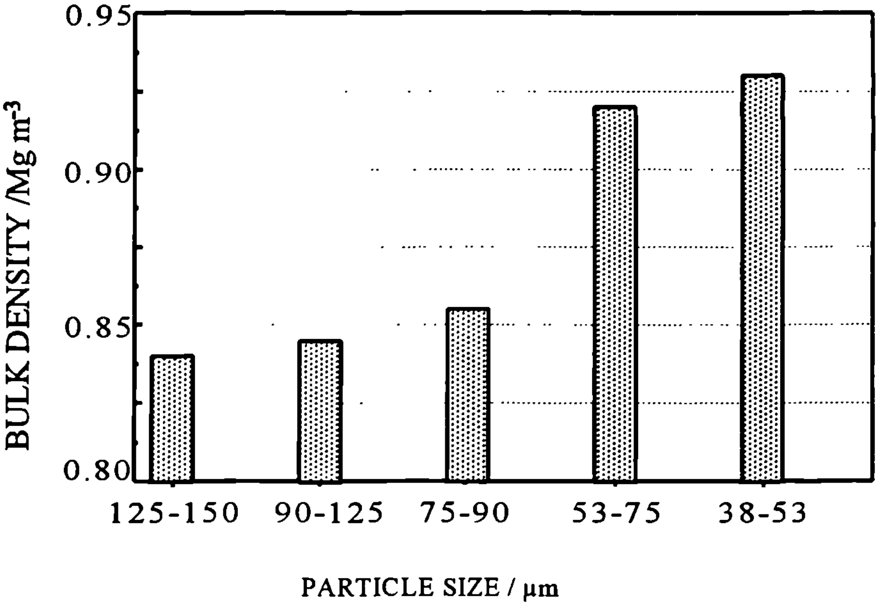

Figure 7.31 Influence of particle size of feedstock powders on the density of polyamide 11 coatings.

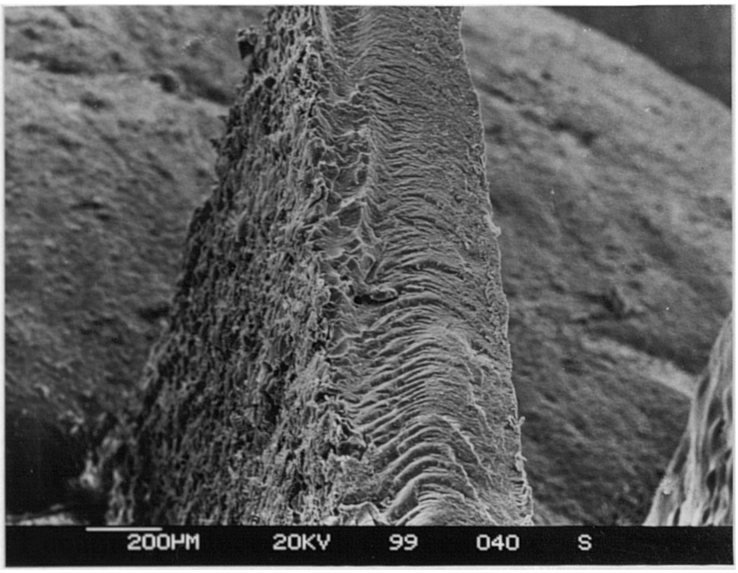

Figure 7.32a SEM micrograph of through-thickness section of polyamide 11 coating produced with the feedstock powder of 38-53μm.

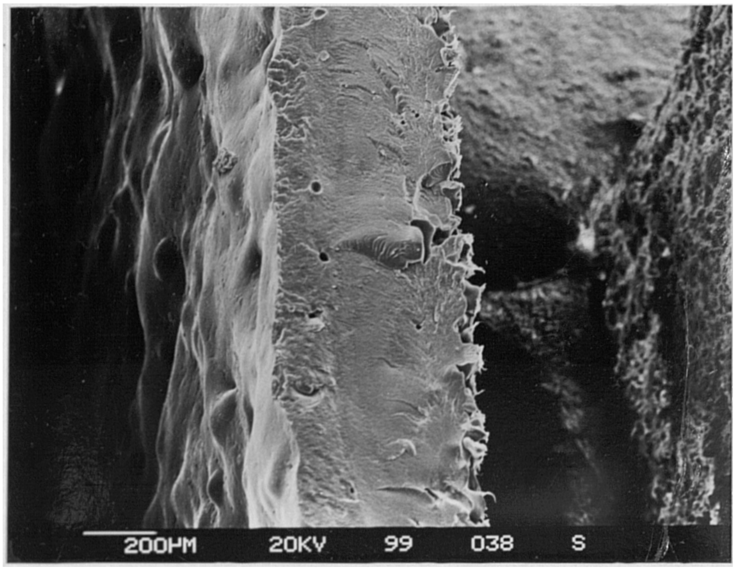

Figure 7.32b SEM micrograph of through-thickness section of polyamide 11 coating produced with the feedstock powder of 53-75μm.

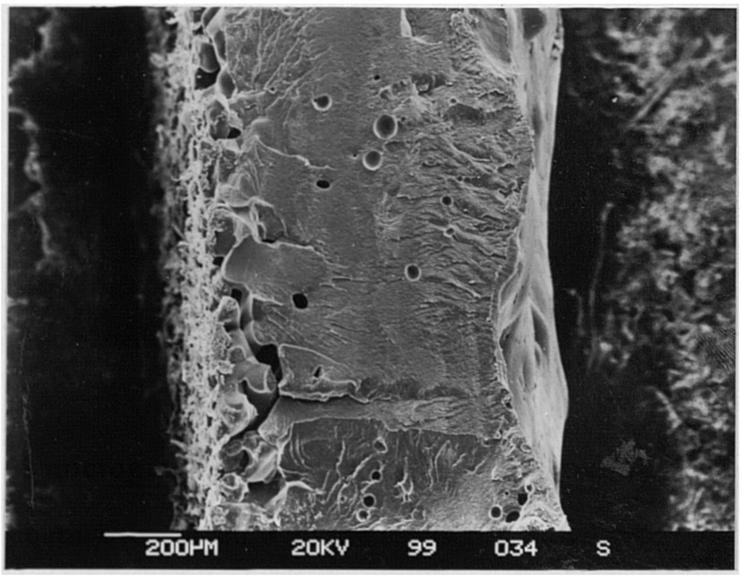

Figure 7.32c SEM micrograph of through-thickness section of polyamide 11 coating produced with the feedstock powder of 90-125μm.

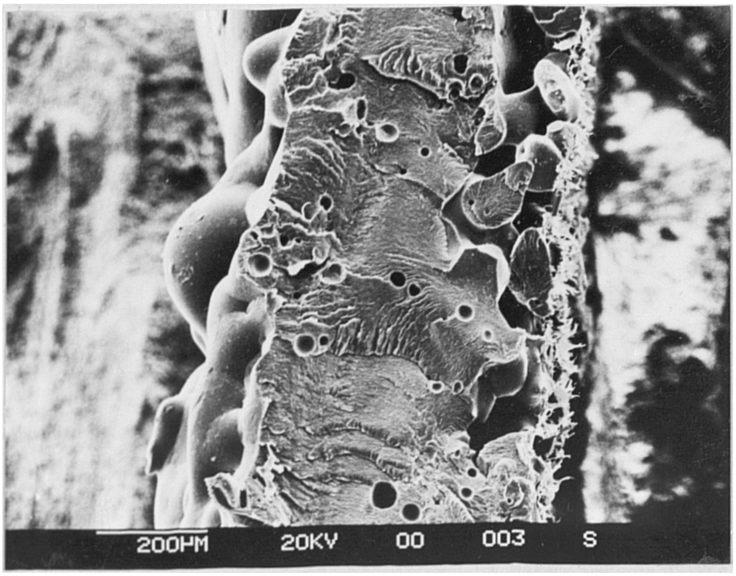

Figure 7.32d SEM micrograph of through-thickness section of polyamide 11 coating produced with the feedstock powder of 125-150μm.

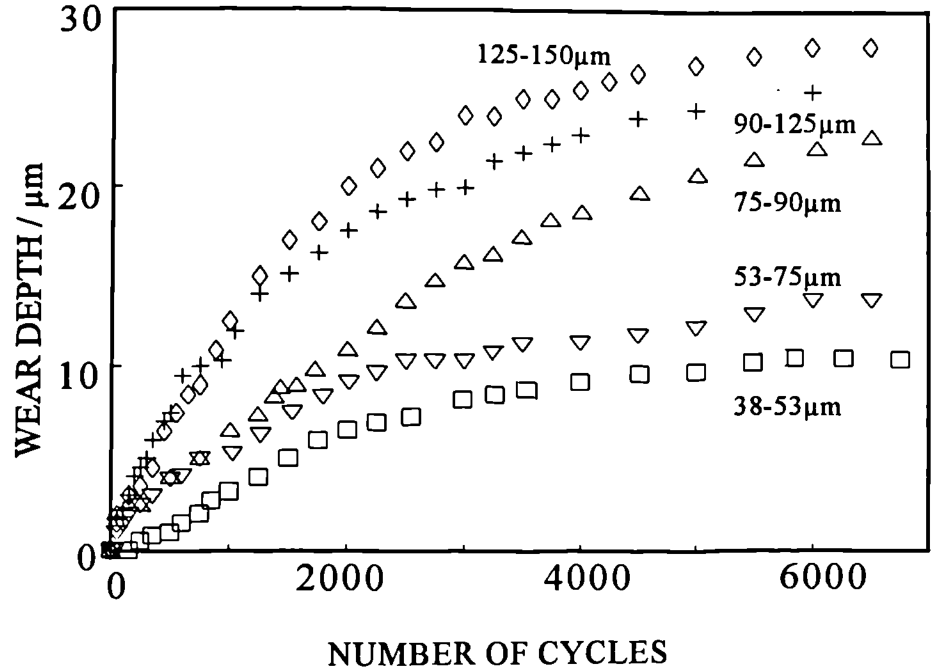

Figure 7.33 Effect of particle size of feedstock powders on the wear of polyamide 11 coatings

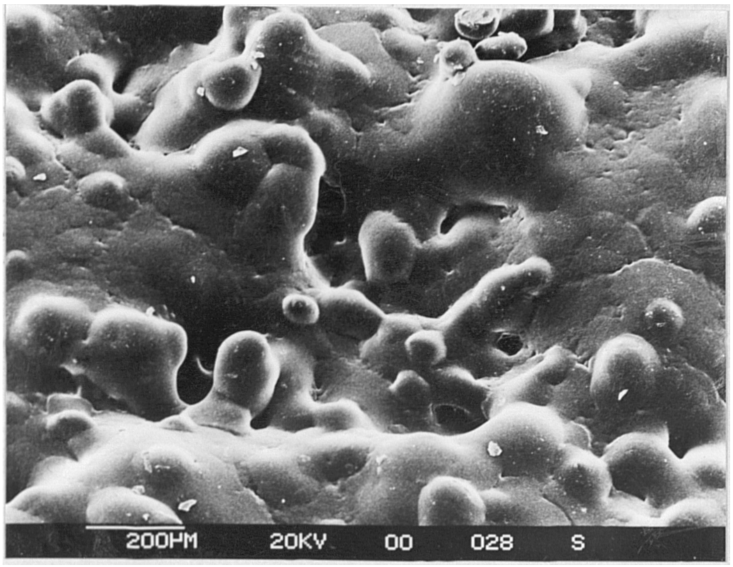

Figure 7.34a SEM micrograph of the top surface of polyamide 11 coating sprayed with 90-125 µm feedstock powder

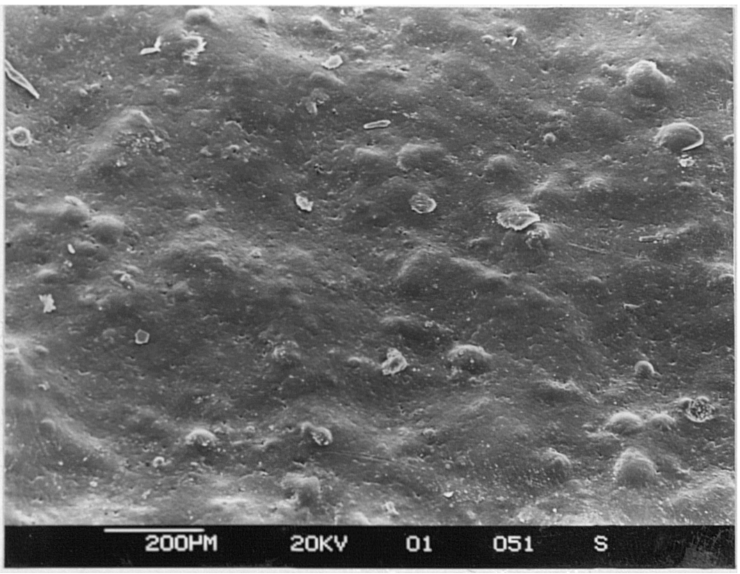

Figure 7.34b SEM micrograph of the top surface of polyamide 11 coating sprayed with 38-53 µm feedstock powder

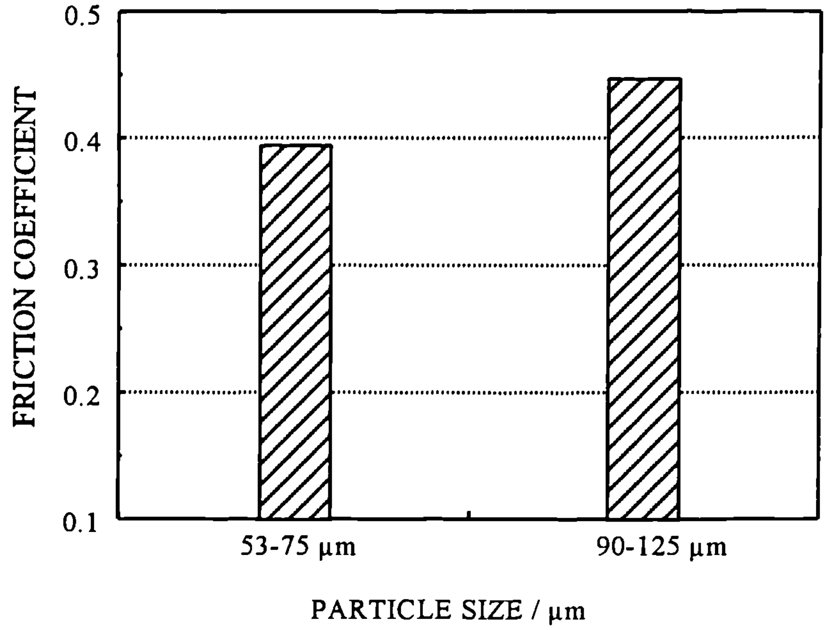

Figure 7.35 Influence of particle size on the friction coefficient of polyamide 11 coatings.

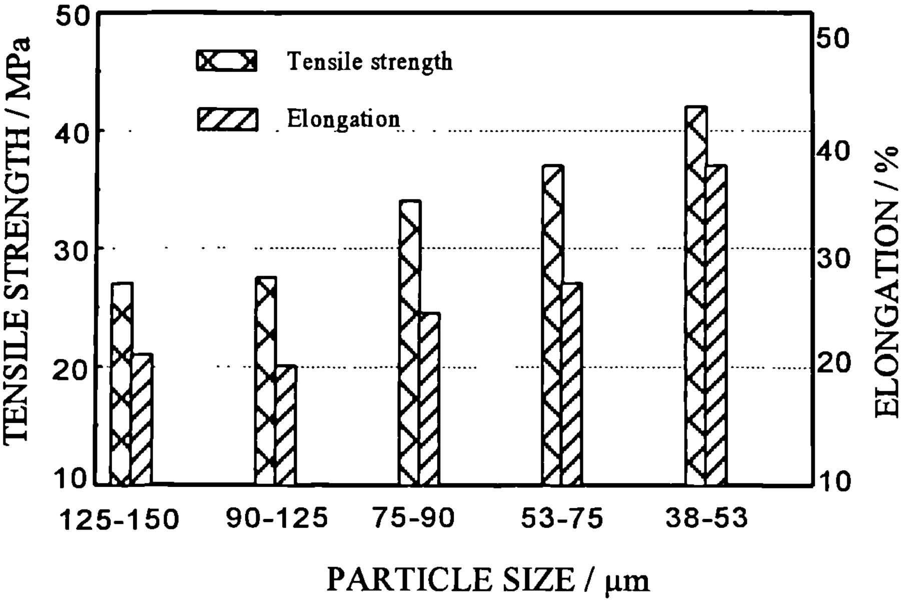

Figure 7.36 Effect of particle size of feedstock powders on the tensile strength and elongation of plasma-sprayed polyamide 11 coatings.

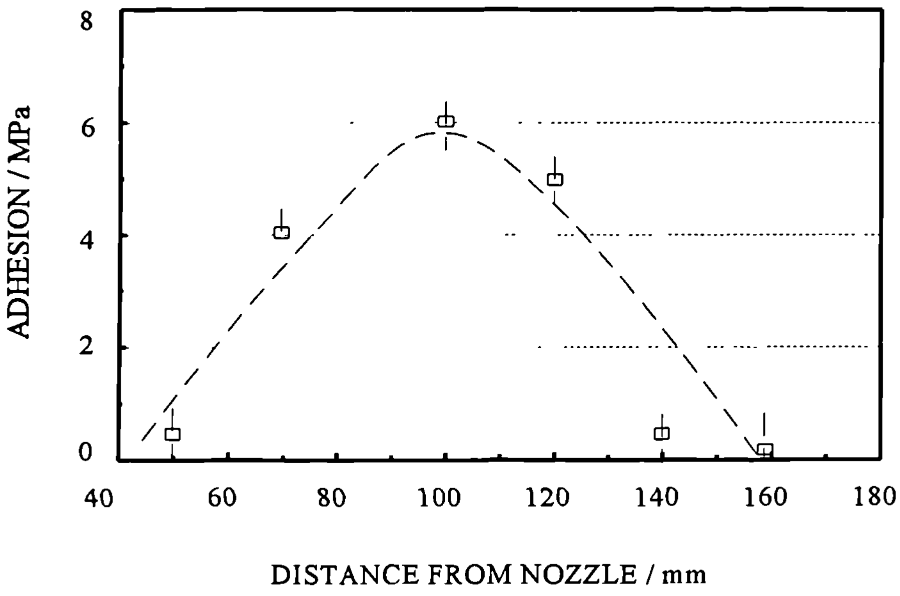

Figure 7.37 Influence of plasma spray distance on the adhesion of polyamide 11 coatings

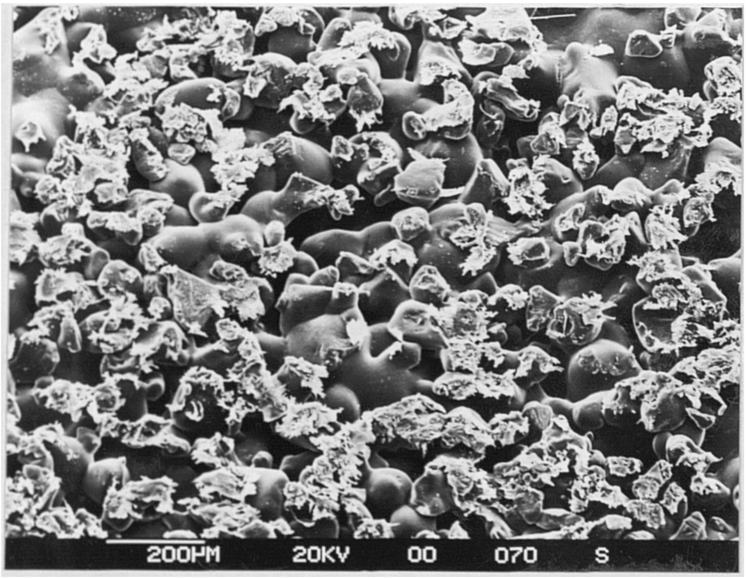

Figure 7.38 SEM micrograph showing adhesion failure of polyamide 11 coating (1MPa tensile adhesive strength)

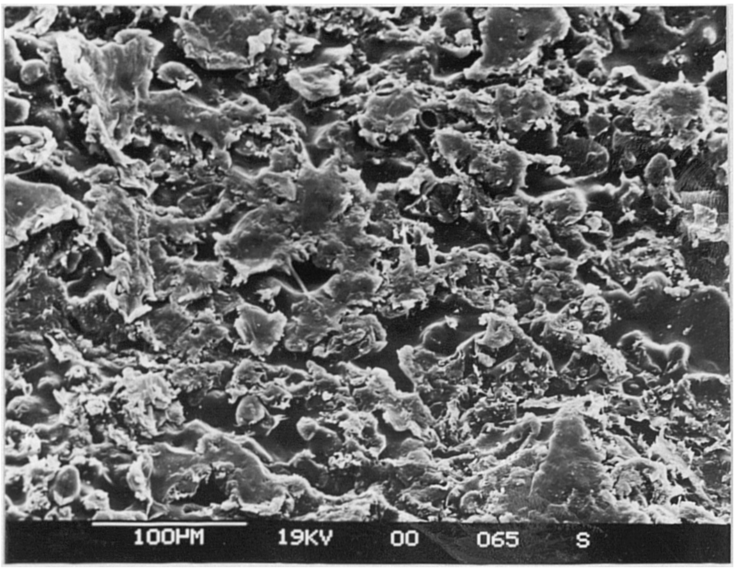

Figure 7.39 SEM micrograph showing adhesion failure of a polyamide 11 coating (6MPa adhesive strength).

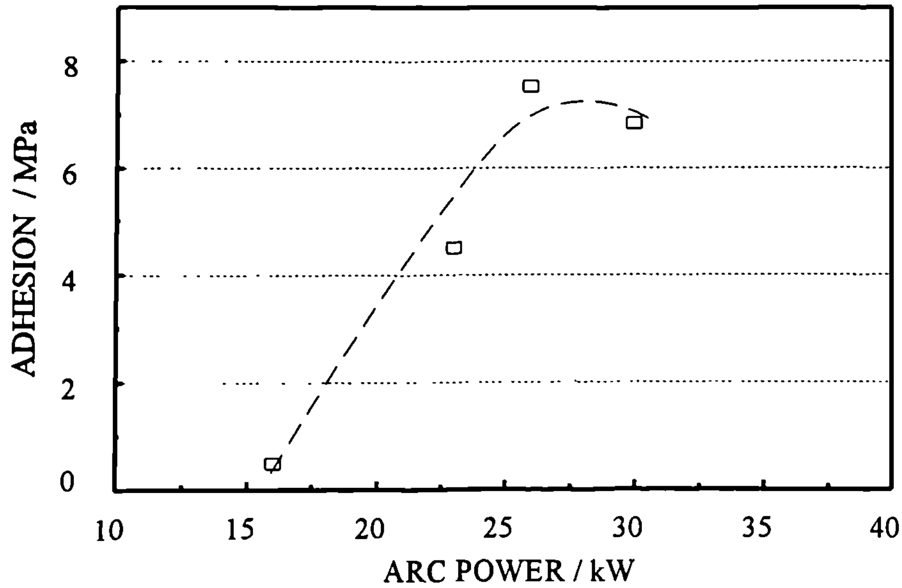

Figure 7.40 The effect of plasma arc power on adhesion of PMMA coatings on steel.

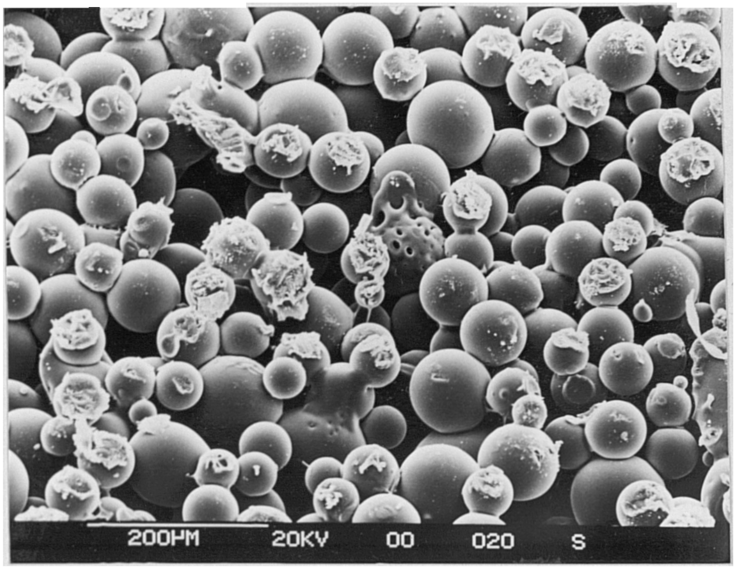

Figure 7.41 SEM micrograph showing adhesion failure of a PMMA coating on steel.

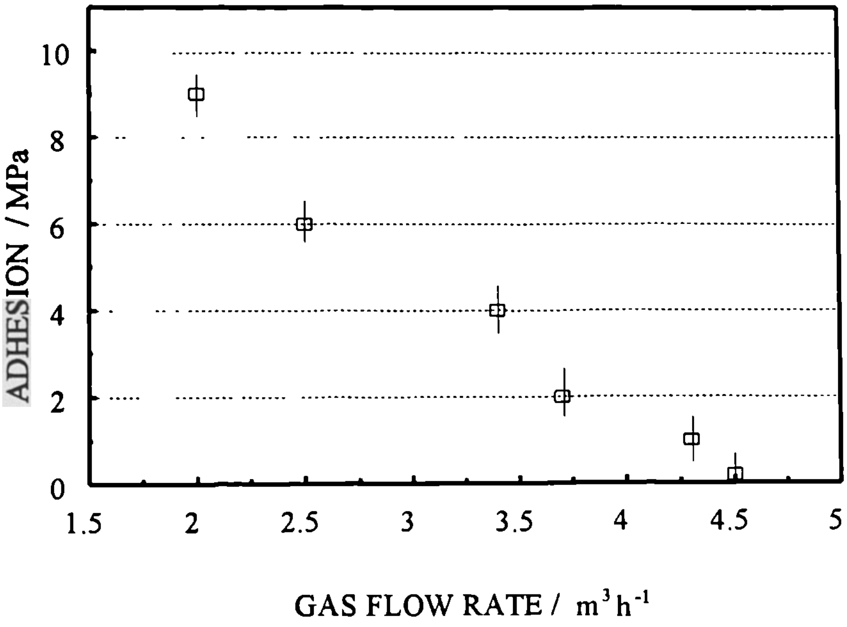

Figure 7.42 Effect of gas flow on adhesion of polyamide 11 coatings on steel.

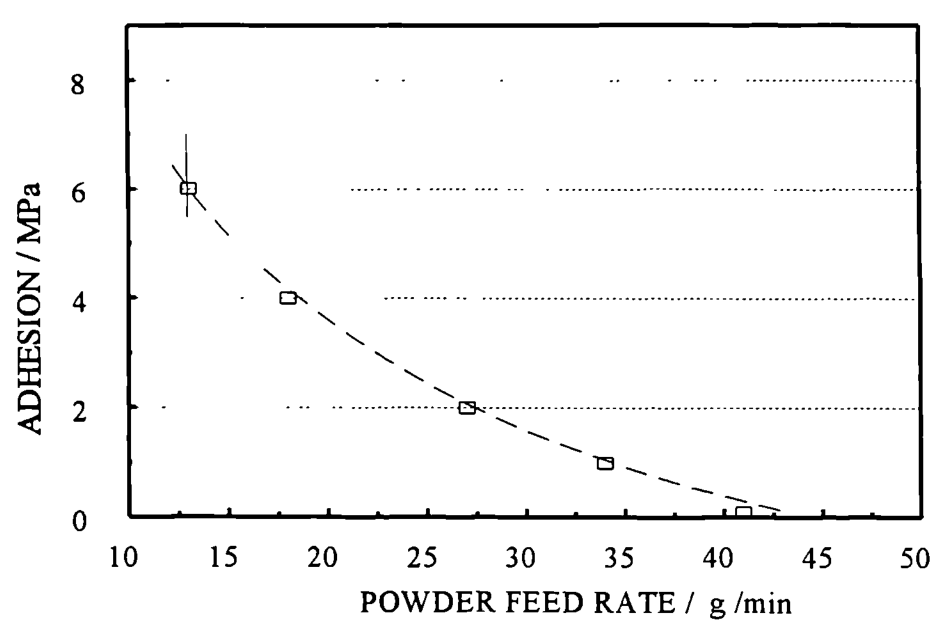

Figure 7.43 Influence of powder feed rate on adhesion of polyamide 11 coatings on steel.

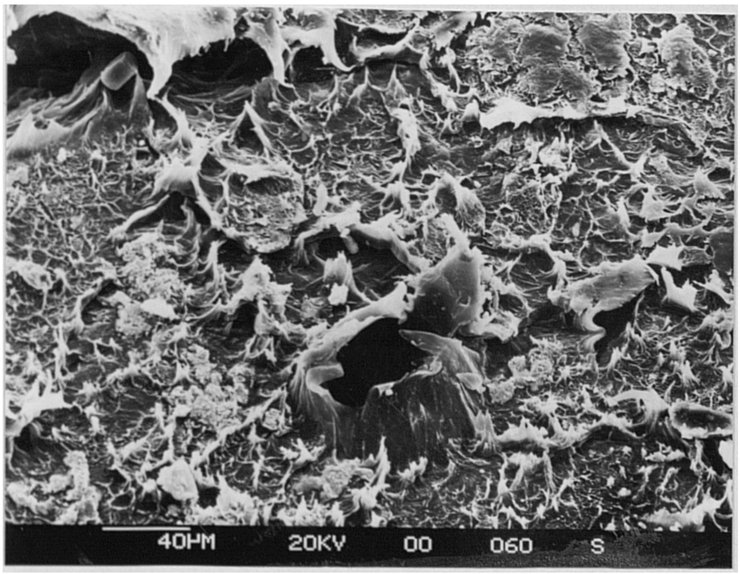

Figure 7.44 SEM micrograph of polyamide 11 coating interface at adhesion failure with a high adhesive strength (>13MPa).

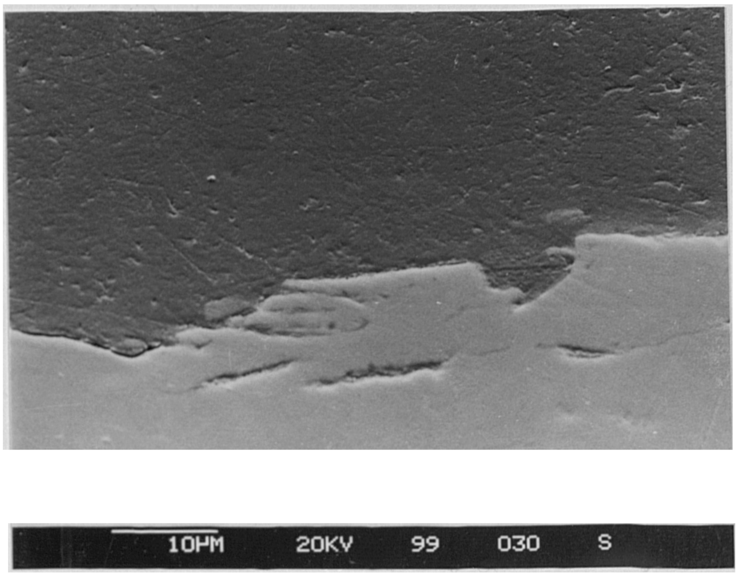

Figure 7.45 SEM micrograph of cross section of polyamide 11 coating interface showing high adhesive strength.

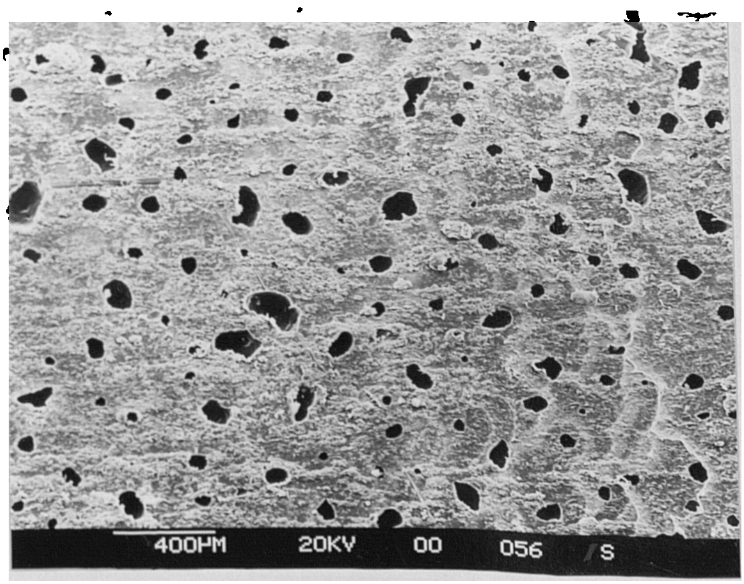

Figure 7.46 SEM micrograph on polyamide 11 coating interface at adhesion failure on overheated substrate.

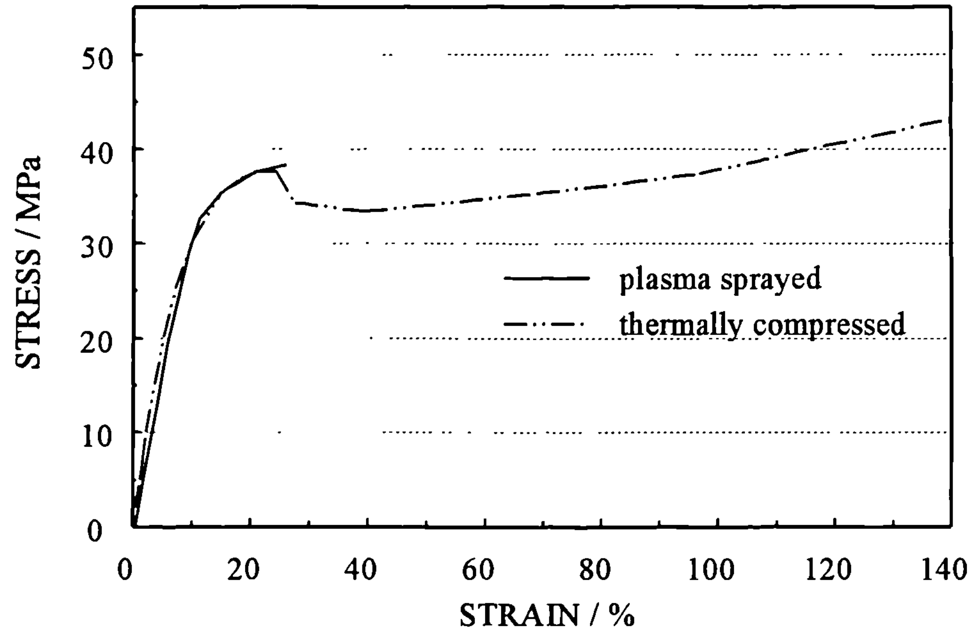

Figure 7.47 The stress - strain relationship of plasma sprayed polyamide 11 coating and that of thermally compressed polyamide 11 film.

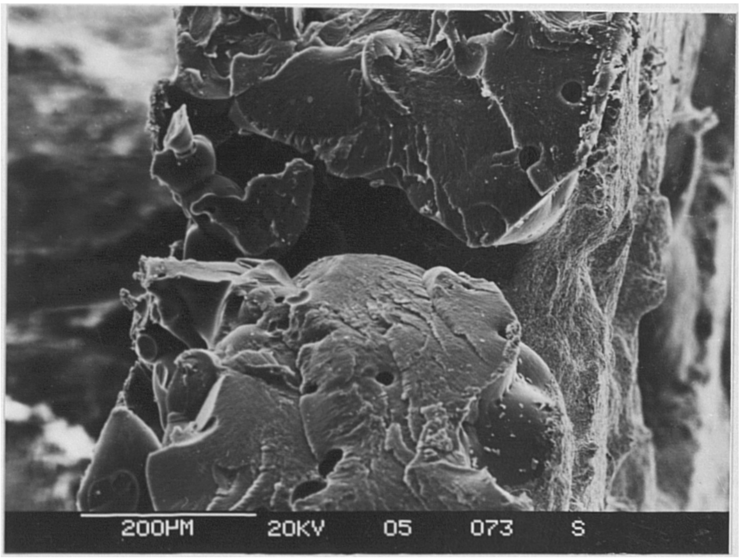

Figure 7.48 Fracture surface of polyamide 11 coating produced at 18 kW

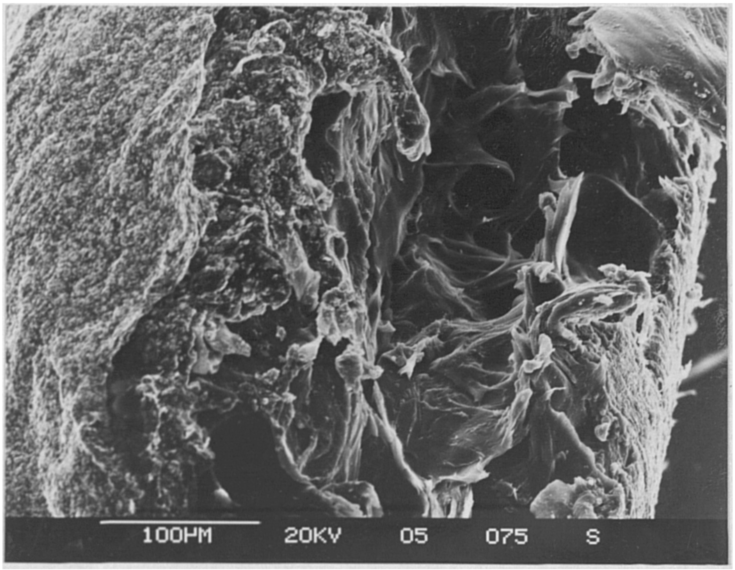

Figure 7.49 Fracture surface of polyamide 11 coating sprayed at 21 kW arc power

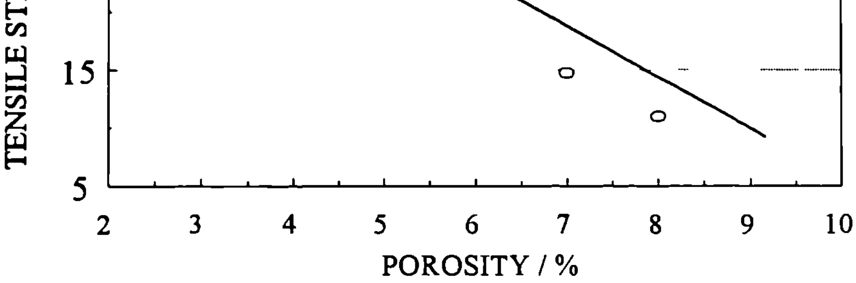

Figure 7.50 Relationship between tensile strength and porosity for polyamide 11 coatings

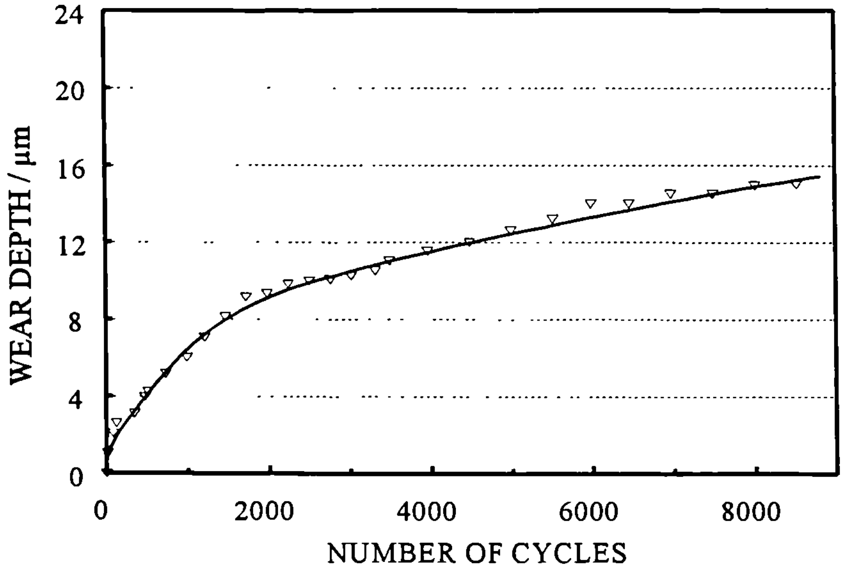

Figure 7.51 Wear of plasma deposited polyamide 11 coatings against a stainless steel ball.

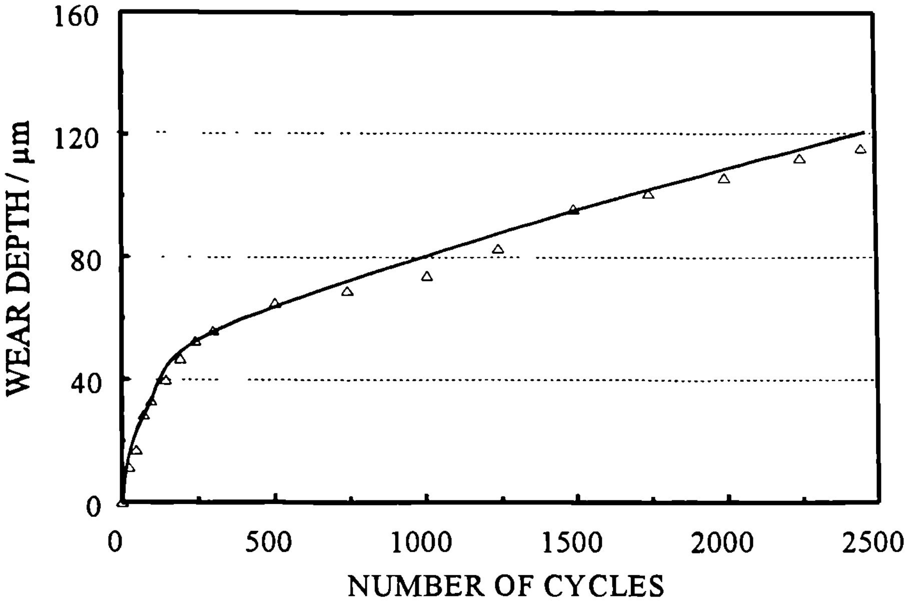

Figure 7.52 Wear of plasma deposited polyamide 11 coatings against a Rockwell diamond stylus.

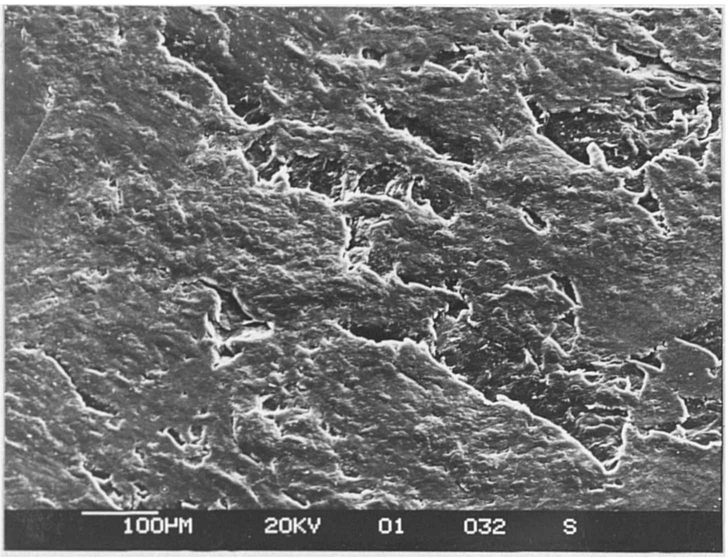

Figure 7.53 Polyamide 11 coating surface after wear against the stainless steel ball.

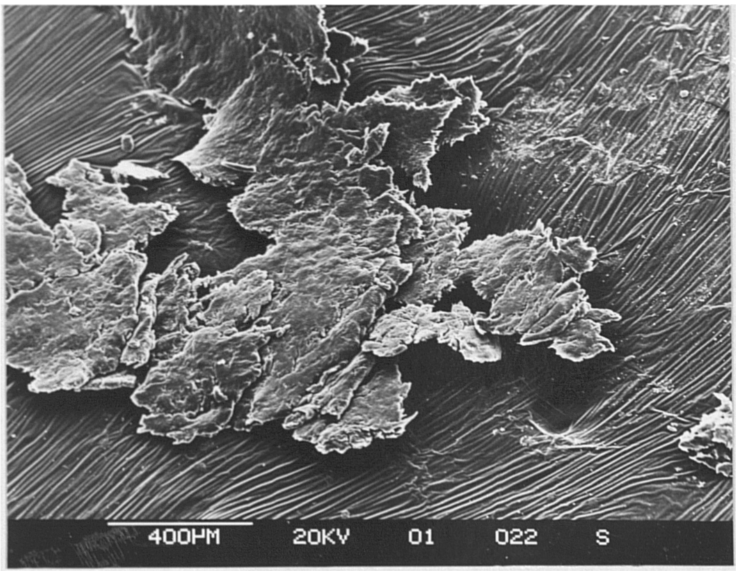

Figure 7.54 Wear debris from sliding of polyamide 11 coating against the stainless steel ball.

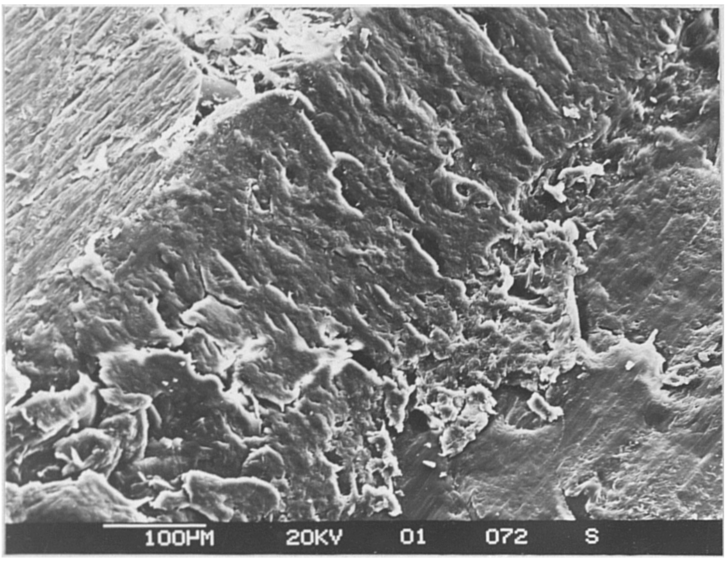

Figure 7.55 Polyamide 11 coating surface after wear against the diamond counterface.

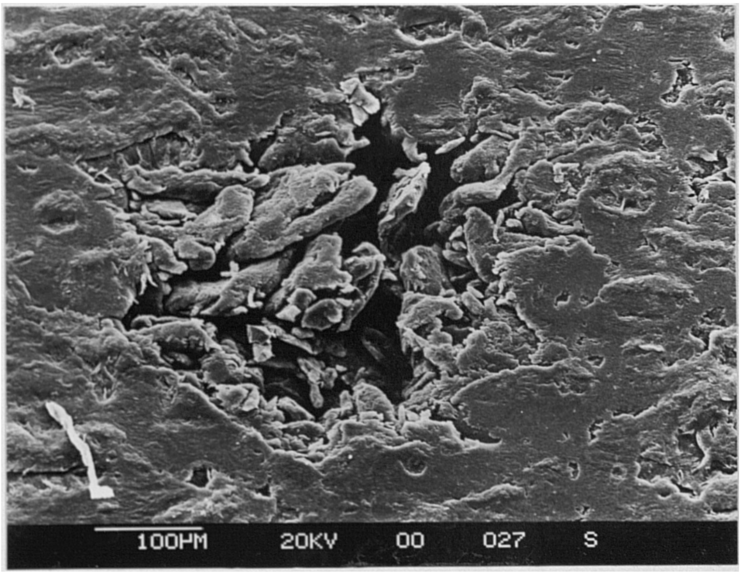

Figure 7.56 Wear track of polyamide 11 coating after sliding against the stainless steel ball.

Figure 7.57 Effect of porosity on wear of polyamide 11 coating against the stainless steel ball.

CHAPTER 8. PLASMA SPRAYING OF THERMOSETS

The heat transfer process of thermoset materials in the plasma environment is expected to be similar to that of thermoplastics since both of them possess a common thermal nature: low thermal conductivity, low melting and decomposition temperatures. The behaviour of both materials during plasma spraying is thus expected to be similar. However, thermosets need to be converted into three-dimensional network structure by means of cross-linking or a curing reaction, since the properties and final use of thermoset materials depend greatly upon the degree of cross-linking. Plasma spray deposition of thermosets have, therefore, more stringent requirements than that of thermoplastics because cross-linking is needed in addition to maximizing melting and minimizing degradation. Theoretical calculations and experimental investigation were thus carried out for the determination of the important factors that affect the quality of the thermoset coatings, in particular, the degree of cross-linking.

The thermoset materials used in the investigation were a range of epoxies, the details of which are given in Table 8.1.

8.1 Theoretical calculations

The theoretical calculations in Chapter 6 has predicted that the resident time of a polymer particle in the plasma flame is only the order of 1 millisecond, although the calculations were based on polyamide, the results can be applied to epoxies due to similar heat transfer properties. The residence time is much less than the gel time of the epoxies (Table 8.2). This suggests that it is impossible for epoxy particles to be cured in the plasma flame. The temperature history of the splats after impact and that of the coatings formed are examined below by theoretical calculations.

8.1.1 Cooling of splats on substrate

The temperature-time conditions of the splat immediately after impact of the molten epoxy particle on substrate were first calculated using the heat transfer equations described in Section 4.2 (modelling Part II).

Figure 8.1 gives the calculated temperature profile through the thickness of a 5 μm thick splat of epoxy at various time from impact on the substrate. Zero thickness refers to the coating-substrate interface. The initial temperature of the substrate was taken as 300 K and the splat temeprature was taken as 600 K. The lower temperatures of cross-linking determined by DSC are superimposed on diagram as a dotted lines Tx_{low}(380 K). Figure 8.1 shows that the heat flow from the hot splat to the cold substrate and how the splat is cooled by the substrate. It is noted that the temperature at the coating-substrate interface exhibits a constant 300 K due to the much larger heat capacity and thermal conductivity of the substrate than those of the splat. It takes only 180 μs for all the splat to cool below the lower cross-linking temperature(the temperature of cross-linking reaction terminating during the cooling of the splat), during which the cross-linking in an isolated splat is not expected to be feasible. In addition, Figure 8.1 indicates that because the heat of the splat dissipates through the substrate, raising the temperature of the substrate can reduce the cooling rate of a splat and might thus promote cross linking

Increasing the time above the cross-linking temperature is clearly of importance for thermosets since the cross-linking reaction is a kinetic process: the degree of cross-linking depends on the reaction temperature (> lower cross-linking temperature) and reaction time. The use of splat thickness or, indirectly, feedstock particle size to achieve this was investigated. Figure 8.2 gives a calculated temperature profile for a 10μm thick splat of epoxy and indicates that the predicted time above the lower cross-linking temperature has now increased three-fold relative to the 5μm splat to 560 μs, which is still far less time than that required for effective curing of the splat. Figure 8.3 shows the calculated cooling curves of splats originating from feedstock particle diameters of 60, 120 and 240 μm which were assumed to have deformed into the ratio (D/d) 4 (refer to Figure 4.4). The temperature in vertical axis represents the temperature at the half-thickness of the splat. It can be seen that the large particles provide much slower cooling rates, suggesting the sensitivity of the cooling of the isolated splat to its thickness.

The heat transfer calculations for isolated splats have thus predicted that the time for a splat above cross-linking temperature can be substantially prolonged by increasing the feedstock particle size and by preheating the substrate. However, the beneficial effect of the particle size needs to be balanced with the need to ensure complete melting of the particles(section 6.4).

The calculations above only consider isolated splats in contact with the steel substrate, whereas the cooling conditions of entire coating layer are likely to be very different. The coating layer is much thicker than that of the splat and the splats are embedded in a contiguous aggregate of other splats with much lower thermal conductivities than steel. In addition, the splats are reheated by new in-coming splats as spray deposition continues and there is also a heating effect from the plasma flame on the top surface of the coating which, in the case of polymers could be significant. The cooling conditions of a coating layers are thus expected to be more conducive to cross-linking than those of an isolated splat.

8.1.2 Cooling of the coatings

Figure 8.4 shows the temperature profiles, calculated using the heat transfer equations described in Section 4.3 (modelling Part III), through a coating deposited on a substrate pre-heated to 65 °C (above glass transition temperature and below cross-linking temperature of the epoxy) at various times from its formation. The initial temperature of the coating was taken to be its decomposition temperature (700K) . The major heat flow is from the hot coating to the cooler substrate but there is also a significant heat flow from the top surface of the coating into the atmosphere. As a result, Figure 8.4 shows that the cooling rate near the coating-substrate interface is very high due to the rapid heat flow into the substrate, the cooling rate in the middle of the coating is much lower due to the slower heat flow through the low conductivity polymer, and, finally, the cooling rate near the top coating surface is significantly higher than that in the mid-thickness due to heat losses to the atmosphere.

These differences in cooling rate result in large variation in temperature through the coating thickness during cooling. For example, Figure 8.4 shows that up to 30 μm of the coating adjacent to the interface falls below the lower limit of cross-linking temperature, Tx_{low}, after only 0.1 second (shown as dotted horizontal line in Figure 8.4), whereas the core of the coating thickness does not fall below this temperature until 1-2 second. This non-uniform temperature distribution through the coating thickness suggests that there may be a variation in cross-linking within a thermoset coating and, in particular, the layer near the substrate will receive minimal cross-linking.

Figure 8.5 shows the calculated temperature profiles for a coating sprayed on a substrate preheated to 120°C (cross-linking temperature range) as compared with 65°C in Figure 8.4. It is seen that the cooling rates throughout the coating thickness are now substantially lower and the coating spends more time above the cross-linking temperature, Tx_{low}: for example, the coating layer adjacent to the interface(30μm from interface) falls below the cross-linking temperature, Tx_{low}, after 15 seconds; the middle layer(240-270μm from interface) falls below Tx_{low}, after 3 seconds and the top layer(470-500μm from interface) takes only 2 seconds. The calculations reveal a more subtle effect: when the coating cools down to below the initial pre-heating substrate temperature(120 °C), the heat flow direction reverses and the net heat transfer is from the substrate to the coating. As a result, the coating layers next to the substrate now spend much longer times above Tx_{low} in contrast to the situation for the lower temperature substrate (Figure 8.4).

Referring to Figure 4.5 and 4.6, the heat now flows from both the coating and the substrate to the cooler environment. Because the substrate is much thicker (6000μm) than that of the coating (500μm) and possesses much larger thermal capacity, the cooling of the system is dominated by the cooling of the substrate (substrate controlling mechanism). The cooling of the coating therefore experiences two stages: when the temperature of the coating is higher than that of the substrate, the net heat flow is from the coating to the substrate, whereas when the temperature of the coating falls down to below the temperature of the substrate, the net heat flow is from the substrate to the coating. Figure 8.6 shows that the time for the latter is much longer than the time for the former. The time for coating to cool down to close to the temperature of the substrate(stage 1) is too short for full cross-linking to take place. This is very important since it suggests the residual heat of the substrate can be used to promote the cross-linking of the coating. The cooling time of the coating can be controlled by the amount of residual heat of the substrate, and the latter is determined by the temperature of the pre-heated substrate and the cooling applied to the substrate.

Figure 8.6 gives the cooling curves for a 300 μm coating sprayed on to substrate preheated to 40, 65, 120 and 180°C respectively: Figure 8.6a provides the temperature of the coating next to coating-substrate interface (0-30μm), Figure 8.6b, the mid-thickness temperature and Figure 8.6c, the surface temperature of the coating. Figure 8.6 shows that after 1 second from cooling, the cooling process of the coating is determined by the preheating temperature of the substrate: the time above cross-linking temperature for the coating preheated to 180 °C is longer than 30 seconds, while that for the coating preheated to 40 °C and 65 is approximately 1 second.

Figure 8.7 shows the influence of the coating thickness on the cooling of the coating deposited on a substrate preheated to 65 °C. The calculations show that the coating thickness has a significant effect on the cooling rate: the thicker the coating, the slower it cools due to the poor thermal conductivity of the epoxy. The calculations also show that the time above the cross-linking temperature even for the thickest coating is only 1.5 second, which suggests that curing of the coatings will not occur with a preheat temperature of 65 °C. Figure 8.8 gives the calculated effect of raising the preheat temperature to 120°C and shows that the 500μm coating(at middle thickness) now spends 3 seconds above the cross-linking temperature. It is noted that besides a reduction in cooling rate at temperatures just above Tx_{low}, the calculations reveal an interesting effect. At the outer surface of the coating at cooling times of over 2 seconds, the ranking order of cooling reverses: the thickest coating begins to show the highest cooling rate and loses the most heat form its outer surface. Figure 8.9 shows the calculated cooling curves for a 180°C preheat temperature. At cooling time of approximately 3 second (after initial rapid cooling), the cooling curves cross over such that the thinner coatings now exhibit the slowest cooling rates: the time above the cross-linking temperature is 100 second for the 100μm coating, 70 second for the 300μm coating and 65 second for the 500μm coating (at mid-thickness, Figure 8.9a). This reversal of the thickness effect on cooling rate is due to the fact that the large heat capacity of the substrate (because it is orders of magnitude thicker than the coating) ensures that the major heat flow is from the substrate into the coating for high preheat temperatures. The residual heat of substrate pre-heated to high temperatures dominates the cooling of the coatings.

Figure 8.10 summarizes the calculated effect of substrate preheating on the residence time of the coating above the cross-linking temperature measured at mid-thickness of the coatings. These residence times are now predicted to be comparable with the reactivity of the experimental epoxy thermosets, which suggests that there is a real possibility of achieving substantial curing in plasma sprayed coatings under these conditions.

8.2 Experimental results and discussions

8.2.1 Determination of the glass transition temperature and enthalpy of curing

Figure 8.11 shows a DSC thermogram obtained for a uncured epoxy precursor powder (MR4014). The vertical axis gives the difference in input heat flow required to maintain the specified heating rate between the sample under test and a reference sample. The horizontal axis gives the temperature. Figure 8.11 shows the major changes of the state that occur in the precursor powder during heating.

The first major deviation from the baseline begins at about 60 °C and requires an increase in heat flow which is indicative of an endothermic change. The change is attributed to the glass transition. The glass transition temperature, T_g, is taken as the intersection of the extrapolated baseline at the lower temperature side of the peak and the tangent to the curve at the inflection point as shown in Figure 8.11. The Tg values determined in this way for epoxy powders are given in Table 8.2

The second major deviation from the baseline is a deep valley occurring at 152 °C. This indicates a major reduction in the required heat input flow and an exothermic reaction. The process is attributed to curing of the epoxy and the heat generated by the cure is directly related to the area of the valley. The values of the enthalpy of curing for precursor epoxy powders from DSC measurements are shown in Table 8.2 and are used in the thermal calculations (section 8.1). The position of the curing exotherm may be defined by the temperature at the minimum heat flow, Tc. The value of Tc is indicative of the reactivity of the thermoset system. The values for precursor epoxy powders are given in Table 8.2 as well.

8.2.2 Evaluation of the degree of cross-linking

In order to obtain different degrees of cross-linking of the epoxies, the powders of MR4014 and BR517 were isothermally stoved at 160°C for 30 s, 60 s, 90 s and 180 s respectively in the DSC apparatus. These treatments are within the curing range and so the powders are expected to show different degrees of cross-linking. The thermal behaviour of the powders were then measured on the DSC apparatus and the data shown in Figure 8.12 to 8.14.

Figure 8.12 indicates that the glass transition temperature, Tg, of two powders increased with the increase of isothermal soaking time. The glass transition temperature of a system reflects the amount of thermal energy required for significant movement of macromelecular segments [136]. During the early stages of curing, cross-linking takes place at a small number of widely separated points in the resin and movement of the macromelecular segments is only slightly restricted. As curing progresses, the spacing between cross-linked points decreases and becomes comparable to that of the length of the segment. As a result, the segments lose their independence of movement and move in groups, which requires additional energy and raises the glass transition temperature. In the extreme case, when the system is completely cross-linked, very little movement of the segments relative to one another can occur and the glass transition temperature extremely high.

Figure 8.13 shows that the enthalpy change for curing, ΔH, decreases with increasing stoving time of the powders. The magnitude of ΔH is related to the proportion of unreacted groups in the powder[102]. A large ΔH indicates that the powder under investigation has undergone extensive cross-linking during DSC testing, which means that it contains a high proportion of unreacted groups and possesses a low degree of curing before testing. When the powder is fully cured, no unreacted groups remain so that no cross-linking reaction occurs during DSC testing resulting in a zero enthalpy change. In summary, the progress of the cross-linking process is followed by an increasing glass transition temperature and a decreasing enthalpy change.

Figure 8.14a and 8.14b show the DSC thermograms for the precursor powders MR4041 and BR517 after being subjected to the various stoving times. The above-mentioned changes of Tg and ΔH are clearly visible. In addition, the position of the curing exotherm valley shifts to higher temperatures indicating that the less reactivity of the coatings than that of the powders.

Above experimental results indicates that the extent of the curing or cross-linking of a thermoset is sensitive to its enthalpy change,ΔH. Conversely, the magnitude of the ΔH measured from DSC can be used as a means of quantifying the degree of cross-linking. However, the ΔH value of a thermoset is related to the structure of the feedstock material which is not convenient for the purpose of comparison among materials. A dimensionless relevant variable is thus defined:

$$X=1-\frac{\Delta H_C}{\Delta H_P} \qquad (8\text{-}1)$$

where X is the fractional degree of cross-linking, ΔH_c and ΔH_p are the enthalpy changes obtained during the given curing treatment for the coating and the precursor powder respectively.

Three plasma sprayed coatings produced from MR4014 powder at different operating conditions were removed from their substrate and subjected to DSC testing. The resulting thermograms are shown in Figure 8.15a, together with the DSC thermograms determined for two extreme cases: (i) the as-ground precursor powder which is known to be uncured; (ii) the plasma sprayed coating after stoving at 160°C for 15 minutes which is known to give complete curing of the epoxy(MR4014). The results in Figure 8.15a show that the enthalpy changes and the glass transition temperatures of the coatings are intermediate between those of precursor powder and the stoved coatings. The implication from these results is that cross-linking occurs during plasma deposition to an extent that depends upon the process conditions: for example, the degree of cross-linking varies in the range from 22 % in the coatings plasma sprayed at 14 kW arc power to 37 % in the coatings plasma sprayed and then plasma post-treated. The results show that substantial curing can be achieved in plasma spray deposition by control of the process parameters. The same experiment was carried out for the BR517 powder and coatings, and similar results were obtained as shown in Figure 8.15b.

Confirmation of the structural changes occurring during processing was obtained through the measurement of wear behaviour, since the mechanical properties of thermosets are directly related to cross-linking [102]. A series of deposits of MR4014 were plasma sprayed under different processing conditions. The enthalpy change and wear performance of the coatings were then evaluated and the data shown in Figure 8.16. The X value of each coating calculated using equation (8-1) is given next to its wear curve. Figure 8.16 shows that the wear rate of the coatings decreases with increasing degree of cross-linking, X value. Curing is expected to improve the wear resistance of thermosets and so the results in Figure 8.16 confirm the occurrence of the curing of the epoxy during the deposition.

8.2.3 Factors affecting degree of cross-linking

(i). Operating conditions

Figure 8.15 has indicated that the degree of cross-linking of the epoxy coatings is related to the plasma arc power. Considering the extremely short resident time, the plasma arc powers are most unlikely to affect the progress of cross-linking reaction directly. However, indirect influences possibly exist through the influence of arc power on the degree of melting of the particles. As indicated in Chapter 6, the degree of melting of in-flight particle and consequent flow of the splats depend greatly on the plasma arc power. Extensive flow will allow the splat to make close thermal contact with the underlying surface profile, which will generally consist of previously deposited polymer. Although the initial cooling rate of the splat is rapid, it will remain at an elevated temperature through deposition due to heat transfer from the subsequent incoming splats and the plasma flame repeatedly scanning over surface. On the other hand, a particle that does not melt (soften in the case of thermoset) throughout its thickness and has a solid core will exhibit limited flow on impact, producing a thick splat having poor thermal contact with the neighbouring splats. Such a splat will have a relatively low core temperature and will receive less heat transfer from subsequent splats with a consequent reduced opportunity for activating curing. Figure 8.17 gives the SEM micrographs of the splats of epoxy (MR4014) produced by wipe testing at different arc power levels. The observations show that splats with smaller diameters and often thicker sections at their centres form at the lower arc power level (14 kW). This suggests that the low power levels result in incomplete softening in the plasma and inadequate flow on impact. This confirms that the effect of plasma arc power on the degree of cross-linking (Figure 8.15) is attributable to the degree of particle softening in the plasma jet.

Scanning the coating with a modified plasma flame after deposition (Figure 8.15) is shown to improve the degree of cross-linking. The heat transfer calculation shown in Figure 8.5 has indicated that there is a significant heat dissipation to the environment.

The heat from plasma flame scanning compensated the heat loss and reheated the coating such as the degree of cross-linking of the coating was improved.

(ii) Substrate preheating

The theoretical calculations in section 8.1.2 predict that substrate preheating will extend the time above the cross-linking temperature and thus promote cross-linking of the coatings. A systematic experimental study was consequently undertaken. Substrate preheating was carried out by traversing the substrate with the plasma flame and measuring the temperature at a series of positions immediately before spraying. Figure 8.18 shows the measured degree of cross-linking in coatings produced from powder MR4014 as a function of substrate temperature. The trend is very similar to that predicted in Figure 8.10: a gradual rise with preheating and a sharp increase at 120°C (cross-linking temperature range). Figure 8.19 shows the effect of preheating on the wear behaviour: the wear rate decreases with preheating and a substantial fall is observed at temperatures above 120°C in agreement with Figures 8.10 and 8.19.

The modelling in the section 8.1.2 predicts a variation in cooling rate and therefore cross-linking through the coating thickness during deposition. In order to investigate this prediction, a 300μm thick coating was cut in half parallel to the interface and the degree of cross-linking, X, measured. The results are given in Figure 8.20 and show that the section adjacent to the preheated substrate ($0<x<150\mu m$) exhibits substantially more cross-linking than the outer section ($150\mu m<x<300\mu m$). These results are consistent with the theoretical model which predicts slower cooling next to the substrate after preheating to 120°C as indicated in Figure 8.5 and 8.8. Figure 8.21 shows how the wear rate varies with depth through the coatings. The wear is high at the coating outer surface (depth = 0, $x = 350\mu m$) due to running-in and the faster cooling rates as predicted in Figure 8.5 and 8.6. The rise in wear rate next to the substrate as shown for the 40°C sample in Figure 8.21 is attributed to the rapid cooling rates at this position as predicted in Figure 8.5, which results in reduced cross-linking. This effect is not observed in the coatings deposited on the substrate preheated to higher temperature, since these coatings are expected to exhibited reduced cooling rates and increased cross-linking in layers next to the substrate (Figure 8.5, 8.8 and 8.9).

Figure 8.22 gives the effect of coating thickness on the wear rate profile of the coatings deposited on the substrate reheated to 120 °C. The thinner coating is shown to possess a much greater wear resistance, which is consistent with the theoretical predictions in Figure 8.9: the thinner coating deposited on the substrate preheated to 120 °C has a slower cooling rate and hence a greater degree of cross-linking.

(ii) Substrate Conductivity

The theoretical heat transfer analysis indicates that the heat content of the as-deposited coating disperses mainly into the substrate under normal conditions. Substrate preheating has been shown to exert control over this process and promote cross-linking. An alternative approach to reducing the rate of heat flow, however, is to lower the thermal conductivity of the substrate. This can be achieved experimentally by applying an undercoat with a low thermal conductivity, which effectively acts as a thermal barrier, to the substrate before spraying. A ceramic coating was chosen, since this can also be preheated without degradation.

A theoretical analysis was first undertaken to determine whether or not such a measure would be expected to provide a sufficient quantitative effect to be successful. A 500μm epoxy coating was assumed to be deposited on the substrate with a 500μm undercoat of alumina. The substrate and undercoat were assumed to be preheated to 120°C. Figure 8.23 gives the calculated results: a substantial reduction in cooling rates is predicted. In view of these encouraging results, an experimental programme was then undertaken. A 500μm thick alumina coating was first sprayed on to a steel substrate preheated to 120°C, and then the thermoset was immediately sprayed on top using the dual powder feed unit. Figure 8.24 shows the results from the DSC: the coating with alumina undercoat gives a trace with virtually no minimum, indicating substantial improvement in cross-linking over the comparable bare steel substrate.

The wear performance of these two thermoset coatings was evaluated and the results in Figure 8.25 show a marked improvement in wear resistance of the coating with the undercoat, which is in agreement with the DSC data in Figure 8.24.

(iii) Curing agent

Up to this stage, the problem of inadequate cross-linking in the thermoset coatings has been addressed by control of heat transfer as a means of prolonging the residence time in the curing temperature range. An alternative approach is to enhance the reactivity of the thermoset system so as to provide a material that will cure in a shorter time in order to accommodate the constraints of the process.

Accordingly, Shell produced a powder (MR4021) with the same resin and filler as the existing MR4014 but with a faster curing agent. The thermal characteristics of the new powder in comparison with the conventional one are given in Figure 8.26. This shows that the new powder has the lower initial cross-linking temperature (93°C) and a lower peak temperature (149°C). Figure 8.27 gives the reaction rate of the cure for the two powders and confirms that MR4021 has the faster cure rate. For example, 85% cross-linking is achieved in MR4021 after 0.5 minutes at 160°C whereas only 30% is obtained in the conventional MR4014 powder.

The new powder, MR4021, was therefore plasma sprayed and the resulting coatings evaluated. Figure 8.28 gives the DSC data for the coatings sprayed on to substrate given various amounts of preheating. Substantial amounts of cross-linking are achieved and the degree increases with the substrate temperature. The new precursor powder in combination with substrate preheating to 120°C provides 84% cross-linking in the coating.

The detailed data for enthalpy, degree of cross-linking and the glass transition are given in table 8.3. Figure 8.29 gives the sliding wear behaviour of the MR4021 coating deposited on the substrate preheated to 40, 100 and 120 °C respectively and shows that substrate preheating to 100°C and 120°C provides a pronounced improvement in wear resistance owing to the enhanced cross-linking. Figure 8.30 compares the wear behaviour of the MR4021 coating with the best conventional coating (MR4014 coating deposited on the substrate preheated to 180 °C): the MR4021 coating shows the superior wear resistance even though it was given less substrate preheating. Figure 8.31 summarises the cross-linking results: the new precursor provides coatings with substantially more cross-linking than the conventional precursor. The new coatings on substrate preheated to 120°C are even more heavily cross-linked than the conventional coatings on substrate preheated to 180°C.

8.3 Summary

Plasma spray deposition of thermosets have more stringent requirements than that of thermoplastics because cross-linking is needed in addition to maximizing melting and minimizing degradation. There are difficulties in achieving cross-linking in plasma sprayed thermoset coatings, primarily because the rapid cooling rates in plasma spraying does not allow enough time for the reaction to occur.

The cooling rate of the splat immediately after impact of the molten epoxy particle on substrate was calculated. The results predict that cross-linking in an isolated splat deposited on a cool substrate is impossible. It also predicts that the time for a splat above cross-linking temperature is important. This time can be substantially prolonged by increasing the splat thickness and by preheating the substrate.

The cooling history of the epoxy coatings produced under various conditions was calculated. The results predicts that adequate cross-linking is unlikely in a coating deposited under normal conditions. However, the calculations predict that preheating the substrate above the lower limit of the cross-linking temperature range should facilitate curing and the extent of cross-linking increases with increasing substrate temperature within the cross-linking range. It also indicates that preheating substrate to higher temperature the cooling rate of the coating is controlled by the residual heat of the substrate. The experimental results were found to be in agreement with the theory.

The degree of cross-linking of thermoset coatings can be determined experimentally from enthalpy changes measured by differential scanning calorimetry. A dimensionless variable X is defined to quantify the degree of cross-linking of the deposits (equation (8.1)).

The theoretical calculations predict large temperature variations through the thickness of the thermoset coatings during cooling with consequent variations in the degree of cross-linking. Experimental work confirmed that the degree of cross-linking and the wear rate varied in accordance with the theoretical predictions.

The theoretical calculations predict that coating thickness will have a major effect on the cooling of the coating depending upon the extent of substrate preheating. The experimental results for the degree of cross-linking and wear behaviours are consistent with the theory.

The theoretical analysis predicts that lowering the thermal conductivity of the substrate, by applying a ceramic thermal barrier undercoat, will prolong the residence time of the coating in the curing range and promote cross-linking. The experimental results for the degree of cross-linking and wear resistance confirmed this prediction.

Reducing the time needed for the curing of a thermoset to meet the requirement of plasma processing is an alternative method for improving the quality of the coating. A new precursor powder with a faster curing agent gave major improvements and in conjunction with substrate preheating to 120°C, produced a coating with 85% cross-linking compared with 30% for the conventional precursor.

Table 8.1 Epoxy powders used

Identity	System	Source	Condition	Pigment
MR4014	Epikote 3003-Epikure DX182/2MI	Shell	As-supplied powder	40wt% TiO_2
BR517	Epikote 517-Epikure 171	Shell	As-supplied granules and then extruded and ground at Brunel	None
MR4021	Epikote 3003-Epicure DX182/2MI	Shell	As-supplied powder	40wt% TiO_2

Table 8.2 Properties of the epoxy powders

Identity	Particle size (μm)	Enthalpy change ΔH (J/mol)	Glass transition temp. T_g (°C)	Curing temp. (°C)	Tc (°C)	Gel time at 180°C (s)
MR4014	~70	58	63	103-217	152	30-40
BR517	< 125	88	60	88-210	165	
MR4021	~70	57	63	93-204	149	10-15

Table 8.3 Thermal characteristics of the coatings made from MR4021 powder

Substrate temperature (°C)	Enthalpy change, ΔH (J/mol)	Cross-linked, X (%)	Glass transition Temp., T_g (°C)
40	42.7	25.3	63
100	11.9	79.2	92
120	9.2	83.8	94
powder	57.1	_	63

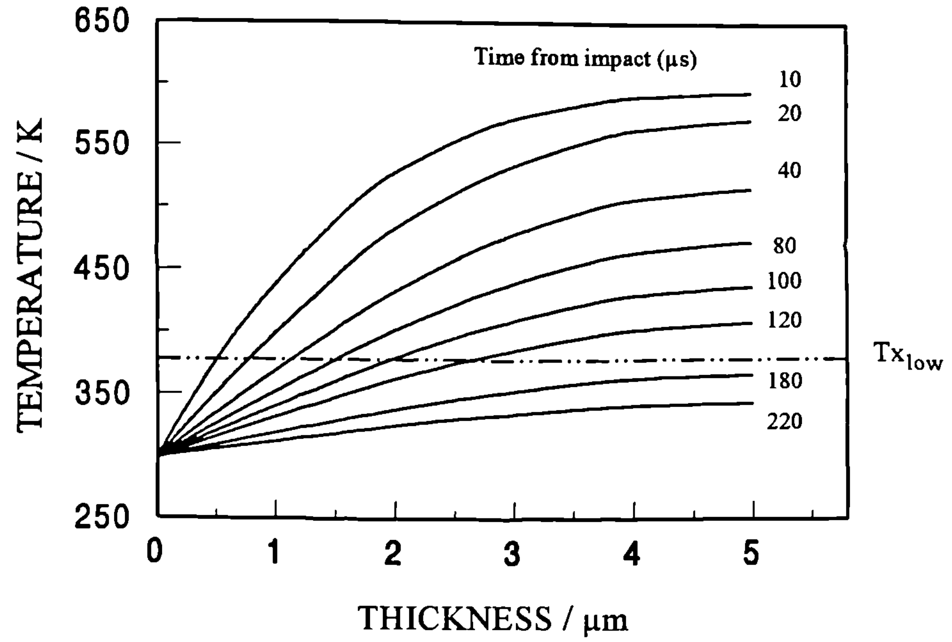

Figure 8.1 Calculated temperatures through the thickness of a 5μm-thick splat at various times from its impact with the substrate.

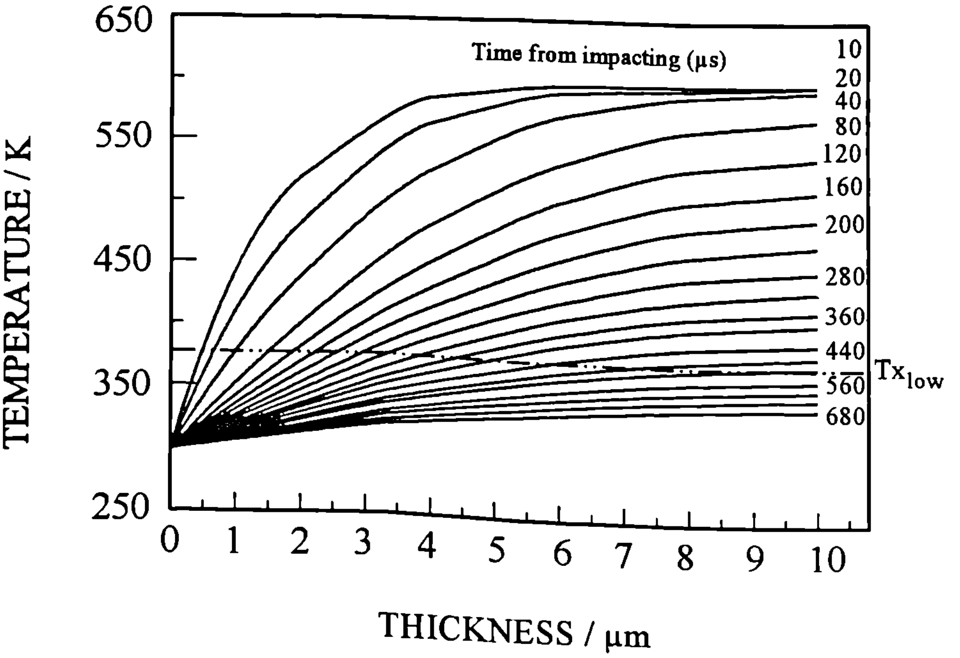

Figure 8.2 Calculated temperature through the thickness of a 10μm-thick splat at various times from its impact with the substrate.

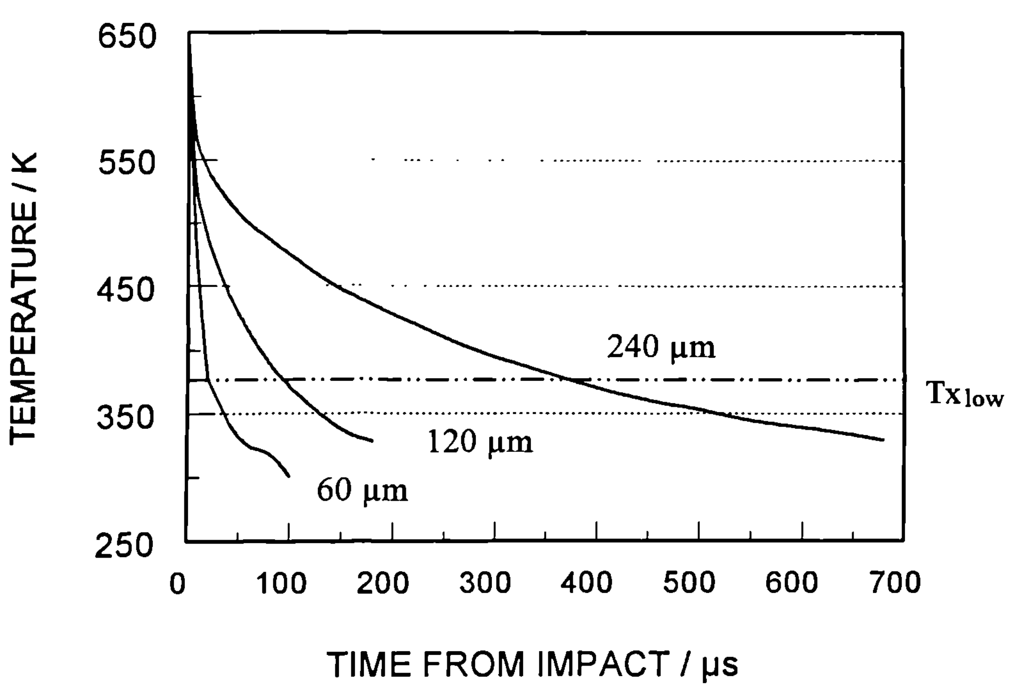

Figure 8.3 Calculated cooling curves of splats originating from 60, 120 and 240μm diameter feedstock particles.

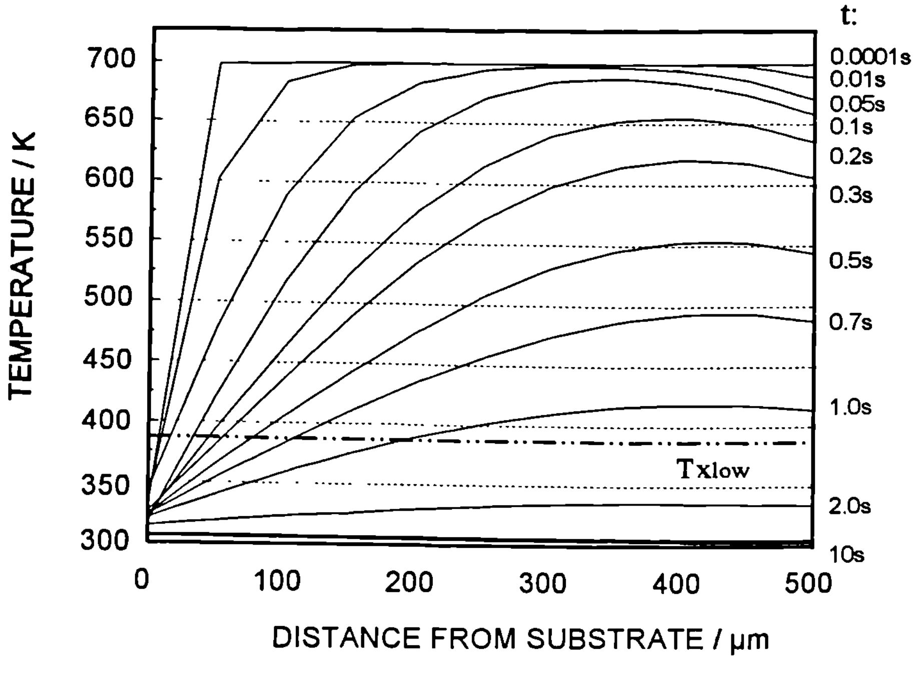

Figure 8.4. Calculated temperature profile through the coating thickness during cooling of a 500μm thick thermoset coating deposited on a substrate preheated to 338K. t is the time from the formation of the coating on the substrate.

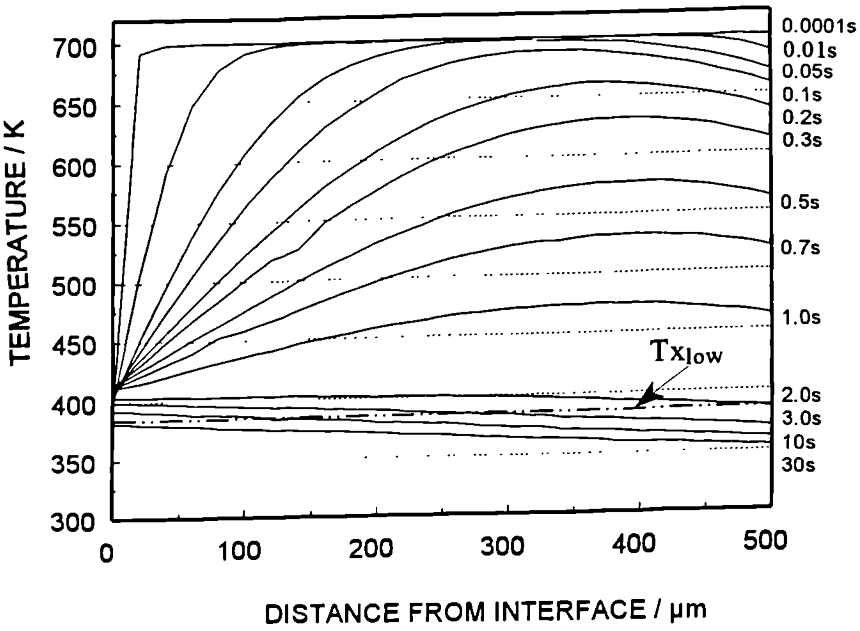

Figure 8.5 Calculated temperature profiles through the thickness of a 500 μm coating deposited on a substrate preheated to 393K(120 °C).

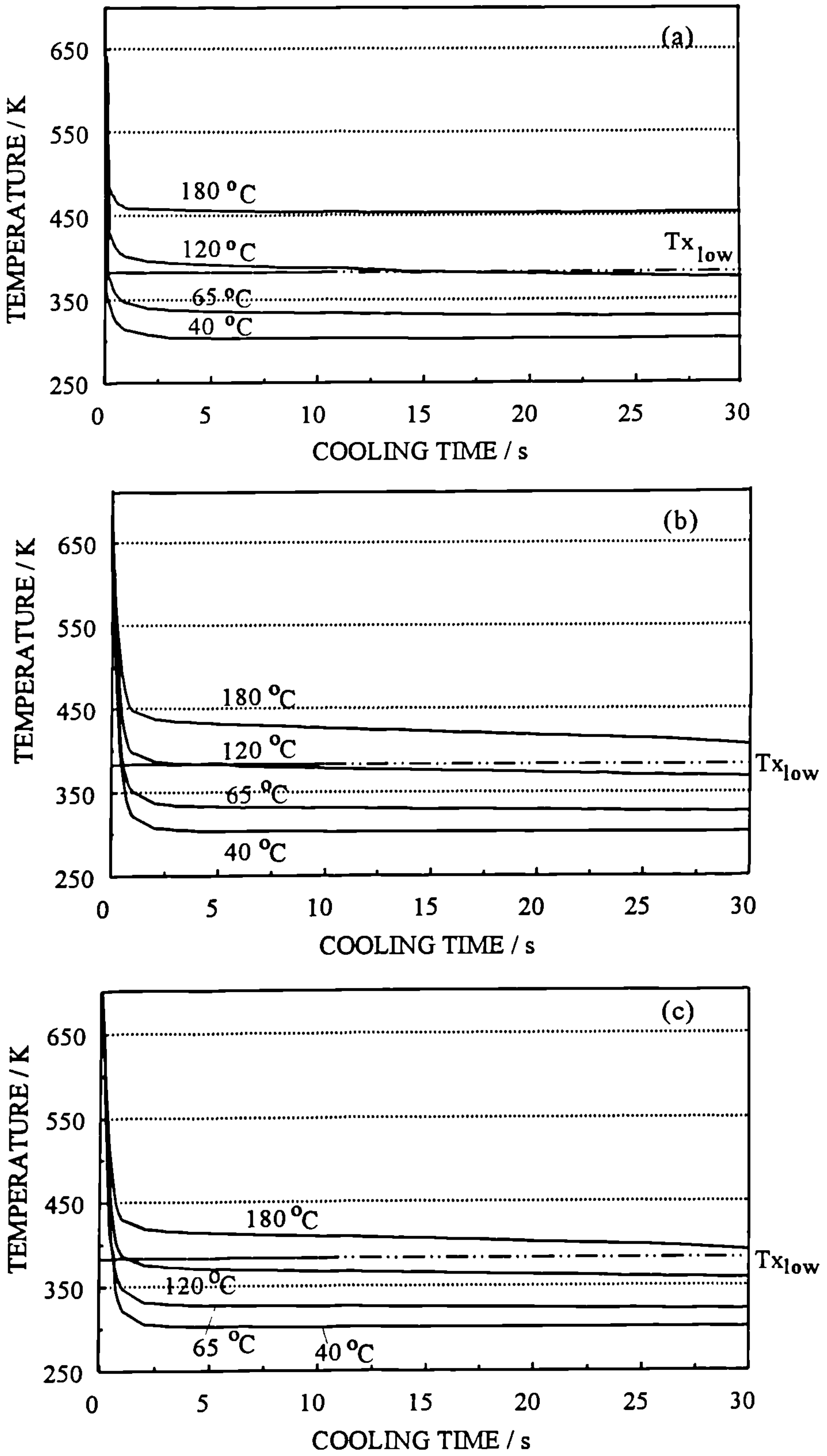

Figure 8.6 The calculated effect of substrate temperature on the cooling of a 300μm thick coating at: (a) coating-substrate interface (b) mid-thickness of the coating, and (c) outer surface of the coating.

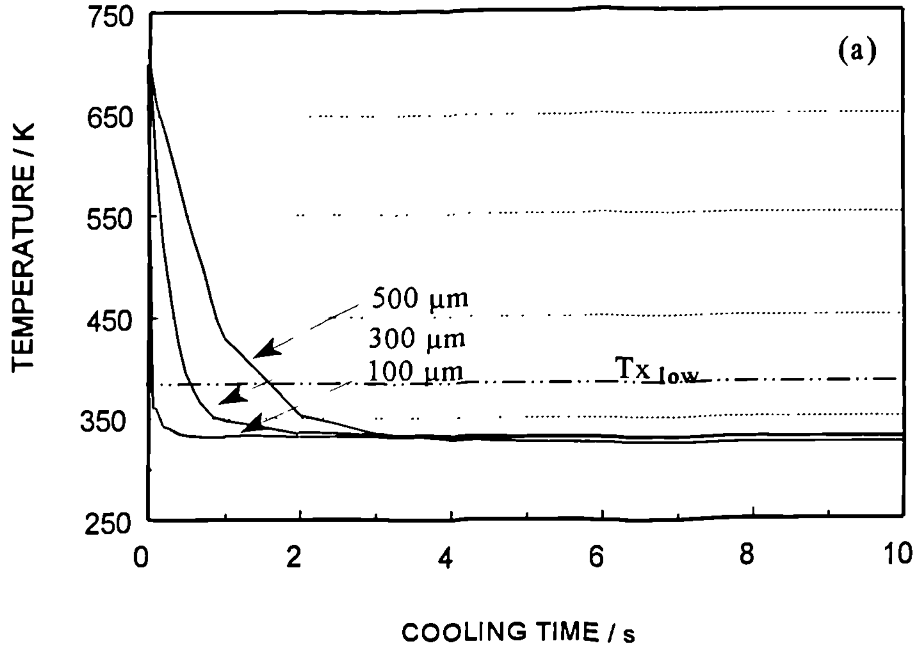

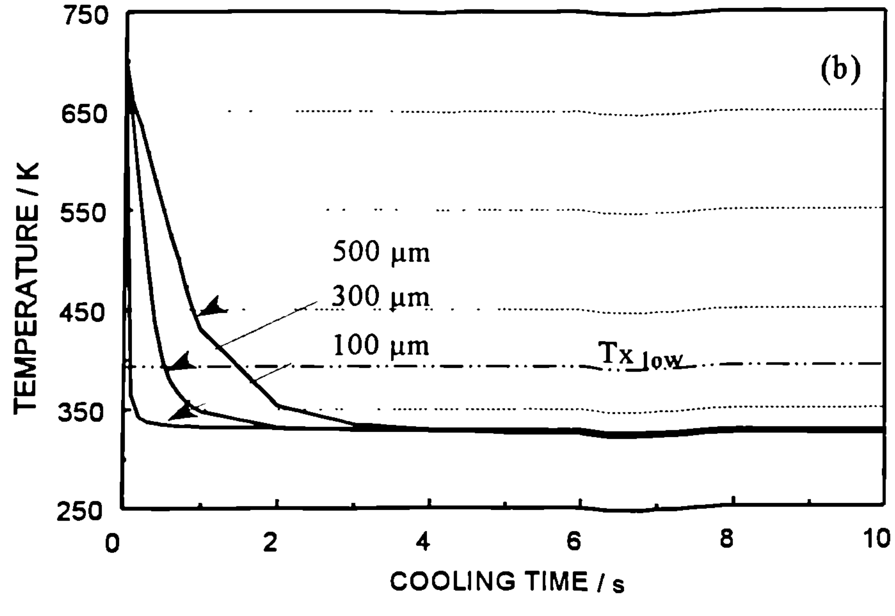

Figure 8.7 Calculated cooling curves for coatings of various thickness deposited on substrate preheated to 338K at: (a) mid-thickness of the coating, (b) outer surface of the coating.

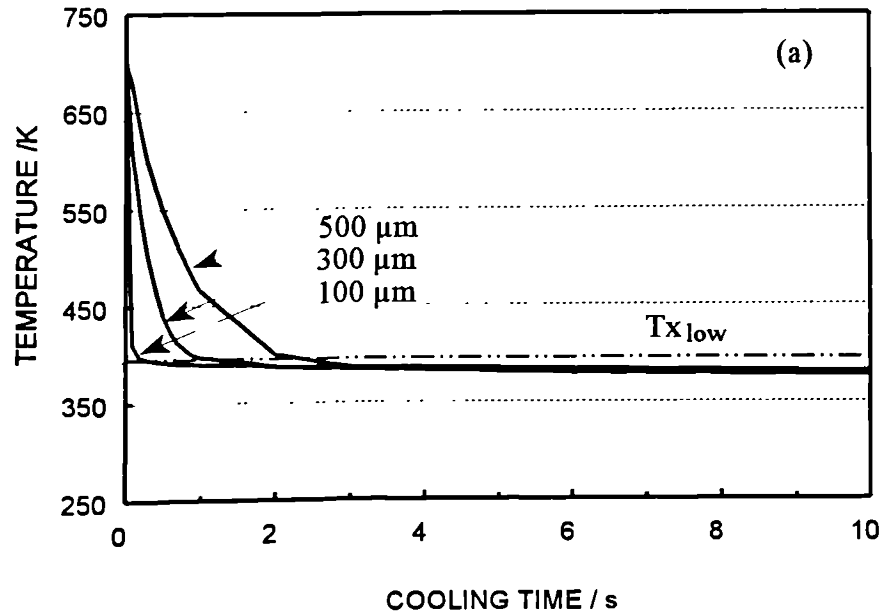

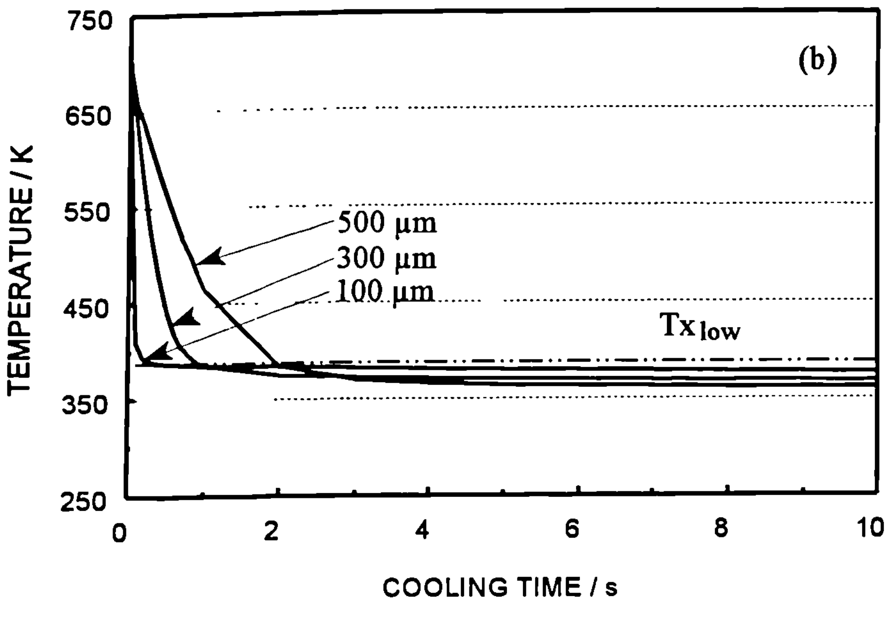

Figure 8.8 Calculated cooling curves for coatings of various thickness deposited on substrate preheated to 393 k (120 °C) at : (a) mid-thickness of the coating, (b) outer surface of the coating.

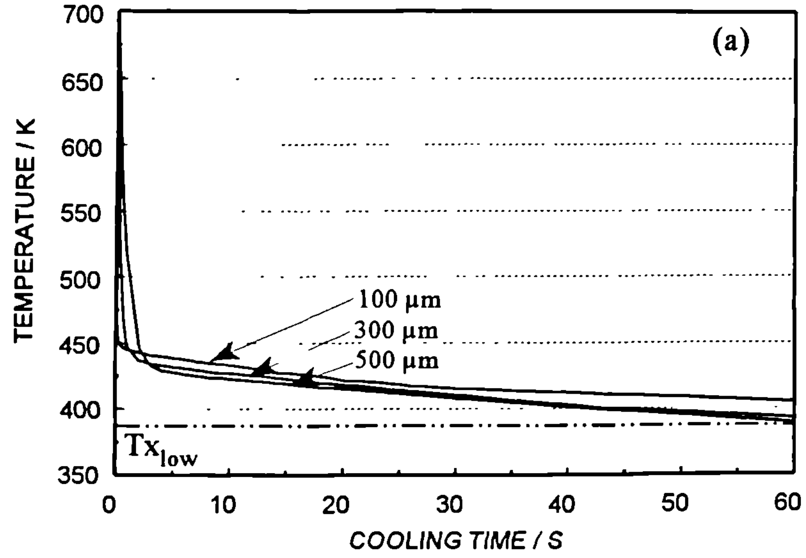

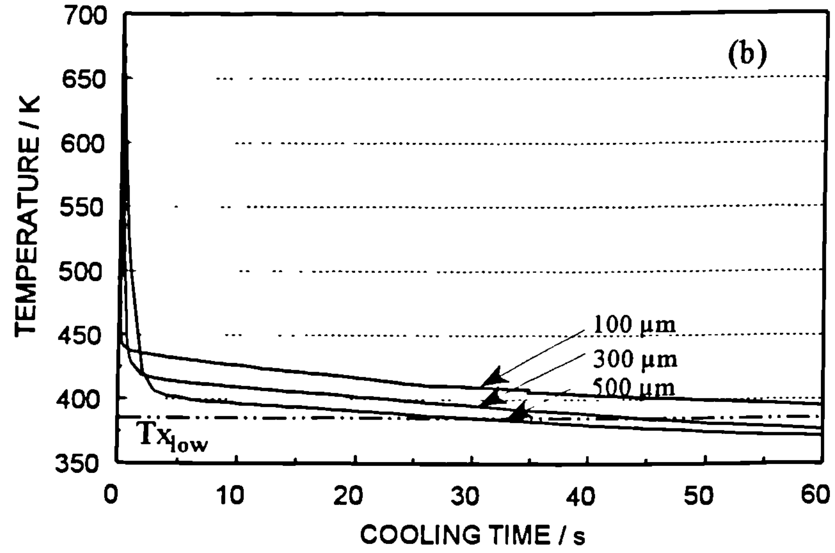

Figure 8.9 Calculated cooling curves for coatings of various thickness deposited on substrate preheated to 453 K (180 °C) at: (a) coating mid-thickness , (b) outer surface of the coating.

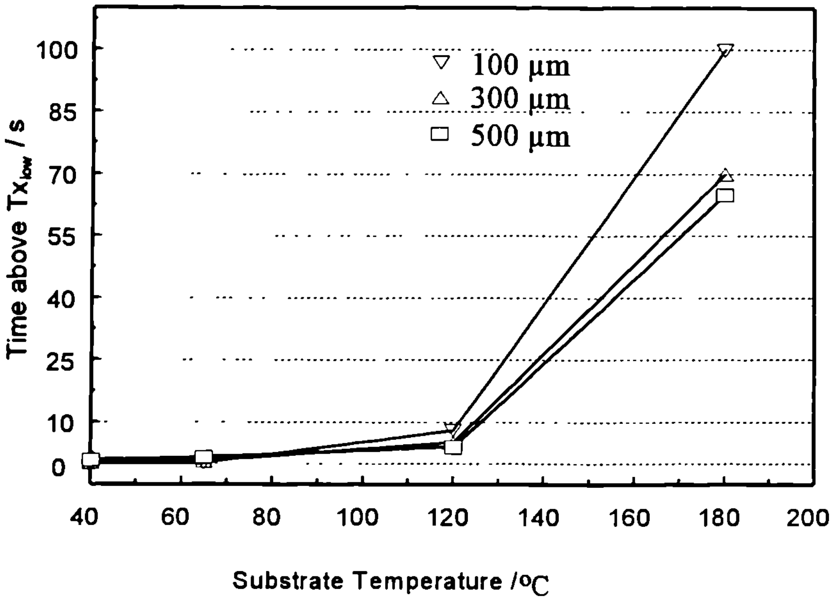

Figure 8.10 The calculated effect of substrate preheating on the coating residence time above the lower cross-linking temperature for various coating thickness.

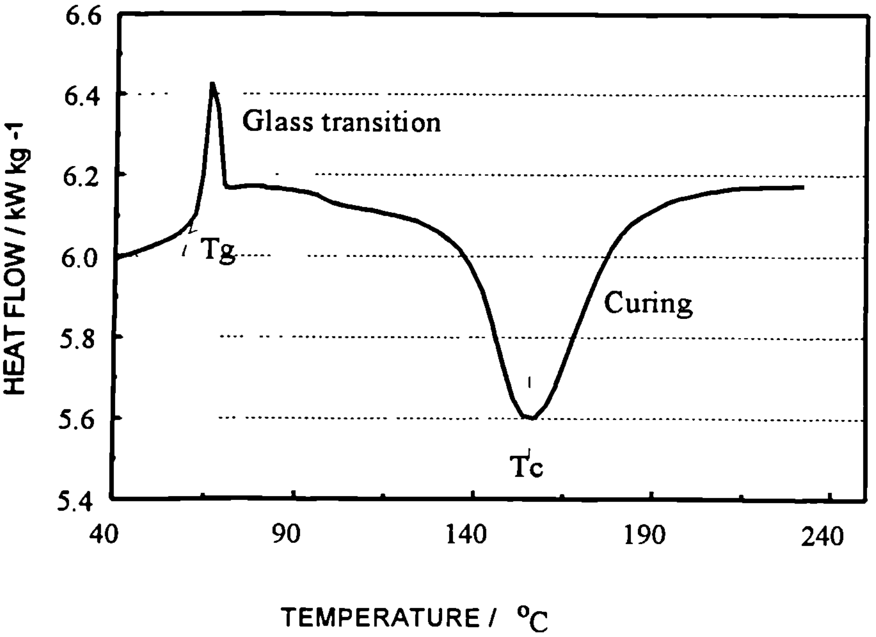

Figure 8.11 Differential scanning calorimetric data for MR4014 feedstock powder.

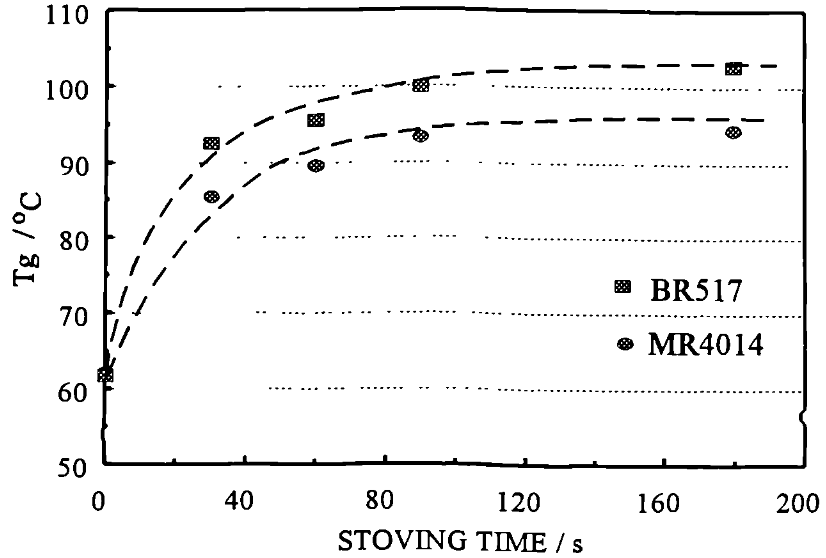

Figure 8.12 Effect of stoving time on the glass transition temperatures of feedstock epoxy powders

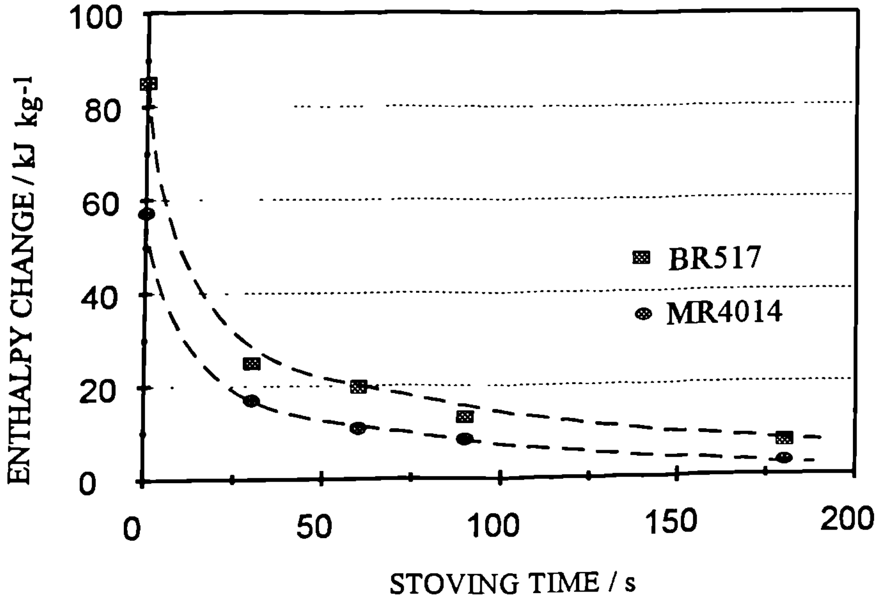

Figure 8.13 Effect of stoving time on the enthalpy changes of feedstock epoxy powders

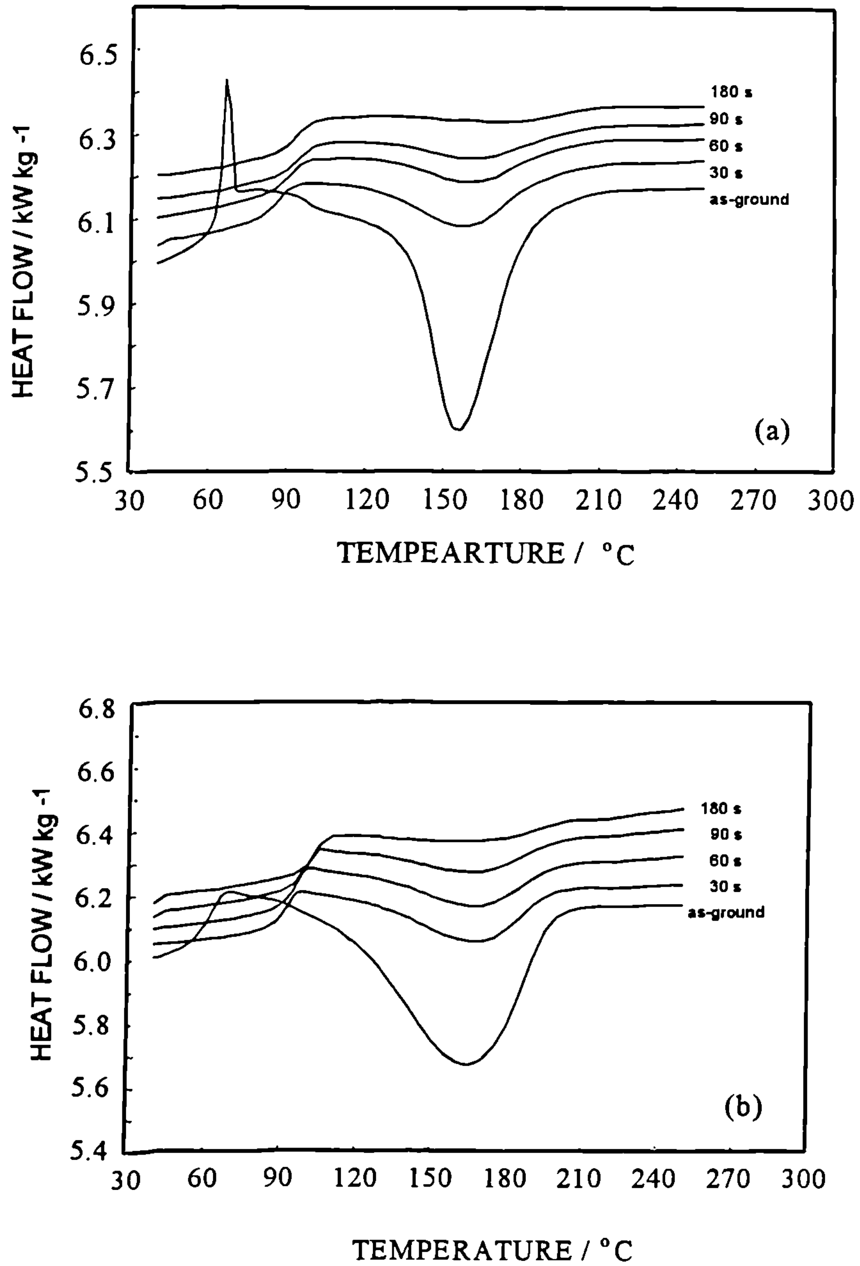

Figure 8.14 Differential scanning calorimetric data for feedstock epoxy powders stoved for various times , (a) MR4014 (b) BR517

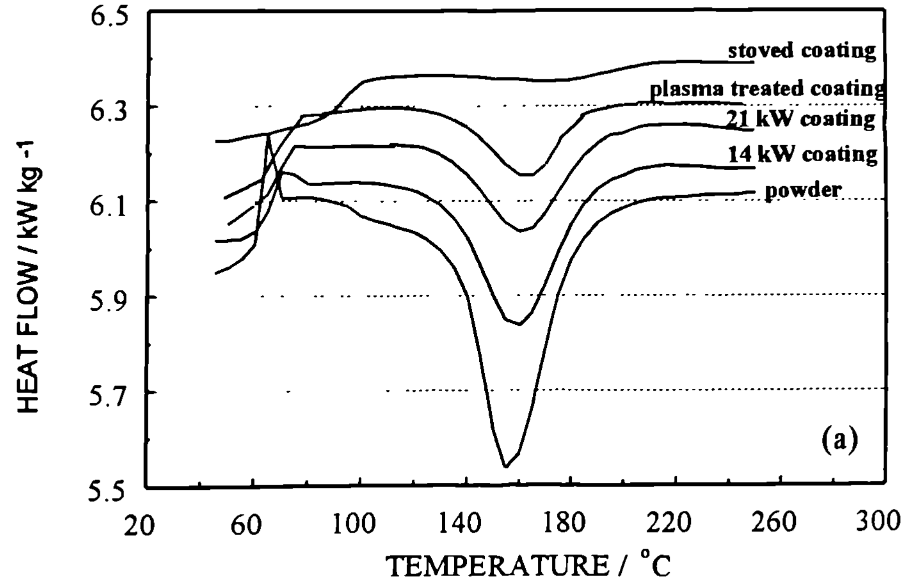

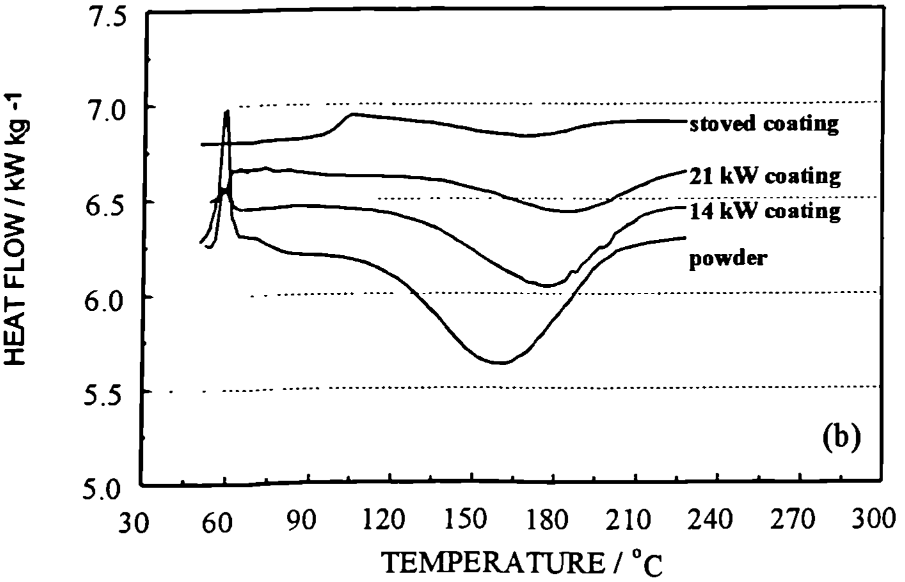

Figure 8.15 DSC traces for plasma deposited epoxy coatings and feedstock powders: (a) MR4014, (b) BR517.

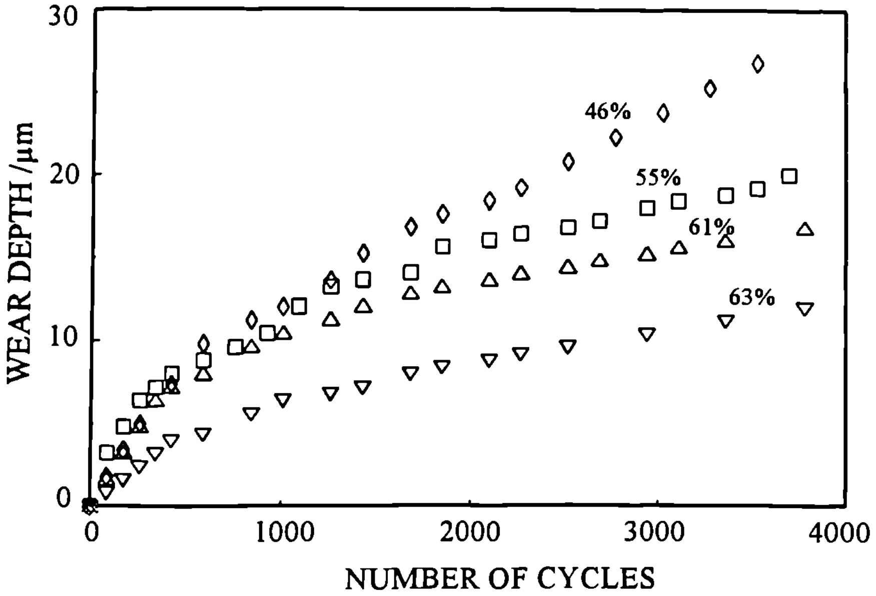

Figure 8.16 Wear behaviour of plasma sprayed epoxy coatings (MR4014). The figure next to each curve refers to the drgree of cross-linking (X value).

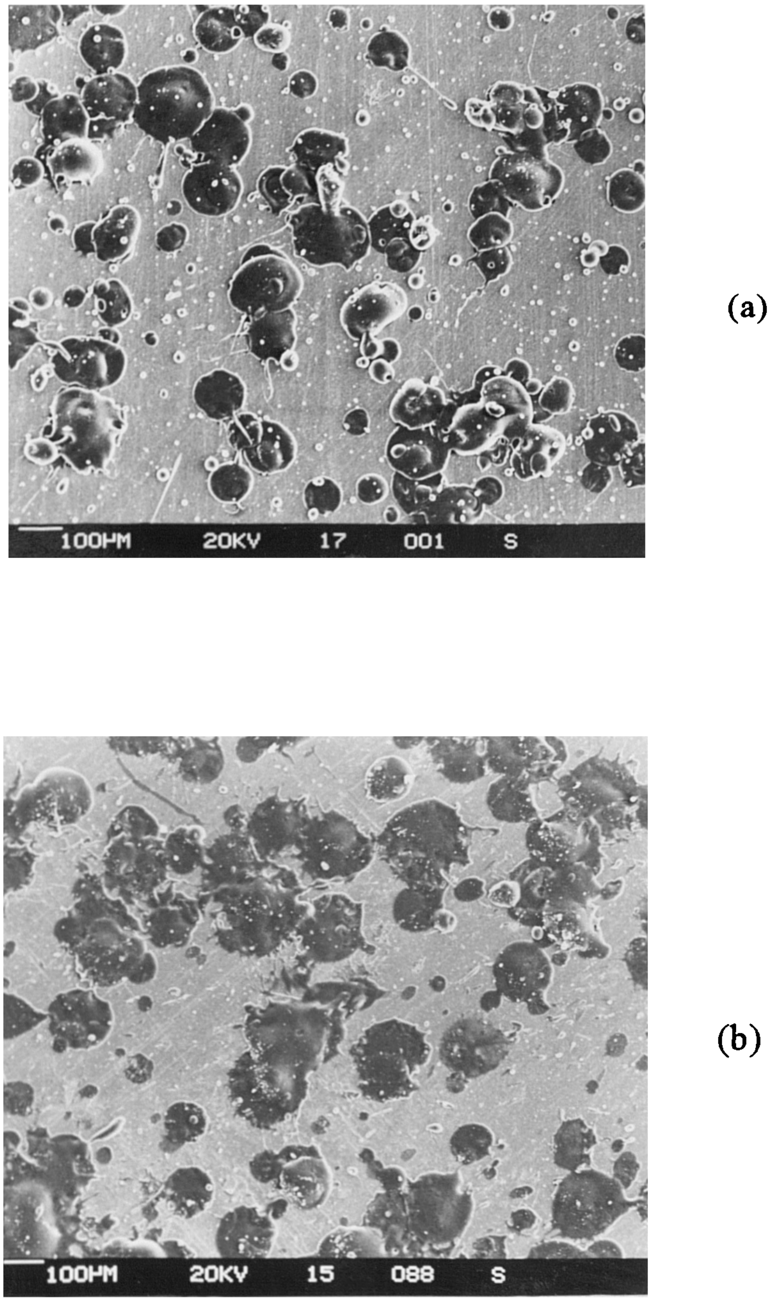

Figure 8.17 SEM micrographs of the epoxy splats (MR4014) produced by wipe testing at different arc power levels: (a) 14 kW, (b) 21 kW.

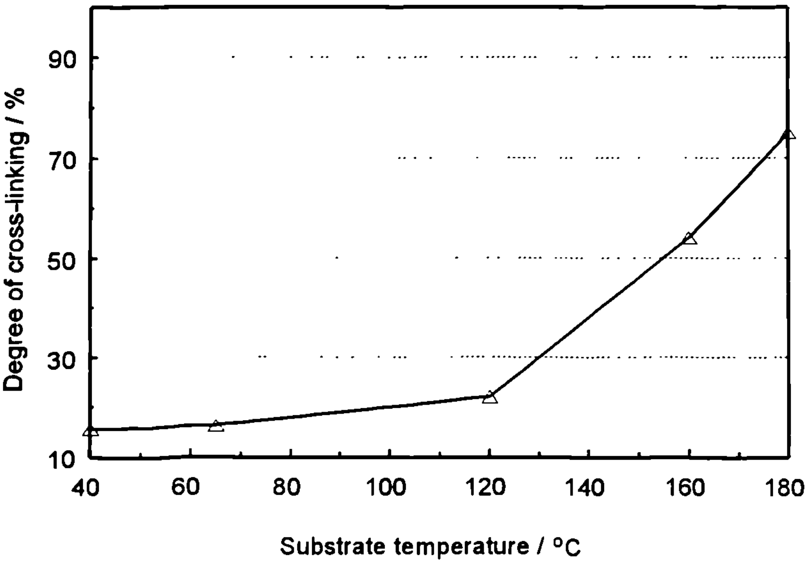

Figure 8.18 Experimental data showing the influence of substrate preheating on the degree of cross-linking of MR 4014 coating of 300 μm thickness.

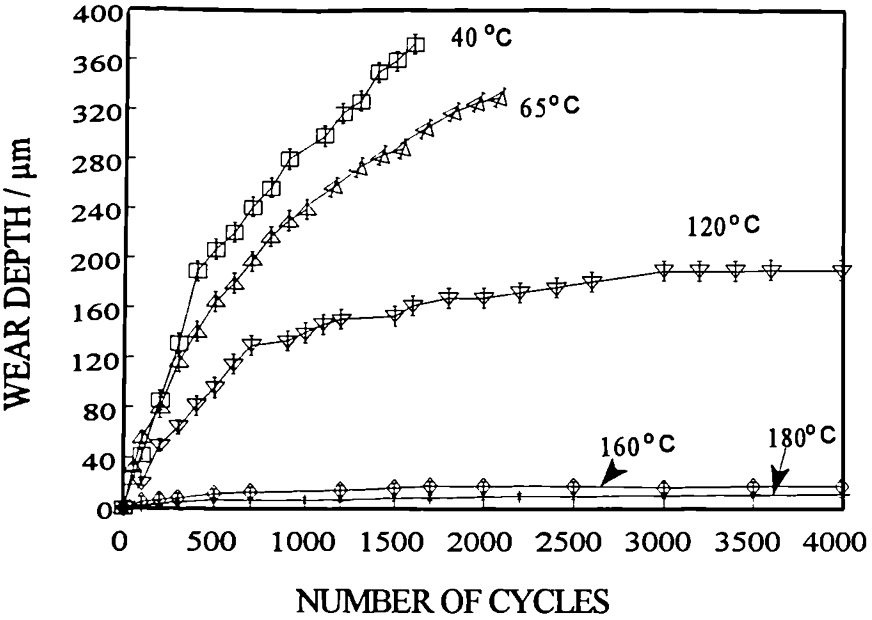

Figure 8.19 The influence of substrate pre-heating on the wear behaviour of MR4014 coatings. The temperature next to each curve refers to the substrate temperature immediately before spraying.

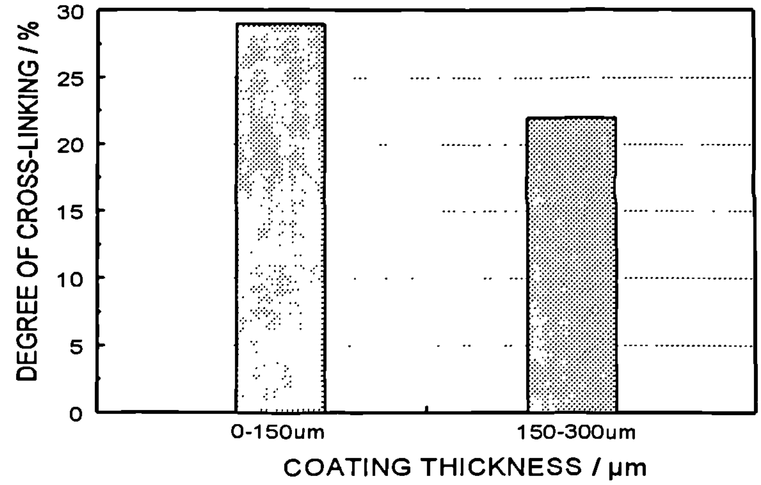

Figure 8.20 The measured cross-linking in the inner and outer thickness section of a 300μm coating produced from MR4014 precursor powder and deposited on a substrate preheated to 120 °C.

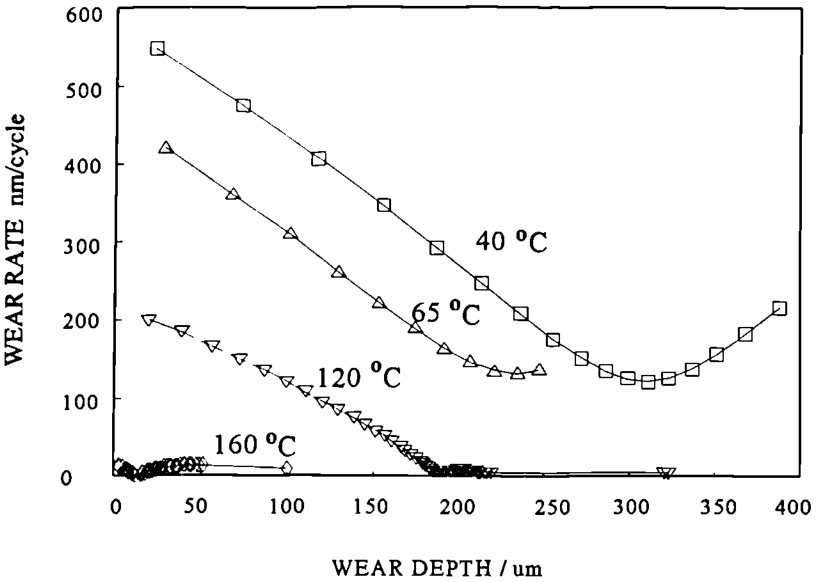

Figure 8.21 The wear rate through the thickness of coatings (MR4014) deposited on substrates preheated to various temperatures. The substrate temperatures are given next to the curves.

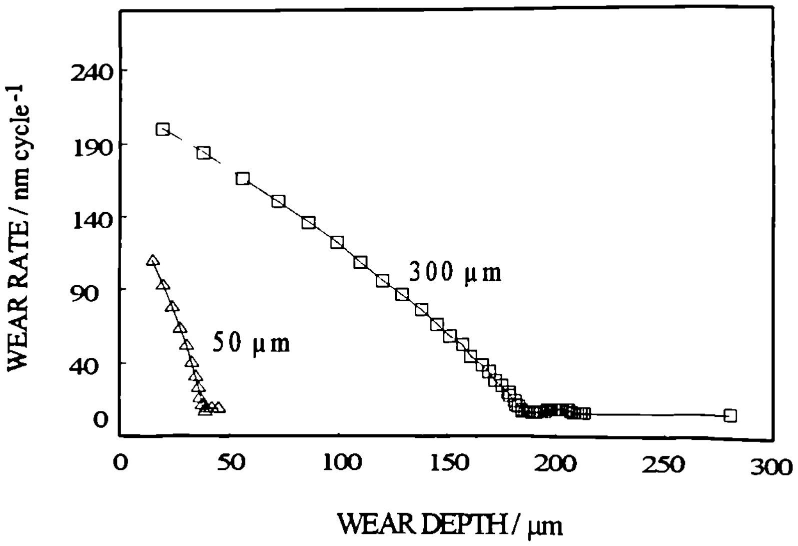

Figure 8.22 The wear rate through the thickness of 50μm and 300μm thick coatings deposited on substrate preheated to 120 °C The precursor powder used was MR4014.

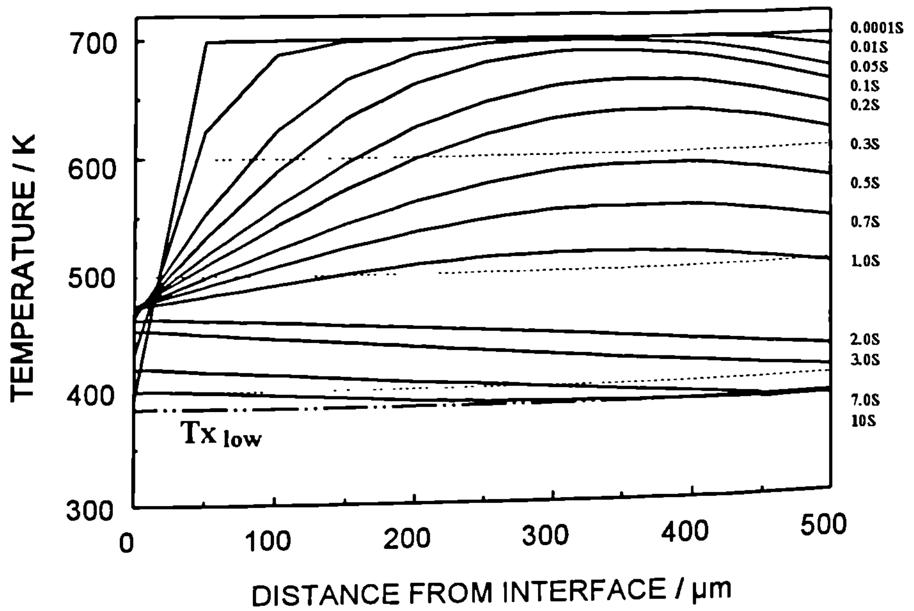

Figure 8.23 Calculated temperature profiles through the thickness of a 500μm coating deposited on the substrate with a 500 μm undercoat of alumina. The substrate-undercoat was assumed to be preheated to 120 °C immediatly before spraying the epoxy.

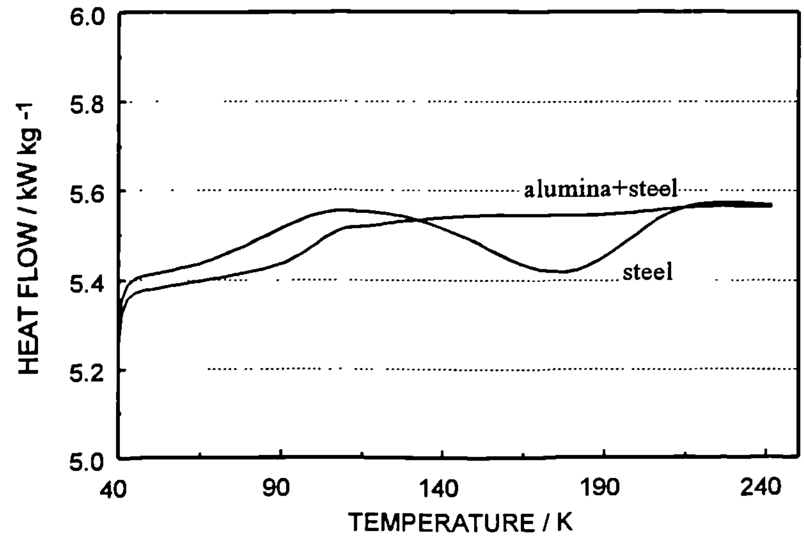

Figure 8.24 DSC traces for thermoset (MR4014) coatings sprayed on to preheated substrates (120 °C). One trace refers to a coating on a substrate with an alumina (500μm thick) undercoat and other on conventional uncoated substrate.

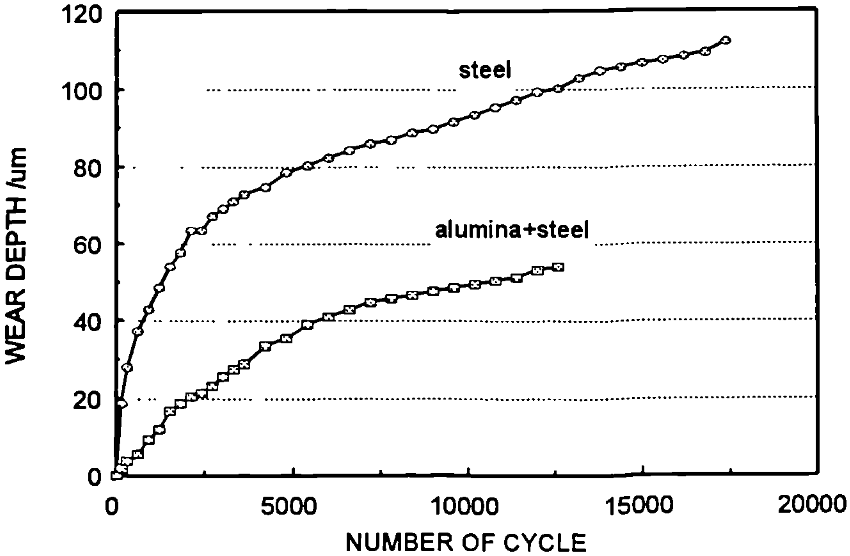

Figure 8.25 Wear behaviour of thermoset (MR4014) coatings sprayed on to preheated substrates (120° C). One curve refers to a coating on a substrate with an alumina (500μm thick) undercoat and the other on to a conventional uncoated substrate.

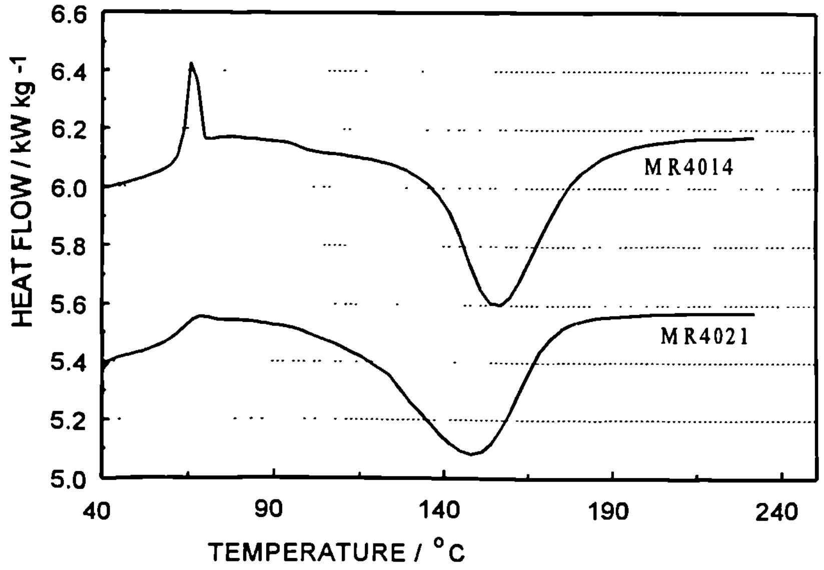

Figure 8.26 Differential scanning calorimetric data for MR4021 precursor powder compared with the conventional MR4014.

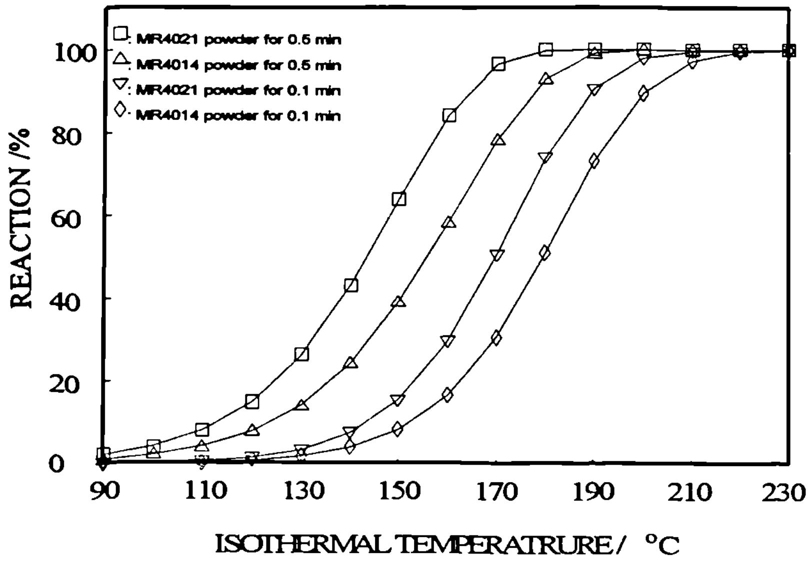

Figure 8.27. Reaction rates of curing for MR4014 and MR4021 precursor powders under isothermal condition

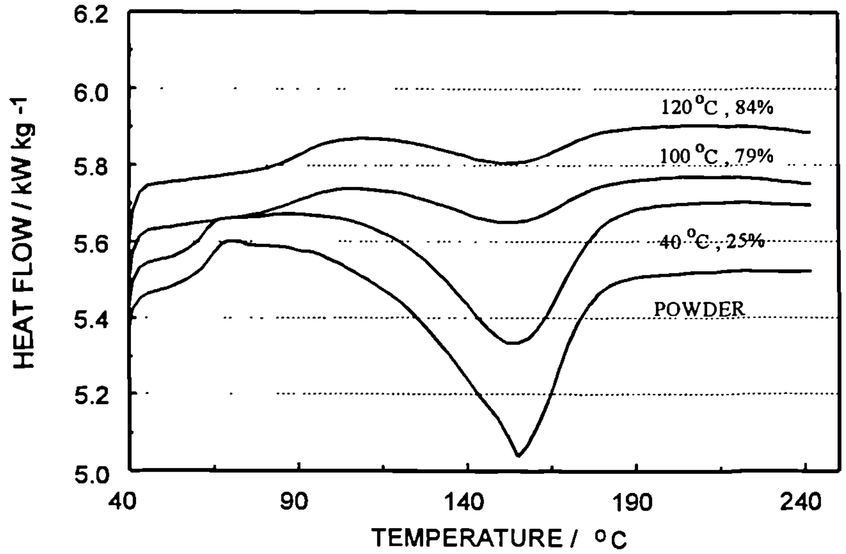

Figure 8.28. Differential scanning calorimetric data for coatings produced using precursor powder MR4021 for various amounts of preheating. The substrate temperature and degree of cross-linking are given next to each curve.

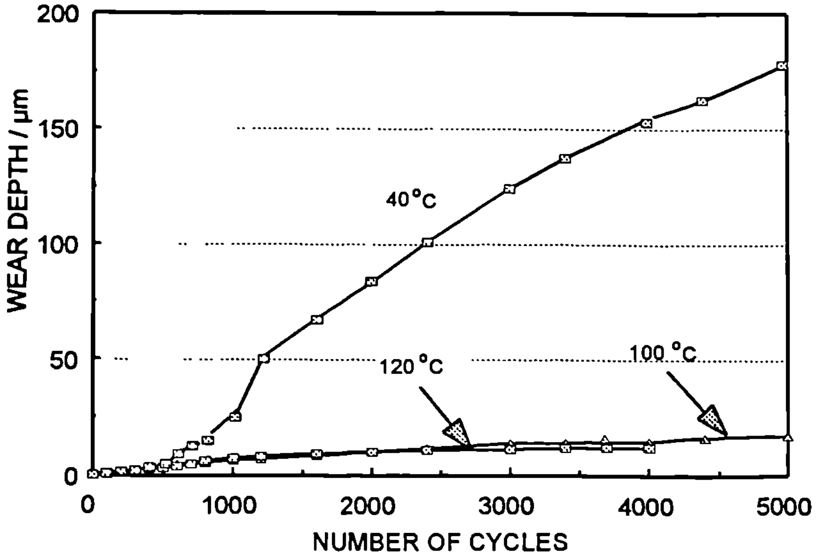

Figure 8.29 Wear behaviour of MR4021coatings under 1kg applied load for various amounts of preheating. The substrate temperatures are given next to each curve.

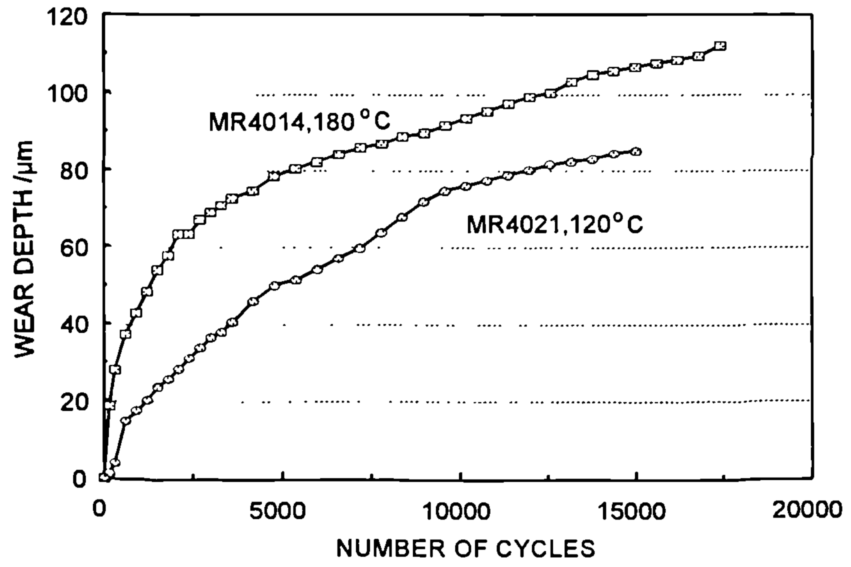

Figure 8.30 Wear behaviour of MR4021 and MR4014 coatings under 6kg applied load. The substrate temperature is given next to the wear curve.

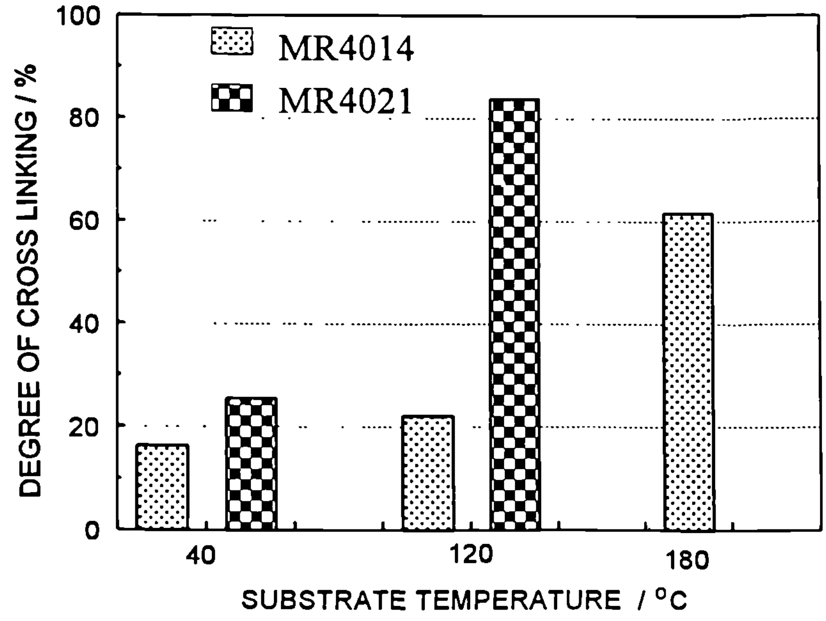

Figure 8.31 Cross-linking in MR4021 coatings and MR4014 coatings deposited on substrates with various amounts of preheating.

CONCLUSIONS

1. Polyamide 11, PMMA and epoxy coatings can be deposited by plasma spraying.
2. Heat transfer analysis under plasma spraying conditions has been carried out and a theoretical model has been developed for the deposition of polymer coatings.
3. The development of large temperature gradients within particles is predicted to be a general characteristic of polymers during plasma spraying and is primarily due to their slow rate of internal heat conduction compared with that of metals and ceramics.
4. Plasma arc power is predicted to affect the temperature, degree of melting and the extent of decomposition of in-flight polymer particles. The optimal arc power level is required to give maximum particle melting and minimum decomposition. The experimental findings show that the optimal arc power giving minimum wear rates and porosity is 21kW for polyamide 11 under the conditions used and this is consistent with the theoretical predictions.
5. The predicted optimal particle size for polyamide under conditions used was 40 to 60 μm. This is consistent with the experimental results which showed maximum density, wear resistance, tensile properties and surface finish of the polyamide 11 coatings processed using this feedstock particle size range.
7. Incompletely melted particles and pores are significant defects within the polymer coatings. The major types of pore observed in the deposits include: (a) those associated with unmelted particles, (b) those resulting from inadequate splat flow, (c) those caused by gas entrapment, (d) those resulting from thermal degradation of the polymer during deposition , and (e) those pre-existing within feedstock particles.
8. The plasma torch traverse speed has a major effect on the plasma spraying of polymers. The critical traverse speed above which no substantial degradation of the deposit takes place is a crucial parameter for plasma spraying of polymers. The critical speed was approximately 100 mms^{-1} for both polyamide

11 and PMMA under the conditions used.

9. The principal mechanism of thermal degradation of polyamide during plasma spraying is considered to be chain scission.
10. The molecular weight of the PMMA coatings decreases with increasing arc power. The profile of the molecular weight distribution changes significantly on plasma spraying with an increase in the volume fraction of small molecules at the expense of a decrease in the volume fraction of large molecules.
11. Preheating the steel substrate up to the melting/softening temperature of the polymer or above substantially improved the coating adhesion.
12. Rough surfaces produced by grit blasting or chemical etching give superior adhesion to clean, smooth surfaces produced by chemical cleaning.
13. Adhesive wear is a major wear mechanism in polyamide 11 coatings with fracture occurring along the splat boundaries. The wear rate increase with increasing porosity of the coatings.
14. The degree of cross-linking of thermoset coatings can be determined experimentally from enthalpy changes measured by differential scanning calorimetry.
15. The theoretical calculations predict that adequate cross-linking is unlikely in an epoxy coating deposited under normal conditions. However, the calculations predict that preheating the substrate, applying a ceramic undercoat and using a faster curing agent will promote crosslinking. The experimental results were found to be in agreement with the theory, and a coating with 85% cross-linking was produced.

FUTURE WORK

Recommendations for future work arising from the studies presented in this thesis are as follows:

1. Investigate the influence of microstructure on the heat transfer of the coating.

2. Extend the range of polymers that can be plasma sprayed, and explore their engineering applications.

3. More detailed examination of the microstructure of plasma sprayed polymers compared with the equivalent bulk polymers.

4. Investigation of possible metastable phases in plasma sprayed polymers.

5. Investigation of the production of the polymer-based composites by plasma spraying.

REFERENCES

1. D.T. Gawne and I.R. Christie, "The UK surface engineering industry". Metals and Materials, 8(1992) pp646-649.
2. K.J. Coeling and T.J. Bublink in J.I. Kroschwitz, ed., "Encyclopedia of polymer science and engineering " vol.3, John Wiley and Sons 1985 pp575-577.
3. J. Gaynor, "Some fundamental aspects of fluidized bed coating". SPE J. 15 (1959) pp1059-1063.
4. W.R. Pascoe, Mater. Des. Eng. 51(2)(1960), p91-95.
5. M.J. Day, "Flame spraying thermoplastics for plastics/metal joining, Part 1-Techniques and experimental procedure". The Welding Institute Research Bulletin. 12(1987), pp409-413.
6. M.F. Brooks, "Plastic (polymer) coatings processes other than flame spraying". Surface Journal International, II(1)(1986) pp26-29.
7. W.E. Ballard in "Metal spraying and the flame deposition of ceramics and plastics". 4th ed publ Griffin, London 1963 pp514-525.
8. F. Schori, "Improved process of and apparatus for atomising", Patent specification 221828, June 11 1925.
9. J. Bishop, "Equipment for the production of flame sprayed plastic coatings". Surface Journal International, 1(1986) pp97-99.
10. J.D. Hearn and R.D. White, "Development of thermal spray equipment for plastic coatings". 9th Int. Thermal Spraying Conf., The Hague, Netherlands, May 1980.
11. J.D. Hearn, "Trends in international thermal spraying of plastics 1979-1984, with a application studies from Europe. USA and Japan". 1st. Int. Conf. on Surface Engineering, Vol. 1: Thermal spraying testing of coatings, Welding Institute. Brighton, June 1985.
12. A.R. Nicoll, A. Bachmann, J.R. Moens and G. Loewe, "The application of high velocity combustion spraying". Proceed. of the Int. Thermal Spray Conf. & Exposition, Orando, Florida, USA, 28 May-5 June 1992, pp149-152.
13. Metallisation Ltd, "Flame sprayed powder coatings for anti-corrosion and

engineering applications", Anti-corrosion, Aug.(1988) p19

14. T.W. Glass and J.A. DePay, "Protective thermoplastic powder coating specifically designed adhesive polymers". Proc. 4th Nat. Thermal Spray Conf. Pittsburgh, PA, USA, 4-10 May 1991, pp345-350.

15. C.E. Blackmore, "Nylon powders and their application as surface coatings using flame spraying", Surface Engineering, 3(1987) pp29-34.

16 E.R. George and J. Reimer, "Flamesprayed thermoplastic powder coatings". Polymer Eng. and Sci. 31(1991) pp789-792.

17. J.Tucker, Vacuum Sci. & Tech. 11(1974) pp725-734.

18. L.N. Moskowitz, "Application of HVOF thermal spraying to solve corrosion problems in the petroleum industry". Proc. of International Thermal Spray Conference & Exposition, Oriando, Florida, USA 28 May-5 June 1992, pp611-618.

19. H. Kreye, "High velocity flame spraying-process and coating characteristics" 2nd Plasma-Technik-Symposium, vol. 1 1992 pp39-47.

20 D.R. Marantz, "The basic principle of electric-arc spraying", in "Science and technology of surface coating". eds B.N. Chapman and J.C. Anderson, Academic Press, London, 1974, pp308-321.

21. B. Gross, B. Grycz and K. Miklossy, "Plasma spraying technology", Iliffe Books Ltd., London 1978, pp11-12.

22. R.M. Gage: US Patent 2806124, Union Carbide Corporation.

23. H. Herman, "Plasma spray deposition processes". MRS Bulletin, Dec.(1988) pp60-67.

24. R.M. Gage, D.H. Nestor and Y.M. Yenni: "Collimaled electric arc powder deposition process". US Patent 3016447, Union Carbide Corporation.

25. B.J. Gill and R.C. Tucker, "Plasma spray coating processes". Materials Science and Technology 2(1986) pp207-213.

26. M. Vardelle, V. Vardelle, P. Fauchais and M.I. Boulos, "Plasma-particle momentum and heat transfer: modelling and measurements". AIChE Journal, 29(1983) pp236-243.

27. A.R. Nicoll, "Plasma spray processing-advanced production features and quality considerations". In "Surface engineering practice-Processes, fundamentals and applications in corrosion and wear", Ellis Horwood, New

York, (1990)pp117-335.

28. K. Kempton, "Where thermal spray coatings are most cost effective". Welding Journal, 8(1981) pp41-44.

29. V. Wilms and H. Herman, "Plasma spray of Al_2O_3 and Al_2O_3-Y_2O_3". Thin Solid Films, 39(1976) pp251-262.

30. H.D. Steffens and M. Mack, "Plasma spraying as an advanced tool in surface engineering". Pure & Appl. Chem. 62(1990) pp1801-1808.

31. D. Matejka and B. Benko, "Plasma spraying of metallic and ceramic materials". John Wiley & Sons, New York, 1989, pp37-39.

32. A.R. Nicoll, H. Gruner, R. Prince and G. Wuest, "Thermal spray coatings for high temperature protection". Surface Engineering 1(1985) pp59-71.

33. P. Mcpherson, "Formation of metastable phases in flame and plasma prepared alumina". J. Mat. Sci. 15(1973) pp3141-3149.

34. R. McPherson, "On the formation of thermally sprayed alumina coatings". J. Mat. Sci. 15(1980) pp3141-3149.

35. C. Robert, J. Tucker, in "Deposition technology for films and coatings: development and applications" Noyes Publications, Park Ridge, N.J., USA, (1982) pp454-489.

36. A.R. Nicoll, H. Gruner, G. Wuest and S. Keller, "Future developments in plasma spray coating". Materials Science and Technology, 2(1986) pp214-219.

37. G. Wuest, S. Keller, A.R. Nicoll and A. Donnelly, "Plasma spray deposition efficiencies". J. Vac. Sci. Technol. A3(6)(1985) pp 2464-2468.

38. Z. Babiak, Wroclaw, "Factors influencing properties of plasma-sprayed layers". Procee. Int. Thermal Spray Conf. DVS 80, (1980) pp64-67.

39. D. Matejka and B. Benko, "Plasma spraying of metallic and ceramic materials". John Wiley & Sons, New York, 1989, p25.

40. J.E. Jackson, "Method of shielding gas effluent". US Patent 3470347, Union Carbide Corporation, 1969.

41. T.A. Taylor, M.P. Overs, B.J. Gill and R.C. Tucker, "Experience with MCrAl and thermal barrier coatings produced via inert gas shrouded plasma deposition". J. Vac. Sci. Technol. A3(1985) pp2526-2531.

42. H. Gruner,"Vacuum plasma spray quality control". Thin Solid Films, 118(1984) pp409-420.

43. M.P. Ducos, "Atmosphere and temperature controlled plasma spraying thick coating and coating on composite resin fibres". 12th Int. Thermal spray. Conf. London, 4-6 June 1989, paper 66.
44. C.W.D. Andrews and B.A. Fuller, "The Deposition of ferrites by arc plasma spraying". Surface Journal, no.5, 1974.
45. D. Matejka and B. Benko, "Plasma spraying of metallic and ceramic materials". John Wiley & Sons, New York, 1989, pp91-125.
46. H.E. Drzeniek, A.K. Sikorski and R. Kaczmarek wroclaw, "Optimization of plasma spraying parameters". Proc. Int. Thermal Spray Conf. DVS80, (1980) pp50-54.
47. Metco Ltd., "Type MCN plasma spray control unit instructions". Metco Ltd., Chobham, Working, England.
48. G.M. Herterick, "Gas selection in plasma spraying". Welding Journal, Feb. 1987, pp27-30.
49. L. Pawlowski, "The science and engineering of thermal spray coatings", John Wiley & Sons, Chichester, UK, 1995, pp22-27.
50. R.L. Apps, "The influence of surface preparation on the bond strength of flame sprayed aluminium coatings into mild steel". J. Vac. Sci. and Technol., 11(1974) pp741-746.
51. J. Wigren, "Grit blasting as surface preparation before plasma spraying". 1st National Thermal Spraying Conference, Orlando, Florida, 14-17 September, (1987) pp99-104.
52. S.V. Joshi and R. Sivakumar, "Prediction of in-flight particle parameters during plasma spraying of ceramic powders". Mat. Sci. & Technol., 8(1992) pp481-488.
53. D.R. Croft and D.G. Lilley, "Heat transfer calculations using finite difference equations". Applied Science Publ. London, 1977 pp 1-87.
54. Y.C. Lee, Y.D. Chyon and E. Pfender, "Particle dynamics and particle heat and mass transfer in thermal plasmas. Part II. particle heat and mass transfer in thermal plasmas". Plasma Chemistry and Plasma Processing, 5(1985) pp391-414.
55. J.A. Lewis and W.H. Gauvin, "Motion of particles entrained in a plasma jet". AIChE Journal 19(1973) pp982-990.

56. M.I. Boulos,"Heating of powders in the fire-ball of an inductive plasma". IEEE Trans. Plasma Sci. 4(1978) pp93-106.
57. T. Yoshida and K. Akashi, "Particle heating in a radio-frequency plasma torch". J. Appl. Phys., 48(1977) p2252.
58. N. El-Kaddah, J. McKelliget and J. Szekely, Metall. Trans. 15B(1984) p59.
59. J.K. Fiszdon, "Melting of powder grains in a plasma flame". Int. J. Heat Mass Transfer, 22(1979) pp749-761.
60. R.B. Bird, W.E. Stewart and E.N. Lightfoot, "Transport phenomena". Moscow, 1974 p.384.
61. I. Kimura and A. Kanzawa, "Experiments on heat transfer to wires in a partially ionized argon plasma". AIAA J13(1965) pp476-481.
62. Y.C. Lee, K.C. Hsu and E. Pfender,"Modelling of particles injected into a D.C. plasma jet". 5th Int. Sym. on Plasma Chemistry, Vol. 2, Heriot-Watt University, Edinburgh, Scotland, 1981, p.795.
63. E. Bourdin, P. Fauchais and M. Boulos, "Transient heat conduction under plasma conditions". Int. J. Heat Mass Transfer, 26(1983) pp567-582.
64. C. Bonet, "Thermal plasma technology for processing of refractory materials" Pure Appl. Chem. 52(1980) p1707-1720.
65. X. Chen and E. Pfender, "Heat transfer to a single particle exposed to a thermal plasma". Plasma Chemistry and Plasma Process, 2(1982) pp185-212.
66. B. Waldie, "Review of recent work on the processing of powders in high-temperature plasmas, Part II: Particle dynamics, heat transfer and mass transfer". Chem. Eng. 259(1972) pp 188-193.
67. G.S. Springer, "Heat transfer in rarefied gases" in "Advances in heat transfer". Vol.7, J.P. Hartnett and T. Irvine, eds., Academic Press, New York (1971) pp163-218.
68. S.A. Schaaf and P.L. Chambre, in "Fundamentals of gas dynamics". H.W. Emmons, ed. Vol. 3, Princeton University Press, Princeton, NJ. 1958.
69. X. Chen and E. Pfender, "Effect of the Knudsen number on heat transfer to a particle immersed into a thermal plasma". Plasma Chemistry and Plasma Processing, 3(1983) pp97-111.
70. X. Chen and E. Pfender, "Behaviour of small particles in a thermal plasma flow". Plasma Chemistry and Plasma Processing, 3(1983) p351.

71. S.V. Joshi, P.R. Taylor and L.S. Richardson, Plasma Chemistry and Plasma Processing, 6(1986) p281.

72. X. Chen, Y.C. Lee, and E.Pfender, "The importance of Knudsen and evaporation effect". 6th Int. Sym. on Plasma Chemistry, Montreal, Canada, 1983.

73. S.K. Rains and R.H. Kadlee, Metall. Trans. 1(1970) p1501

74. P. D. Johnston, "The rate of decomposition of silica particles in an augmented flame". Combust. Flame 18(1974) p.373.

75. X. chen and E. Pfender, "Unsteady heating and radiation effects of small particles in a thermal plasma". Plasma Chem. Plasma Process. 2(1982) pp293-316.

76. E.V. Seymour, "The hydrodynamic drag on a small sphere in an ionized gas". Trans. ASME - J. Appl. Mech. Dec. (1971) pp739-748.

77. G.D. Smith, "Numerical solution of partial differential equations". Oxford University Press, London, 1965.

78. V.Voller and M. Cross, "Accurate solutions of moving boundary problems using the enthalpy method". Int. J. Heat. Mass Transfer. 24(1981) pp545-556.

79. J. Szekely and R.G. Lee, "The effect of slag thickness on heat loss from ladles holding molten steel". Trans. Am. Inst. Min. Engrs - TMS, 242(1968) p961.

80. G.H. Meyer, "Multidimensional Stefan problems", J. Num. Anal. 10(1973) p522.

81. D.R. Atthey, "A finite difference scheme for melting problems". J. Inst. Maths. Applics. 13(1974) p353.

82. D.W. Vankervelen and P.J. Hoftyzer, "Properties of polymers". Elsevier Scientific Publ. Oxford 1976, pp93-97.

83. D.W. Vankervelen and P.J. Hoftyzer, "Properties of polymers". Elsevier Scientific Publ. Oxford 1976, p21.

84. D.W. Vankervelen and P.J. Hoftyzer, "Properties of polymers". Elsevier Scientific Publ. Oxford 1976, pp459-466.

85. W.E. Nelson, "Nylon plastics technology". Newnes-Butterworths, London, 1976.

86. A. Tager, "Physical chemistry of polymers". MIR Publishers, Moscow, 1978, p19.

87. D.R. Croft and D.G. Lilley, "Heat transfer calculations using finite difference equations". Applied Science Publ. London, 1977, pp139-181.

88. J. Madejski, "Solidification of droplets on a cold surface". Int. Heat Mass Transfer, 19(1976) pp1009-1013.

89. H. Jones, "Cooling, freezing and substrate impact of droplets formed by rotary atomization". J. Physics, 4(1971), pp1657-1660.

90. Borgerding and H.J. Solter, "Computer simulation of temperature distribution within thermally sprayed coatings during the plasma spraying process". 2nd Plasma Tecnnik Symposium vol.1 1992, pp65-73.

91. R. MacPherson, "The relationship between the mechanism of formation, microstructure and properties of plasma sprayed coatings". Thin Solid Films 83(1981) pp297-310.

92. H. Hamatani, T. Okada, T. Yoshida, Proceedings of Intern. Symp. on Plasma Chemistry, Bochum, Germany, August 1989, pp1527-1732.

93. O.P. Solonenko, "Complex investigation of thermophysical processes in plasma-jet spraying ". Pure and Applied Chemistry, 62(1990) pp 1783-1800.

94. G. Trapaga and J. Szekely, "Mathematical-modelling of the isothermal impingement of liquid droplets in spraying processes". Metallurgical Transactions B, 22(1991) pp901-914.

95. S. Fantassi, M. Vardelle, A. Vardelle and P. Fauchais, "Influence of the velocity of plasma sprayed particles on the splat formation". Proceeding of Nation. Thermal Spray Conf., Anaheim, CA, USA, 7-11 June 1993, pp1-6.

96. L. Pawlowski and P. Fauchais, "Thermal transport properties of thermally sprayed coatings". International Materials Reviews, 37(1992) pp271-289.

97. R.C. Progelhoe, J.L. Throne and R.R. Ruetsch, "Methods for predicting the thermal conductivity of composite systems: - A review". Polymer Eng. Sci. 16(1976) pp615-625.

98. R. McPherson, "A review of microstructure and properties of plasma sprayed ceramic coatings". Surf. Coat. Technol., 39/40(1989) pp 173-181.

99. R. McPherson, "A model for the thermal conductivity of plasma sprayed ceramic coatings". Thin Solid Films, 112(1984) pp89-95.

100. ICI plc. "DIAKON" Technical manual. R&D Department, Petrochemical and Plastic Division, Imperial Chemical Industry plc.

101. J.W. Nicholson, "The chemistry of polymers". Royal Society of Chemistry, Paperbacks, Thomas Graham House, Cambridge, 1991, pp1-25.
102. H. Lee and K. Neville, "Epoxy Resins: their application and technology". McGraw-Hill Book Company, London, 1957.
103. W.G. Potter, "Epoxide Resins". Butterworth & Co. Ltd. London, 1970.
104. J.A. Sprackling, "Epoxy powder coatings: an introduction". Surface Coatings, March (1965) pp80-83.
105. J.A. Sprackling, "Epoxy powder coatings: an Assessment". Surface Coatings, March (1965) pp90-94
106. "Marine tank protection, corrosion problems and their solution". Surface Coatings, Feb. (1965) pp49-52.
107. T.R. Crompton, "Analysis of polymers : An introduction". Pergamon Press, Oxford, 1989, pp214-215.
108. "Users manual for DSC 7 Differential Scanning Calorimeter", Perkin-Elmer Ltd. Beaconsfield, Bucks, England.
109. D.H. Williams and I. Fleming, "Spectroscopic methods in organic chemistry". 2nd edi. McGraw-Hill Book Company Ltd. London, 1973, pp35-73.
110. "Technical Information for 680 Infrared Spectrophotometer", Perkin-Elmer Ltd., Beaconsfield, England.
111. B.D. Cullity, "Elements of x-ray diffraction". 2nd edi. Addison-Wesley Publishing Company, London, 1978, pp86-87.
112. P.W. Clark and J. White, Trans. Brit. Ceram. Soc. 49(1950) pp305.
113. "Standard test method for tensile properties of plastics", ASTM D638-77a.
114. "Rubber, vulcanized or thermoplastic - determination of tensile stress-strain properties". British Standard Institution, BS 903: Part A2, 1995.
115. British Standard Methods of test for paints: " Part E10. Pull-off test for adhesion". British Standard Institution, BS 3900: Part E10, 1979.
116. "Standard test method for kinematic viscosity of transparent and opaque liquid and the calculation of dynamic viscosity", ASTM D445-79.
117. "Standard specifications and operating instructions for glass capillary kinematic viscosities", ASTM D446-74.
118. R.M. Ogorkiewicz, "Engineering properties of thermoplastics". John Wiley & Sons, London, 1971, pp61-273.

119. R. Morrell, "Handbook of properties of technical & engineering ceramics, Part 2, data reviewsumina ceramics". H.M.S.O., London , 1978, pp95-99.

120. Y.S. Touloukian, R.W. Powell, C.Y. Ho and P.G. Klemens, "Thermophsical properties of matter, vol. 1 - Thermal conductivity Metallic elements and alloys". IFI/Plenum, New York, 1970, pp415-423.

121. R.A. Farrington and A. Daniels, "Physical chemistry". 5th edi. John Wiley & Sons, New York, 1980.

122. B.G. Achhammer, F.W. Reinhart and G.M. Kline, "Mechanism of the degradation of polyamides". J. Res. Nat. Bureau standards, 46(1951) pp391-421.

123 S. Strauss and L.A. Wall, "Pyrolysis of polyamides". J. Res. Nat. Bureau standards, 60(1958) pp391-421.

124. B. Kamerbeek, G.H. Kroes and W. Grolle, in "High temperature resistance and thermal degradation of polymers", Soc. Chem. Indust. Monograph 13(1961) p357.

125. G.W. Harding and B.J. MacNulty, in " "High temperature resistance and thermal degradation of polymers", Soc. Chem. Indust. Monograph 13(1961) p393-412.

126. A.V. Tobolsky, in "Polymer science and materials", edited by A.V. Tobolsky and H.F. Mark, Wiley-Interscience, 1971 pp83-94.

127. T. Kashiwagi, T. Hirata and J.E. Brown, "Thermal and oxidative degradation of poly(methylmethacrylate): molecular weight". Macromolecules, 18(1985) pp131-138.

128. J.R. MacCallum, "The thermal degradation of poly(methyl methacrylate)". Makromol. chem., 83(1965) pp137-147.

129. Y.N. Sun, M.D. Sacks and J.W. Willims, "Pyrolysis behaviour of acrylic polymers and acrylic polymer/ceramic mixtures". pp538-548.

130. B. Wunderlich, "Macromelecular physics", Volume 1, Academic Press, London, 1980, p132.

131. B. Wunderlich, "Macromelecular physics", Volume 3, Academic Press, London, 1980, pp23-44.

132. K. Slichter, J. Polymer Sci. 36(1959) p259.

133. H.S. Ingham, Jr, "Adhesion of flame-sprayed coatings". In "Adhesion

measurement of thin films, thick films, and bulk coatings", editor: K.L. Mittal, American Society for Testing and Materials, ASTM Special Technical Publication 640, Philadelphia, 1976, pp285-292.

134. K.L. Mittal, "Adhesion measurement recent progress, unsolved problems and prospects". In "Adhesion measurement of thin films, thick films, and bulk coatings", editor: K.L. Mittal, American Society for Testing and Materials, ASTM Special Technical Publication 640, Philadelphia, 1976, pp5-16.

135. A. Ghijsels and C.H. Klaren, "Fundamental factors governing the appearance and performance of epoxy powder coating films". XIIth FATIPEC Congress book, 1974, pp269-275.

136. J.M.G. Cowie, "Polymers: Chemistry and physics of modern materials". International Textbook Company Ltd. 1973, pp209-222.